

**ADVANCED STRATEGIES FOR IMAGING MASS SPECTROMETRY  
AND ION MOBILITY - MASS SPECTROMETRY**

JAY GARRETT FORSYTHE

Dissertation

Submitted to the Faculty of the  
Graduate School of Vanderbilt University  
in partial fulfillment of the requirements

for the degree of

DOCTOR OF PHILOSOPHY

in

Chemistry

May, 2014

Nashville, Tennessee

Approved:

John A. McLean, Ph.D.

David E. Cliffler, Ph.D.

David W. Wright, Ph.D.

Donna J. Webb, Ph.D.

This work is dedicated to my grandfather, James Elton Cloud (1919-2009).

I think G. K. Chesterton was writing about you when he said “supreme strength is shown in levity.” Your legacy of love and gentleness will never pass away.

## ACKNOWLEDGEMENTS

First of all, I would like to thank my Ph.D. advisor, Professor John McLean, for being a good man and a helpful advisor. I have learned a great deal from you about science, teaching, and life. Thank you for giving me freedom and space to explore and develop my own ideas. Also, thank you for encouraging me in my teaching endeavors instead of seeing them as a hindrance to my research. I am very fortunate to have worked in your laboratory and expect it to produce top-notch science for many years to come.

Thank you to my Ph.D. committee, Professor David Cliffler, Professor David Wright, and Professor Donna Webb, for challenging and refining my abilities as a scientist, both during and outside of official committee meetings. Your input not only made me a better researcher but also directly increased the quality of the scientific publications on which I worked. In addition, thank you to Professor Webb for being a wonderful collaborator on the NIMS project.

Thank you to Professor Sharon Weiss for collaborating on the NIMS project and allowing me to fabricate the substrates in your lab. The research described in this dissertation would have never been possible without your help.

Thank you to Professor David Hercules for being like a second advisor to me. I have learned a lot from you about mass spectrometry and materials chemistry, and thoroughly enjoyed our conversations.

Thank you to all of the former and current graduate students and postdoctoral researchers in the McLean research laboratory: Jody May, Larissa Fenn, Kellen Harkness, Josh Kerr, Randi Gant-Branum, Michal Kliman, Sevugarajan Sundarapandian, Jeff Enders, Cody Goodwin, Seth Byers, Kelly Hines, Sarah Stow, Nichole Lareau, Katie Leaptrot, Rafael Montenegro, Caleb Morris, Andy Cognata, and Chatney Spencer. I am honored to call you co-workers. In particular, I want to thank Michal Kliman for your mentorship when I was an early graduate student. Also, thank you to collaborators from other research labs, especially Joshua Broussard, Jenifer Lawrie, Yang Jiao, and Jeremy Mares.

Thank you to the funding sources which supported this research: the Vanderbilt University College of Arts and Sciences, Vanderbilt Institute of Chemical Biology, Vanderbilt

Institute for Integrative Biosystems Research and Education, the National Institutes of Health (RC2DA028981, RO1GM092218, RO1HD064727, and UH2TR000491), and the US Defense Threat Reduction Agency (HDTRAI-09-1-001 and DE-001165).

Thank you to everyone at Belmont UMC for your friendship and support. You continually reminded me about the most important things in life. In particular, thanks to Ken Edwards, Pam Hawkins, Gayle Morin, Ed Batsel, Jim Strickland, Hugh Wright, Louis and Mary Kaye Jordan, and Bart Perkey for involving me in the work and community of the church. Belmont will always be a “home away from home” for me.

Thank you to all of my friends in Nashville who have helped to make these past 4+ years a wonderful period in my life, especially Kent Miller, Ben Konecny, Chris Gulka, Dan Hermanson, Matt O'Reilly, Evan Gizzie, Matt Casey, Kelly Hines, Seth Byers, Nick Chrisohon, Lindsey Solomon, Stephen Jackson, Betsy Thomas, Tadarius Turner, Will Young, and the VU soccer crew. In particular, thanks to Kent Miller and Ben Konecny for being such great roommates over the past several years. You are both great men who are making the world a better place. I am very fortunate to consider you as friends.

Thank you to my friends from Pennsylvania and from Furman, especially Jeff Smyth, Phil Grenier, Jonathan Lester, Jacob Carlson, Jay Moneymaker, Todd Stiles, Tyler Ferrier, T.J. Cofield, Will Whitson, Patrick Wallace, Wes Donaldson, Stephen Ramey, Zach Prudowsky, Derek Pitman, Madison McClendon, and Cody Morelock. Your friendship has been and surely will continue to be a blessing.

Finally, thank you to my family: Mom, Dad, Keri, Casey, Grandma and Papa Forsythe, Aunt Patty, and the whole Wortz gang. I cannot even put into words how grateful I am for each and every one of you.

## TABLE OF CONTENTS

ACKNOWLEDGEMENTS .....	iii
LIST OF TABLES .....	vii
LIST OF FIGURES .....	viii
LIST OF ABBREVIATIONS .....	x
CHAPTERS	
1. NANOMATERIAL-BASED MATRICES FOR MATRIX-ASSISTED LASER DESORPTION / IONIZATION (MALDI) MASS SPECTROMETRY IMAGING	
1.1 An Introduction to MALDI Mass Spectrometry .....	1
1.2 Nanomaterial Matrices in MALDI .....	9
1.3 Biological Tissue Imaging using Nanomaterial Matrices .....	12
1.4 Prospects in Single-cell Imaging .....	16
1.5 Conclusions and Objectives .....	17
1.6 References .....	20
2. SEMI-TRANSPARENT NANOMATERIAL THIN FILMS FOR MASS SPECTROMETRY IMAGING AND OPTICAL MICROSCOPY	
2.1 Introduction .....	28
2.2 Experimental Section .....	29
2.3 Results and Discussion .....	32
2.4 Conclusions .....	46
2.5 Acknowledgements .....	46
2.6 References .....	47
3. HYBRID ORGANIC-INORGANIC NANOMATERIAL TARGET SUBSTRATES FOR ENHANCED IONIZATION OF BIOLOGICAL MOLECULES	
3.1 Introduction .....	50
3.2 Experimental Section .....	52
3.3 Results and Discussion .....	55
3.4 Conclusions .....	65
3.5 Acknowledgements .....	65
3.6 References .....	66

4.	STRUCTURAL ANALYSIS OF ISOMERIC POLYMER PRECURSORS BY MASS SPECTROMETRY AND ION MOBILITY - MASS SPECTROMETRY	
4.1	Introduction .....	68
4.2	Experimental Section .....	72
4.3	Results and Discussion .....	75
4.4	Conclusions .....	92
4.5	Acknowledgements .....	92
4.6	References .....	93
5.	CONCLUSIONS AND FUTURE DIRECTIONS	
5.1	Conclusions .....	97
5.2	Dynamic Light Patterning-based NIMS Imaging .....	98
5.3	Phosphopeptide-affinity NIMS Targets .....	99
5.4	Structural Analysis of Multimeric MDA .....	105
5.5	References .....	111
	APPENDIX .....	112
A.	Protocol for Fabrication of NIMS Substrates	
B.	Protocol for SEM of NIMS Substrates	
C.	SEM Images of NIMS Substrates	
D.	NIMS Supplemental Material	
E.	MDA Supplemental Material	
F.	Raw Mass Spectrometry Data from Dissertation Figures	
G.	Raw Ion Mobility Data Shown in Dissertation Figures	
H.	References of Adaptation for Chapters	
I.	Curriculum Vitae	

## LIST OF TABLES

<b>Table 1-1</b>	Common Organic Matrices for MALDI-MS .....	3
<b>Table 1-2</b>	Summary of Nanomaterial-based MALDI Matrices used for MS Imaging .....	18
<b>Table 2-1</b>	Etching Conditions for NIMS Substrates and Surface Characteristics .....	35
<b>Table 3-1</b>	General Information on Novel Matrices for Hybrid NIMS-MALDI Surface .....	54
<b>Table 4-1</b>	Potential Structures of Commonly Observed MDA Fragment Ions .....	78
<b>Table 4-2</b>	Collision Cross Section Values of MDA Ions .....	82
<b>Table 4-3</b>	Relative Stability of MDA Ions in the Gas Phase .....	88

## LIST OF FIGURES

<b>Figure 1-1</b>	General Schematic of Matrix-assisted Laser Desorption/Ionization.....	2
<b>Figure 1-2</b>	nano-MALDI Web of Science™ Citation Chart .....	11
<b>Figure 2-1</b>	SEM Imaging of Semi-transparent NIMS Substrates .....	34
<b>Figure 2-2</b>	Optimization of Semi-transparent NIMS Substrates .....	36
<b>Figure 2-3</b>	Qualitative Evaluation of Transparency .....	37
<b>Figure 2-4</b>	Background Signals in NIMS Analysis .....	39
<b>Figure 2-5</b>	Stability and Sensitivity of NIMS Substrates .....	40
<b>Figure 2-6</b>	Optical and NIMS Imaging of Cell Monolayer .....	41
<b>Figure 2-7</b>	Instrumentation for NIMS Imaging .....	43
<b>Figure 2-8</b>	NIMS Imaging Pixel Size .....	44
<b>Figure 2-9</b>	Identification of Imaged Lipids by Post-source Decay .....	45
<b>Figure 3-1</b>	Molecular Structures of Initiator and Novel Matrices .....	51
<b>Figure 3-2</b>	Hypothesized Surface Interactions between Initiator and Matrix .....	53
<b>Figure 3-3</b>	Evaluation of Matrix Performance and UV Absorption Profiles .....	57
<b>Figure 3-4</b>	Comparison of MALDI, NIMS, and Hybrid NIMS-MALDI .....	59
<b>Figure 3-5</b>	DHB-59 Matrix Photo-fragmentation .....	60
<b>Figure 3-6</b>	Matrix Control Experiment .....	61
<b>Figure 3-7</b>	Matrix Suppression Effect in NIMS-MALDI .....	63
<b>Figure 3-8</b>	Improved MS Detection of Peptides and Proteins .....	64



<b>Figure 4-1</b>	Structure of Polyurethane .....	69
<b>Figure 4-2</b>	MDA Structural Isomers .....	70
<b>Figure 4-3</b>	MS and Tandem MS of MDA Isomers .....	76
<b>Figure 4-4</b>	Tandem MS of Unexpected 211 Da Signal .....	79
<b>Figure 4-5</b>	Evaluation of Isomer Gas Phase Stability by Tandem MS .....	80
<b>Figure 4-6</b>	Extracted Ion Mobility Chromatograms and Computational Clusters .....	84
<b>Figure 4-7</b>	Extracted IM-MS/MS Chromatograms of MDA Isomers .....	85
<b>Figure 4-8</b>	Structures of MDA Isomers in the Gas Phase .....	89
<b>Figure 4-9</b>	Mechanisms of 199 Da → 106 Da Fragmentation Pathways .....	91
<b>Figure 5-1</b>	Laser Focusing using DLP Optical Train .....	100
<b>Figure 5-2</b>	DLP Optical Train .....	101
<b>Figure 5-3</b>	Detection of Phosphopeptide Standard from NIMS Substrate .....	103
<b>Figure 5-4</b>	Characterization of TiO <sub>2</sub> Particles for Phosphopeptide Enrichment .....	104
<b>Figure 5-5</b>	Favorable Structures of MDA Trimer .....	106
<b>Figure 5-6</b>	Zoomed-in Mass Spectrum of MDA Trimer .....	107
<b>Figure 5-7</b>	Tandem Mass Spectra of [M-H] <sup>+</sup> Ions Generated by MALDI .....	109

## LIST OF ABBREVIATIONS

<b>BisF17</b>	Bis(heptadecafluoro-1,1,2,2-tetrahydrodecyl)tetramethyldisiloxane
<b>CCS</b>	Collision Cross Section
<b>CHCA</b>	$\alpha$ -cyano-4-Hydroxycinnamic Acid
<b>CID</b>	Collision Induced Dissociation
<b>COM</b>	Center-of-mass
<b>DHB</b>	2,5-Dihydroxybenzoic Acid
<b>DLP</b>	Dynamic Light Patterning
<b>DMEM</b>	Dulbeco's Modified Eagles Medium
<b>DTIM</b>	Drift Tube Ion Mobility
<b>EDX</b>	Energy-dispersive X-ray Spectroscopy
<b>ESI</b>	Electrospray Ionization
<b>ESPT</b>	Excited-state Proton Transfer
<b>eV</b>	Electron-volt
<b>GC-MS</b>	Gas Chromatography - Mass Spectrometry
<b>IM-MS</b>	Ion Mobility - Mass Spectrometry
<b>IM-MS/MS</b>	Ion Mobility - Tandem Mass Spectrometry
<b>IR</b>	Infrared
<b>ITO</b>	Indium Tin Oxide
<b>LAESI</b>	Laser Ablation Electrospray Ionization

<b>LA-ICP-MS</b>	Laser Ablation - Inductively Coupled Plasma - Mass Spectrometry
<b>LC-MS</b>	Liquid Chromatography - Mass Spectrometry
<b>LC-MS/MS</b>	Liquid Chromatography - Tandem Mass Spectrometry
<b>MALDI</b>	Matrix-assisted Laser Desorption/Ionization
<b>MDA</b>	Methylenedianiline
<b>MDI</b>	Methylene Diphenyl Diisocyanate
<b>MS</b>	Mass Spectrometry
<b>MS/MS</b>	Tandem Mass Spectrometry
<b>M/Z</b>	Mass-to-charge ratio
<b>NALDI</b>	Nano-assisted Laser Desorption/Ionization
<b>Nano-MALDI</b>	Nanomaterial-based Matrix-assisted Laser Desorption/Ionization
<b>Nano-PALDI</b>	Nanoparticle-assisted Laser Desorption/Ionization
<b>Nd:YAG</b>	Neodymium-doped Yttrium-aluminum-garnet
<b>NIMS</b>	Nanostructure-initiator Mass Spectrometry
<b>NMR</b>	Nuclear Magnetic Resonance Spectroscopy
<b>PC</b>	Phosphatidylcholine
<b>pSi</b>	Porous Silicon
<b>RESP</b>	Restrained Electrostatic Potential
<b>RSD</b>	Relative Standard Deviation
<b>SA</b>	Sinapinic Acid

<b>SALDI</b>	Surface-assisted Laser Desorption/Ionization
<b>SEM</b>	Scanning Electron Microscopy
<b>SIMS</b>	Secondary Ion Mass Spectrometry
<b>SMALDI</b>	Scanning Microprobe Matrix Assisted Laser Desorption/Ionization
<b>THAP</b>	2,4,6-Tryhydroxyacetophenone
<b>TLC</b>	Thin Layer Chromatography
<b>TOF</b>	Time-of-flight Mass Analyzer
<b>T-wave</b>	Traveling-wave Ion Mobility
<b>UV</b>	Ultraviolet

## CHAPTER I

### NANOMATERIAL-BASED MATRICES FOR MATRIX-ASSISTED LASER DESORPTION / IONIZATION (MALDI) MASS SPECTROMETRY IMAGING

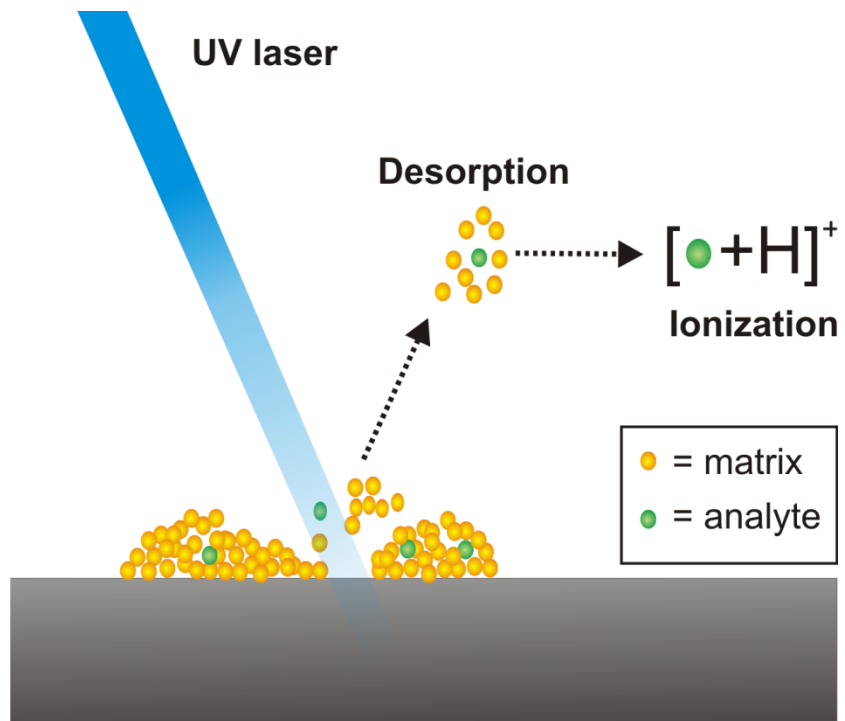
#### **1.1 *An Introduction to MALDI Mass Spectrometry***

Mass spectrometry (MS) is an inherently label-free method of chemical analysis which separates and detects ionized molecules based on their mass to charge ratio ( $m/z$ ). As MS can only detect ionized molecules, the ionization process is integral to the quality of the observed mass spectrum. Low-energy, *i.e.* soft, ionization processes such as matrix-assisted laser desorption/ionization (MALDI) are capable of converting large molecules, *e.g.* proteins, to intact ions.<sup>1-2</sup> In traditional MALDI, weak-organic-acid matrix molecules, shown in **Table 1-1**, are mixed and co-crystallized with non-volatile analytes. The matrix absorbs laser irradiation, leading to analyte desorption/ionization for MS, as shown in **Figure 1-1**. Over the past two decades, MALDI has proven to be crucial for molecular analysis. Several notable research areas which rely upon MALDI include label-free imaging of biomolecules directly from tissues and cells,<sup>3-5</sup> rapid bacterial strain identification,<sup>6</sup> and determination of polymer molecular weights with high accuracy.<sup>7-8</sup>

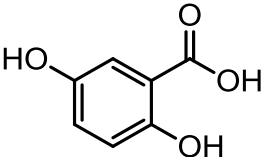
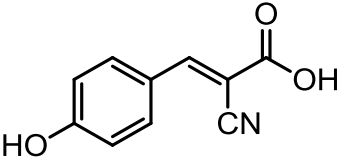
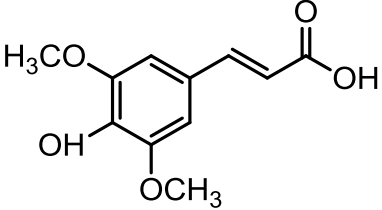
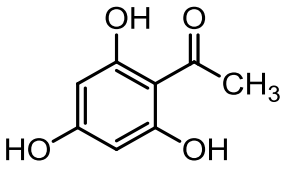
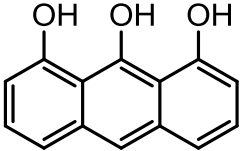
#### *Analyte and Matrix Co-crystallization*

Comprehensive mixing of matrix and analyte is critical for efficient MALDI-MS performance. Previous molecular imaging experiments have confirmed that analyte ion yields increase with analyte-matrix heterogeneity, and that analytes are often directly incorporated into organic matrix crystals.<sup>9-10</sup> For these reasons, solution-based methods for analyte and matrix mixing and co-crystallization described below continue to be utilized, even as more reproducible but less heterogeneous methods such as matrix sublimation have been introduced.<sup>11</sup>

Two primary methods exist for solution-based matrix and analyte co-crystallization. The most commonly used approach for mixing and spotting is the dried-droplet method, which can be traced back to the founding of MALDI in 1988.<sup>1</sup> In the dried-droplet method, analyte and matrix



**Figure 1-1.** General schematic of matrix-assisted laser desorption/ionization (MALDI). The matrix is mixed with analyte and absorbs the UV laser irradiation, leading to matrix and analyte desorption from the substrate and ionization. Specific models for desorption and ionization are discussed in the text.

Name	Exact Mass (Da)	Molecular Structure
2,5-dihydroxybenzoic acid (DHB)	154.0266	
$\alpha$ -cyano-4-hydroxycinnamic acid (CHCA)	189.0426	
sinapinic acid (SA)	224.0685	
2',4',6'-Trihydroxyacetophenone (THAP)	168.0423	
dithranol	226.0630	

**Table 1-1.** Commonly used weak-organic-acid matrices for MALDI-MS.

are either pre-mixed and spotted on the plate or spotted from separate solutions on top of each other. Typically a total volume of 0.5 - 2  $\mu\text{L}$  is used. The spot is allowed to dry at room temperature and pressure, or with slight heating. The solution is frequently a mixture of slightly-acidic water and polar-organic solvent (e.g. ethanol), so drying is on the order of several minutes. Assuming the MALDI target has a hydrophobic coating on the surface, increasing the ratio of water to organic solvent will increase the contact angle of the droplet on the target and solvent evaporation time. In this case, matrix and/or analyte can precipitate out of solution before all liquid evaporates. As a result, analytes with some nonpolar character are typically incorporated into the center of the matrix crystal, whereas highly soluble species such as salts are found at crystal edges.<sup>10</sup>

The primary drawback of co-crystallization by the dried-droplet method is poor reproducibility. Matrix and analyte disperse unevenly during solvent evaporation, causing some matrix crystals to incorporate small amounts of analyte and others large amounts of analyte.<sup>9</sup> The resulting matrix and analyte distributions can vary greatly, not only within the spot but also between replicate MALDI spots, limiting dried-droplet reproducibility. It is also thought that crystals which have high uptake of analyte generate the most ions for MS and contribute to the impressive limits-of-detection of MALDI-MS (typically low fmol to amol);<sup>12</sup> these regions of high analyte uptake are known as hot-spots. Therefore, irregular crystallization is both the cause of both the main drawback and the main advantage of dried-droplet spotting.

In contrast with the dried-droplet approach, decreasing the aqueous content of the solution speeds up the evaporation process and leads to more homogenous matrix-analyte co-crystallization. Known as either the fast evaporation or thin layer method,<sup>13-16</sup> matrix is spotted first on the plate from an organic solvent such as acetone. The matrix spreads out rapidly, producing uniform sub-micrometer crystals. Analyte is then spotted on top of matrix. Thus, analyte is incorporated evenly into the top layer of crystals and does not penetrate below. However, this method has two primary drawbacks. First, because organic solvents have lower surface tension than water and spread across a wide area on the plate, analytes are less concentrated due to the large spot. This results in less hot-spot formation and higher limits-of-



detection. Second, this approach typically requires a wash step which may remove some analytes. Rapid evaporation methods such as these are used occasionally but not as frequently as standard dried-droplet spotting, which is typically simpler to perform and more sensitive.

### *Desorption*

In order to desorb both matrix and analyte from the crystalline state, laser energy must first be absorbed by the matrix. All matrices listed in **Table 1-1** strongly absorb ultraviolet (UV) irradiation, and thus gas-phase and solid-state UV lasers are most commonly used for MALDI-MS. Matrix ionization potentials are typically two to three times greater than the energy of a single UV laser photon (e.g. 3.7 eV for 337 nm emission).<sup>17</sup> It had been suggested that matrix excitation may be a multi-photon event; however, most researchers now think that this energy gap is achieved by energy pooling due to the high number of matrix molecules present, as discussed below.<sup>18</sup>

After laser absorption, the majority of this excess energy is converted to heat. However, the required time for heat dissipation within a matrix crystal (approx. 10 ns) is typically longer than a UV laser pulse width by a factor of two or three.<sup>18</sup> If the matrix is unable to dissipate the heat in time, thermal confinement causes a “phase explosion” leading to ejection of matrix and trapped analyte from the top 10-100 nm of the crystal.<sup>19</sup> It is thought the primary cause for desorption in UV laser MALDI-MS is this thermal confinement. Crucial to this process is that analytes are not overheated so that metastable fragmentation is minimized. Vertes *et al.* suggested this occurs via a “bottleneck” mechanism.<sup>20</sup> Incorporation of analyte into the matrix lattice produces defects in the crystal; at these defects, energy transfer is less efficient as adjacent wavefunctions are not in-phase. As a result, trapped analytes are cooler than matrix and are simply desorbed along with the surrounding material. Even fragile analytes may be desorbed without thermal degradation according to this model.

Laser fluence, energy per pulse per unit area, is also critical in the desorption process. Threshold MALDI fluence values are approximately 30 - 100 J/m<sup>2</sup>, depending somewhat on laser beam shape and matrix-to-analyte ratio.<sup>21</sup> From detailed computational modeling studies,

Garrison *et al.* suggested there may actually be two thresholds: one threshold fluence for simple molecular desorption, and one threshold fluence for bulk desorption of molecules and clusters.<sup>22</sup> It was suggested the latter threshold may correspond to experimentally-observed fluence thresholds in MALDI-MS. As fluence increases above the experimental threshold, ion signal increases significantly. However, at some point chemical noise also increases, causing a reduction in signal-to-noise. Typically, optimal MALDI-MS performance is observed 2-3 times greater than threshold fluence.<sup>18</sup>

It has been proposed that vibrational confinement due to photoacoustic stress may play a role in phase explosion as well,<sup>23</sup> but it is likely more significant for infrared (IR) laser MALDI in which the laser penetration depth is on the order of micrometers instead of nanometers.<sup>24</sup> Due to the poor spatial focusing of IR lasers in MS imaging experiments, IR laser MALDI is outside the scope of this document and will not be used in subsequent chapters.

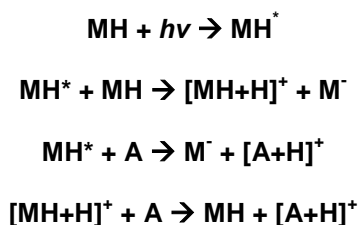
### *Ionization*

Two general models are used to explain the mechanism of MALDI ionization: the cluster or “lucky survivor” model, and the gas phase protonation or excited-state proton transfer (ESPT) model. In the cluster model, it is thought analytes retain solution-based charges when crystallized with the matrix.<sup>25-27</sup> Upon laser irradiation, analyte and matrix clusters are released into the gas phase, where charge neutralization occurs through charge transfer pathways with counter ions present. Hence, desorbed analytes which retain their charge for mass spectrometry are known as lucky survivors. One example of cluster-based neutralization is shown below:



where **M** is matrix, **A** is analyte, and **X<sup>-</sup>** is a negative counter ion. Matrix aggregates observed in MALDI mass spectra are considered the primary evidence for the cluster-based ionization model. These are most evident in atmospheric pressure MALDI, where collisional cooling often stabilizes these intermediates.

In the gas-phase protonation model, analytes are crystallized with matrix as neutrals or zwitterions.<sup>28-31</sup> Upon laser irradiation, excited matrix molecules undergo gas-phase proton transfer reactions between each other, resulting in protonated matrix ions, or between matrix and analyte, resulting in protonated analyte ions in the plume, as shown below:



where **M** is matrix and **A** is analyte.<sup>32</sup> As mentioned above, energy pooling likely plays a role in this process. It is likely multiple excited-state matrix molecules work together to generate a single analyte ion.<sup>33</sup> The body of evidence for the ESPT model is more developed than that of the cluster mechanism, and as a result most researchers consider this mechanism more applicable to common MALDI situations. However, evidence exists for both mechanisms. Recent efforts have focused on providing a unified mechanism of MALDI,<sup>34</sup> but the unification of both models remains controversial.<sup>35-36</sup> Nevertheless, for both models it is generally agreed upon that the matrix plays key roles in analyte ion production, including: (i) suspension of analyte in solid crystals; (ii) absorption of laser irradiation to protect analyte from laser-induced fragmentation; (iii) desorption from the target surface; and (iv) formation of analyte ions for mass spectrometry. It is likely these protonation (or de-protonation) mechanisms occur in the matrix plume after desorption.

The MALDI process is typically most efficient when a high matrix-to-analyte mole ratio is utilized (500:1 - 5000:1), possibly due to the bottleneck model described above. A high matrix-to-analyte ratio ensures that the majority of laser irradiation will strike matrix instead of analytes. If analytes are ionized intact, then additional ion isolation and fragmentation experiments may be performed post-ionization to provide insight into the structure of the selected ion of interest. This is known as tandem mass spectrometry (MS/MS).<sup>37-38</sup>

When a high matrix-to-analyte ratio is used, matrix molecules also ionize each other, introducing matrix-based chemical noise into the mass spectrum. Matrix signals and clusters are habitually detected in the low-mass region of the spectrum (< 500 Da). As a result, MALDI matrix signals may overlap with low-molecular-weight analytes, complicating the spectrum and the resulting data analysis. Conversely, using a low matrix-to-analyte ratio (e.g. 25:1) can minimize or even eliminate this noise,<sup>39-41</sup> however, this raises MALDI limits-of-detection and may also increase analyte in-source fragmentation due to direct laser absorption. For these reasons, non-ionizing nanomaterials have been attracting interest as matrices for MALDI mass spectrometry.

#### *Time-of-flight Mass Analyzer*

Although MALDI sources have been coupled to many different types of mass analyzers, by far the most common coupled to MALDI ionization is the time-of-flight (TOF) mass analyzer. TOF mass analyzers operate based upon the classic kinetic energy equation, solved for time:

$$t = \left( \frac{m}{2eV} \right)^{\frac{1}{2}} * D \quad (1)$$

where **t** is ion flight time, **m** is ion mass, **e** is the elementary charge, **V** is applied voltage, and **D** is length of the flight tube.<sup>42</sup> All ions in the source are imparted with the same kinetic energy (eV), and traverse through a field-free region towards the ion detector. Assuming all ions generated by MALDI are singly-charged, signals are resolved in time based upon inherent differences in their mass. TOF mass analyzers are commonly coupled with MALDI ionization (MALDI-TOF) due to the pulsed nature of both methods. In every TOF sequence, a common start time ( $t_0$ ) is needed, and various ion flight times correlate to analyte ion mass-to-charge ( $m/z$ ) values. Similarly, many UV lasers are inherently pulsed in nature. Therefore, individual UV laser pulses provide a sharp  $t_0$  for each TOF sequence. In practice, it is difficult to impart all ions with exactly the same kinetic energy. Typically a narrow distribution of kinetic energies is imparted, and the width of this distribution is directly related to TOF resolution. Time-lag focusing and the reflectron ion mirror are two commonly used solutions to correct for this in MALDI-TOF-MS.<sup>42</sup>

## 1.2 Nanomaterial MALDI Matrices

The use of nanomaterials as absorbing substrates for MALDI-TOF-MS dates back to 1988 when Tanaka and colleagues utilized 30 nm cobalt nanoparticles suspended in glycerol to ionize intact proteins.<sup>43</sup> Over the past several decades, advances in the fields of nanotechnology and mass spectrometry have led to many new types of matrices, including but not limited to nanoparticles, nanoporous substrates, quantum dots, nanotubes, nanowires, and graphene.<sup>44</sup> Nevertheless, it remains more common for researchers to utilize weak organic acids listed in Table 1-1 for co-crystallization with analytes and MALDI-MS analysis.

Similar to organic acid MALDI, it is thought thermal confinement plays a key role in desorption from nanoscale materials. Most nanomaterials have critical dimensions (particle diameter, pore-to-pore distance, post diameter, *etc.*) less than the thermal dissipation length (up to 200 nm).<sup>45</sup> Rapid UV laser pulses generate heat in the material, leading to bulk desorption. However, other confinement processes are likely involved as well.<sup>46</sup> Similar to the classic field desorption/ionization method in MS, materials with nanoscale posts or protrusions exhibit localized field enhancement which can lead to increased local temperatures and thus desorption efficiencies.<sup>47</sup> Surface plasmon absorption in metallic nanoparticles appears to correlate with LDI performance as well.<sup>48</sup> In these cases, nanomaterial size and shape (or aspect ratio) plays a crucial role in the absorption of UV irradiation and resulting confinement phenomena.

In contrast with organic acid MALDI, however, most nanomaterials are not direct proton sources. Analytes are frequently cationized (*e.g.*  $[M+Na]^+$ ) from nanomaterial matrices due to latent salt present either on the material surface or in the analyte solution.<sup>49</sup> Protonated analyte ions may be detected from some nanomaterials, but the source of additional protons remains unclear. Potential proton sources include trapped acid molecules from solution, acidic surface groups (*e.g.* excited-state Si-OH from porous silicon), or pre-formed ions through a lucky survivor-like mechanism.<sup>50-52</sup>

Although both weak organic acids and nanomaterials are used as matrices for MALDI-MS, functional differences exist between the two approaches. These differences include: (i) weak organic acids often generate intense chemical noise below 500 Da due to protonation,

fragmentation, and clustering, whereas many nanomaterials do not exhibit these traits;<sup>53</sup> (ii) optimal weak organic acid to biomolecule mole ratios typically range from  $10^3:1$  to  $10^4:1$ , whereas nanoparticle to analyte ratios can oftentimes be inverted ( $\sim 1:10^7$ - $10^9$ );<sup>49</sup> and (iii) weak organic acids absorb most strongly at ultraviolet (UV) laser wavelengths, whereas nanomaterials such as porous silicon absorb a broad portion of the UV-visible spectrum.<sup>53-54</sup> For these reasons, there appears to be an effort to distinguish between weak organic acid and nanomaterial MALDI-MS. In the recent literature, terms such as surface-assisted LDI (SALDI),<sup>55</sup> matrix-free LDI,<sup>53</sup> nanomaterial-assisted LDI (NALDI),<sup>56</sup> and nanoparticle-assisted LDI (nano-PALDI)<sup>57</sup> have been used to describe nanomaterial-based methods. Substrate-based techniques such as desorption/ionization on porous silicon (DIOS)<sup>58</sup> and nanostructure-initiator mass spectrometry (NIMS)<sup>59</sup> also fall under the umbrella of nanomaterial matrices. At the current time, SALDI is the most common term to collectively describe these nanomaterial-based methods. However, the terminology in this field remains inconsistent.

From another perspective, all of these nanomaterial-based methods can be considered fundamentally MALDI in that nanoscale inorganic materials act as the matrix. Both weak organic acids and nanomaterials provide many of the same desirable qualities expected of a matrix, directly or indirectly, including a chromophore for the irradiation wavelength and a source of protonating or cationizing species. For purposes of clarity in this chapter, nanomaterial-based LDI is defined as nano-MALDI and weak organic acid LDI as MALDI.

Interest in nano-MALDI techniques has grown appreciably over the past several years, as shown in **Figure 1-2**. The appeal of using nanomaterials in mass spectrometry can be attributed to efficient absorption of laser irradiation, tunable optical properties based on morphological characteristics (e.g. nanoparticle size and shape),<sup>49</sup> high surface area for analyte adsorption and pre-concentration,<sup>60</sup> and surface derivatization capabilities for improved ionization efficiency<sup>61</sup> or analyte capture.<sup>62</sup> To date, the classic limitation of the nano-MALDI approaches has been an inability to ionize large proteins and other high-mass analytes, although recent data from Chiang *et al.* shows that HgTe nanostructures can be used to ionize 150 kDa proteins

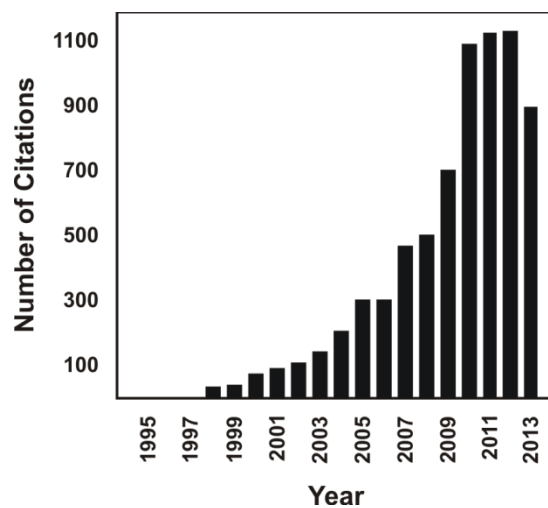


**Figure 1-2.** Web of Science™ citations of nano-MALDI techniques, beginning with the first paper to use SALDI terminology in 1995 (Sunner *et al.*; Ref. 55). Specific search terms were: “Desorption Ionization on Silicon,” “DIOS Mass Spectrometry,” “Nanostructure Initiator Mass Spectrometry,” “NIMS Mass Spectrometry,” “Surface Assisted Laser Desorption Ionization,” “SALDI Mass Spectrometry,” “Nanoparticle Assisted Laser Desorption Ionization,” “nano-PALDI Mass Spectrometry,” and “Nanoparticle MALDI matrix.” Chart was compiled November 2013.

without additional liquid or crystalline matrix.<sup>63</sup> An additional shortcoming is that the efficiency of analyte protonation for nano-MALDI is often less than for MALDI. Whereas MALDI produces mainly protonated quasi-molecular ions, many nanomaterial-based approaches, especially nanoparticles, generate a more varied distribution of protonated and cationized species. Several excellent reviews discuss these advantages and limitations of nano-MALDI in detail.<sup>45-46,53,64-65</sup>

MS imaging allows molecules to be detected based on their mass-to-charge ratio ( $m/z$ ) and spatial location.<sup>3-5</sup> As with MALDI, nano-MALDI may be used to generate molecular images from biological samples. In addition to the advantages of nano-MALDI for profiling measurements described above, nanomaterials also allow MS imaging to be performed using high spatial resolution. For MALDI-based MS imaging, the spatial resolution is primarily dependent upon UV laser spot size, typically 20-150  $\mu\text{m}$ , and the size and homogeneity of the organic matrix crystals.<sup>66</sup> Although the sizes of individual matrix crystals vary depending on solvent conditions and method of application, they are typically on a similar length scale as the laser spot size. In contrast, individual nanomaterial features (particle sizes, nanotube dimensions, etc.) are typically 10-200 nm, which are much smaller than the spot size of a UV laser. Therefore, spatial resolution in nano-MALDI is primarily dependent on the laser spot size.

Since comprehensive reviews on general nano-MALDI have been recently published (e.g. Refs. 45-46), the remainder of this chapter will focus on nano-MALDI as an MS imaging platform for the analysis of intact plant and animal tissue sections, as well as the potential of nano-MALDI in single-cell imaging.

### **1.3 Biological Tissue Imaging using Nanomaterial Matrices**

#### *Plant Tissues*

In 2000, the genome of the flowering plant *Arabidopsis thaliana* was completed.<sup>67</sup> Since then, researchers have been using MS to explore protein, lipid and metabolite profiles of *A. thaliana* in order to better understand systems-biology interactions.<sup>68</sup>

Current nano-MALDI methods are better suited for determining the spatial distributions of metabolites rather than proteins in *A. thaliana*. Flower petals are coated with a waxy protective



layer which makes it difficult to determine the location of proteins underneath the surface. Fortunately, however, lipids and nonpolar metabolites adsorb readily to both graphite and silver nanoparticles, and have been detected using LDI-MS imaging.<sup>69-70</sup> In these experiments, nanoparticles are suspended in 2-propanol and coated onto the petals using a N<sub>2</sub>-based airbrush sprayer. Using this methodology, the solvent evaporates before reaching the sample, producing a homogenous colloidal layer.<sup>69</sup> Additionally, surface analytes do not diffuse from their native locations before image acquisition.

Using nano-MALDI several classes of analytes have been detected and imaged from *A. thaliana* petals. In particular, surface lipids generated intense signals when cationized with silver from the colloidal layer.<sup>70</sup> A limitation of the silver colloid method is that ionized silver clusters are also generated and give intense signals in the mass spectrum. However, these signals can be used to normalize analyte signal intensities, improving the reproducibility of the method.

Secondary metabolites are also commonly observed from *A. thaliana* petals. Unlike waxy lipids which cationized with silver (specifically because silver is electrophilic and coordinates with sites of unsaturation),<sup>71</sup> secondary metabolites such as flavonoids and glycosidic flavonoids were ionized as [M-H]<sup>-</sup> negative ions. In one study, graphite-based LDI-MS imaging was used to demonstrate the role of the enzyme flavonoid 3'-hydroxylase in the synthesis of quercetin and isorhamnetin.<sup>72</sup> These two flavonoids were not observed in flavonoid 3'-hydroxylase knockouts, verifying the enzyme is directly involved in their synthetic pathways. Flavonoids themselves absorb UV irradiation and can be imaged from *A. thaliana* petals without nanomaterial target substrates;<sup>73</sup> nevertheless, in-source fragmentation can occur due to the analyte absorbing excess energy. In contrast, multiple glycoside species can be detected intact and imaged using graphite.

Two important aspects of high-quality MS imaging are spatial resolution and mass resolution. The highest imaging spatial resolution achieved to date by nano-MALDI on *A. thaliana* was 12 μm; this was done using a nitrogen laser, a fiber-optic cable, and a laser spot size of 25 μm using oversampling.<sup>69</sup> However, a potential challenge with this optical approach is the large beam divergence from optical fibers resulting in energy loss at the desired target and

consequently decreased ion yields. While spatial resolution is primarily determined by the optical train in nano-MALDI, mass resolution is primarily determined by the mass analyzer (and the internal energy spread in the resulting ions imparted by the ion source). Using an LTQ-Orbitrap mass analyzer, two surface metabolites which differed by 0.035 Da were easily resolved and MS imaged using silver.<sup>70</sup> A typical limitation of Orbitrap-based MS imaging is slow acquisition time, especially using high spatial resolution. However, a recently-described spiral rastering motion can accelerate Orbitrap image acquisition time by up to 50%.<sup>74</sup>

### *Animal Tissues*

The majority of nano-MALDI imaging performed to date has been on animal tissue sections cut to thicknesses of 3-20  $\mu\text{m}$  using a cryostat. These section dimensions are complementary for both MALDI and nano-MALDI imaging MS, such that: (i) in order to generate quality molecular images from entire sections, routine lateral spatial resolutions (50-150  $\mu\text{m}$ ) are often sufficient; (ii) many small molecules and lipids are ionized from tissue with high efficiency; and (iii) tissue imaging data in the MALDI literature can be used as a frame-of-reference for novel nano-MALDI approaches.

When nanoparticles are used for MS imaging, typically they are applied to the tissue section using an airbrush sprayer. Silver,<sup>75</sup> gold,<sup>76-77</sup> iron<sup>57,78</sup> and titanium dioxide<sup>79</sup> particles have been applied in this manner. However, particles may also be generated solvent-free using a sputter-coater<sup>80</sup> or by implantation into tissue.<sup>81</sup> These approaches are similar to soft-landing MS techniques,<sup>82-84</sup> dry-coating techniques are particularly intriguing due to their ability to control both particle size and deposition layer thickness.

On the other hand, in order to perform MS imaging from nanostructured surfaces, the tissue section must be applied to the nanostructures. One nanostructure-based approach, nanostructure-initiator mass spectrometry (NIMS), features a porous silicon surface containing fluorinated silane (initiator) molecules.<sup>59,85-89</sup> In order to perform NIMS imaging, tissues are carefully sectioned to 3-5  $\mu\text{m}$  in thickness and thaw mounted to the surface.<sup>87</sup> Because the laser must pass through the tissue to reach the nanostructures, thicker sections reduce the energy to

the substrate and decrease ion yields. Somewhat thicker sections (15  $\mu\text{m}$ ) have been thaw mounted to graphene oxide/carbon nanotube surfaces for MS imaging, however.<sup>90</sup> Commercially-available NALDI™ targets have also been used for tissue imaging.<sup>56,91-92</sup> Instead of thaw mounting tissue to the substrates, surface analytes have been transferred to the target by either imprinting<sup>56,91</sup> or laser ablation.<sup>92</sup> It is possible these new sample transfer methods may help to circumvent issues with sample thickness on nanostructured targets.

The majority of nano-MALDI images in the literature reveal the spatial distribution of lipids and fatty acid metabolites. Different lipid classes such as phospholipids, fatty acids, sphingolipids, and sterols have been imaged from tissue sections using nano-MALDI.<sup>56-57,59,75-78,87-88,90-93</sup> Phospholipids and sphingolipids are abundant in tissue and are frequently detected as  $[\text{M}+\text{H}]^+$ ,  $[\text{M}+\text{Na}]^+$ , or  $[\text{M}+\text{K}]^+$  species. Fatty acids are typically detected in negative ion mode, whereas sterols are typically cationized with silver in positive ion mode.

As mentioned earlier, emerging nano-MALDI approaches are capable of detecting proteins larger than 100 kDa.<sup>65</sup> However, in the context of MS imaging, 1.9 kDa is the largest  $m/z$  value for which a molecular image has been generated to date.<sup>77</sup> Therefore, it is expected nano-MALDI imaging of peptides and proteins will emerge in the near future.

Small analytes such as endogenous amino acids and exogenous drug molecules have also been imaged using nano-MALDI.<sup>79-80,86,88,94-96</sup> While quantitation of small molecules by MS imaging is difficult,  $\text{TiO}_2$  nanoparticles allowed for the amino acid histidine to be quantitatively imaged with a relative standard deviation (RSD) of approximately 12%.<sup>79</sup> An  $R^2$  value of 0.9976 was obtained across a linear concentration range of 0.1-1.6  $\mu\text{g}$  histidine/ $\text{mm}^3$  tissue.

Small molecules have also been imaged in three dimensions using serial tissue sections.<sup>89</sup> Thin serial sections were thaw mounted to NIMS substrates and the two-dimensional images were acquired. After acquisition, molecular maps were aligned vertically using MATLAB.

Tissue imaging can be performed using high spatial and mass resolution when nano-MALDI is coupled to proper MS instrumentation. Small regions of tissue have been imaged with 10  $\mu\text{m}$  spatial resolution using TOF mass analyzers.<sup>75,78</sup> Most reflector-TOF instruments have good ion transmission and relatively high mass resolution ( $m/\Delta m$  typically 5,000-10,000), which is

sufficient for imaging low mass analytes. For larger analytes, higher mass resolution may be desired to resolve overlapping signals. Nanomaterial-based tissue imaging using an Orbitrap mass analyzer allows species to be resolved by small differences in  $m/z$  and identified by tandem MS. As mentioned earlier, the primary drawback of both high-spatial and high-mass resolution Orbitrap imaging is long data acquisition times.

#### **1.4 Prospects in Single-cell Imaging**

While nano-MALDI imaging of plant and tissue sections is becoming more established in the literature, imaging intact molecules from individual cells presents a much greater challenge. In order to generate quality images of most cells, spatial resolution needs to approach 1  $\mu\text{m}$  or less. At this resolution, UV lasers must be focused to a point scarcely wider than their diffraction limit (discussed further in Chapter 5). Additionally, small irradiation areas contain very few analyte molecules, requiring a very efficient and sensitive ionization process to generate sufficient signal-to-noise.<sup>97</sup>

Given these challenges, nano-MALDI may prove to be a useful technique for high-spatial-resolution MS imaging from cells. Nanomaterials have very high surface areas which allow analytes to be pre-concentrated in nanometer-sized regions before laser irradiation. As a result, these techniques require low fluence values for ionization,<sup>98</sup> generate minimal in-source fragmentation,<sup>99</sup> and ensure analytes remain in their native locations. Moreover, nano-MALDI methods have demonstrated impressive limits of detection for small molecules, down to zeptomole<sup>100</sup> and potentially sub-zeptomole<sup>59</sup> amounts. Because of these advantages, methods such as NIMS,<sup>59</sup> nanopost array (NAPA),<sup>100</sup> and DIOS<sup>58,101</sup> are capable of detecting small molecules and lipids from individual cells. It is important to note several other laser-based approaches such as laser ablation electrospray ionization (LAESI)<sup>102</sup> and single-cell MALDI<sup>103-105</sup> have begun to demonstrate this ability as well. Cells used in all of these proof-of-concept experiments were rather large, however. Secondary ion mass spectrometry (SIMS) techniques have been capable of detecting analytes from sub-cellular regions for some time, but secondary ion yields of intact biomolecules are typically low.<sup>106</sup> Developments in polyatomic cluster ion

beams such as C<sub>60</sub> for SIMS may improve the detection of several types of biological molecules >500 Da.<sup>107</sup> Nevertheless, due to a combination of spatial accuracy, soft ionization, and low limits of detection, nano-MALDI methods are particularly well-suited for direct imaging of intact metabolites and lipids from sub-cellular regions.

Regardless of the material used for LDI, further improvements in laser and/or ion optics are needed in order to detect molecules from single-micrometer regions within a cell. Noteworthy advances in high-resolution MALDI imaging include scanning microprobe laser optics,<sup>108-111</sup> spatial-preserving ion optics for ion microscopy,<sup>112-113</sup> and transmission-geometry.<sup>105,114-115</sup> Although fundamentally distinct, each method has achieved low- $\mu\text{m}$  spatial resolutions while maintaining relatively soft ionization. However, none have been coupled with nanomaterial-based targets. Optical methods such as these can be coupled with nano-MALDI for more sensitive sub-cellular imaging of intact biological molecules.

## **1.5 Conclusions and Objectives**

Specific nano-MALDI methods previously used for MS imaging are summarized in **Table 1-2**. Together, these approaches are well-suited for imaging small metabolites and lipids from plant and animal tissue samples. Although the majority of nano-MALDI imaging techniques have been limited in their usable mass range, several emerging approaches are able to ionize kDa species and may be utilized for MS imaging of larger molecules such as proteins in the future. Due to high sensitivity, soft ionization, spatial resolution unhindered by organic matrix crystals, and potential integration with microscopy techniques, it is suggested that nano-MALDI techniques be coupled with recent developments in laser and/or ion optics for single-cell and even sub-cellular MS imaging.

The primary purpose of my research in the McLean laboratory was to explore the NIMS platform for high-resolution MS imaging. In Chapter 2, the optimization of novel semi-transparent NIMS substrates for MS and optical imaging of cells is discussed. In Chapter 3, a hybrid NIMS-MALDI strategy is evaluated, for the purpose of increasing ion yields such that sub-cellular sensitivity may be attained.

<b>Approach</b>	<b>Material(s)</b>	<b>General Comments</b>	<b>Imaging Applications</b>	<b>Key Refs.</b>
DIOS	Nanoporous <i>n</i> -type pSi surface	Sensitive, low noise, surface reproducibility/ stability can be an issue	Cells, tissues	58, 101
NIMS	Nanoporous <i>p</i> -type pSi surface w/ coating	Sensitive, low noise, more robust than DIOS, requires very thin tissue sections	Cells, tissues	59, 88
NALDI	Nanowire surface (ZnO, GaN, etc.) w/ coating	Very similar to NIMS	Tissues	56, 91
GO-MWCNT	Combined graphene oxide / carbon nanotubes	Ions are primarily cationized, good surface reproducibility/ stability	Tissues	90
Nanoparticle-based methods (SALDI, GALDI, etc.)	Au, Ag, TiO <sub>2</sub> , Graphite, Fe, etc.	Ions are primarily cationized, NPs applied directly onto sample (no issues with tissue thickness)	Tissues	57, 70, 75, 79

**Table 1-2.** Summary of nano-MALDI approaches used in biological MS imaging.

As described in this chapter, materials are proving to be increasingly useful in MS research. On the other hand, structural MS techniques are also proving to be extremely useful in materials characterization. Another purpose of my research was to use structural MS techniques to characterize small molecules involved in materials chemistry processes. In Chapter 4, these isomeric species are characterized and differentiated by several MS and computational modeling methods.

## 1.6 References

1. Karas, M.; Hillenkamp, F. Laser Desorption Ionization of Proteins with Molecular Masses Exceeding 10000 Daltons. *Anal. Chem.* **1988**, *60*, 2299-2301.
2. Cole, R. B., ed. *Electrospray and MALDI Mass Spectrometry, 2<sup>nd</sup> Edition*. Hoboken: John Wiley & Sons, 2010.
3. Caprioli, R. M.; Farmer, T. B.; Gile, J. Molecular Imaging of Biological Samples: Localization of Peptides and Proteins using MALDI-TOF MS. *Anal. Chem.* **1997**, *69*, 4751-4760.
4. Cornett, D. S.; Reyzer, M. L.; Chaurand, P.; Caprioli, R. M. MALDI Imaging Mass Spectrometry: Molecular Snapshots of Biochemical Systems. *Nat. Methods* **2007**, *4*, 828-833.
5. McDonnell, L. A.; Heeren, R. M. A. Imaging Mass Spectrometry. *Mass Spectrom. Rev.* **2007**, *26*, 606-643.
6. Fenselau, C.; Demirev, P. A. Characterization of Intact Microorganisms by MALDI Mass Spectrometry. *Mass Spectrom. Rev.* **2001**, *20*, 157-171.
7. Nielen, M. W. F. MALDI Time-of-flight Mass Spectrometry of Synthetic Polymers. *Mass Spectrom. Rev.* **1999**, *18*, 309-344.
8. Murgasova, R.; Hercules, D. M. MALDI of Synthetic Polymers - an Update. *Int. J. Mass Spectrom.* **2003**, *226*, 151-162.
9. Dai, Y.; Whittall, R. M.; Li, L. Confocal Fluorescence Microscopic Imaging for Investigating the Analyte Distribution in MALDI Matrices. *Anal. Chem.* **1996**, *68*, 2494-2500.
10. Bouschen, W.; Spengler, B. Artifacts of MALDI Sample Preparation Investigated by High-Resolution Scanning Microprobe Matrix-Assisted Laser Desorption/Ionization (SMALDI) Imaging Mass Spectrometry. *Int. J. Mass Spectrom.* **2007**, *266*, 129-137.
11. Hankin, J. A.; Barkley, R. M.; Murphy, R. C. Sublimation as a Method of Matrix Application for Mass Spectrometric Imaging. *J. Am. Soc. Mass Spectrom.* **2007**, *18*, 1646-1652.
12. Keller, B. O.; Li, L. Detection of 25,000 Molecules of Substance P by MALDI-TOF Mass Spectrometry and Investigations into the Fundamental Limits of Detection in MALDI. *J. Am. Soc. Mass Spectrom.* **2001**, *12*, 1055-1063.
13. Vorm, O.; Roepstorff, P.; Mann, M. Improved Resolution and Very High Sensitivity in MALDI TOF of Matrix Surfaces Made by Fast Evaporation. *Anal. Chem.* **1994**, *66*, 3281-3287.
14. Cohen, S. L.; Chait, B. T. Influence of Matrix Solution Conditions on the MALDI-MS Analysis of Peptides and Proteins. *Anal. Chem.* **1996**, *68*, 31-37.
15. Dai, Y.; Whittall, R. M.; Li, L. Two-Layer Sample Preparation: A Method for MALDI-MS Analysis of Complex Peptide and Protein Mixtures. *Anal. Chem.* **1999**, *71*, 1087-1091.
16. Fenyo, D.; Wang, Q.; DeGrasse, J. A.; Padovan, J. C.; Cadene, M.; Chait, B. T. MALDI Sample Preparation: the Ultra Thin Layer Method. *JoVE*, *3*, doi:10.3791/192.



17. Knochenmuss, R. Photoionization Pathways and Free Electrons in UV-MALDI. *Anal. Chem.* **2004**, *76*, 3179-3184.
18. Dreiseward, K. The Desorption Process in MALDI. *Chem. Rev.* **2003**, *103*, 395-425.
19. Zhigilei, L. V.; Garrison, B. J. Mechanisms of Laser Ablation from Molecular Dynamics Simulations: Dependence on the Initial Temperature and Pulse Duration. *Appl. Phys. A.* **1999**, *69*, S75-S80.
20. Vertes, A.; Gijbels, R.; Levine, R. D. Homogenous Bottleneck Model of Matrix-assisted Ultraviolet Laser Desorption of Large Molecules. *Rapid Commun. Mass Spectrom.* **1990**, *4*, 228-233.
21. Kampmeier, J.; Dreisewerd, K.; Schürenberg, M.; Strupat, K. Investigations of 2,5-DHB and Succinic Acid as Matrices for IR and UV MALDI. Part I: UV and IR Laser Ablation in the MALDI Process. *Int. J. Mass Spectrom.* **1997**, *169/170*, 31-41.
22. Zhigilei, L. V.; Kodali, P. B. S.; Garrison, B. J. On the Threshold Behavior in Laser Ablation of Organic Solids. *Chem. Phys. Lett.* **1997**, *276*, 269-273.
23. Johnson, R. E. Models for Matrix-assisted Desorption by a Laser Pulse. *Int. J. Mass Spectrom.* **1994**, *139*, 25-38.
24. Rohlffing, A.; Menzel, C.; Kukreja, L. M.; Hillenkamp, F.; Dreisewerd, K. Photoacoustic Analysis of Matrix-assisted Laser Desorption/Ionization Processes with Pulsed Infrared Lasers. *J. Phys. Chem. B* **2003**, *107*, 12275-12286.
25. Karas, M.; Glückmann, M.; Schäfer, J. Ionization in Matrix-assisted Laser Desorption/Ionization: Singly Charged Molecular Ions Are the Lucky Survivors. *J. Mass Spectrom.* **2000**, *35*, 1-12.
26. Karas, M.; Krüger, R. Ion Formation in MALDI: The Cluster Ionization Mechanism. *Chem. Rev.* **2003**, *103*, 427-439.
27. Trimpin, S.; Wang, B.; Inutan, E. D.; Li, J.; Lietz, C. B.; Harron, A.; Pagnotti, V. S.; Sardelis, D.; McEwen, C. N. A Mechanism for Ionization of Nonvolatile Compounds in Mass Spectrometry: Considerations from MALDI and Inlet Ionization. *J. Amer. Soc. Mass Spectrom.* **2012**, *23*, 1644-1660.
28. Chiarelli, M. P.; Sharkey, Jr., A. G.; Hercules, D. M. Excited-state Proton Transfer in Laser Mass Spectrometry. *Anal. Chem.* **1993**, *65*, 307-311.
29. Karbach, V.; Knochenmuss, R. Do Single Matrix Molecules Generate Primary Ions in Ultraviolet Matrix-assisted Laser Desorption/Ionization. *Rapid Commun. Mass Spectrom.* **1998**, *12*, 968-974.
30. Knochenmuss, R.; Zenobi, R. MALDI Ionization: The Role of In-Plume Processes. *Chem. Rev.* **2003**, *103*, 441-452.
31. Knochenmuss, R. A Quantitative Model of Ultraviolet Matrix-assisted Laser Desorption/Ionization Including Analyte Ion Generation. *Anal. Chem.* **2003**, *75*, 2199-2207.
32. Gimón-Kinsel, M.; Preston-Schaffter, L. M.; Kinsel, G. R.; Russell, D. H. Effects of Matrix Structure/Acidity on Ion Formation in Matrix-assisted Laser Desorption Ionization Mass Spectrometry. *J. Am. Chem. Soc.* **1997**, *119*, 2534-2540.

33. Knochenmuss, R. A Quantitative Model of Ultraviolet Matrix-assisted Laser Desorption/Ionization. *J. Mass Spectrom.* **2002**, *37*, 867-877.
34. Jaskolla, T. W.; Karas, M. Compelling Evidence for Lucky Survivor and Gas Phase Protonation: The Unified MALDI Analyte Protonation Mechanism. *J. Am. Soc. Mass Spectrom.* **2011**, *22*, 976-988.
35. Knochenmuss, R. MALDI Ionization Mechanisms: the Coupled Photophysical and Chemical Dynamics Model Correctly Predicts 'Temperature'-selected Spectra. *J. Mass Spectrom.* **2013**, *48*, 998-1004.
36. Liang, C. W.; Lee, C. H.; Lee, Y. T.; Ni, C. K. MALDI Mechanism of Dihydroxybenzoic Acid Isomers: Desorption of Neutral Matrix and Analyte. *J. Phys. Chem. B* **2013**, *117*, 5058-5064.
37. McLafferty, F. W. Tandem Mass Spectrometry. *Science* **1981**, *214*, 280-287.
38. McLafferty, F. W.; Tureček, F. *Interpretation of Mass Spectra, 4<sup>th</sup> Edition*. Sausalito: University Science Books: 1993.
39. McCombie, G.; Knochenmuss, R. Small-molecule MALDI using the Matrix Suppression Effect to Reduce or Eliminate Matrix Background Interferences. *Anal. Chem.* **2004**, *76*, 4990-4997.
40. Knochenmuss, R.; Dubois, F.; Dale, M. J.; Zenobi, R. The Matrix Suppression Effect and Ionization Mechanisms in Matrix-assisted Laser Desorption/Ionization. *Rapid Commun. Mass Spectrom.* **1998**, *10*, 871-877.
41. Shroff, R.; Rulisek, L.; Doubsky, J.; Svatoš, A. Acid-base-driven Matrix-assisted Mass Spectrometry for Targeted Metabolomics. *Proc. Natl. Acad. Sci. USA* **2009**, *106*, 10092-10096.
42. Cotter, R. J. Time-of-flight Mass Spectrometry. In *Electrospray and MALDI Mass Spectrometry, 2<sup>nd</sup> Edition*. Hoboken: John Wiley & Sons, 2010.
43. Tanaka, K.; Waki, H.; Ido, Y.; Akita, S.; Yoshida, Y.; Yoshida, T. Protein and Polymer Analyses up to m/z 100000 by Laser Ionization Time-of-flight Mass Spectrometry. *Rapid Commun. Mass Spectrom.* **1988**, *2*, 151-153.
44. Arakawa, R.; Kawasaki, H. Functionalized Nanoparticles and Nanostructured Surfaces for Surface-Assisted Laser Desorption/Ionization Mass Spectrometry. *Anal. Sci.* **2010**, *26*, 1229-1240.
45. Stolee, J. A.; Walker, B. N.; Zorba, V.; Russo, R. E.; Vertes, A. Laser-nanostructure Interactions for Ion Production. *Phys. Chem. Chem. Phys.* **2012**, *14*, 8453-8471.
46. Silina, Y. E.; Volmer, D. A. Nanostructured Solid Substrates for Efficient Laser Desorption/Ionization Mass Spectrometry (LDI-MS) of Low Molecular Weight Compounds. *Analyst* **2013**, *138*, 7053-7065.
47. Schulten, H. R.; Beckey, H. D. Field Desorption Mass Spectrometry with High Temperature Activated Emitters. *Org. Mass Spectrom.* **1972**, *6*, 885-895.
48. Spencer, M. T.; Furutani, H.; Oldenburg, S. J.; Darlington, T. K.; Prather, K. A. Gold Nanoparticles as a Matrix for Visible-wavelength Single-particle Matrix-assisted Laser Desorption/Ionization Mass Spectrometry of Small Biomolecules. *J. Phys. Chem. C* **2008**, *112*, 4083-4090.

49. McLean, J. A.; Stumpo, K. A.; Russell, D. H. Size-selected (2-10 nm) Gold Nanoparticles for Matrix Assisted Laser Desorption Ionization of Peptides. *J. Am. Chem. Soc.* **2005**, *127*, 5304-5305.
50. Chen, C. T.; Chen, Y. C. Desorption/Ionization Mass Spectrometry on Nanocrystalline Titania Sol-gel-deposited Films. *Rapid Commun. Mass Spectrom.* **2004**, *18*, 1956-1964.
51. Northen, T. R.; Woo, H. K.; Northen, M. T.; Nordstrom, A.; Uritboonthail, W.; Turner, K. L.; Siuzdak, G. High Surface Area of Porous Silicon Drives Desorption of Intact Molecules. *J. Am. Soc. Mass Spectrom.* **2007**, *18*, 1945-1949.
52. Liu, Q.; He, L. Quantitative Study of Solvent and Surface Effects on Analyte Ionization in Desorption Ionization on Silicon (DIOS) Mass Spectrometry. *J. Am. Soc. Mass Spectrom.* **2008**, *19*, 8-13.
53. Peterson, D. S. Matrix-free Methods for Laser Desorption/Ionization Mass Spectrometry. *Mass Spectrom. Rev.* **2007**, *26*, 19-34.
54. Zenobi, R.; Knochenmuss, R. Ion Formation in MALDI Mass Spectrometry. *Mass Spectrom. Rev.* **1998**, *17*, 337-366.
55. Sunner, J.; Dratz, E.; Chen, Y. C. Graphite Surface-assisted Laser Desorption/Ionization Time-of-flight Mass Spectrometry of Peptides and Proteins from Liquid Solutions. *Anal. Chem.* **1995**, *23*, 4335-4342.
56. Vidova, V.; Novak, P.; Strohalm, M.; Pol, J.; Havlicek, V.; Volny, M. Laser Desorption-Ionization of Lipid Transfers: Tissue Mass Spectrometry Imaging without MALDI Matrix. *Anal. Chem.* **2010**, *82*, 4994-4997.
57. Taira, S.; Sugiura, Y.; Moritake, S.; Shimma, S.; Ichiyanagi, Y.; Setou, M. Nanoparticle-assisted Laser Desorption/Ionization Based Mass Imaging with Cellular Resolution. *Anal. Chem.* **2008**, *80*, 4761-4766.
58. Wei, J.; Buriak, J. M.; Siuzdak, G. Desorption-ionization Mass Spectrometry on Porous Silicon. *Nature* **1999**, *399*, 243-246.
59. Northen, T. R.; Yanes, O.; Northen, M. T.; Marrinucci, D.; Uritboonthai, W.; Apon, J.; Golledge, S. L.; Nordstrom, A.; Siuzdak, G. Clathrate Nanostructures for Mass Spectrometry. *Nature* **2007**, *449*, 1033-1036.
60. Shrivastava, K.; Wu, H. Multifunctional Nanoparticles Composite for MALDI-MS: Cd(2+)-doped Carbon Nanotubes with CdS Nanoparticles as the Matrix, Preconcentrating and Accelerating Probes of Microwave Enzymatic Digestions of Peptides and Proteins for Direct MALDI-MS Analysis. *J. Mass Spectrom.* **2010**, *45*, 1452-1460.
61. Castellana, E. T.; Russell, D. H. Tailoring Nanoparticle Surface Chemistry to Enhance Laser Desorption Ionization of Peptides and Proteins. *Nano Lett.* **2007**, *7*, 3023-3025.
62. Meng, J. C.; Siuzdak, G.; Finn, M. G. Affinity Mass Spectrometry from a Tailored Porous Silicon Surface. *Chem. Commun.* **2004**, 2108-2109.
63. Chiang, C. K.; Yang, Z.; Lin, Y. W.; Chen, W. T.; Lin, H. J.; Chang, H. T. Detection of Proteins and Protein-Ligand Complexes Using HgTe Nanostructure Matrixes in Surface-Assisted Laser Desorption/Ionization Mass Spectrometry. *Anal. Chem.* **2010**, *82*, 4543-4550.
64. Guo, Z.; Ganawi, A. A.; Liu, Q.; He, L., Nanomaterials in Mass Spectrometry Ionization and Prospects for Biological Application. *Anal. Bioanal. Chem.* **2006**, *384*, 584-592.

65. Chiang, C. K.; Chen, W. T.; Chang, H. T. Nanoparticle-based Mass Spectrometry for the Analysis of Biomolecules. *Chem. Soc. Rev.* **2011**, *40*, 1269-1281.
66. Chughtai, K.; Heeren, R. M. A. Mass Spectrometric Imaging for Biomedical Tissue Analysis. *Chem. Rev.* **2010**, *110*, 3237-3277.
67. The Arabidopsis Initiative. Analysis of the Genome Sequence of the Flowering Plant *Arabidopsis thaliana*. *Nature* **2000**, *408*, 796-815.
68. Glinski, M.; Weckwerth, W. The Role of Mass Spectrometry in Plant Systems Biology. *Mass Spectrom. Rev.* **2006**, *25*, 173-214.
69. Cha, S.; Zhang, H.; Ilarslan, H. I.; Wurtele, E. S.; Brachova, L.; Nikolau, B. J.; Yeung, E. S. Direct Profiling and Imaging of Plant Metabolites in Intact Tissues by using Colloidal Graphite-assisted Laser Desorption Ionization Mass Spectrometry. *Plant J.* **2008**, *55*, 348-360.
70. Jun, J. H.; Song, Z.; Liu, B.; Nikolau, B. J.; Yeung, E. S.; Lee, Y. J. High-spatial and High-mass Resolution Imaging of Surface Metabolites of *Arabidopsis thaliana* by Laser Desorption-ionization Mass Spectrometry using Colloidal Silver. *Anal. Chem.* **2010**, *82*, 3255-3265.
71. Bayer, E.; Gfrörer, P.; Rentel, C. Coordination-ionspray-MS (CIS-MS), a Universal Detection and Characterization Method for Direct Coupling with Separation Techniques. *Angew. Chem. Int. Ed.* **1999**, *38*, 992-995.
72. Korte, A. R.; Song, Z.; Nikolau, B. J.; Lee, Y. J. Mass Spectrometric Imaging as a High-spatial resolution Tool for Functional Genomics: Tissue-specific Gene Expression of TT7 Inferred from Heterogeneous Distribution of Metabolites in *Arabidopsis* Flowers. *Anal. Methods* **2012**, *4*, 474-481.
73. Hölscher, D.; Shroff, R.; Knop, K.; Gottschaldt, M.; Crecelius, A.; Schneider, B.; Heckel, D. G.; Schubert, U. S.; Svatoš, A. Matrix-free UV-laser Desorption/Ionization (LDI) Mass Spectrometric Imaging at the Single-cell Level: Distribution of Secondary Metabolites of *Arabidopsis thaliana* and *Hypericum* Species. *Plant J.* **2009**, *60*, 907-918.
74. Perdian, D. C.; Lee, Y. J. Imaging MS Methodology for More Chemical Information in Less Data Acquisition Time Utilizing a Hybrid Linear Ion Trap-Orbitrap Mass Spectrometer. *Anal. Chem.* **2010**, *82*, 9393-9400.
75. Hayasaka, T.; Goto-Inoue, N.; Zaima, N.; Shrivastava, K.; Kashiwagi, Y.; Yamamoto, M.; Nakamoto, M.; Setou, M. Imaging Mass Spectrometry with Silver Nanoparticles Reveals the Distribution of Fatty Acids in Mouse Retinal Sections. *J. Am. Soc. Mass. Spectrom.* **2010**, *21*, 1446-1454.
76. Jackson, S. N.; Ugarov, M.; Egan, T.; Post, J. D.; Langlais, D.; Schultz, J. A.; Woods, A. S. MALDI-ion mobility-TOFMS Imaging of Lipids in Rat Brain Tissue. *J. Mass Spectrom.* **2007**, *42*, 1093-1098.
77. Goto-Inoue, N.; Hayasaka, T.; Zaima, N.; Kashiwagi, Y.; Yamamoto, M.; Nakamoto, M.; Setou, M. The Detection of Glycosphingolipids in Brain Tissue Sections by Imaging Mass Spectrometry using Gold Nanoparticles. *J. Am. Soc. Mass. Spectrom.* **2010**, *21*, 1940-1943.
78. Ageta, H.; Asai, S.; Sugiura, Y.; Goto-Inoue, N.; Zaima, N.; Setou, M. Layer-specific Sulfatide Localization in Rat Hippocampus Middle Molecular Layer is Revealed by Nanoparticle-assisted Laser Desorption/Ionization Imaging Mass Spectrometry. *Med. Mol. Morphol.* **2009**, *42*, 16-23.

79. Shrivastava, K.; Hayasaka, T.; Sugiura, Y.; Setou, M. Method for Simultaneous Imaging of Endogenous Low Molecular Weight Metabolites in Mouse Brain Using TiO<sub>2</sub> Nanoparticles in Nanoparticle-Assisted Laser Desorption/Ionization-Imaging Mass Spectrometry. *Anal. Chem.* **2011**, *83*, 7283-7289.
80. Tang, H. W.; Wong, M. Y.; Lam, W.; Cheng, Y. C.; Che, C. M.; Ng, K. M. Molecular Histology Analysis by Matrix-assisted Laser Desorption/Ionization Imaging Mass Spectrometry using Gold Nanoparticles as Matrix. *Rapid Commun. Mass Spectrom.* **2011**, *25*, 3690-3696.
81. Tempez, A.; Ugarov, M.; Egan, T.; Schultz, J. A.; Novikov, A.; Della-Negra, S.; Lebeyec, Y.; Pautrat, M.; Caroff, M.; Smentkowski, V. S.; Wang, H. Y. J.; Jackson, S. N.; Woods, A. S. Matrix Implanted Laser Desorption Ionization (MILDI) Combined with Ion Mobility - Mass Spectrometry for Bio-surface Analysis. *J. Proteome Res.* **2005**, *4*, 540-545.
82. Gologan, B.; Green, J. R.; Alvarez, J.; Laskin, J.; Cooks, R. G. Ion/Surface Reactions and Ion Soft-landing. *Phys. Chem. Chem. Phys.* **2005**, *7*, 1490-1500.
83. Johnson, G. E.; Wang, C.; Priest, T.; Laskin, J. Monodisperse Au<sub>11</sub> Clusters Prepared by Soft Landing of Mass Selected Ions. *Anal. Chem.* **2011**, *83*, 8069-8072.
84. Verbeck, G.; Hoffmann, W.; Walton, B. Soft-landing Preparative Mass Spectrometry. *Analyst* **2012**, *137*, 4393-4407.
85. Yanes, O.; Woo, H. K.; Northen, T. R.; Oppenheimer, S. R.; Shriver, L.; Apon, J.; Estrada, M. N.; Potchoiba, M. J.; Steenwyk, R.; Manchester, M.; Siuzdak, G. Nanostructure Initiator Mass Spectrometry: Tissue Imaging and Direct Biofluid Analysis. *Anal. Chem.* **2009**, *81*, 2969-2975.
86. Patti, G. J.; Woo, H. K.; Yanes, O.; Shriver, L.; Thomas, D.; Uritboonthai, W.; Apon, J. V.; Steenwyk, R.; Manchester, M.; Siuzdak, G. Detection of Carbohydrates and Steroids by Cation-Enhanced Nanostructure-initiator Mass Spectrometry (NIMS) for Biofluid Analysis and Tissue Imaging. *Anal. Chem.* **2010**, *82*, 121-128.
87. Calavia, R.; Annanouch, F.; Correig, X.; Yanes, O. Nanostructure Initiator Mass Spectrometry for Tissue Imaging in Metabolomics: Future Prospects and Perspectives. *J. Proteomics* **2012**, *75*, 5061-5068.
88. Lee, D. Y.; Platt, V.; Bowen, B.; Louie, K.; Canaria, C. A.; McMurray, C. T.; Northen, T. R. Resolving Brain Regions using Nanostructure Initiator Mass Spectrometry Imaging of Phospholipids. *Integr. Biol.* **2012**, *4*, 693-699.
89. Reindl, W.; Bowen, B.; Balamotis, M. A.; Green, J. E.; Northen, T. R. Multivariate Analysis of a 3D Mass Spectral Image for Examining Tissue Heterogeneity. *Integr. Biol.* **2011**, *3*, 460-467.
90. Kim, Y. K.; Na, H. K.; Kwack, S. J.; Ryoo, S. R.; Lee, Y.; Hong, S.; Jeong, Y.; Min, D. H. Synergistic Effect of Graphene Oxide/MWCNT Films in Laser Desorption/Ionization Mass Spectrometry of Small Molecules and Tissue Imaging. *ACS Nano* **2011**, *5*, 4550-4561.
91. Tata, A.; Fernandes, A. M. A. P.; Santos, V. G.; Alberici, R. M.; Araldi, D.; Parada, C. A.; Braguini, W.; Veronez, L.; Bisson, G. S.; Reis, F. H. Z.; Alberici, L. C.; Eberlin, M. N. Nanoassisted Laser Desorption-Ionization-MS Imaging of Tumors. *Anal. Chem.* **2012**, *84*, 6341-6345.
92. Park, S. G.; Murray, K. K. Infrared Laser Ablation Sample Transfer for MALDI Imaging. *Anal. Chem.* **2012**, *84*, 3240-3245.

93. Louie, K. B.; Bowen, B. P.; McAlhany, S.; Huang, Y.; Price, J. C.; Mao, J. H.; Hellerstein, M.; Northen, T. R. Mass Spectrometry Imaging for *in situ* Kinetic Histochemistry. *Sci. Rep.* **2013**, doi:10.0138/srep01656.
94. Patti, G. J.; Shriver, L. P.; Wassif, C. A.; Woo, H. K.; Uritboonthai, W.; Apon, J.; Manchester, M.; Porter, F. D.; Siuzdak, G. Nanostructure-initiator Mass Spectrometry (NIMS) Imaging of Brain Cholesterol Metabolites in Smith-Lemli-Opitz Syndrome. *Neuroscience* **2010**, *170*, 858-864.
95. Waki, M. L.; Onoue, K.; Takahashi, T.; Goto, K.; Saito, Y.; Inami, K.; Makita, I.; Angata, Y.; Suzuki, T.; Yamashita, M.; Sato, N.; Nakamura, S.; Yuki, D.; Sugiura, Y.; Zaima, N.; Goto-Inoue, N.; Hayasaka, T.; Shimomura, Y.; Setou, M. Investigation by Imaging Mass Spectrometry of Biomarker Candidates for Aging in the Hair Cortex. *PLoS One* **2011**, *6*, e26721.
96. Ronci, M.; Rudd, D.; Guinan, T.; Benkendorff, K.; Voelcker, N. H. Mass Spectrometry Imaging on Porous Silicon: Investigating the Distribution of Bioactives in Marine Mollusc Tissues. *Anal. Chem.* **2012**, *84*, 8996-9001.
97. Lanni, E. J.; Rubakhin, S. S.; Sweedler, J. V. Mass Spectrometry Imaging and Profiling of Single Cells. *J. Proteomics* **2012**, *75*, 5036-5051.
98. Wen, X.; Dagan, S.; Wysocki, V. H. Small-molecule Analysis with Silicon-nanoparticle-assisted Laser Desorption/Ionization Mass Spectrometry. *Anal. Chem.* **2007**, *79*, 434-444.
99. Woo, H. K.; Northen, T. R.; Yanes, O. Siuzdak, G. Nanostructure-initiator Mass Spectrometry: a Protocol for Preparing and Applying NIMS Surfaces for High-sensitivity Mass Analysis. *Nat. Protoc.* **2008**, *3*, 1341-1349.
100. Walker, B. N.; Stolee, J. A.; Vertes, A. Nanophotonic Ionization for Ultratrace and Single Cell Analysis by Mass Spectrometry. *Anal. Chem.* **2012**, *84*, 7756-7762.
101. Liu, Q.; Guo, Z.; He, L. Mass Spectrometry Imaging of Small Molecules Using Desorption/Ionization on Silicon (DIOS). *Anal. Chem.* **2007**, *79*, 3535-3541.
102. Shrestha, B.; Vertes, A. In Situ Metabolic Profiling of Single Cells by Laser Ablation Electrospray Ionization Mass Spectrometry. *Anal. Chem.* **2009**, *81*, 8265-8271.
103. Rubakhin, S. S.; Greenough, W. T.; Sweedler, J. V. Spatial Profiling with MALDI MS: Distribution of Neuropeptides within Single Neurons. *Anal. Chem.* **2003**, *75*, 5374-5380.
104. Schober, Y.; Guenther, S.; Spengler, B.; Römpf, A. Single Cell Matrix-assisted Laser Desorption/Ionization Mass Spectrometry Imaging. *Anal. Chem.* **2012**, *84*, 6293-6297.
105. Zavalin, A.; Todd, E. M.; Rawhouser, P. D.; Yang, J.; Norris, J. L.; Caprioli, R. M. Direct Imaging of Single Cells and Tissue at Sub-cellular Spatial Resolution using Transmission Geometry MALDI MS. *J. Mass. Spectrom.* **2012**, *47*, 1473-1481.
106. Boxer, S. G.; Kraft, M. L.; Weber, P. K. Advances in Imaging Secondary Ion Mass Spectrometry for Biological Samples. *Annu. Rev. Biophys.* **2009**, *38*, 53-74.
107. Wong, S. C. C.; Hill, R.; Blenkinsopp, P.; Lockyer, N. P.; Weibel, D. E.; Vickerman, J. C. Development of a C<sub>60</sub><sup>+</sup> Ion Gun for Static SIMS and Chemical Imaging. *Appl. Surf. Sci.* **2003**, *203-204*, 219-222.

108. Spengler, B.; Hubert, M. Scanning Microprobe Matrix-assisted Laser Desorption Ionization (SMALDI) Mass Spectrometry: Instrumentation for Sub-micrometer Resolved LDI and MALDI Surface Analysis. *J. Am. Soc. Mass. Spectrom.* **2002**, *13*, 735-748.
109. Römpp, A.; Guenther, S.; Schober, Y.; Schulz, O.; Takats, Z.; Kummer, W.; Spengler, B. Histology by Mass Spectrometry: Label-free Tissue Characterization Obtained from High-Accuracy Bioanalytical Imaging. *Angew. Chem. Int. Ed.* **2010**, *49*, 3834–3838.
110. Chaurand, P.; Schriver, K. E.; Caprioli, R. M. Instrument Design and Characterization for High Resolution MALDI-MS Imaging of Tissue Sections. *J. Mass Spectrom.* **2007**, *42*, 476-489.
111. Guenther, S.; Römpp, A.; Kummer, W.; Spengler, B. AP-MALDI Imaging of Neuropeptides in Mouse Pituitary Gland with 5 $\mu$ m Spatial Resolution and High Mass Accuracy. *Int. J. Mass Spectrom.* **2011**, *305*, 228-237.
112. Luxembourg, S. L.; Mize, T. H.; McDonnell, L. A.; Heeren, R. M. A. High-spatial Resolution Mass Spectrometric Imaging of Peptide and Protein Distributions on a Surface. *Anal. Chem.* **2004**, *76*, 5339-5344.
113. Klerk, L. A.; Altelaar, A. F. M.; Froesch, M.; McDonnell, L. A.; Heeren, R. M. A. Fast and Automated Large-area Imaging MALDI Mass Spectrometry in Microprobe and Microscope Mode. *Int. J. Mass Spectrom.* **2009**, *285*, 19-25.
114. Schürenberg, M.; Schulz, T.; Dreisewerd, K.; Hillenkamp, F. Matrix-assisted Laser Desorption/Ionization in Transmission Geometry: Instrumental Implementation and Mechanistic Implications. *Rapid Comm. Mass Spectrom.* **1996**, *10*, 1873-1880.
115. Galicia, M. C.; Vertes, A.; Callahan, J. H. Atmospheric Pressure Matrix-assisted Laser Desorption/Ionization in Transmission Geometry. *Anal. Chem.* **2002**, *74*, 1891-1895.

## CHAPTER II

### SEMI-TRANSPARENT NANOMATERIAL THIN FILMS FOR MASS SPECTROMETRY IMAGING AND OPTICAL MICROSCOPY

#### **2.1 Introduction**

A number of irradiation-based methods may be used to perform MS imaging, including but not limited to SIMS,<sup>1-3</sup> MALDI,<sup>4-5</sup> laser ablation – inductively coupled plasma (LA-ICP-MS),<sup>6-7</sup> and LAESI.<sup>8-9</sup> Traditionally, SIMS has achieved the best spatial resolution (sub- $\mu\text{m}$ ), but its ability to ionize intact biological molecules has been limited. However, recent cluster-based ion beams such as  $\text{C}_{60}^+$  have improved the usable mass range to approximately 1 kDa using low- $\mu\text{m}$  spatial resolution.<sup>10</sup> High-resolution MALDI imaging approaches such as scanning-microprobe MALDI (SMALDI) and ion microscopy make use of unique optics and instrumentation to image with spatial resolutions less than 10  $\mu\text{m}$ .<sup>11-14</sup> At this resolution, MALDI matrix application and the resulting co-crystallization with sample plays a significant role in the resulting quality of the images.<sup>15</sup> LA-ICP-MS is capable of quantitative imaging, but is essentially limited to elemental analysis. The primary advantage of LAESI is that desorption occurs at atmospheric pressure, so little to no sample preparation is needed.<sup>16</sup> Nevertheless, LAESI utilizes IR lasers which have cannot be focused as sharply as UV lasers used in MALDI or LA-ICP-MS due to diffraction limits.

While these methods differ in terms of strengths and limitations, a common trend has emerged: as imaging spatial resolution increases, sensitivity decreases. There are several likely causes for this observation. First, as sample desorption area decreases, there are fewer molecules to be ionized; therefore, ion yields decrease. Second, for techniques such as SIMS and MALDI, the energy required to ionize molecules increases significantly as the irradiation area is reduced.<sup>17-18</sup> The resulting excess energy can induce analytes to fragment in the source region of the mass spectrometer. A goal of the biological MS imaging community is to circumvent these limitations in order to generate images with sub-cellular spatial resolution, high sensitivity, and soft ionization.



Another method introduced in the previous chapter, NIMS, may lead to sub-cellular spatial resolution, high sensitivity and soft ionization of biomolecules.<sup>19-20</sup> NIMS ionization utilizes energy-absorbing (laser- or ion-beam) nanoporous silicon substrates coated with viscous liquid initiators; these initiators help transfer energy to sample molecules but rarely ionize, generating mass spectra with very low background noise. This reduction in chemical noise leads to impressive sensitivity, especially in the low  $m/z$  region.<sup>19,21</sup> Several factors likely contribute to this sensitivity, including efficient desorption from porous silicon (pSi) and initiators which can extract and pre-concentrate biological molecules.<sup>22</sup> Although it is more common to use hydrophobic initiators, hydrophilic initiators have been shown to extract and ionize polar molecules as well.<sup>23</sup> Moreover, pores ~10 nm in diameter limit lateral diffusion of analyte molecules and ensure that MS images obtained using NIMS are spatially accurate.<sup>24</sup> Current substrates, however, are formed on non-transparent Si wafers which do not allow for the visualization of cells by microscopy. In this chapter, novel semi-transparent NIMS films are introduced for both MS imaging and optical microscopy.

## **2.2 Experimental Section**

### *Materials*

Angiotensin II and ethanol were obtained from Sigma-Aldrich USA. Hydrofluoric acid (48-51% in water) was purchased from Acros Organics. Hydrogen peroxide (30%) and concentrated sulfuric acid were from Fisher Scientific. Bovine insulin (5 pmol/ $\mu$ L stock) was obtained from Waters Corporation and bis(heptadecafluoro-1,1,2,2-tetrahydrodecyl)tetramethyldisiloxane (BisF17) was obtained from Gelest. Transparent indium tin oxide (ITO) glass slides were obtained from Delta Technologies.

### *Fabrication and Preparation of NIMS Films*

P-type crystalline silicon wafers (Boron-doped,  $\langle 100 \rangle$  orientation, 0.01  $\Omega$  resistivity) were cut into squares using a diamond tip pen, were rinsed with deionized water, and then were soaked in piranha (2:1 concentrated  $H_2SO_4$  : 30%  $H_2O_2$ ) solution for 30 minutes. Chips were

rinsed thoroughly with deionized water and dried with nitrogen. Porous silicon was then formed using a 25% hydrofluoric acid solution (1:1 50% HF and ethanol) in a custom Teflon etching chamber with an etching area of 2 cm<sup>2</sup>.

In order to form semi-transparent films, a two-step etching process was used. First, a constant current density was applied to etch pores perpendicular to the surface. For this step, both etching times and applied current densities were varied in order to produce pSi films with different porosities and thicknesses and to determine how the parameters affect film transparency and NIMS performance (see **Table 2-1**). Second, a higher current density was applied in a pulsed manner to break off the pSi films. Because of the high current density, a region of effectively 100% porosity is formed at the pSi – Si wafer interface, resulting in film detachment.<sup>25</sup> All films were removed using the following procedure. A current density of 250 mA/cm<sup>2</sup> was applied for 1.7 seconds and followed by 1.7 seconds of rest before the next current density pulse was applied. This was performed 2x over a time of 6.8 seconds. Then a current density of 210 mA/cm<sup>2</sup> was applied for 1.7 seconds followed by 6.0 seconds of rest. This was repeated 10x over a time of 77.0 seconds. Films were rinsed with ethanol and transferred from the silicon wafer to ITO-coated slides using tweezers. Films were manually attached to ITO-coated glass in a dish of ethanol. After attachment, films were oven dried at 80°C for 5 minutes to remove the trapped solvent.

Before the addition of analytes for MS analysis, bare pSi films were briefly rinsed with 1% HNO<sub>3</sub>, deionized water and dried. Then, 30 µL of BisF17 initiator was spotted onto each pSi film, which was incubated for 45 minutes and then dried (N<sub>2</sub> gas and low heat, repeated 3x). It was important to use a gentle stream of N<sub>2</sub> when drying, or else films could crack or separate from the ITO-coated glass slides. NIMS films not used for cell imaging were stored at room temperature.

#### *SEM Imaging of Porous Silicon*

Average pore diameters and film thicknesses were measured from SEM images using ImageJ software (NIH, <http://rsbweb.nih.gov/ij/>). Images were obtained on either a Hitachi S-4200 or a Raith eLiNE microscope, both of which are in the Vanderbilt Institute of Nanoscale Science and Engineering (VINSE) core laboratory. Small pieces of pSi were broken off from larger films

and attached to conductive carbon tape for SEM surface imaging. Film thicknesses were determined by etching layers into a silicon wafer (each layer corresponding to the etching conditions of an individual film), cleaving the wafer in half and performing cross-sectional SEM imaging.

#### *NIMS Optimization and Analysis*

Optical density measurements were performed on a Cary UV-vis spectrometer. MS optimization experiments were performed on a Voyager-DE-STR mass spectrometer (Applied Biosystems) in both linear and reflectron TOF modes. The linear mode settings were as follows: 100 ns delayed extraction, 95% grid, and 50 shots per spectrum. Reflectron mode was used with the following settings: 140 ns delay, 70% grid, and 40 shots per spectrum. A nitrogen gas laser (337 nm) was used in all non-imaging experiments. A stock solution composed of 250 fmol/ $\mu$ L angiotensin II and 500 fmol/ $\mu$ L bovine insulin was prepared and used for MS optimization studies. On each film, three 1.0  $\mu$ L spots were placed, and three spectra were taken for each spot (0-7000  $m/z$  range). Ion signal intensities were determined using the centroid function in Data Explorer 4.3 software (Applied Biosystems) and averaged. Error bars correspond to one standard deviation.

#### *Cell Preparation*

Cells were loaded onto NIMS substrates by Joshua Broussard (Webb group). HT1080 cells were maintained in Dulbecco's Modified Eagles Medium or DMEM (Invitrogen) with 10% fetal bovine serum (FBS) (HyClone) and 1% penicillin/streptomycin (Invitrogen). Cells were then trypsinized with 0.25% Trypsin-EDTA (Invitrogen) and plated on the NIMS film. Cells were allowed to become confluent, and a scratch wound was made using a 20  $\mu$ L pipet tip. Three hours post wounding, the growth media was removed and the sample was washed twice with dilute PBS. Excess PBS was aspirated, and the sample was frozen at -80 °C until analysis.

### *NIMS Imaging*

Images were acquired using an external Nd:YAG laser (frequency tripled, 355 nm), a digital micromirror array,<sup>26-27</sup> a Voyager DE-STR mass spectrometer (in linear mode) and MALDI MS Imaging Tool software (Novartis, maldi-msi.org). Images were obtained using 14  $\mu\text{m}$  raster steps in MALDI MS Imaging Tool and processed using BioMap software (Novartis, maldi-msi.org) without normalization. Single-pixel mass spectra were baseline corrected and processed using Data Explorer. Post-source decay (PSD) experiments were performed using the Voyager DE-STR mass spectrometer using high laser energy and the timed ion selector (TIS). Lipids from the cell monolayer were extracted using 4:1 MeOH:H<sub>2</sub>O and placed on a clean NIMS film for PSD analysis.

### *Optical Microscopy*

Phase-contrast microscopy was performed on a Leica DMIL microscope with a NPLAN 5x phase 0 (NA 0.12) objective lens.

### *Safety*

Piranha solution (2:1 concentrated H<sub>2</sub>SO<sub>4</sub> : 30% H<sub>2</sub>O<sub>2</sub>) is a strong oxidant. All work with piranha solutions should be performed in a fume hood using the proper protective equipment, glass beakers and stainless steel tweezers. Let piranha waste cool for at least 24 hours before storage or neutralization.

Hydrofluoric acid (HF) is extremely toxic. In addition to reading the MSDS report for HF, please consult reference 28. All HF chemistry should be performed in a fume hood with proper protective equipment, using Teflon or plastic containers and plastic tools.

## **2.3 Results and Discussion**

### *NIMS Film Optimization*

The purpose of our optimization experiments was to determine the best film parameters (pore size and film thickness) for both NIMS and optical microscopy. Pore diameters and film

thicknesses (i.e. pore depths) were first measured by SEM (**Figure 2-1**) because multiple substrates were prepared under different anodic etching conditions (**Table 2-1**). For all substrates, average pore diameters ( $< 20$  nm) were three orders of magnitude less than pore depths ( $< 20$   $\mu\text{m}$ ). For constant etching times, increasing the applied current density increased the etching rate and, thus, the resulting film thickness (**Table 2-1**). When current density was held constant, longer etching times also produced thicker films (**Table 2-1**). The etching time did not have a significant effect on pore diameter (**Table 2-1**). In summary, it was observed that both current density and etching time affected the film thickness, but current density affected the pore size more than etching time. These trends are consistent with prior studies on porous silicon.<sup>29</sup>

The film thickness plays a significant role in the transparency of the film. The pore size does not affect film transparency; the pores are small compared to visible wavelengths and hence are not expected to cause scattering losses that would reduce transparency. Silicon absorbs light of energy below the bandgap (1.1 eV), which includes UV and visible wavelengths. Optical density measurements were used to quantify the relationship between film thicknesses and light absorption (**Figure 2-2A**). UV and visible light absorption increased with increasing film thickness. Higher-energy visible wavelengths and UV light were absorbed strongly, while lower-energy visible wavelengths were absorbed to a lesser degree. In order to determine a threshold for evaluating transparency, percent transmission values at 700 nm were compared. Films less than 15  $\mu\text{m}$  in thickness transmitted  $>15\%$  of 700 nm light and were considered sufficiently transparent. Films more than 15  $\mu\text{m}$  in thickness allowed  $<15\%$  of 700 nm through and were considered insufficiently transparent. A qualitative evaluation of transparency was also performed, and correlated well with our spectrophotometry studies (**Figure 2-3**).

NIMS performance was plotted against film thickness (**Figure 2-2B**). Films less than 15  $\mu\text{m}$  are shown as open shapes in **Figure 2-2B**, and films above 15  $\mu\text{m}$  are shown as dark shapes. Angiotensin II peptide ( $[\text{M}+\text{H}]^+ = 1046.5$  Da, 250 femtomoles in a  $\sim 100$   $\mu\text{m}$  spot) was the biomolecular standard which was desorbed from the surface and ionized. Between 8-13  $\mu\text{m}$ ,

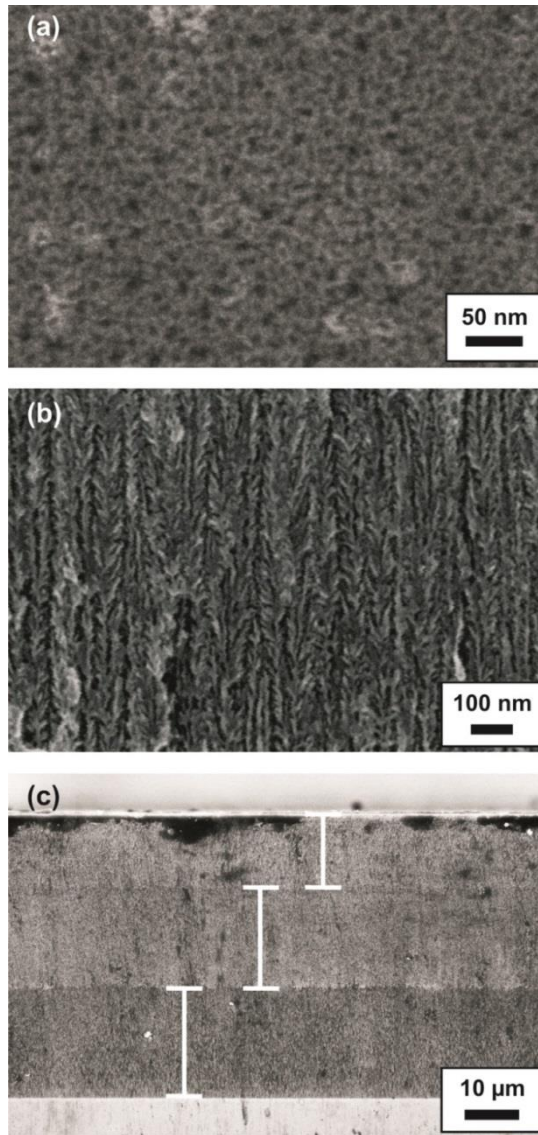


**Figure 2-1.** Characterization of semi-transparent substrates by SEM. (a) Top view. Pores are approximately 10 nm in diameter. (b) Cross-sectional view. (c) Three pSi layers were etched on top of one another, and film thicknesses were measured. All film thickness values are presented in **Table 2-1**.

Film #	Etch Time (s)	Current Density (mA/cm <sup>2</sup> )	Pore Depth (μm)	Avg. Pore Diameter (nm)
1	300	24	7.8	7 ± 3 (n = 101)
2	300	36	9.8	12 ± 3 (n = 92)
3	300	48	10.7	18 ± 5 (n = 85)
4	450	24	11.9	9 ± 5 (n = 100)
5	450	36	14.9	13 ± 5 (n = 80)
6	450	48	16.1	17 ± 8 (n = 56)
7	600	24	12.8	7 ± 4 (n = 72)
8	600	36	16.9	11 ± 4 (n = 125)
9	600	48	18.7	14 ± 7 (n = 195)

**Table 2-1.** Relating etching conditions with film parameters. Film thicknesses and pore diameters were measured with SEM. Etching times and current densities correspond to non-pulsed etching which generated the porous silicon layers. All films were removed from the silicon wafer using the same procedure.

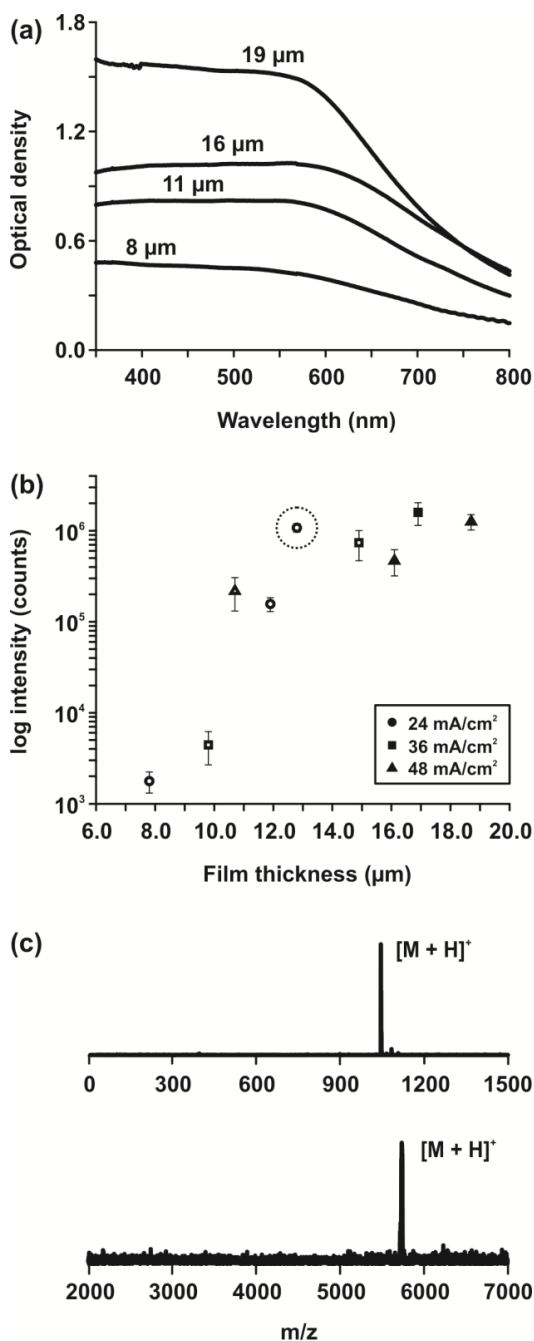


**Figure 2-2.** Optimization of semi-transparent substrates. (a) Optical density measurements of substrates with thicknesses of 8, 11, 16, and 19  $\mu\text{m}$ . (b) Relating film thickness to NIMS performance. Intensities are the logarithm of peak areas generated from 250 femtomoles angiotensin II peptide. Different shapes correspond to different etching current densities from **Table 2-1**. Open shapes correspond to substrates which were sufficiently transparent (>15% transmission at 700 nm), while dark shapes correspond to substrates which were not sufficiently transparent for microscopy. The optimized film thickness (13  $\mu\text{m}$ ) for NIMS and optical microscopy is circled. (c) Characteristic mass spectra from optimized NIMS substrate. (*top*) 250 femtomoles angiotensin II peptide (DRVYIPHF,  $[\text{M}+\text{H}]^+$  = 1046.5 Da); (*bottom*) 500 femtomoles bovine insulin ( $[\text{M}+\text{H}]^+$  = 5734 Da).



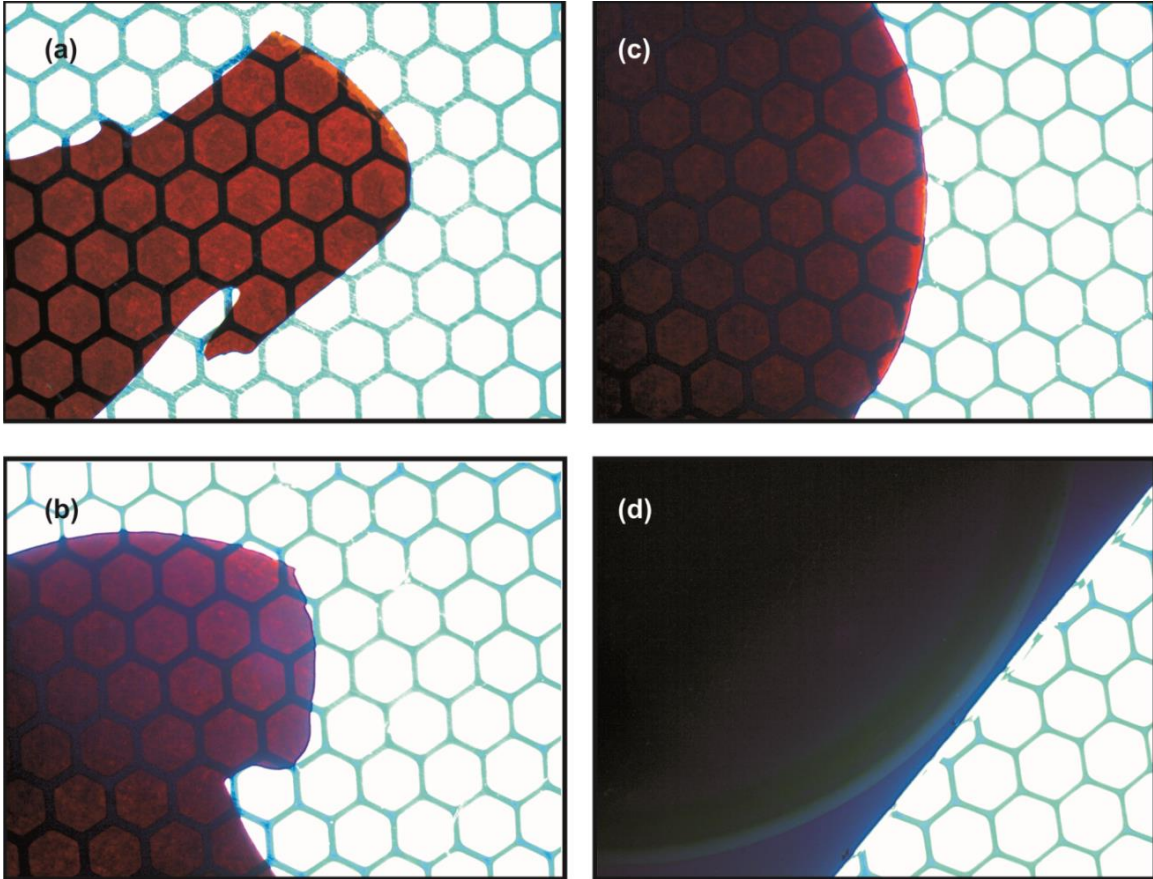


**Figure 2-3.** Backlit CCD photographs of NIMS substrates above a metal grid. Semi-transparent NIMS films have thicknesses of (a) 10  $\mu\text{m}$ , (b) 13  $\mu\text{m}$ , and (c) 19  $\mu\text{m}$ . Substrates for parts a-c are attached to ITO-coated glass slides. (d) Traditional NIMS surfaces on silicon wafers are not transparent.

signal from our substrates increased with film thickness. Similarly, Woo et. al. reported signal to noise increases using longer etching times (hence, thicker pSi) for standard NIMS.<sup>21</sup> However, signal intensities began to level off above 13  $\mu\text{m}$  due to detector saturation. Therefore, for optimum NIMS performance and transparency, it was determined that semi-transparent films should have thicknesses of 13  $\mu\text{m}$ .

Like standard NIMS wafers, our optimized films generated very low chemical noise in the low  $m/z$  region (**Figure 2-2C**, *top*). Several low-mass background peaks were observed rarely, however, and more pronounced when a spot without analyte was laser-irradiated (**Figure 2-4**). These molecules have been suggested to be alkylammonium salts used in the silicon fabrication process,<sup>30</sup> and were minimized by a quick 1%  $\text{HNO}_3$  rinse before the addition of initiator. Although NIMS films produced very clean mass spectra, sensitivity decreased when analyzing larger molecules, resulting in a sensitive (femtomole) mass dynamic range of approximately 6 kDa (**Figure 2-2C**, *bottom*). Substrates were stable at room temperature for several months without a significant loss in performance (**Figure 2-5**).

### *Cell Imaging*

Cell signaling and collective cell migration play vital roles in many biological processes, including cancer.<sup>31</sup> Therefore, this imaging platform was used to visualize molecular distributions at the leading edge of migrating cells. As a proof-of-concept experiment, a scratch-wounded HT1080 fibrosarcoma cell monolayer was imaged. A phase-contrast microscope image was obtained from the wounded cell monolayer on the semi-transparent NIMS surface prior to mass spectrometry imaging (**Figure 2-6**), verifying that enough visible light passes through the film for optical microscopy. Because material is laser-ablated for NIMS, optical microscopy was performed off-line, before MS imaging. Improvements in our MS instrumentation are required in order to perform microscopy and NIMS imaging in direct succession.

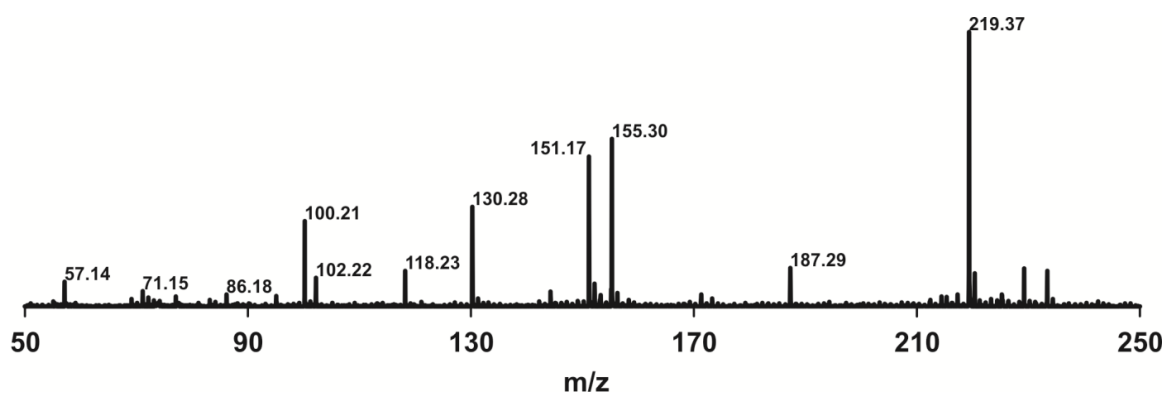


**Figure 2-4.** Background NIMS signals - observed only when irradiating an analyte-free region on the film using high laser fluence. Several peaks (86, 102, 130, 155 Da) correspond to those described in Wen *et. al.* (Ref. 30), which were suggested to be alkylammonium salts used in the silicon fabrication process.

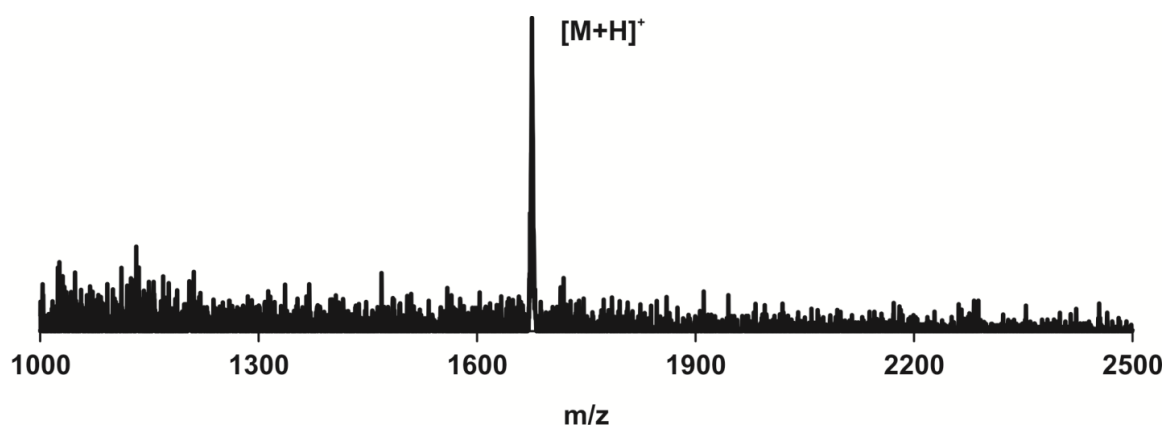


**Figure 2-5.** Detection of 10 femtomoles of neurotensin peptide ( $[M+H]^+ = 1673$  Da). Spectrum was obtained from 3-month-old NIMS film stored at room temperature and air.

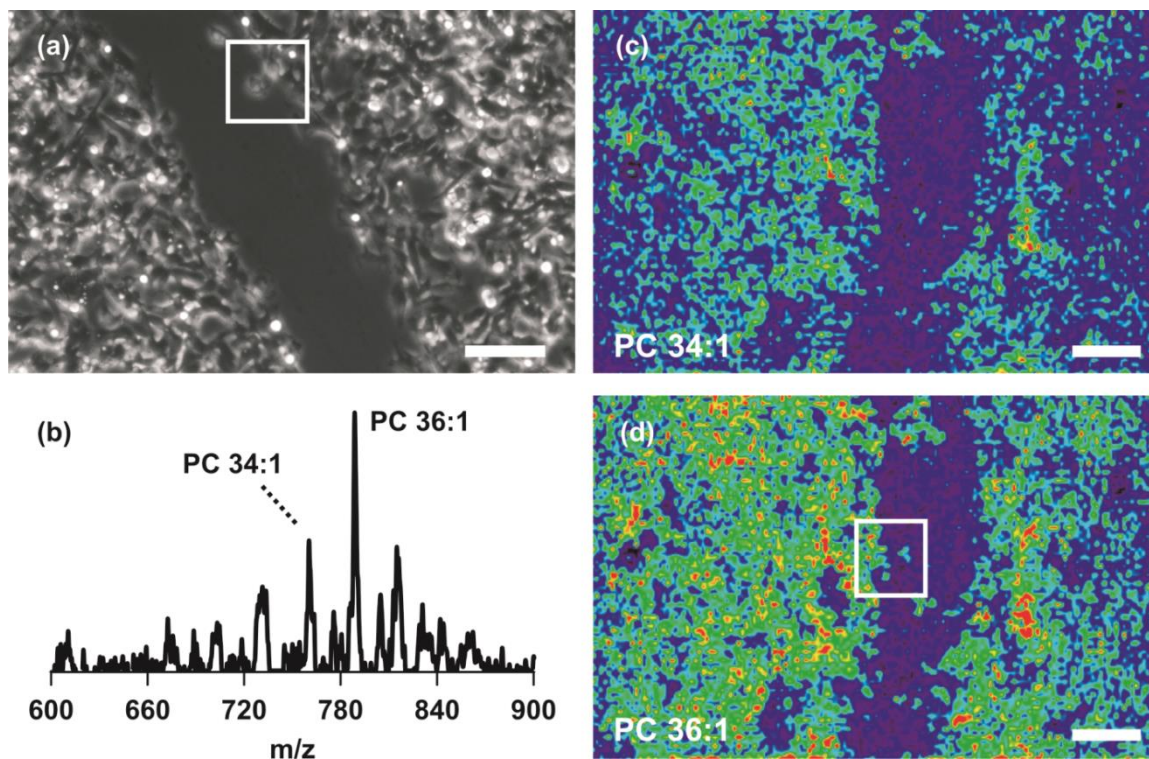


**Figure 2-6.** NIMS imaging and optical microscopy of cells. (a) Phase-contrast microscope image of scratch-wounded HT1080 cell monolayer on semi-transparent NIMS film. Scale bar is 250  $\mu\text{m}$ . A single cell at the wound edge is contained in a 250 x 250  $\mu\text{m}$  white box. (b) Single-pixel NIMS mass spectrum from wounded cell monolayer. Imaged masses are labeled. Mass spectrometry images of (c) PC 34:1 ( $[M+H]^+ = 760.5$  Da) and (d) PC 36:1 ( $[M+H]^+ = 788.5$  Da) allow cell membranes to be located. NIMS images were obtained with a spatial resolution of 14  $\mu\text{m}$ . Signal intensities are expressed using a false coloring scale (low/*blue*  $\rightarrow$  high/*red*). MS image scale bars correspond to 250  $\mu\text{m}$ . Individual cells at the wound edge are contained in the 250 x 250  $\mu\text{m}$  white box in part (d).

For the imaging experiment outlined in this manuscript, a simplified version of an external laser-focusing system and a commercial TOF mass spectrometer was used to confirm the practicality of NIMS imaging (**Figure 2-7**). A single-pixel NIMS mass spectrum using 3 laser shots is shown in **Figure 2-6B**. Each image pixel was 14  $\mu\text{m}$  in height and width (**Figure 2-8**). Two-dimensional images of phosphatidylcholine or PC 34:1 (760.5 Da) and PC 36:1 (788.5 Da) are presented in **Figures 2-6C** and **2-6D**, respectively. These lipids were specific to cell membranes, allowing for the wound to be differentiated from the cell monolayer and visualized in blue. Single cells at the wound edge are shown in the white 250 x 250  $\mu\text{m}$  box in **Figure 2-6D**. Here, the ability to resolve PC lipids by their intact  $m/z$  values is demonstrated while maintaining a relatively high spatial resolution. Lipid identifications were supported by post-source decay (PSD) experiments (**Figure 2-9**). However, a more robust tandem MS approach (*e.g.* collision-induced dissociation) is needed to determine the exact composition of fatty acid tails.

Because NIMS is a surface-based technique, the efficiency of the laser desorption/ionization process is repressed when thick layers of material are present. Consequently, Siuzdak and colleagues have used very thin serial sections (3-5  $\mu\text{m}$ ) when performing NIMS tissue imaging experiments.<sup>32</sup> Before our cell imaging experiments, monolayers attached to the NIMS film were placed in vacuum for at least 3 hours to degas the cells, decreasing their thickness and improving MS performance slightly. The BisF17 initiator has an extremely low vapor pressure, so the NIMS substrate was stable under high vacuum ( $\leq 10^{-7}$  Torr). Nevertheless, detecting biomolecules directly from cells was less efficient than from solutions spotted on the surface. As with standard NIMS, a primary limitation of semi-transparent NIMS is that sensitivity decreases with thick samples.

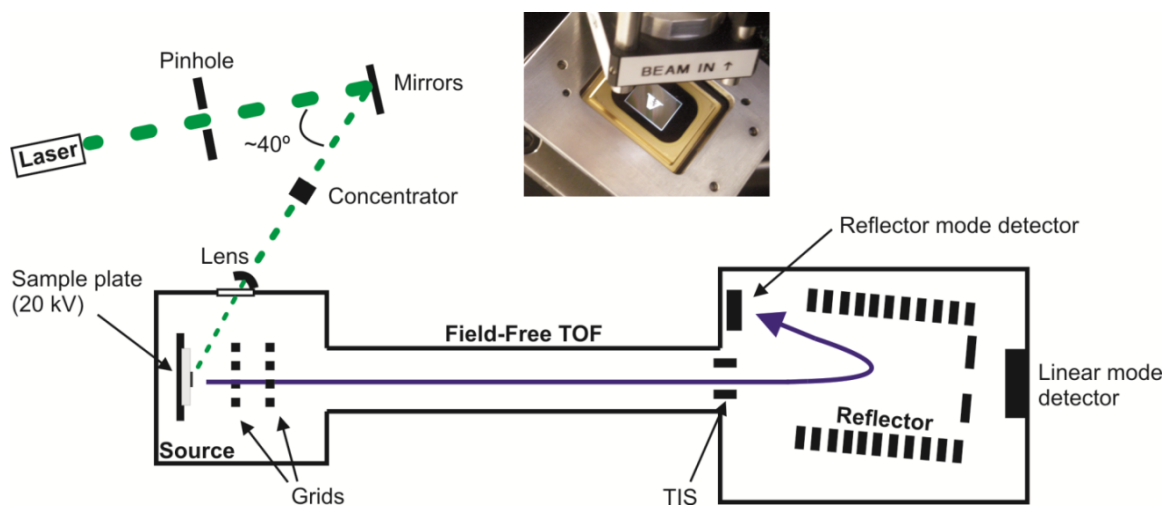


**Figure 2-7.** Schematic of instrumentation used for NIMS imaging. A frequency-tripled Nd:YAG laser (355 nm) is fired onto a digital micromirror device (*inset*), which redirects a small, selected portion of the beam towards the Voyager DE-STR mass spectrometer. The mass spectrometer is operated in either linear or reflector TOF mode. The timed ion selector (TIS) can be used to isolate  $m/z$  values for PSD fragmentation.

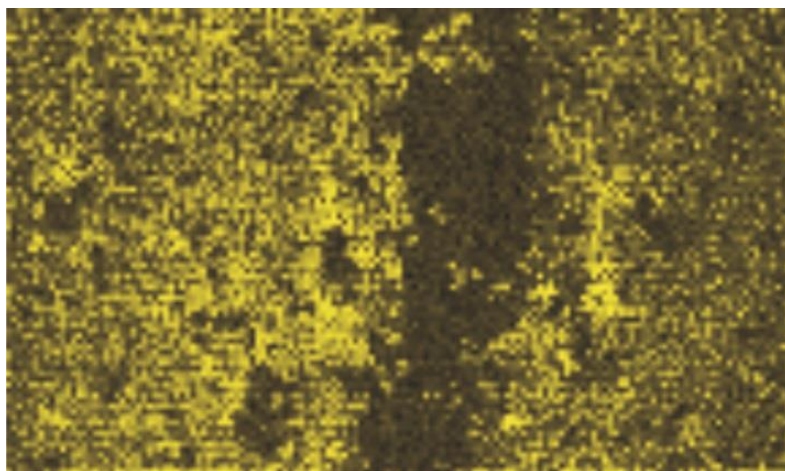


**Figure 2-8.** Raw NIMS image of  $m/z$  788.5 (PC 36:1) from scratch-wounded HT1080 cell monolayer. Image was acquired using MALDI MS Imaging Tool software. Individual pixels are 14 x 14  $\mu\text{m}$ . Image covers a total area of 2.1 mm by 1.2 mm.



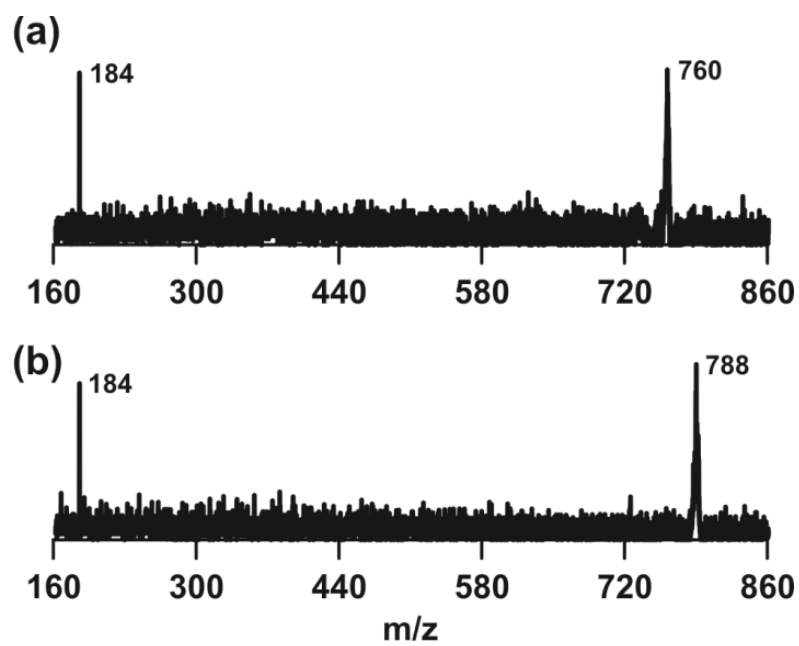


**Figure 2-9.** NIMS post-source decay (PSD) mass spectra of imaged phospholipids (760.5 Da, PC 34:1; 788.5 Da, PC 36:1). Fragments of 184 Da support PC assignments. Lipids were extracted from cells using 4:1 methanol to water and placed on a fresh substrate before analysis.

An additional limitation of this approach is that, like MALDI, higher fluence is needed to generate sufficient signal for imaging from low-micrometer dimensions. This tends to introduce more chemical noise into the NIMS mass spectrum and can reduce the softness of ionization. Theoretically, NIMS imaging resolution is limited only by the diffraction limit of the laser used, and not by crystal size of a co-crystalizing MALDI matrix. Practically, however, NIMS spatial resolution is determined not only by laser spot size but also laser fluence and sensitivity.

## **2.4 Conclusions**

In conclusion, porous silicon films have been developed which allow for the pairing of optical microscopy and the molecular mapping capabilities of NIMS. Unlike MALDI, NIMS generates little chemical noise and is thus a powerful method for analyzing small molecules, metabolites, peptides and even small proteins with sensitivity and 14  $\mu\text{m}$  spatial resolution. As our instrumentation and spatial resolution improves, the strength of coupling NIMS with optical microscopy is the potential to target specific biological molecules in precisely defined sub-cellular regions.

## **2.5 Acknowledgements**

Thank you to the Vanderbilt Institute for Nanoscale Science and Engineering (VINSE) for use of core facilities and SEM training as well as Judson Ryckman for providing high resolution SEM images. Thank you to Dr. Kellen Harkness and Dr. Jody May for helpful suggestions with the text. This work was supported by the National Science Foundation (ECCS0746296 to Y.J.), the Army Research Office (W911NF-08-1-0200 to J.L.L. and W911NF-09-1-0101 to Y.J.), the National Institutes of Health (GM092914 to D.J.W., T32CA078136 to J.A.B. and RC2DA028981 and RO1GM092218 to J.A.M.), the Vanderbilt Institute of Chemical Biology, the Vanderbilt Institute for Integrative Biosystems Research and Education, and the Vanderbilt University College of Arts and Sciences.

## 2.6 References

1. Boxer, S. G.; Kraft, M. L.; Weber, P. K. Advances in Imaging Secondary Ion Mass Spectrometry for Biological Samples. *Annu. Rev. Biophys.* **2009**, *38*, 53-74.
2. Ostrowski, S. G.; Van Bell, C. T.; Winograd, N.; Ewing, A. G. Mass Spectrometric Imaging of Highly Curved Membranes During *Tetrahymena* Mating. *Science* **2004**, *305*, 71-73.
3. Tucker, K. R.; Li, Z.; Rubakhin, S. S.; Sweedler, J. V. Secondary Ion Mass Spectrometry Imaging of Molecular Distributions in Cultured Neurons and Their Processes: Comparative Analysis of Sample Preparation. *J. Am. Soc. Mass. Spectrom.* **2012**, *23*, 1931-1938.
4. Seeley, E. H.; Caprioli, R. M. Molecular Imaging of Proteins in Tissues by Mass Spectrometry. *Proc. Natl. Acad. Sci. U.S.A.* **2008**, *105*, 18126-18131.
5. Zimmerman, T. A.; Rubakhin, S. S.; Sweedler, J. V. MALDI Mass Spectrometry Imaging of Neuronal Cell Cultures. *J. Am. Soc. Mass Spectrom.* **2011**, *22*, 828-836.
6. Becker, J. S.; Zoriy, M.; Becker, J. S.; Dobrowolska, J.; Matusch, A. Laser Ablation Inductively Coupled Plasma Mass Spectrometry (LA-ICP-MS) in Elemental Imaging of Biological Tissues and in Proteomics. *J. Anal. At. Spectrom.* **2007**, *22*, 736-744.
7. Wu, B.; Becker, J. S. Imaging of Elements and Molecules in Biological Tissues and Cells in the Low-micrometer and Nanometer Range. *Int. J. Mass Spectrom.* **2011**, *307*, 112-122.
8. Nemes, P.; Woods, A. S.; Vertes, A. Simultaneous Imaging of Small Metabolites and Lipids in Rat Brain Tissues at Atmospheric Pressure by Laser Ablation Electrospray Ionization Mass Spectrometry. *Anal. Chem.* **2010**, *82*, 982-988.
9. Shrestha, B.; Patt, J. M.; Vertes, A. In Situ Cell-by-Cell Imaging and Analysis of Small Cell Populations by Mass Spectrometry. *Anal. Chem.* **2011**, *83*, 2947-2955.
10. Fletcher, J. S.; Lockyer, N. P.; Vaidyanathan, S.; Vickerman, J. C. TOF-SIMS 3D Biomolecular Imaging of *Xenopus laevis* Oocytes using Buckminsterfullerene (C<sub>60</sub>) Primary Ions. *Anal. Chem.* **2007**, *79*, 2199-2206.
11. Spengler, B.; Hubert, M. Scanning Microprobe Matrix-Assisted Laser Desorption/Ionization (SMALDI) Mass Spectrometry: Instrumentation for Sub-micrometer Resolved LDI and MALDI Surface Analysis. *J. Am. Soc. Mass Spectrom.* **2002**, *13*, 735-748.
12. Rompp, A.; Guenther, S.; Schober, Y.; Schulz, O.; Takats, Z.; Kummer, W.; Spengler, B. Histology by Mass Spectrometry: Label-free Tissue Characterization Obtained from High-Accuracy Bioanalytical Imaging. *Angew. Chem. Int. Ed.* **2010**, *49*, 3834-3838.
13. Luxembourg, S. L.; Mize, T. H.; McDonnell, L. A.; Heeren, R. M. A. High-Spatial Resolution Mass Spectrometric Imaging of Peptide and Protein Distributions on a Surface. *Anal. Chem.* **2004**, *76*, 5339-5344.
14. Jungmann, J. H.; MacAleese, L.; Visser, J.; Vrakking, M. J. J.; Heeren, R. M. A. High Dynamic Range Bio-Molecular Ion Microscopy with the Timepix Detector. *Anal. Chem.* **2011**, *83*, 7888-7894.

15. Bouschen, W.; Schulz, O.; Eikel, D.; Spengler, B. Matrix Vapor Deposition/Recrystallization and Dedicated Spray Preparation for High-Resolution Scanning Microprobe Matrix-Assisted Laser Desorption/Ionization Imaging Mass Spectrometry (SMALDI-MS) of Tissue and Single Cells. *Rapid Comm. Mass Spectrom.* **2010**, *24*, 355-364.
16. Harris, G. A.; Galhena, A. S.; Fernandez, F. M. Ambient Sampling/Ionization Mass Spectrometry: Applications and Current Trends. *Anal. Chem.* **2011**, *83*, 4508-4538.
17. Fletcher, J. S.; Lockyer, N. P.; Vickerman, J. C. Molecular SIMS Imaging; Spatial Resolution and Molecular Sensitivity: Have We Reached the End of the Road? Is There Light at the End of the Tunnel? *Surf. Interface Anal.* **2011**, *43*, 253-256.
18. Dreisewerd, K. The Desorption Process in MALDI. *Chem. Rev.* **2003**, *103*, 395-425.
19. Northen, T. R.; Yanes, O.; Northen, M. T.; Marrinucci, D.; Uritboonthai, W.; Apon, J.; Golledge, S. L.; Nordström, A.; Siuzdak, G. Clathrate Nanostructures for Mass Spectrometry. *Nature* **2007**, *449*, 1033-1036.
20. Northen, T. R.; Lee, J. C.; Hoang, L.; Raymond, J.; Hwang, D. R.; Yannone, S. M.; Wong, C. H.; Siuzdak, G. A Nanostructure-initiator Mass Spectrometry-based Enzyme Activity Assay. *Proc. Natl. Acad. Sci. U.S.A.* **2008**, *105*, 3678-3683.
21. Woo, H. K.; Northen, T. R.; Yanes, O.; Siuzdak, G. Nanostructure-initiator Mass Spectrometry: A Protocol for Preparing and Applying NIMS Surfaces for High-sensitivity Mass Analysis. *Nat. Protoc.* **2008**, *3*, 1341-1349.
22. Northen, T. R.; Woo, H. K.; Northen, M. T.; Nordström, A.; Uritboonthai, W.; Turner, K. L.; Siuzdak, G. High Surface Area of Porous Silicon Drives Desorption of Intact Molecules. *J. Am. Soc. Mass Spectrom.* **2007**, *18*, 1945-1949.
23. Amantonico, A.; Flamigni, L.; Glaus, R.; Zenobi, R. Negative Mode Nanostructure-initiator Mass Spectrometry for Detection of Phosphorylated Metabolites. *Metabolomics* **2009**, *5*, 346-353.
24. Yanes, O.; Woo, H. K.; Northen, T. R.; Oppenheimer, S. R.; Shriver, L.; Apon, J.; Estrada, M. N.; Potchoiba, M. J.; Steenwyk, R.; Manchester, M.; Siuzdak, G. Nanostructure Initiator Mass Spectrometry: Tissue Imaging and Direct Biofluid Analysis. *Anal. Chem.* **2009**, *81*, 2969-2975.
25. Solanki, C. S.; Bilyalov, R. R.; Poortmans, J.; Celis, J. P.; Nijs, J.; Mertens, R. Self-standing Porous Silicon Films by One-step Anodizing. *J. Electrochem. Soc.* **2004**, *151*, C307-C314.
26. McLean, J. A.; Russell, D. H. Advanced Optics for Rapidly Patterned Laser Profiles in Analytical Spectrometry. US Patent 7,282,706, Oct 16, 2007.
27. Sherrod, S. D.; Castellana, E. T.; McLean, J. A.; Russell, D. H. Spatially Dynamic Laser Patterning using Advanced Optics for Imaging Matrix Assisted Laser Desorption/Ionization (MALDI) Mass Spectrometry. *Int. J. Mass Spectrom.* **2007**, *262*, 256-262.
28. Segal, E. B. First Aid for a Unique Acid, HF: A Sequel. *Chem. Health Saf.* **2000**, *7*, 18-23.
29. Canham, L. T., ed. *Properties of Porous Silicon*. London: IEE INSPEC, 1997.

30. Wen, X. J.; Dagan, S.; Wysocki, V. H. Small-molecule Analysis with Silicon-nanoparticle-assisted Laser Desorption/Ionization Mass Spectrometry. *Anal. Chem.* **2007**, *79*, 434-444.
31. Friedl, P.; Gilmour, D. Collective Cell Migration in Morphogenesis, Regeneration and Cancer. *Nat. Rev. Mol. Cell Biol.* **2009**, *10*, 445-457.
32. Patti, G. J.; Woo, H. K.; Yanes, O.; Shriver, L.; Thomas, D.; Uritboonthai, W.; Apon, J. V.; Steenwyk, R.; Manchester, M.; Siuzdak, G. Detection of Carbohydrates and Steroids by Cation-Enhanced Nanostructure-initiator Mass Spectrometry (NIMS) for Biofluid Analysis and Tissue Imaging. *Anal. Chem.* **2010**, *82*, 121-128.

## CHAPTER III

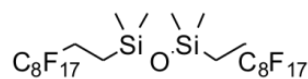
### HYBRID ORGANIC-INORGANIC NANOMATERIAL MATRIX FOR ENHANCED IONIZATION OF BIOLOGICAL MOLECULES

#### 3.1 Introduction

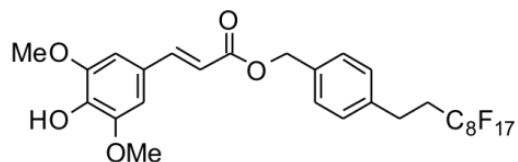
Several advantageous properties of the NIMS platform previously described - low chemical noise, high-specificity surface interactions based on fluorine-fluorine affinity, high sensitivity for small analytes, *etc.* - can be attributed to the Teflon-like BisF17 initiator shown in **Figure 3-1a**.<sup>1-4</sup> For example, the low background noise in NIMS is likely due to the UV transparency of the BisF17 initiator. When the substrate is irradiated, the laser energy passes through the initiator and is absorbed strongly by top layer of porous silicon. Energy is transferred rapidly to the initiator as heat, leading to soft desorption of initiator and analyte. Due to the low proton affinity of the initiator, however, only the analyte is detected by the mass spectrometer. On the other hand, because the initiator is not a direct proton source like organic MALDI matrix, analytes with low proton affinities are typically detected as cationized species.

However, the primary limitation of NIMS when compared to traditional MALDI is reduced sensitivity for higher-mass analytes such as large peptides and proteins.<sup>5</sup> There are likely two main causes for this observation. First, the energy cost of large-analyte desorption is likely higher in NIMS than in MALDI. In traditional MALDI, peptides and proteins are directly incorporated into organic matrix crystals.<sup>6</sup> Although the energetic cost of desorbing a large analyte molecule (*e.g.* protein) is higher than a small analyte molecule (*e.g.* metabolite), large analytes are diluted in the matrix crystal so that adjacent matrix molecules can pool excess energy together and release the analyte into the gas phase as described in Chapter 1. In NIMS, no mixing occurs between the pSi matrix target and analytes. The initiator absorbs energy from the pSi as heat and desorbs with analyte. Therefore, localized energy pooling is reduced and fewer intact analytes are desorbed. Second, analyte protonation is likely a less efficient process in NIMS than in MALDI. In traditional MALDI, gas-phase protonation occurs so that desorbed neutrals are ionized in the matrix plume. In NIMS, the initiator is not a proton source. It is unclear if gas-phase protonation occurs via

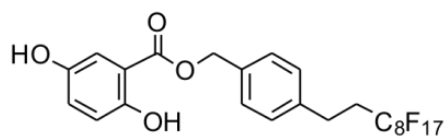
(a) BisF17 NIMS Initiator



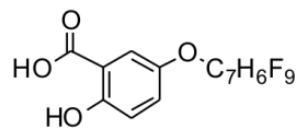
(b) SA-56 Matrix



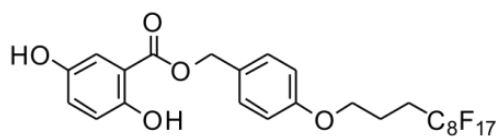
(c) DHB-57 Matrix



(d) DHB-58 Matrix



(e) DHB-59 Matrix



(f) CHCA-60 Matrix

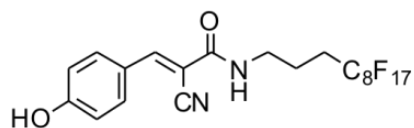


**Figure 3-1.** Tested compounds for composite matrix-initiator surface. (a) BisF17, or bis(heptadecafluoro-1,1,2,2-tetrahydrodecyl)tetramethyldisiloxane; (b)-(f) Novel perfluorinated matrix compounds designed and synthesized at Vanderbilt.

desorbed Si-OH clusters.<sup>7</sup> If it does occur, it is possible the efficiency of this mechanism is lower than in MALDI.

Motivated by previous surface chemistry strategies for improved specificity and/or sensitivity in nano-MALDI,<sup>4,8-13</sup> it was hypothesized a photoactive MALDI matrix containing a perfluorinated tag which has affinity for the initiator could both improve NIMS ion yields of higher-mass analytes and suppress chemical noise in the mass spectrum. To test this hypothesis, five matrix derivatives (**Figure 3-1b - 3-1f**) were synthesized to interact with the BisF17 initiator via fluorine-fluorine interactions as shown in **Figure 3-2**. Three compounds were modelled after 2,5-dihydroxybenzoic acid (2,5-DHB), one after sinapinic acid (SA), and one after alpha-cyano-4-hydroxycinnamic acid (CHCA), organic matrices shown in **Table 1-1**. In this chapter, NIMS performance of each matrix was monitored, and a potential hybrid mechanism was determined.

### **3.2 Experimental Section**

#### *Materials*

NIMS substrates were synthesized as in Chapter 2. Novel matrix compounds were synthesized by Plamen Christov of the Vanderbilt Institute for Chemical Biology Chemical Synthesis core and were characterized by nuclear magnetic resonance (NMR; Plamen), IR, and accurate mass (**Table 3-1**). These details are presented in Appendix D. Matrices were dissolved in 99.9% ethanol / 0.1% formic acid and applied to the target. The bis(heptadecafluoro-1,1,2,2-tetrahydrodecyl)tetramethyldisiloxane (BisF17) initiator was obtained from Gelest. Peptides and proteins were obtained from Sigma.

#### *Mass Spectrometry*

NIMS-MALDI experiments were performed using a Voyager DE-STR mass spectrometer in the reflector TOF configuration, except for in the analysis of ubiquitin protein (linear TOF configuration). Reflector mode TOF settings were as follows: 20 kV acceleration voltage, 70% grid voltage, 200 ns extraction delay,  $m/z$  range 100 - 2000, 50 shots per spectrum, laser intensity ranging from 1800 - 2500 (arb. units). Linear mode TOF settings were as follows: 20 kV



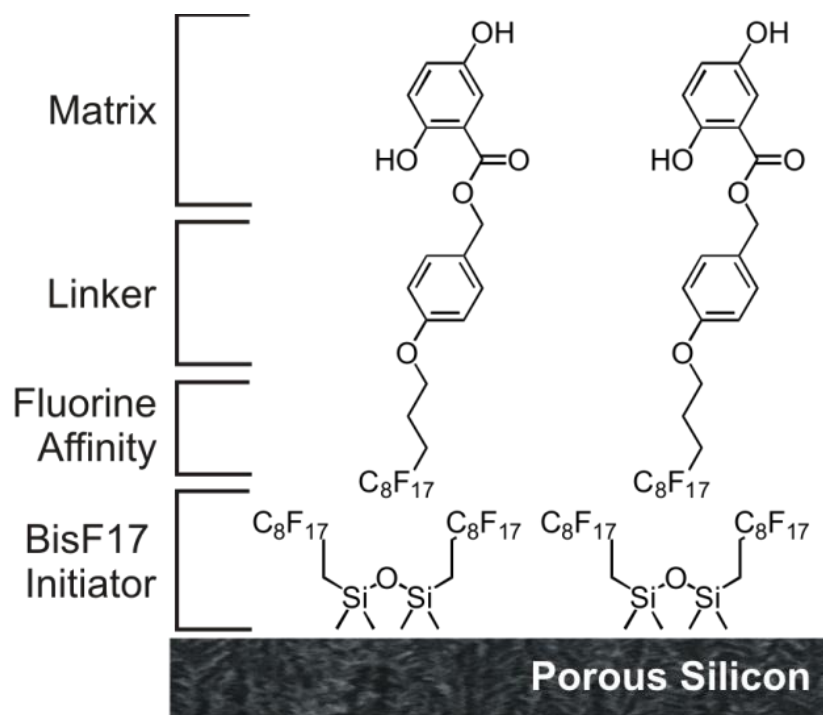


**Figure 3-2.** Hypothesized surface orientation for perfluorinated MALDI matrices on NIMS surface.

Matrix Compound	Molecular Formula	Theo. Mass (Da)	Meas. Mass (Da)	Error (ppm)	$\epsilon$ at 337 nm ( $M^{-1} cm^{-1}$ )
VU0470056 (SA-56)	$C_{26}H_{15}F_{17}O_3$	698.0749, $[M]^+$	698.0751	+0.29	$2.7 \pm 0.3 \times 10^4$
VU0470057 (DHB-57)	$C_{24}H_{15}F_{17}O_4$	689.0620, $[M-H]^+$	689.0605	-2.18	$8.7 \pm 0.5 \times 10^3$
VU0470058 (DHB-58)	$C_{14}H_{11}F_9O_4$	453.0151, $[M+K]^+$	453.0132	-4.19	$1.3 \pm 0.1 \times 10^3$
VU0470059 (DHB-59)	$C_{25}H_{17}F_{17}O_5$	719.0726, $[M-H]^+$	719.0740	+1.95	$7.7 \pm 0.6 \times 10^3$
VU0470060 (CHCA-60)	$C_{21}H_{13}F_{17}N_2O_2$	649.0778, $[M+H]^+$	649.0789	+1.69	$3.5 \pm 0.3 \times 10^4$

**Table 3-1.** General information for 5 compounds. Accurate mass and molar absorptivity raw data may be found in Appendix D.

acceleration voltage, 90% grid voltage, 400 ns extraction delay,  $m/z$  range 2000 - 20000, 75 shots per spectrum, laser intensity ranging from 2200 - 2600 (arb. units).

Accurate mass measurements on novel matrices were performed without additional MALDI matrix using a Synapt G2-S mass spectrometer in LDI-IM-MS resolution mode. Synapt G2-S instrument settings include:  $m/z$  range 300 - 2000, laser intensity 250 (arb. units), IM wave velocity 650 m/s, IM wave height 40.0 V. All G2-S settings are provided in the Appendix.

#### *UV-Vis Spectroscopy*

UV-Vis measurements were performed on a Cary UV-Vis spectrometer. Each compound was 25  $\mu\text{M}$  in 100% ethanol and diluted in series as necessary. Data was continuously background subtracted using an ethanol blank. Molar absorptivity values were calculated at 337 nm, the wavelength of nitrogen laser used with the Voyager DE-STR mass spectrometer.

#### *Bond Energies*

Bond energy calculations were performed by Sarah Stow (McLean group) using Gaussian 09 software.<sup>14</sup>

### **3.3 Results and Discussion**

Previous studies on MALDI matrix selection show that it can be difficult to predict the success or failure of a specific compound based solely on structure.<sup>15-16</sup> In these studies, various positional isomers were evaluated for MALDI performance (e.g. 2,5-DHB vs. 2,6-DHB) and several interesting observations were made, including: excited-state matrix processes appear to be related to the position of -OH and -COOH functional groups; ion yields increase when the matrix surface area increases; and the strength of laser absorption is not directly correlated to matrix performance. Based on these observations, probing the relationship of matrix performance and UV laser absorption in our system was of great interest for practical purposes and for better understanding of the NIMS mechanism. In particular, the prospect of a hybrid NIMS-MALDI

mechanism was intriguing because the NIMS surface itself has high surface area and absorbs UV laser irradiation.

The neuropeptide bradykinin (RPPGFSPFR) and an acidic analog (DPPGFSPFD) were used to compare MS performance between different matrix-initiator combinations and against a NIMS control having only initiator as shown in **Figure 3-3a**. When SA-56, DHB-58, or CHCA-60 were combined with initiator, decreases in signal were observed compared to the control. Combining DHB-57 matrix with initiator resulted in similar performance for the bradykinin peptide as the control, yet lower performance for the acidic analog. In contrast, we observed a significant improvement in bradykinin signal when DHB-59 was combined with initiator relative to the control. However, ion yields for the acidic analog were effectively the same relative to control. We find it particularly interesting that, for both DHB-57 and DHB-59, there was a greater difference in signal between the basic peptide and the acidic peptide relative to traditional NIMS control (see below).

In addition, UV-vis absorption spectroscopy was performed on all five compounds for NIMS enhancement (**Fig. 3-3b**). Additionally, the molar absorptivity of each was determined at 337 nm, the wavelength of nitrogen lasers commonly used for LDI (**Table 3-1**). DHB-56 and CHCA-60 absorbed strongly in the UV, whereas DHB-57 and DHB-59 absorbed UV light less strongly. DHB-58 absorbed the least amount of UV light of the five compounds.

From the MS and UV-Vis absorption data, three potential mechanisms exist for composite matrix-NIMS: two which suppress ion signal, and one which can (potentially) enhance ion signal. For the compounds which absorb strongly at 337 nm (SA-56 and CHCA-60), both matrix and analyte directly desorb from the NIMS surface without allowing the laser irradiation to enter the pores. As a result, advantages of using the NIMS surface (high surface area, acidic surface chemistry, *etc.*) are minimized and ion yields are low. Ion yields are low also for the compound which does not absorb strongly at 337 nm (DHB-58). In this second mechanism, only a small amount of laser energy is absorbed by the surface matrix, preventing the laser from penetrating down to the NIMS surface. As a result, the thick layers of inactive material likely stifle desorption and reduce ion yields. Two reports on nano-MALDI confirm that sensitivity decreases when large amounts of material are present on the surface, clogging up the pores.<sup>17-18</sup>

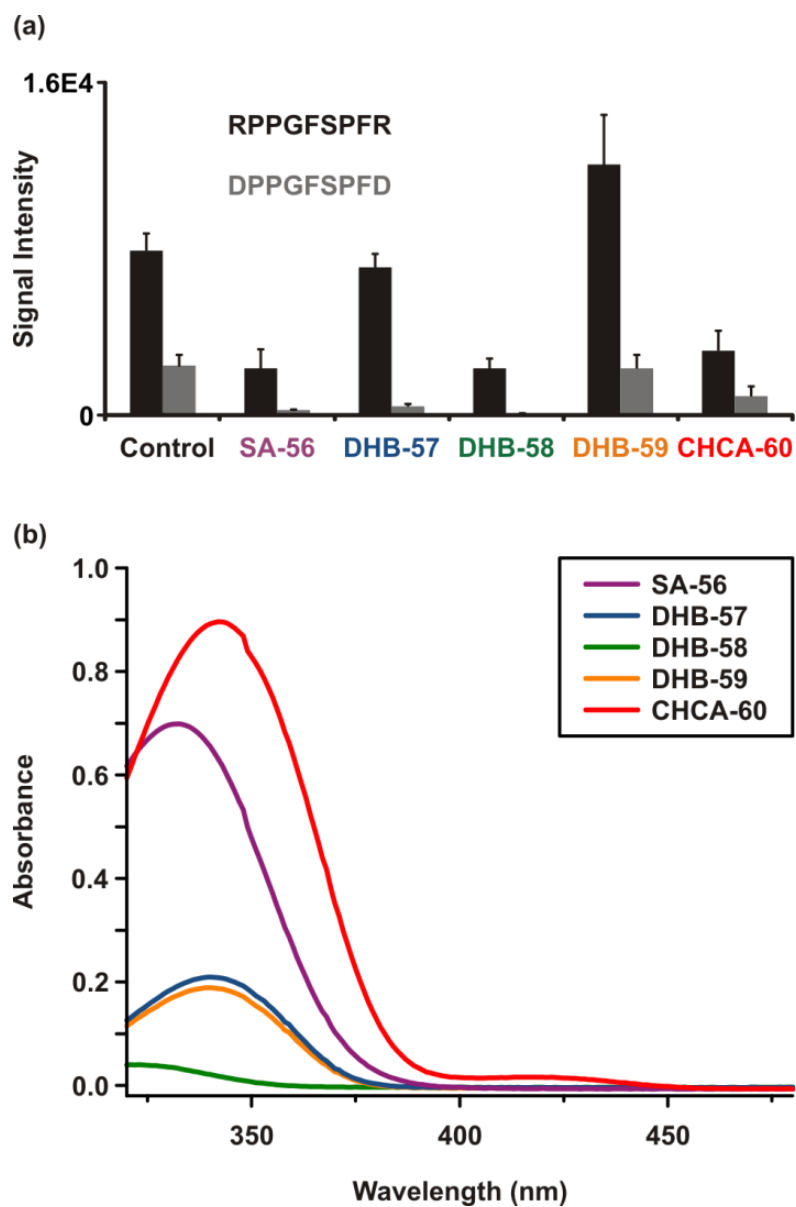


**Figure 3-3.** (a) Comparison of novel matrices for hybrid NIMS-MALDI relative to standard NIMS (Control). Intensity values were obtained by integrating peak areas ( $n=3$ ). A basic (RPPGFSPFR) and an acidic peptide (DPPGFSPFD) were used for comparative purposes. (b) UV-visible absorption spectra of 5 compounds. Common UV wavelengths for NIMS and/or MALDI are 337 nm and 355 nm.

In contrast with these two suppressive mechanisms, it was observed that the compounds which absorbed moderately at 337 nm (DHB-57 and DHB-59) demonstrated acceptable LDI-MS performance. In fact, using DHB-59 in combination with BisF17 initiator showed considerable improvement over traditional NIMS. **Figure 3-4** shows the mass spectrum of bradykinin obtained using (a) traditional MALDI (2,5-DHB), (b) only DHB-59 matrix without NIMS, (c) traditional NIMS without DHB-59 matrix, and (d) NIMS with DHB-59 matrix. When a moderately-absorbing matrix and the BisF17 initiator are combined, the matrix can both absorb laser energy to assist in LDI while also allowing laser energy into the pores for sufficient absorption and release of initiator, matrix, and analyte into the gas phase.

To probe this third mechanism further, it was explored whether DHB-59 could act as a matrix without the NIMS substrate. Direct LDI-MS data was obtained for the matrix, and also when the matrix was mixed with bradykinin. Direct LDI-MS of DHB-59 generated a minor  $[M+Na]^+$  peak at 743 Da and a more intense fragment peak at 567 Da which corresponds to cleavage of the ester bond between the DHB moiety and the rest of the molecule as shown in Figure 3-5a. Bond energy calculations showed this was the weakest cleavable bond (2.04 eV). This energy is less than the energy of a single nitrogen laser photon (3.68 eV), further validating DHB-59 is photocleaved (**Fig. 3-5b-c**). It is notable the  $[M+H]^+$  ion was not observed for DHB-59. Moreover, no signal for the matrix fragment was observed, suggesting this moiety neutralizes back to 2,5-DHB in the gas phase. The re-neutralized matrix molecule may be a source of protons for analytes; however, it appears to be in a low-energy state, as it is much less efficient at analyte protonation than in traditional MALDI. When DHB-59 was laser-irradiated with bradykinin, signal was not observed at normal laser fluence (**Fig. 3-4b**), and only faintly at high laser fluence as shown in **Figure 3-6**.

While the photocleaved matrix portion of DHB-59 may assist marginally in analyte protonation, the majority of evidence suggests signal enhancement comes from another matrix role. This is also consistent with earlier data, which showed large differences in signal between RPPGFSPFR and DPPGFSPFD (**Fig. 3-3a**). If DHB-59 is a significant proton source, increased

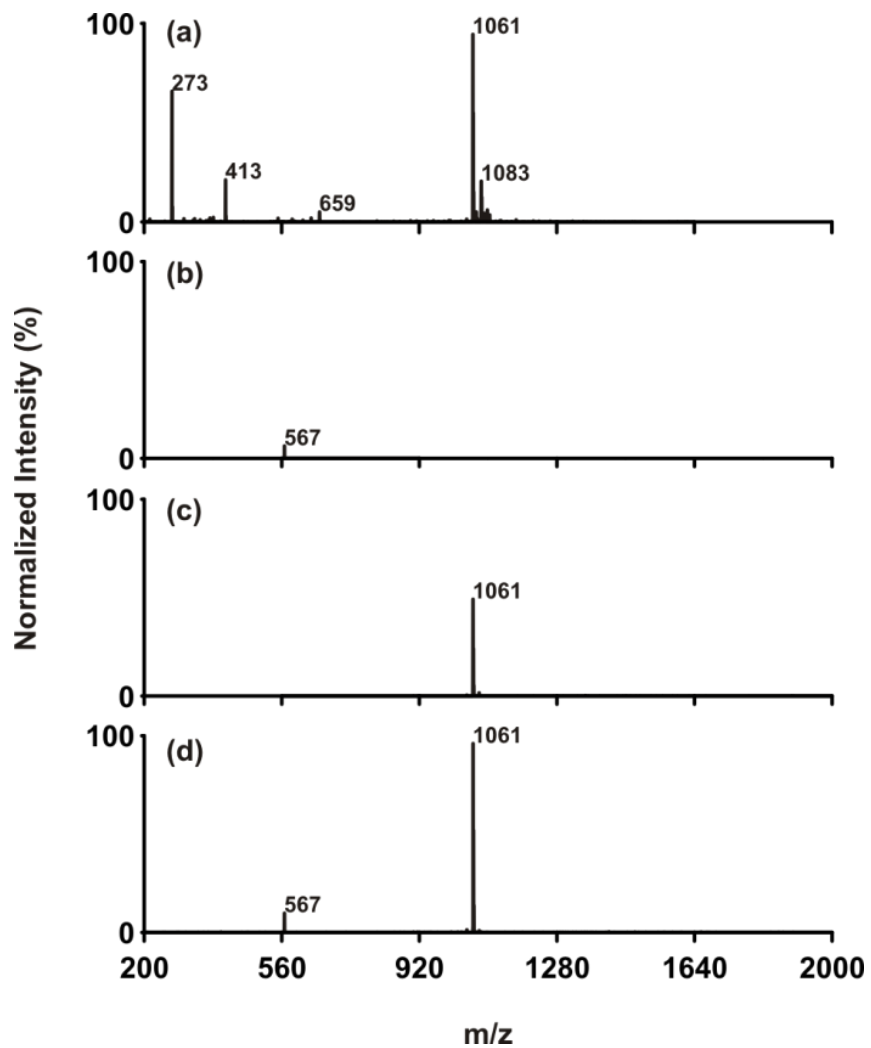


**Figure 3-4.** Mass spectra of 50 pmol bradykinin peptide (RPPGFSPFR, 1061 Da) using (a) traditional MALDI matrix (2,5-DHB); (b) only DHB-59 matrix (no NIMS), (c) traditional NIMS without DHB-59 matrix, and (d) NIMS combined with DHB-59 matrix. Peptide was detected using Voyager DE-STR in positive ion mode and reflector TOF configuration.

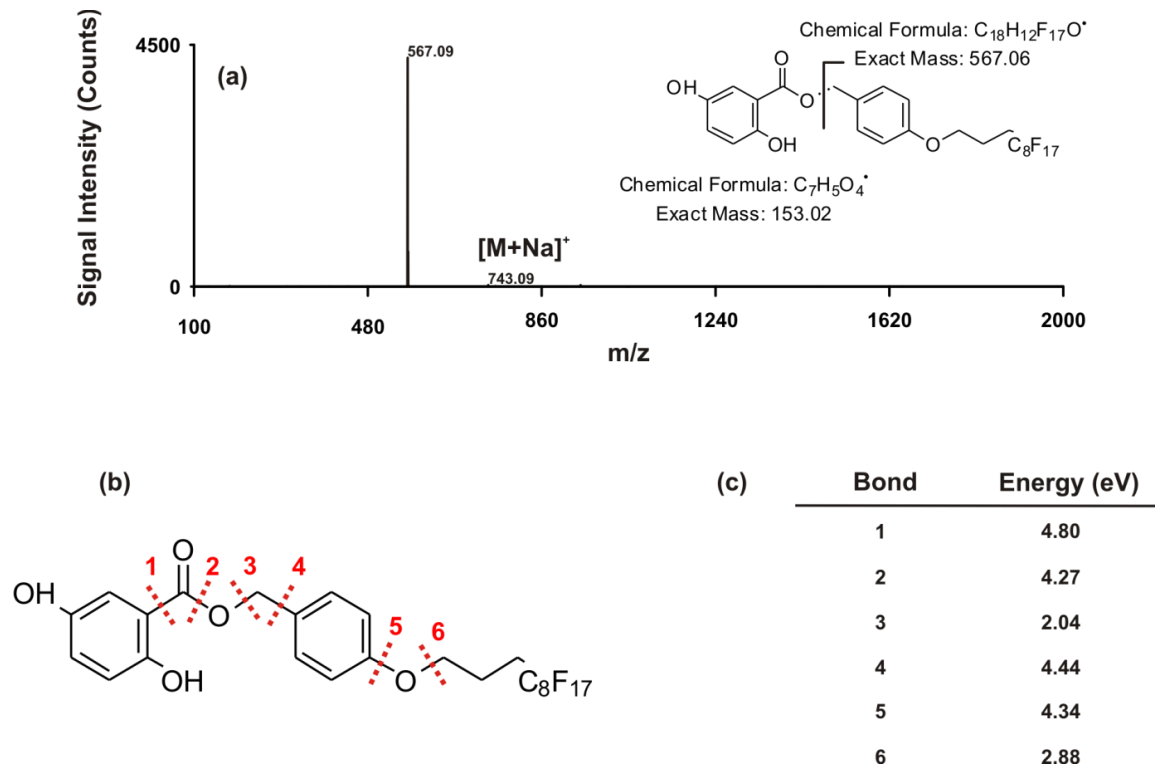


**Figure 3-5.** Evidence for photocleaving of DHB-59. (a) Direct laser desorption/ionization mass spectrum of DHB-59. The fragment at 567 Da is the base peak of the spectrum. However, no signal is observed for the matrix moiety. (b) Six bond energies were calculated for DHB-59 using Gaussian 09 software. (c) Calculations confirm the ester bond is the weakest. The energy of the bond, 2.04 eV, is significantly less than the energy of a single 337 nm photon (3.68 eV).



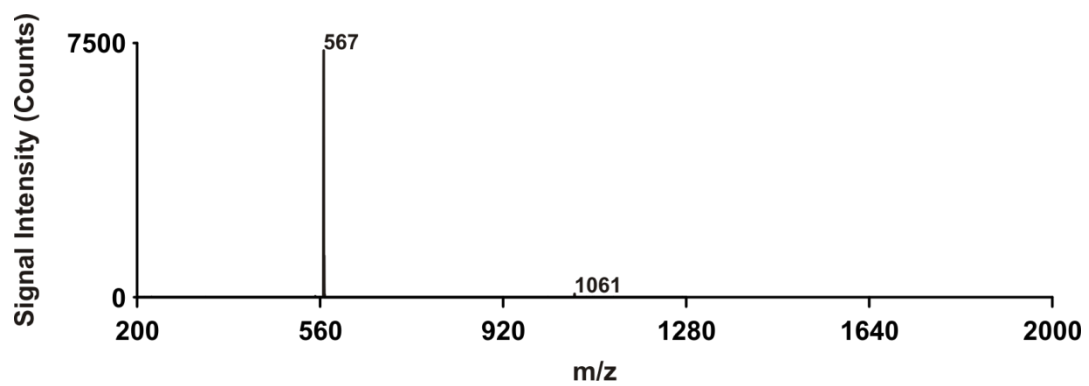


**Figure 3-6.** Detection of bradykinin peptide (1061 Da, 97 counts) was minimal using DHB-59 as a matrix without NIMS substrate. High laser energy was required to observe any signal.

ion signal for both basic and acidic peptides relative to the NIMS control would be expected. Surprisingly, the proton source likely remains either Si-OH surface groups or acidified solvent trapped in the pores, resulting in pre-formed ions – possibly both.<sup>12,19</sup>

The primary area of enhancement is likely analyte mixing and dilution on the NIMS surface. The matrix moiety likely orients itself away from the porous silicon surface, as shown in **Figure 3-2** (similar to that in Ref. 4). Acting similar to a surfactant, it reduces analyte clumping and allows more material to adsorb to the NIMS surface for desorption/ionization. Evidence for this can be observed *via* the CCD camera in the source of the mass spectrometer. Without matrix, analyte tends to clump on the NIMS surface coated with initiator. However, with the matrix present as well, less clumping is observed. In this case, the analyte can better interact with the surface for LDI-MS. This would also explain the better performance of the DHB-59 matrix over the DHB-57 matrix. DHB-59 has an additional oxygen atom in the linker region which reduces the overall hydrophobicity of the matrix molecule, resulting in better analyte/matrix mixing.

Similar to traditional MALDI matrix,<sup>20</sup> DHB-59 matrix signal can be suppressed using a low matrix-to-analyte ratio as shown in **Figure 3-7**. A matrix-to-analyte ratio of approximately 10:1 - 25:1 gave optimal performance. Notably, when combining NIMS and MALDI approaches, increasing the amount of analyte is not necessary to minimize matrix signals and simplify the mass spectrum. Because of the presence of the NIMS surface, simply decreasing the amount of matrix can generate mass spectra with (at most) one background signal.

Using this hybrid surface, we improved the detection capabilities of ACTH(18-39) peptide and ubiquitin protein (**Figure 3-8**). To our knowledge, singly-charged ubiquitin (8.6 kDa) is the highest  $m/z$  value detected by NIMS to date. A previous report showed that NIMS can generate multiply-charged ions of a 29 kDa protein with a lower net  $m/z$ ,<sup>1</sup> however, we have not observed this phenomenon in our work, and no other NIMS manuscripts in the literature have described this behavior. If multiple-charging does occur from NIMS surfaces, it is likely not possible at biologically relevant concentrations.

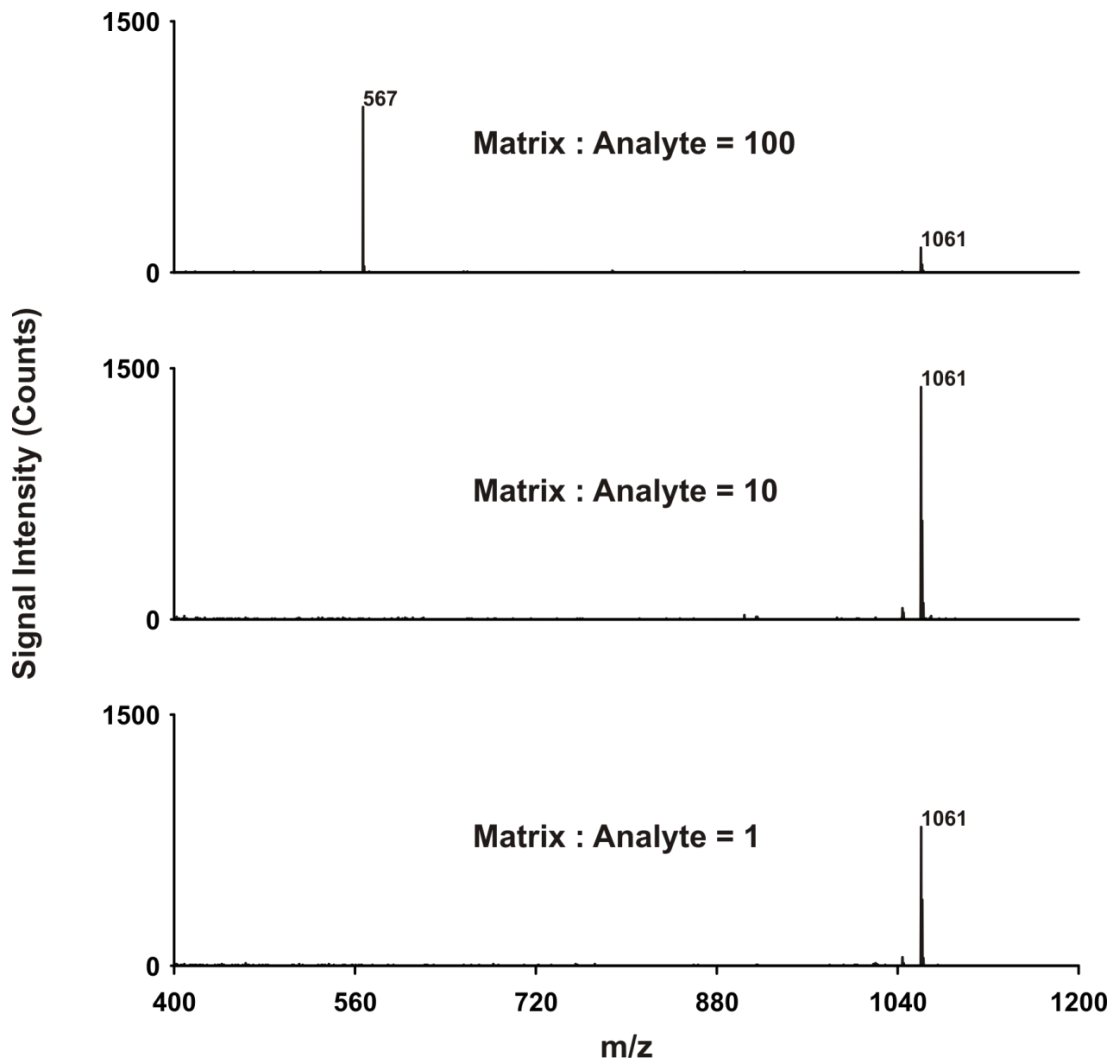


**Figure 3-7.** Demonstration of the matrix suppression effect using DHB-59 matrix and NIMS surface. Matrix to analyte ratios are reported in mol:mol. The amount of analyte (bradykinin, 1061 Da) was held constant at 50 pmol.

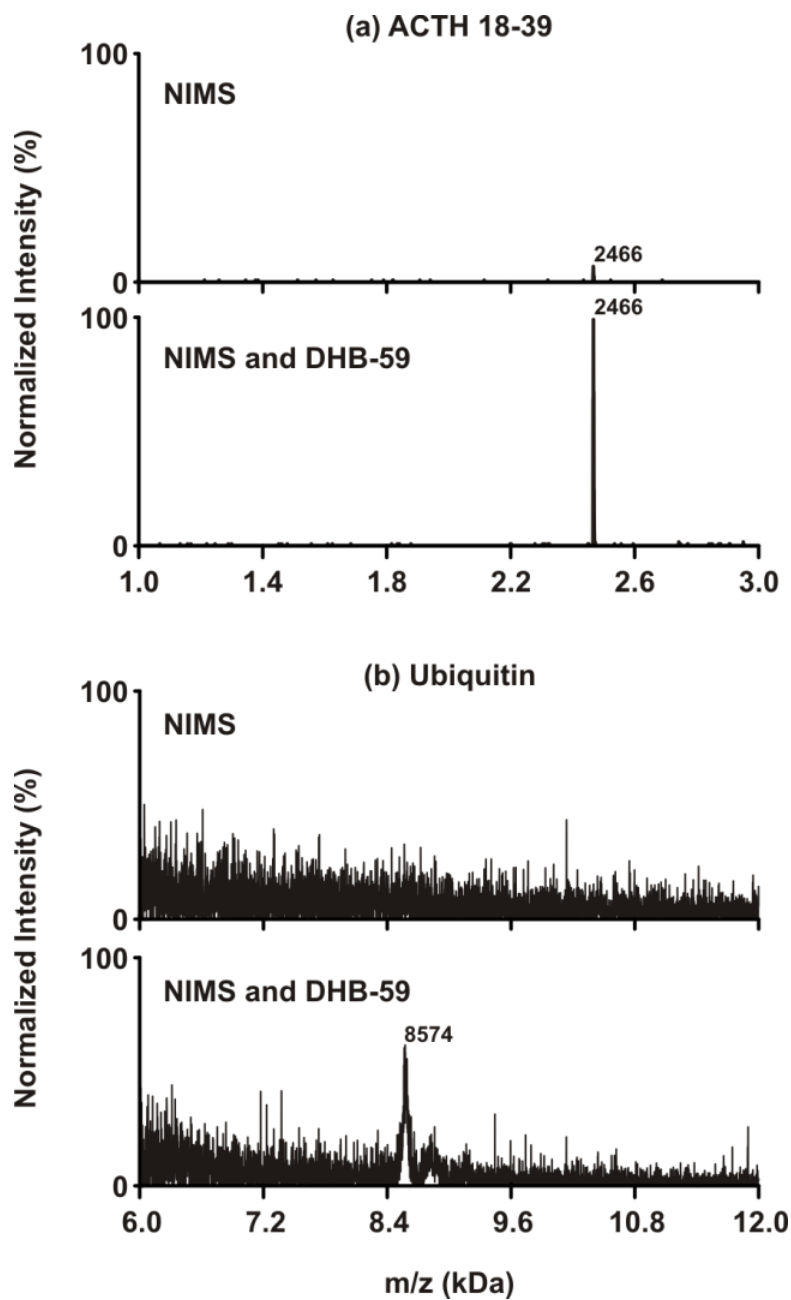


**Figure 3-8.** Improved detection of peptides and proteins. (a) Mass spectrum of ACTH 18-39 peptide (2465 Da, the second isotope is most intense) using (*top*) BisF17 initiator only and (*bottom*) BisF17 initiator with DHB-59. Peptide was at 35 pmol concentration. (b) Mass spectrum of ubiquitin protein (8565 Da) using (*top*) BisF17 initiator only and (*bottom*) BisF17 initiator with DHB-59. Protein was at 1 pmol concentration, detected using linear TOF configuration. Ubiquitin spectra were baseline corrected.

### **3.4 Conclusions**

In summary, DHB-59 was found to improve MS performance of peptides and proteins when combined with the NIMS substrate. At this point in our work, matrix-enhanced NIMS demonstrates consistently clean spectra (containing one background signal) across a mass dynamic range of 0 - 8.5 kDa.

Here, significant evidence is presented which supports the idea that DHB-59 acts as a mediator between analytes and the perfluorinated NIMS surface. This allows for more efficient energy transfer during desorption and improved ion yields of large analytes. Future structure/activity relationship studies on DHB-59 may lead to better analyte protonation capabilities as well, further extending the mass range and improving signal-to-noise for high spatial resolution MS imaging of peptides and proteins in biological systems.

### **3.5 Acknowledgements**

Thank you to Dr. Kwangho Kim of the Vanderbilt Institute of Chemical Biology Chemical Synthesis Core for helpful discussions concerning synthesis and characterization of compounds. Thank you to Prof. Don Stec (Vanderbilt U.) for helpful characterization of the compounds by NMR, and Prof. Sharon Weiss (Vanderbilt U.) for enabling us to fabricate NIMS targets in her laboratories. Financial support for this work was provided by the National Institutes of Health (RO1GM092218, RO1HD064727, and UH2TR000491), the US Defense Threat Reduction Agency (HDTRAI-09-1-001 and DE-001165), the Vanderbilt Institute of Chemical Biology, and the Vanderbilt Institute for Integrative Biosystems Research and Education.

### 3.6 References

1. Northen, T. R.; Yanes, O.; Northen, M. T.; Marrinucci, D.; Uritboonthai, W.; Apon, J.; Golledge, S. L.; Nordstrom, A.; Siuzdak, G. Clathrate Nanostructures for Mass Spectrometry. *Nature* **2007**, *449*, 1033-1036.
2. Greving, M. P.; Patti, G. J.; Siuzdak, G. Nanostructure-initiator Mass Spectrometry Metabolite Analysis and Imaging. *Anal. Chem.* **2011**, *83*, 2-7.
3. Northen, T. R.; Lee, J. C.; Hoang, L.; Raymond, J.; Hwang, D. R.; Yannone, S. M.; Wong, C. H.; Siuzdak, G. A Nanostructure-initiator Mass Spectrometry-based Enzyme Activity Assay. *Proc. Natl. Acad. Sci. U.S.A.* **2008**, *105*, 3678-3683.
4. Li, J.; Lipson, R. H. Assays using a NIMS Chip: Loosely Bound but Highly Selective. *Anal. Chem.* **2013**, *85*, 6860-6865.
5. Sturm, R. M.; Greer, T.; Chen, R.; Hensen, B.; Li, L. Comparison of NIMS and MALDI Platforms for Neuropeptide and Lipid Mass Spectrometric Imaging in *C. borealis* Brain Tissue. *Anal. Methods* **2013**, *5*, 1623-1628.
6. Bouschen, W.; Spengler, B. Artifacts of MALDI Sample Preparation Investigated by High-Resolution Scanning Microprobe Matrix-Assisted Laser Desorption/Ionization (SMALDI) Imaging Mass Spectrometry. *Int. J. Mass Spectrom.* **2007**, *266*, 129-137.
7. Zhabin, S. N.; Pento, A. V.; Grechnikov, A. A.; Borodkov, A. S.; Sartakov, B. G.; Simanovsky, Y. O.; Nikiforov, S. M.; Alimpiev, S. S. On the Role of Laser Irradiation in the Process of Laser Desorption/Ionisation from Silicon Surfaces. *Quantum Electron.* **2011**, *41*, 835-842.
8. Meng, J. C.; Averbuj, C.; Lewis, W. G.; Siuzdak, G.; Finn, M. G. Cleavable Linkers for Porous Silicon-based Mass Spectrometry. *Angew. Chem. Int. Ed.* **2004**, *43*, 1255-1260.
9. Castellana, E. T.; Russell, D. H. Tailoring Nanoparticle Surface Chemistry to Enhance Laser Desorption Ionization of Peptides and Proteins. *Nano Lett.* **2007**, *7*, 3023-3025.
10. Liu, Q.; Xiao, Y.; Pagan-Miranda, C.; Chiu, Y. M.; He, L. Metabolite Imaging using Matrix-enhanced Surface-assisted Laser Desorption/Ionization Mass Spectrometry (ME-SALDI-MS). *J. Am. Soc. Mass Spectrom.* **2009**, *20*, 80-88.
11. Liu, Q.; He, L. Ionic Matrix for Matrix-enhanced Surface-assisted Laser Desorption/Ionization Mass Spectrometry Imaging (ME-SALDI-MSI). *J. Am. Soc. Mass Spectrom.* **2009**, *20*, 2229-2237.
12. Calavia, R.; Annanouch, F.; Correig, X.; Yanes, O. Nanostructure Initiator Mass Spectrometry for Tissue Imaging in Metabolomics: Future Prospects and Perspectives. *J. Proteomics* **2012**, *75*, 5061-5068.
13. Mengistu, T. Z.; DeSouza, L.; Morin, S. Functionalized Porous Silicon Surfaces as MALDI-MS Substrates for Protein Identification Studies. *Chem. Comm.* **2005**, 5659-5661.
14. Gaussian 09, Revision A.02, Frisch, M. J.; Trucks, G. W.; Schlegel, H. B.; Scuseria, G. E.; Robb, M. A.; Cheeseman, J. R.; Scalmani, G.; Barone, V.; Mennucci, B.;

Petersson, G. A.; Nakatsuji, H.; Caricato, M.; Li, X.; Hratchian, H. P.; Izmaylov, A. F.; Bloino, J.; Zheng, G.; Sonnenberg, J. L.; Hada, M.; Ehara, M.; Toyota, K.; Fukuda, R.; Hasegawa, J.; Ishida, M.; Nakajima, T.; Honda, Y.; Kitao, O.; Nakai, H.; Vreven, T.; Montgomery, Jr., J. A.; Peralta, J. E.; Ogliaro, F.; Bearpark, M.; Heyd, J. J.; Brothers, E.; Kudin, K. N.; Staroverov, V. N.; Kobayashi, R.; Normand, J.; Raghavachari, K.; Rendell, A.; Burant, J. C.; Iyengar, S. S.; Tomasi, J.; Cossi, M.; Rega, N.; Millam, J. M.; Klene, M.; Knox, J. E.; Cross, J. B.; Bakken, V.; Adamo, C.; Jaramillo, J.; Gomperts, R.; Stratmann, R. E.; Yazyev, O.; Austin, A. J.; Cammi, R.; Pomelli, C.; Ochterski, J. W.; Martin, R. L.; Morokuma, K.; Zakrzewski, V. G.; Voth, G. A.; Salvador, P.; Dannenberg, J. J.; Dapprich, S.; Daniels, A. D.; Farkas, O.; Foresman, J. B.; Ortiz, J. V.; Cioslowski, J.; Fox, D. J. Gaussian, Inc., Wallingford CT, 2009.

15. Krause, J.; Stoeckli, M.; Schlunegger, U. P. Studies on the Selection of New Matrices for Ultraviolet Matrix-assisted Laser Desorption/Ionization Time-of-flight Mass Spectrometry. *Rapid Commun. Mass Spectrom.* **1996**, *10*, 1927-1933.
16. Horneffer, V.; Dreisewerd, K.; Lüdemann, H. C.; Hillenkamp, F.; Läge, M.; Strupat, K. Is the Incorporation of Analytes into Matrix Crystals a Prerequisite for Matrix-assisted Laser Desorption/Ionization Mass Spectrometry? A Study of Five Positional Isomers of Dihydroxybenzoic Acid. *Int. J. Mass Spectrom.* **1999**, *185*, 859-870.
17. Woo, H. K.; Northen, T. R.; Yanes, O.; Siuzdak, G. Nanostructure-initiator Mass Spectrometry: A Protocol for Preparing and Applying NIMS Surfaces for High-sensitivity Mass Analysis. *Nat. Protoc.* **2008**, *3*, 1341-1349.
18. Walker, B. N.; Stolee, J. A.; Vertes, A. Nanophotonic Ionization for Ultratrace and Single-cell Analysis by Mass Spectrometry. *Anal. Chem.* **2012**, *84*, 7756-7762.
19. Liu, Q.; He, L. Quantitative Study of Solvent and Surface Effects on Analyte Ionization in Desorption Ionization on Silicon (DIOS) Mass Spectrometry. *J. Am. Soc. Mass Spectrom.* **2008**, *19*, 8-13.
20. Knochenmuss, R.; Dubois, F.; Dale, M. J.; Zenobi, R. The Matrix Suppression Effect and Ionization Mechanisms in Matrix-assisted Laser Desorption/Ionization. *Rapid Commun. Mass Spectrom.* **1996**, *10*, 871-877.

## CHAPTER IV

### STRUCTURAL ANALYSIS OF ISOMERIC POLYMER PRECURSORS BY MASS SPECTROMETRY AND ION MOBILITY - MASS SPECTROMETRY

#### 4.1 Introduction

As discussed in previous chapters, materials chemistry can provide unique advantages in mass spectrometry research, such as the development of novel matrices for MALDI-MS. On the other hand, mass spectrometry-based methods can provide unique information concerning the characterization of both inorganic materials<sup>1-5</sup> and organic polymers.<sup>6-8</sup> This chapter will focus on the analysis of polymer precursor molecules by electrospray ionization (ESI), a continuous ion source directly from solution introduced by Fenn *et al.* in 1989.<sup>9</sup>

One ubiquitous type of polymer is polyurethane (**Figure 4-1**). Polyurethanes are inherently complex and thus structural characterization of these polymers can be challenging. Intrinsic distributions of molecular size and cross-linking produce structural heterogeneity,<sup>10</sup> even amongst purified samples. Additional heterogeneity can arise from varying amounts of hard and soft block segments and structural variations within the segments themselves.

Methylenedianiline (MDA) is used to synthesize methylene diphenyl diisocyanate (MDI), the major hard block component of polyurethanes. Most formulations of industrial grade MDA primarily contain 4,4'-MDA, along with a number of structural isomers and multimers.<sup>11-13</sup> The purpose of this research is to fully characterize structural variations within MDA mixtures and eventually MDI mixtures. However, in order to better understand complex mixtures of MDA and MDI, it is first necessary to study dimeric MDA regioisomers that differ only by the position of amine functional groups, as shown in **Figure 4-2** (asterisks indicate unique protonation sites). By characterizing specific dimer species, we can gain insight into the behavior of more complex multimeric structures, and eventually determine relative abundances in complex MDA mixtures. Previous MDA studies in the literature were typically done in a workplace exposure context, and utilized gas chromatography - mass spectrometry (GC-MS),<sup>13-15</sup> or more recently liquid chromatography - mass spectrometry (LC-MS) detection.<sup>16-21</sup> Limitations of these methods for



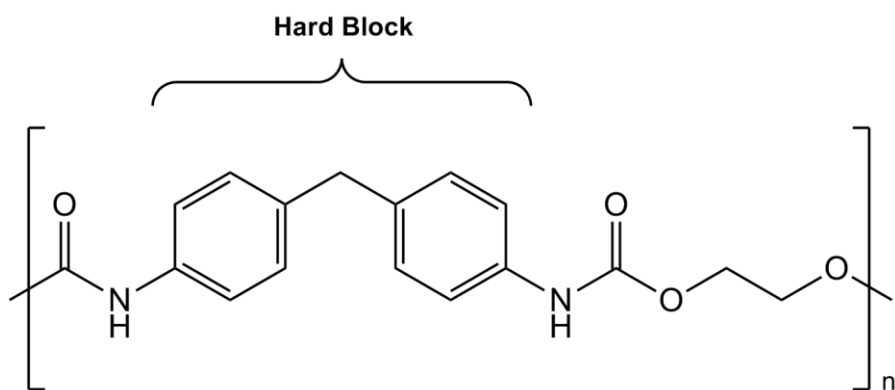


**Figure 4-1.** Basic structure of polyurethane. The subject of this study is methylenedianiline (MDA), a precursor to the hard block segment.

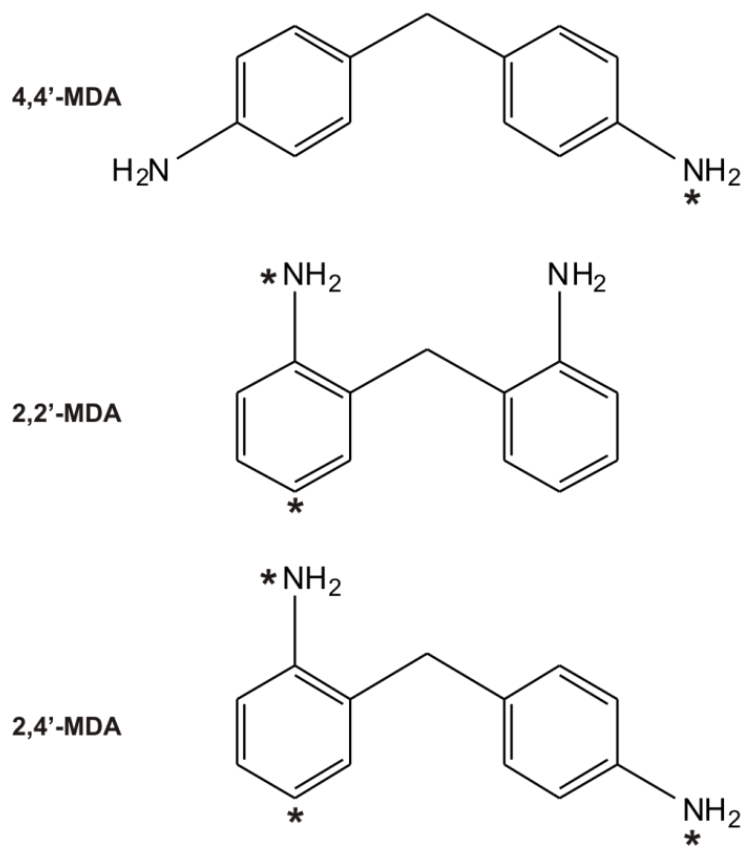


**Figure 4-2.** Structures of MDA positional isomers (*theo.* neutral molecule monoisotopic mass = 198.12 Da). Potential protonation sites are labeled with an asterisk.

MDA characterization include the necessity for sample derivatization (GC-MS), and an inability to detect and differentiate low abundance isomers such as 2,4'-MDA and 2,2'-MDA (both GC-MS and LC-MS). In contrast, techniques which probe gas-phase structural conformations may provide insight into the characterization and discrimination of even low-abundance isomers without requiring sample pre-treatment.

Ion mobility - mass spectrometry (IM-MS) is a gas-phase electrophoretic separation technique coupled to a mass measurement technique and thus is capable of differentiating isomeric species and characterizing these species by ion size and mass. In IM, ions are subject to low energy collisions with a neutral buffer gas, and subsequently separated by their effective gas-phase surface area.<sup>22-25</sup> Ions which possess a large cross-sectional area experience a high number of collisions and are impeded, whereas ions which possess a smaller cross-sectional area experience fewer collisions and traverse the IM drift region more rapidly. The mobility of ions can be expressed using the following equation:

$$K = \frac{l}{E * t_0} \quad (2)$$

where **K** is defined as the mobility, **l** is the length of the tube, **E** is the voltage gradient, and **t<sub>0</sub>** is the drift time. Due to differences in temperature and pressure, the reduced mobility **K<sub>0</sub>** is commonly reported also:

$$K_0 = \left( \frac{l}{E * t_0} \right) * \left( \frac{273}{T} \right) * \left( \frac{P}{760} \right) \quad (3)$$

where **T** is the temperature (in Kelvin) and **P** is the buffer gas pressure (in Torr). Gas-phase ion size and shape are described by the molecular collision cross section (CCS), which can be calculated directly using the elution time from an electrostatic drift tube (typically on the order of milliseconds) using the Mason-Schamp equation:

$$\Omega = \left( \frac{\sqrt{18\pi}}{16} \right) * \left( \frac{ze}{\sqrt{k_B T}} \right) * \left( \sqrt{\left( \frac{1}{m_A} + \frac{1}{m_B} \right)} \right) * \left[ \left( \frac{1}{K} \right) * \left( \frac{P}{760} \right) * \left( \frac{273.15}{T} \right) \right] * \left( \frac{1}{N_0} \right) \quad (4)$$

where **Ω** is the CCS, **z** is the charge state of the ion, **e** is the elementary charge, **k<sub>B</sub>** is the Boltzmann constant, **T** is the temperature, **m<sub>A</sub>** is the mass of the analyte ion, **m<sub>B</sub>** is the mass of

the neutral buffer gas,  $\mathbf{K}$  is the mobility of the ion (see Equation 2 above),  $\mathbf{P}$  is the pressure, and  $\mathbf{N}_0$  is the gas number density constant. Coupled with molecular modeling studies, CCS data can be used to investigate three-dimensional gas-phase structures. A more detailed explanation of IM-MS methodology as well as potential applications for polymer analysis can be found elsewhere in the literature.<sup>26-33</sup>

The additional dimension of separation based on the size and shape of gas-phase ions allows for the differentiation of isobaric species based on CCS. IM characterization of low-molecular-weight structural isomers was first studied by Hagen over two decades ago using a stand-alone (no MS) ambient pressure drift tube instrument.<sup>34-35</sup> Small but reproducible CCS differences were observed for isomers due to factors such as the position of unique atoms (e.g. nitrogen in a carbon ring system), location of functional groups, and connectivity of aromatic ring systems. For example, a consistent trend was observed for substituted toluene isomers, where substitution at the *meta* position led to higher CCS values than substitutions at *para* or *ortho* positions.<sup>34</sup> Nevertheless, at the time Hagen was limited in his ability to fully interpret the data due to the lack of robust MS detection.

Inspired by Hagen's work, MS/MS, IM-MS, and IM-MS/MS methods were used to fully characterize and differentiate MDA dimeric standards. CCS values were obtained for each isomer, which provides significant insight into isomeric gas-phase conformation(s) and their respective stabilities. Moreover, computational modeling was utilized to assist our interpretation of IM-MS data, and to facilitate connecting isomeric differences in CCS with molecular structures.

## **4.2 Experimental Section**

### *Materials*

4,4'-MDA, 2,4'-MDA, and 2,2'-MDA were provided by Dr. Stefan Wershofen, Bayer MaterialScience AG, 47812 Krefeld, Germany. Their authenticity was established by <sup>13</sup>C and <sup>1</sup>H NMR. Methanol and formic acid were obtained from Sigma-Aldrich USA. Alkali salts and tetralkylammonium salts were obtained from Sigma-Aldrich with the exception of sodium chloride (Thermo Fisher Scientific).

## *Instrumentation*

### *Traveling-wave IM-MS*

MS, MS/MS, and traveling-wave IM-MS (T-wave) data were obtained on interchangeable Synapt G2 and G2-S (Waters Corporation, Milford, MA) mass spectrometers. The T-wave platform differs from traditional drift-tube ion mobility (DTIM) in that it utilizes electrodynamic rather than electrostatic fields. Thus, T-wave drift times cannot be inserted directly into the Mason-Schamp equation, as the exact quantitative nature of the T-wave electrodynamic field is unknown. Nevertheless, T-wave CCS values can be determined when measurements are calibrated using DTIM CCS values from the literature.<sup>26</sup> In order to obtain CCS values from T-wave measurements, a series of quaternary ammonium salts were used as calibration standards in conjunction with their literature DTIM CCS values.<sup>36</sup>

All samples were analyzed as positive ions. The T-wave drift cell was operated with a pressure of 3 mbar (2.25 Torr), an electrodynamic wave height of 35 V and velocity of 700 m/s, and the TOF resolution ( $m/\Delta m$ ) was approximately 20,000. Polymer samples were dissolved at a concentration of 0.10 mg/mL in 9:1 methanol:water containing 0.1% formic acid (v/v). When metal salts were used, each was at a final concentration of 0.050 mg/mL. A direct infusion flow rate of 6.00  $\mu\text{L}/\text{min}$  was used for all samples. Other instrument settings were as follows: 3.00 kV capillary voltage, 80 °C source temperature, 150 °C desolvation temperature, 10 V sampling cone, 2 V extraction cone, 20 L/hr cone gas flow, 1 mL/min trap gas flow, 90 mL/min IMS gas flow. All collision-induced dissociation (CID) experiments were performed prior to T-wave mobility separation. The TOF calibration was performed using sodium formate clusters.

Center-of-mass (COM) collision energies were converted from lab-frame collision energies using the following equation:

$$E_{\text{COM}} = E_{\text{LAB}} \left( \frac{m_{\text{gas}}}{m_{\text{gas}} + m_{\text{ion}}} \right) \quad (5)$$

Lab-frame energies are the voltages applied in the tandem MS instrumentation, while COM energy is essentially the available energy for molecular rearrangement or fragmentation.<sup>37</sup>

Therefore, COM energy typically has more useful interpretation power across various instrument platforms.<sup>38</sup>

#### *Electrostatic Drift-tube IM-MS*

DTIM measurements using N<sub>2</sub> buffer gas were performed on a prototype ESI-IM-QTOFMS instrument (Agilent Technologies, Santa Clara, CA).<sup>39</sup> Details of this instrumentation are provided elsewhere, but briefly the IM-MS consists of a 78 cm uniform-field drift tube coupled to a high resolution quadrupole-TOF-MS ( $m/\Delta m$  40,000). The buffer gas was maintained at a pressure of *ca.* 4 Torr and drift voltages were varied in order to correct for the non-IM flight time of ions through the interfacing ion optics. CCS values were calculated from drift times using the Mason-Schamp equation. Polymer samples were at a concentration of 0.095 mg/mL in 9:1 methanol:water containing 0.1% formic acid (*v/v*); also, LiCl and NaCl were added to the solution so that each had a final concentration of 0.025 mg/mL. A direct infusion flow rate of 6.00  $\mu\text{L}/\text{min}$  was used.

#### *Computational and Modeling Data*

As IM is a coarse-grained structural measurement, IM-MS results are often supplemented with computational studies to gain further insight into the gas phase conformations of the molecules of interest.<sup>40</sup> These studies generally include two steps: 1) computationally sampling of the conformational space and 2) theoretical determination of CCS values for the generated conformations. More detailed structural information can then be inferred from closer inspection of generated conformations that align with experimental CCS values. Although different methods exist for both conformational sampling and theoretical determination of CCS values, the following protocol was used by Sarah Stow (McLean group). A geometry optimization at the Hartree-Fock level with a 6-31G\* basis set was performed with Gaussian 09 for all of the possible protonation sites on each isomer (2,2'-MDA: 2 sites, 2,4'-MDA: 3 sites, and 4,4'-MDA: 1 site).<sup>41</sup> Partial charges for each molecule were derived from *ab initio* electrostatic potential calculations using a 6-31G\* basis set. These partial charges were then fitted using the restrained

electrostatic potential (RESP) program in AMBER.<sup>42-43</sup> For each of the protonated, isomers, a short energy minimization was performed in AMBER followed by a 10 ps molecular dynamic simulation to heat the molecule to 1200K. Then, a long molecular dynamic simulation was run at 1200K for 9,000 ps. Structural snapshots were saved every 16,667 steps during the simulation, resulting in 3,000 structural snapshots. These high-energy structural snapshots were then cooled to 300K during a 15 ps molecular dynamic simulation.

MOBCAL software was used to theoretically determine the collision cross section of the resulting conformations.<sup>44-46</sup> First, the projection approximation was used to generate helium collision cross section values. For comparison with the nitrogen experimental values, nitrogen trajectory method values were determined for a set of conformations spanning the entire collision cross section range. These values were used to create a linear function to convert the remaining projection approximation values to nitrogen trajectory method values. The computational conformational space plots were then aligned with the experimental data to give structural insight to the MDA isomers.<sup>47</sup>

### **4.3 Results and Discussion**

#### *I. Characterization by MS and Tandem MS*

Previously, underivatized 4,4'-MDA has been studied using LC-MS/MS instrumentation.<sup>16-21</sup> In these studies, the fragmentation of the 4,4'-MDA parent ion ( $[M+H]^+ = 199$  Da) was monitored by means of a transition characteristic signal at 106 Da. However, to the best of our knowledge no research has been reported for 2,2'-MDA and 2,4'-MDA structural isomers using modern LC-MS techniques.

In the present study, both of these signals (199 Da, 106 Da) were observed in the 4,4'-MDA, 2,2'-MDA and 2,4'-MDA direct infusion mass spectra as shown in **Figure 4-3a - Figure 4-3c**. The base peak of the 4,4'-MDA spectrum is the  $[M+H]^+$  signal at 199 Da, but for 2,2'-MDA and 2,4'-MDA the 106 Da fragment is the base peak. An additional signal, although low in abundance, is observed at 211 Da (see below).

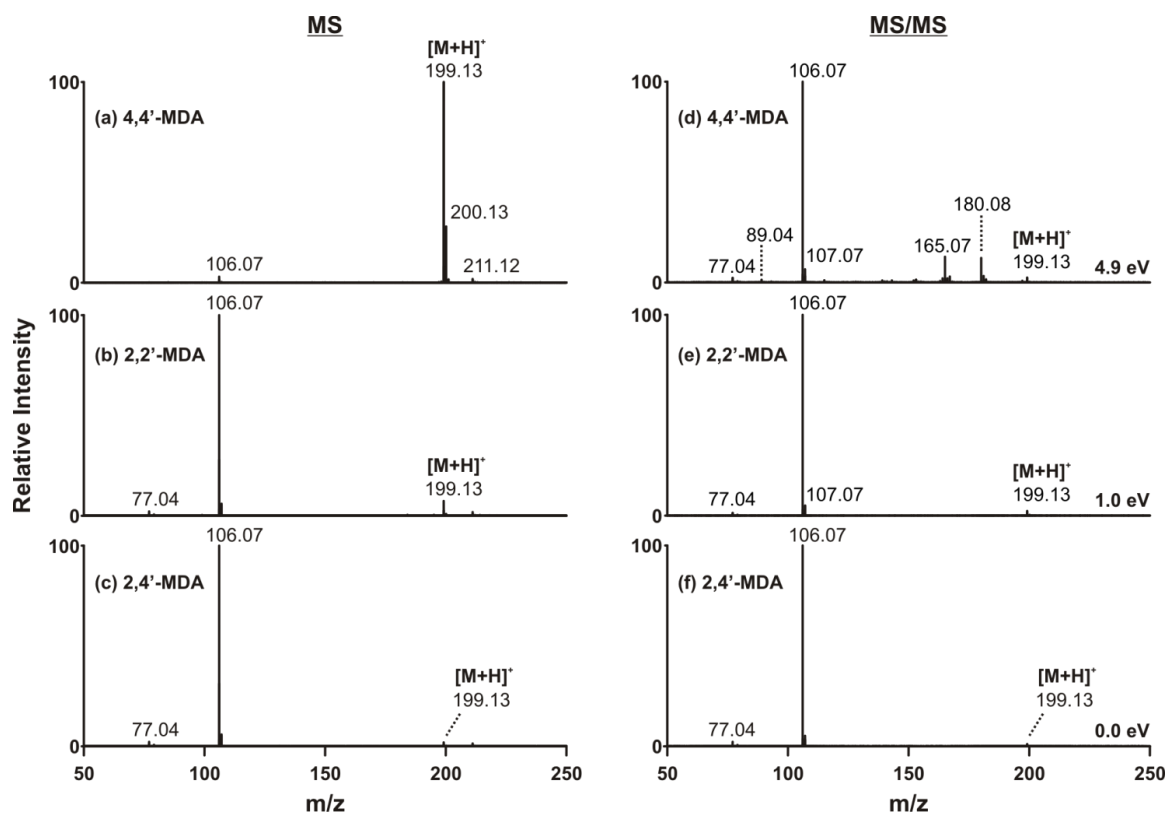


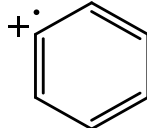
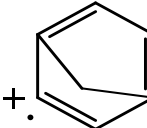
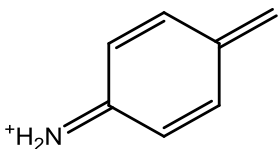
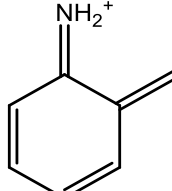
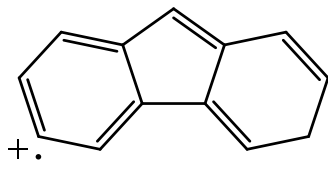
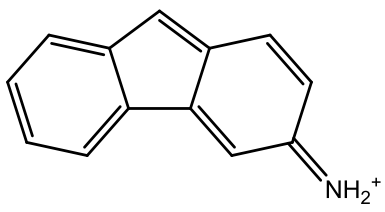
**Figure 4-3.** (left) Mass spectra of MDA isomers using direct infusion ESI-TOFMS for (a) 4,4'-MDA, (b) 2,2'-MDA, and (c) 2,4'-MDA. (right) Tandem mass spectra for parent ions ([M+H]<sup>+</sup> = 199.13 Da) of (d) 4,4'-MDA, (e) 2,2'-MDA, and (f) 2,4'-MDA. Center-of-mass collision energies are shown at right; corresponding lab-frame collision energies are 40 eV, 8 eV, and 0 eV, respectively. For 2,4'-MDA, no collision energy was required for dissociation.



Tandem mass spectra of protonated 4,4'-MDA, 2,2'-MDA and 2,4'-MDA are presented in **Figure 4-3d - Figure 4-3f**, and potential corresponding structures of fragment signals are shown in **Table 4-1**. Unsurprisingly, the fragmentation spectra of all the isomers are relatively similar. However, while 4,4'-MDA required high collision energy to generate fragments (**Fig. 4-3d**), 2,2'-MDA and 2,4'-MDA required minimal or no additional energy to induce dissociation (**Fig. 4-3e, 4-3f**). Because of the high collision energy required to fragment 4,4'-MDA, additional signals of 165 Da and 180 Da are observed which are not present in 2,2'-MDA and 2,4'-MDA tandem mass spectra. Additional fragmentation data concerning the low-intensity 211 Da signal is shown in **Figure 4-4**. The likely source of this ion is a very low abundance multimer which fragments into the 211 Da structure.

In order to compare the gas-phase stabilities of the three isomers, the conversion from 199 Da to 106 Da was monitored as a function of applied collision energy for all three isomers as shown in **Figure 4-5**. Both lab-frame and center-of-mass (COM) collision energies are displayed. It is clear that 4,4'-MDA (double *para*-substitution) is significantly more stable than either 2,2'-MDA (double *ortho*-substitution) or 2,4'-MDA (combined *ortho*- and *para*-substitution). For example, when 2.0 eV (COM) are applied to the 4,4'-MDA isomer, over 95% of the normalized signal remains in the 199 Da parent ion. However, at that same energy, the 199 Da parent ions for both 2,2'-MDA and 2,4'-MDA are entirely depleted. The underlying cause of this key difference as well as minor differences in the gas-phase behavior of 2,2'-MDA and 2,4'-MDA will be discussed later in the manuscript, as these observations were corroborated by other methods of structural analysis.

A potential complicating factor in MS-based analysis of these compounds is the uncertain location of the additional proton that creates the  $[M+H]^+$  ions. Literature on aniline suggests two potential protonation sites in the gas-phase, one on the amine and one on the aromatic ring *para* to the amine.<sup>48-52</sup> Recently, Eberlin and coworkers demonstrated that aniline molecules protonated at the amine group can be resolved from those protonated on the ring using T-wave separation.<sup>53</sup> Because MDA isomers are essentially two aniline molecules connected by a methylene bridge, it is probable this behavior applies to MDA as well. Therefore, as tandem MS

Theoretical <i>m/z</i>	Observed <i>m/z</i>	Proposed Structure(s)
77.04	77.04	
89.04	89.04	
106.07	106.07	 
165.07	165.07	
180.08	180.08	

**Table 4-1.** Possible structures of commonly-observed MDA fragment ions.

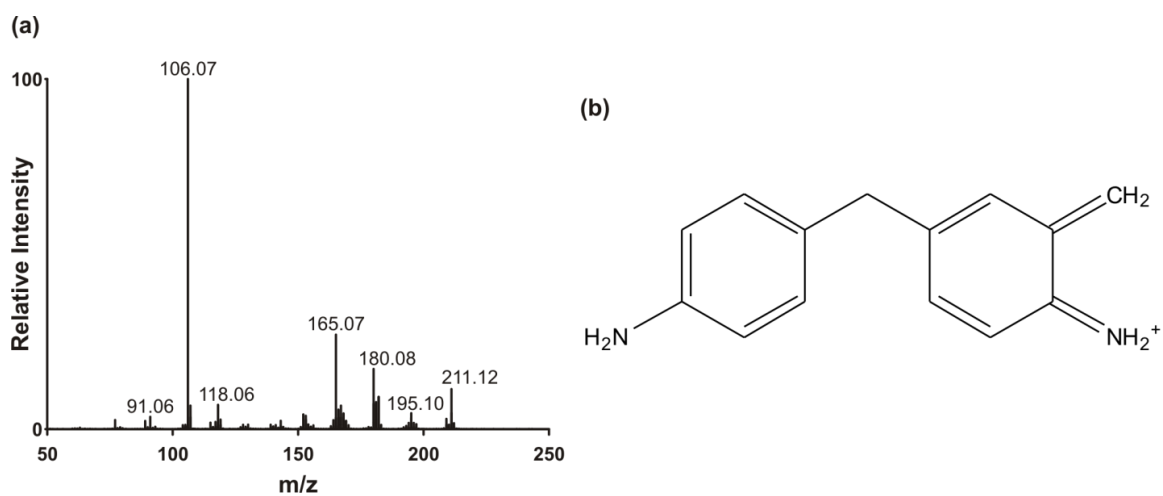


**Figure 4-4** (a) Tandem mass spectrum for 211 Da observed in the 4,4'-MDA sample. A center-of-mass collision energy of 4.9 eV was applied (40 eV lab-frame). (b) Proposed structure for the 211 Da species. Most fragment signals for 211 Da match the 199 Da fragments shown in **Table 4-1**, suggesting a similar structure to the MDA isomers.

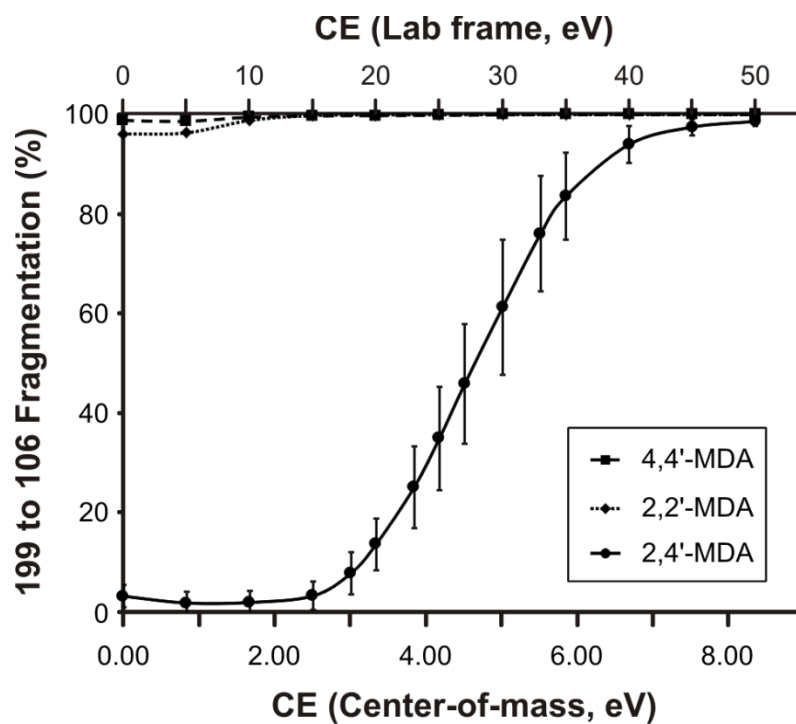


**Figure 4-5.** Collision-induced dissociation curves monitoring the transition of respective 199 Da parent ions to 106 Da fragment ions. Individual curves for 4,4'-MDA (solid line; circles), 2,2'-MDA (short dash, squares), and 2,4'-MDA (long dash; triangles) are superimposed. Both center-of-mass and lab-frame collision energies are shown.

alone was unable to provide clarity about how protonation sites affect gas-phase structures, structural analysis by IM and computational methods were required.

## II. *Structural analysis using IM-MS and computational methods*

Using both T-wave and DTIM instrumentation, CCS values were obtained for the  $[M+H]^+$ ,  $[M+Li]^+$ , and  $[M+Na]^+$  ions of the three isomers as shown in **Table 4-2**. Due to inherent differences in instrumentation and data analysis between T-wave and DTIM methodology, small differences for CCS values between platforms were expected, as observed in **Table 4-2**. In order to obtain CCS values from T-wave instrumentation, the use of calibration standards is required; in contrast, DTIM CCS values can be directly calculated from the kinetic theory of gases using the Mason-Schamp equation.<sup>22-24</sup> Therefore, it is expected that the DTIM CCS values are more accurate than the T-wave CCS values. In this study, DTIM CCS values were systematically higher than T-wave CCS values by  $3.4 \pm 0.5\% \text{ \AA}^2 (\text{N}_2)$ . The hypothesis is that this systematic difference between T-wave and DTIM CCS values results from the calibration of the former and from the exposure of the charge on the MDA molecules. For the tetraalkylammonium ions used for T-wave CCS calibration, the charge resides in the center of the molecule and is surrounded by hydrocarbon tails. These tails essentially shield the charged region from the polarizable  $\text{N}_2$  drift gas. As a result, only weak inelastic collisions occur between the tetraalkylammonium calibrants and  $\text{N}_2$ . However, in our MDA system, the charge is not shielded, and thus the MDA ions are expected to experience stronger inelastic interactions with  $\text{N}_2$  which are not accounted for using the current calibration strategy.

Within each data set, the CCS values for the  $[M+Li]^+$  and  $[M+Na]^+$  ions were similar. This suggests that metal cations interact with both electron-rich aromatic rings in the gas phase. In contrast, significant differences in CCS for the  $[M+H]^+$  ions were observed between 4,4'-MDA and 2,2'-MDA, suggesting the protonation site is not centrally located in the structure. For 2,4'-MDA, two CCS values in T-wave were observed, but only one corresponding CCS value for DTIM was observed. This will be discussed later, as further analysis of the role of protonation on gas-phase stability was necessary to explain this observation.

MDA Species (Ion)	T-wave N <sub>2</sub> (Å <sup>2</sup> )	DTIM N <sub>2</sub> (Å <sup>2</sup> )
4,4' [M+H] <sup>+</sup>	156.0 ± 0.7	162.7 ± 0.3
4,4' [M+Li] <sup>+</sup>	143.4 ± 1.9	147.8 ± 0.3
4,4' [M+Na] <sup>+</sup>	145.5 ± 1.0	149.7 ± 0.3
2,2' [M+H] <sup>+</sup>	139.9 ± 1.8	145.0 ± 0.2
2,2' [M+Li] <sup>+</sup>	143.5 ± 0.6	148.6 ± 0.2
2,2' [M+Na] <sup>+</sup>	144.2 ± 1.9	149.1 ± 0.3
2,4' [M+H] <sup>+</sup> (#1)	139.9 ± 1.1	145.4 ± 0.4
2,4' [M+H] <sup>+</sup> (#2)	155.9 ± 0.5	N/A
2,4' [M+Li] <sup>+</sup>	143.3 ± 0.3	147.1 ± 0.4
2,4' [M+Na] <sup>+</sup>	144.6 ± 2.1	150.3 ± 0.5

**Table 4-2.** Collision cross-section values of various MDA ions obtained on T-wave and drift tube IM-MS instrumentation. Errors shown represent the respective standard deviations.

Only one type of protonation site is available for 4,4'-MDA, at the *para*-amino groups (*p*-NH<sub>2</sub>). However, two potential sites exist for 2,2'-MDA and three for 2,4'-MDA, as shown by the asterisks in **Fig. 4-2**. For 2,2'-MDA, protonation can occur at either the *ortho*-amino groups (*o*-NH<sub>2</sub>) or the aromatic ring opposite the *ortho*-amino group (*ring*). On 2,4'-MDA, *p*-NH<sub>2</sub>, *o*-NH<sub>2</sub> and *ring* sites are all present, and any one of these may be protonated.

While CCS measurements were obtained using both T-wave and DTIM platforms, the majority of IM-MS and IM-MS/MS data was obtained using the T-wave platform and will therefore be the focus of this report. Extracted CCS profiles of the protonated isomers (199 Da) obtained using IM-MS are shown in **Figure 4-6a**. One conformation of 4,4'-MDA was generated with a CCS of 156 Å<sup>2</sup> while 2,2'-MDA generated one conformation with a CCS of 140 Å<sup>2</sup>. In contrast, 2,4'-MDA generated two conformations having CCS values of 156 Å<sup>2</sup> and 140 Å<sup>2</sup>. The alignment of these two values with the 4,4'-MDA and 2,2'-MDA CCS values in **Fig. 4-6a** (dotted line) indicate similar respective conformations.

Additionally, an IM-MS/MS structural depletion study was performed to connect the gas-phase stabilities of these conformations with potential protonation sites. In **Figure 4-7**, IM profiles were obtained for the protonated isomers using different collision energies and corresponding drift times were converted to CCS values. Consistent with earlier tandem MS data, 4,4'-MDA has one primary conformation (156 Å<sup>2</sup>) which begins to deplete when high collision energy (3.1 eV) is applied as shown in **Fig. 4-7a**. We can assign this CCS value to a conformation which is *p*-NH<sub>2</sub> protonated, as 4,4'-MDA cannot be protonated at other positions. Because 2,4'-MDA contains one *p*-NH<sub>2</sub> site as well, its CCS value of 156 Å<sup>2</sup> is also assigned to *p*-NH<sub>2</sub> protonation. Evidence for this is shown in **Figure 4-7b**, where the ~45% depletion rate of the larger 2,4'-MDA conformation for 3.1 eV matches that of 4,4'-MDA shown in **Fig. 4-7a**. Because both of these conformations are rather resistant to collisionally-induced depletion and fragmentation, it is deduced that *p*-NH<sub>2</sub> protonation generates species that are relatively stable in the gas-phase.

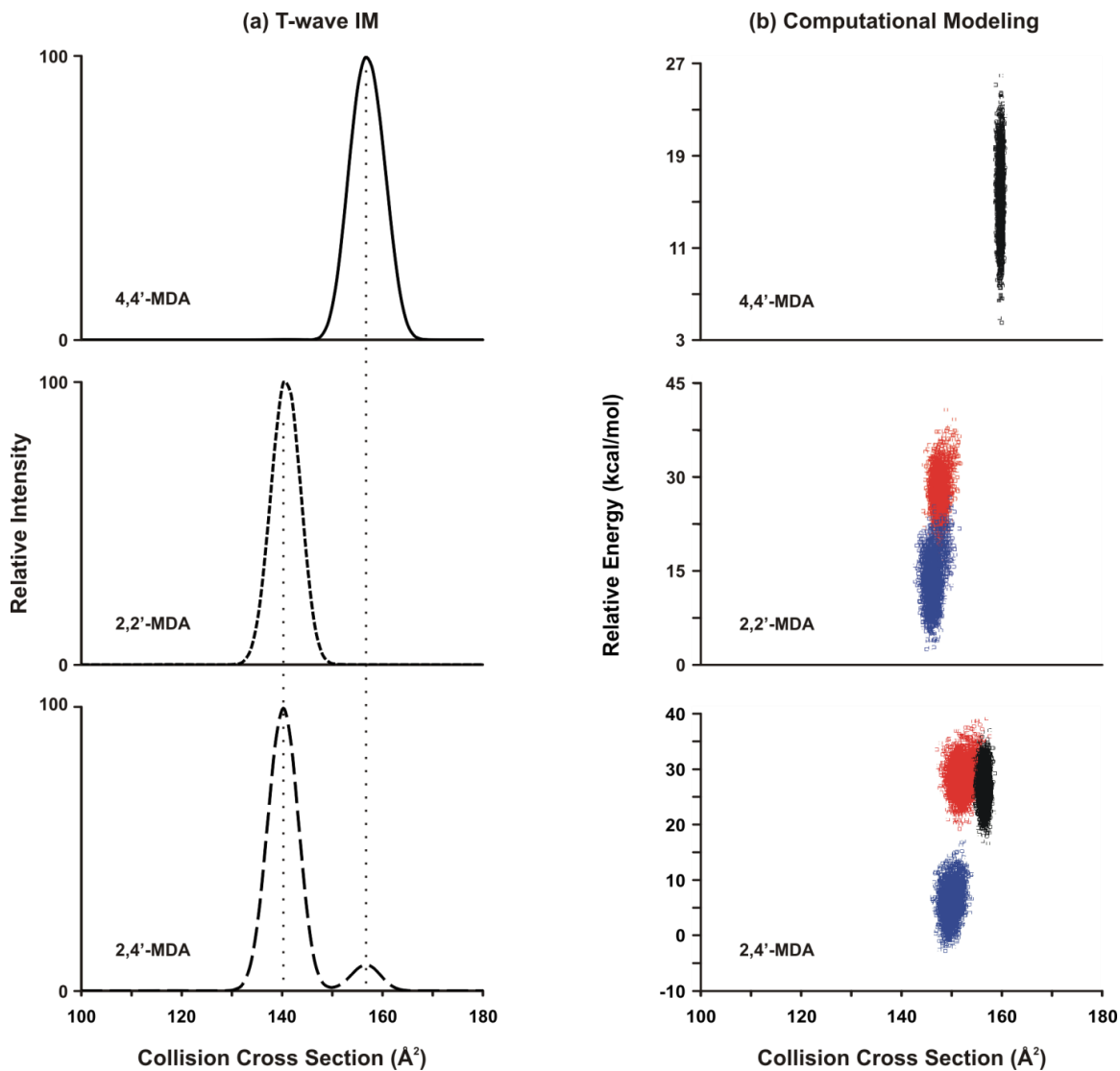


**Figure 4-6.** (a) CCS profiles of 4,4'-MDA (*solid line*), 2,2'-MDA (*short dash*), and 2,4'-MDA (*long dash*)  $[M+H]^+$  ions extracted from T-wave data. Vertical lines are added for visual alignment. (b) Conformations for the possible protonation sites for the (a) 4,4'-MDA, (b) 2,2'-MDA, and (c) 2,4'-MDA were generated using computational conformational search methods. The theoretical nitrogen CCS is plotted against the relative energy for each computationally generated conformation. Conformations for the *p*-NH<sub>2</sub> protonated isomers are shown in black, the *o*-NH<sub>2</sub> protonated isomers are shown in red and the *ring* protonated isomers in blue.



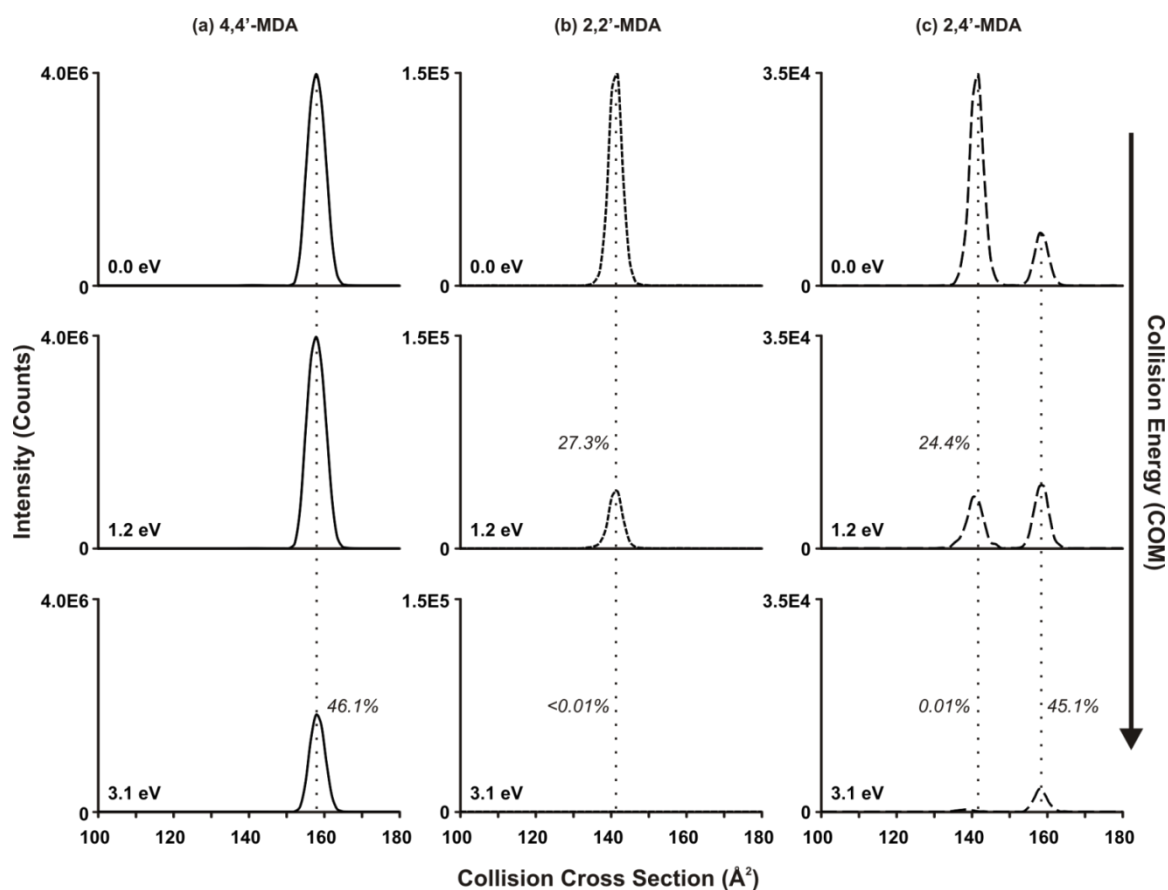


**Figure 4-7.** Collisionally-activated CCS profiles of  $[M+H]^+$  ions for (a) 4,4'-MDA, (b) 2,2'-MDA, and (c) 2,4'-MDA. Center-of-mass energies are shown; corresponding lab-frame energies are 0 eV, 10 eV, and 25 eV, respectively. Note the difference in scales of the y-axes for (a) - (c). Inset relative percentages represent signal intensities compared to those without collisional activation. Vertical lines are added for visual alignment.

In contrast, the low-intensity conformations for 2,2'-MDA and 2,4'-MDA of  $140 \text{ \AA}^2$  were less stable, leading to significant depletion upon collisional activation (**Fig. 4-7b - 4-7c**). Both of these conformations were entirely depleted when 3.1 eV of energy was applied. These are more difficult to assign structurally, as two remaining protonation sites exist for the isomers (*o*-NH<sub>2</sub> and *ring*). Conformations of all the possible protonation sites for the three isomers were generated using theoretical conformational search methods to provide further structural insight. For each of the six protonation sites 3,000 conformations were generated and the theoretical CCS value and energy was determined and plotted for each conformation in **Figure 4-6b**. The protonation sites are indicated by the following colors: the *p*-NH<sub>2</sub> conformations are shown in black, the *o*-NH<sub>2</sub> conformations are shown in red, and the *ring* conformations are shown in blue. The *p*-NH<sub>2</sub> conformations for both the 2,4'-MDA isomer and the 4,4'-MDA isomer demonstrate close theoretical CCS alignment and thus support the assignment of the larger observed CCS value. For *o*-NH<sub>2</sub> and *ring* protonation sites in 2,2'-MDA and 2,4'-MDA, theoretical CCS values are similar, which makes it difficult to differentiate these protonation sites by CCS. However, the 2,2'-MDA and 2,4'-MDA maps shown in **Fig. 4-6b** do suggest that protonation at the *o*-NH<sub>2</sub> position creates higher energy conformations than those with *ring* protonation. High-energy conformations likely correspond to species that undergo metastable fragmentation in the mass spectrometer, which was observed for 2,2'-MDA and 2,4'-MDA as noted earlier in **Figs. 4-3** and **4-4**. Therefore, it is likely that *o*-NH<sub>2</sub> protonation leads to metastable fragmentation into 106 Da, whereas *ring* protonation is somewhat more stable and allows detection of (at least some of) these ions as intact 199 Da species.

Although the stability of the MDA isomers is related to protonation site, it should be noted that small differences in energy can change the relative abundances of each site. As shown in **Table 4-2**, the *p*-NH<sub>2</sub> protonation site for 2,4'-MDA was not observed using DTIM instrumentation, while this protonation site was observed in low abundance using T-wave instrumentation (e.g. **Fig. 4-6a**). This is likely due to the different ion sources for the two platforms, which results in different voltages, ion transmission efficiencies, etc. As mentioned earlier, previous studies on aniline protonation in the gas-phase suggest that the two protonation sites (*-NH<sub>2</sub>* or *ring*) are

relatively close in energy. Therefore, the relative abundances of aniline protonation sites can fluctuate due to small changes in experimental conditions [39]. Likewise, MDA protonation sites appear to be close in energy, and the relative abundances of the protonation sites can change as well. This explains why the *p*-NH<sub>2</sub> conformation of 2,4'-MDA is observed in low abundance using T-wave instrumentation but not using DTIM instrumentation. However, once the MDA compounds are protonated, the relative order of stability across both platforms is consistent as shown in **Table 4-3**.

A closer look at computationally generated conformations gives further insight into the metastable nature of the *o*-NH<sub>2</sub> protonated isomers. The conformations were clustered based on root-mean-square deviation (RMSD) resulting in ten representative structures. These structures for the possible protonation sites for the three isomers can be found in the Supplemental Information, but the most populated conformations are shown in **Figure 4-8**. The most populated conformation for 4,4'-MDA is shown in **Fig. 4-8a**. This molecule exhibits an extended structure, consistent with experimental CCS data shown in **Table 4-2**. Conformations for 2,2'-MDA are shown in **Fig. 4-8b - 4-8d**. The conformations in **Fig. 4-7b - 4-7c** show *o*-NH<sub>2</sub> protonated 2,2'-MDA, whereas the conformation in **Fig. 4-8d** shows *ring* protonation. Two *o*-NH<sub>2</sub> protonated isomers are needed here to explain two of our experimental observations. **Fig. 4-8b** is representative of the metastable *o*-NH<sub>2</sub> protonation, while **Fig. 4-8c** is representative of a slightly more stable and highly populated *o*-NH<sub>2</sub> protonation. When the proton resides between the two amine groups, a more stable conformation is achieved, which may explain why a slightly more stable 2,2'-MDA isomer is shown in **Fig. 4-4** compared to the 2,4'-MDA isomer. These three conformations are all representative of a smaller structure, which is consistent with the experimental CCS data shown in **Table 4-2**. Conformations for 2,4'-MDA are shown in **Fig. 4-8e - 4-8g**. **Fig. 4-8e** shows the *p*-NH<sub>2</sub> protonation whereas **Fig. 4-8f** shows *o*-NH<sub>2</sub> protonation and **Fig. 4-8g** shows *ring* protonation. The conformation in **Fig. 4-8e** is representative of the extended structure similar to the conformation shown in **Fig. 4-8a**, which supports the experimental CCS alignment for both 4,4'-MDA and the larger 2,4'-MDA conformation.

<b>[M+H]<sup>+</sup> Species</b>	<b>T-wave IM</b>	<b>DTIM</b>
4,4'-MDA	97 ± 2%	99.89 ± 0.01%
2,2'-MDA	3.9 ± 0.1%	47.1 ± 0.2%
2,4'-MDA	0.9 ± 0.4%	37.6 ± 0.6%

**Table 4-3.** Comparison of relative gas-phase stabilities (100% max) between traveling-wave IM and DTIM instrument platforms. Values reflect the percent abundance of the 199 Da parent ion relative to the 106 Da fragment.  $n = 3$  for each value. For both instrument platforms, 4,4'-MDA is significantly more stable than 2,2'-MDA and 2,4'-MDA. However, in both cases 2,2'-MDA is slightly more stable than 2,4'-MDA.

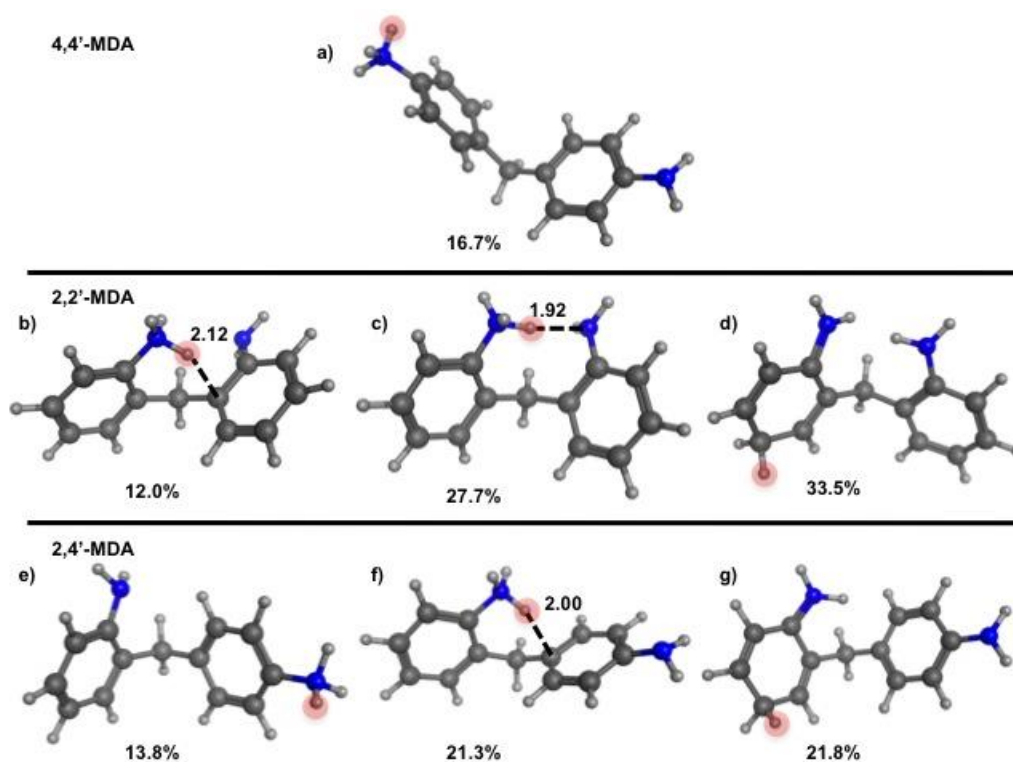


**Figure 4-8.** RMSD clustering representatives from computational conformational sampling are shown for each of the protonation sites. (a) 4,4'-MDA *p*-NH<sub>2</sub> protonated, (b) 2,2'-MDA *o*-NH<sub>2</sub> protonated, (c) 2,2'-MDA *o*-NH<sub>2</sub> protonated, (d) 2,2'-MDA *ring* protonated, (e) 2,4'-MDA *p*-NH<sub>2</sub> protonated, (f) 2,4'-MDA *o*-NH<sub>2</sub> protonated, and (g) 2,4'-MDA *ring* protonated. Red circles indicate the additional proton. Labeled bond distances are used to show the proximity of the additional proton to the bridging carbon that would lead to a 1-5 hydrogen shift fragmentation of the dimer. A percentage is shown below each conformation to show how many conformations the selected one represents, as a result of RMSD clustering. Two conformations are shown for the 2,2-MDA *o*-NH<sub>2</sub> protonated dimer due to two favorable conformations that result from this protonation. experimental CCS alignment for both 4,4'-MDA and the larger 2,4'-MDA conformation.

The conformations shown in **Fig. 4-8f - 4-8g** are representative of a smaller structure, which is also consistent with the experimental CCS data in **Table 4-2**. The smaller structures observed for the *o*-NH<sub>2</sub> protonation and *ring* protonation for 2,2'-MDA and 2,4'-MDA support the alignment of their experimental CCS values.

### *III. Mechanism for protonation and fragmentation of MDA isomers*

Combining tandem MS, IM-MS, IM-MS/MS, and computational modeling data, mechanisms for protonation and fragmentation of MDA structural isomers are proposed in **Figure 4-9**. The gas-phase stability of each isomer is inherently related to both the position of the amine groups and the location of the additional proton. The 4,4'-MDA isomer can only be protonated at *p*-NH<sub>2</sub> groups and is the most stable gas-phase ion that was observed. When a large collision energy is applied to the 4,4'-MDA parent ion, a loss of a hydrogen radical occurs, leading to *alpha* cleavage and formation of the 106 Da fragment. As collision energy continues to increase, other pathways also emerge, forming other fragments (**Fig. 4-3d**). On the other hand, 2,2'-MDA can be protonated at either the *o*-NH<sub>2</sub> or *ring* position. When 2,2'-MDA is protonated on an *o*-NH<sub>2</sub> group, even without applied collision energy, it readily undergoes a 1,5-hydrogen shift, due to the proximity of the amine hydrogen to the bridging carbon on the opposite aromatic ring (**Fig. 4-8b**), which leads to formation of the 106 Da fragment and neutral aniline. The driving force for this process is likely the stability of the products: aniline can either remain neutral or further decompose to 77 Da as shown in **Fig. 4-3e - 4-3f**, and the 106 Da fragment can further rearrange to a tropylium-like ion of the same mass (see Refs. 16, 48). This mechanism which describes the metastable behavior of these ions explains why detection of *o*-NH<sub>2</sub> protonated 2,4'-MDA or 2,2'-MDA is minimal. As a result, the primary conformation observed for the 2,2'-MDA [M+H]<sup>+</sup> ion (199 Da) is composed of *ring* protonated species. When a moderate collision energy is applied to ring protonated 2,2'-MDA, loss of a hydrogen radical on the ring leads to rearrangement and formation of the 106 Da fragment as well. Finally, 2,4'-MDA may be protonated at all three sites. Protonation at the *o*-NH<sub>2</sub> leads to significant metastable fragmentation due to a 1,5-hydrogen shift (**Fig. 4-8f**) as in 2,2'-MDA, and protonation at the *ring* position leads to hydrogen radical loss and

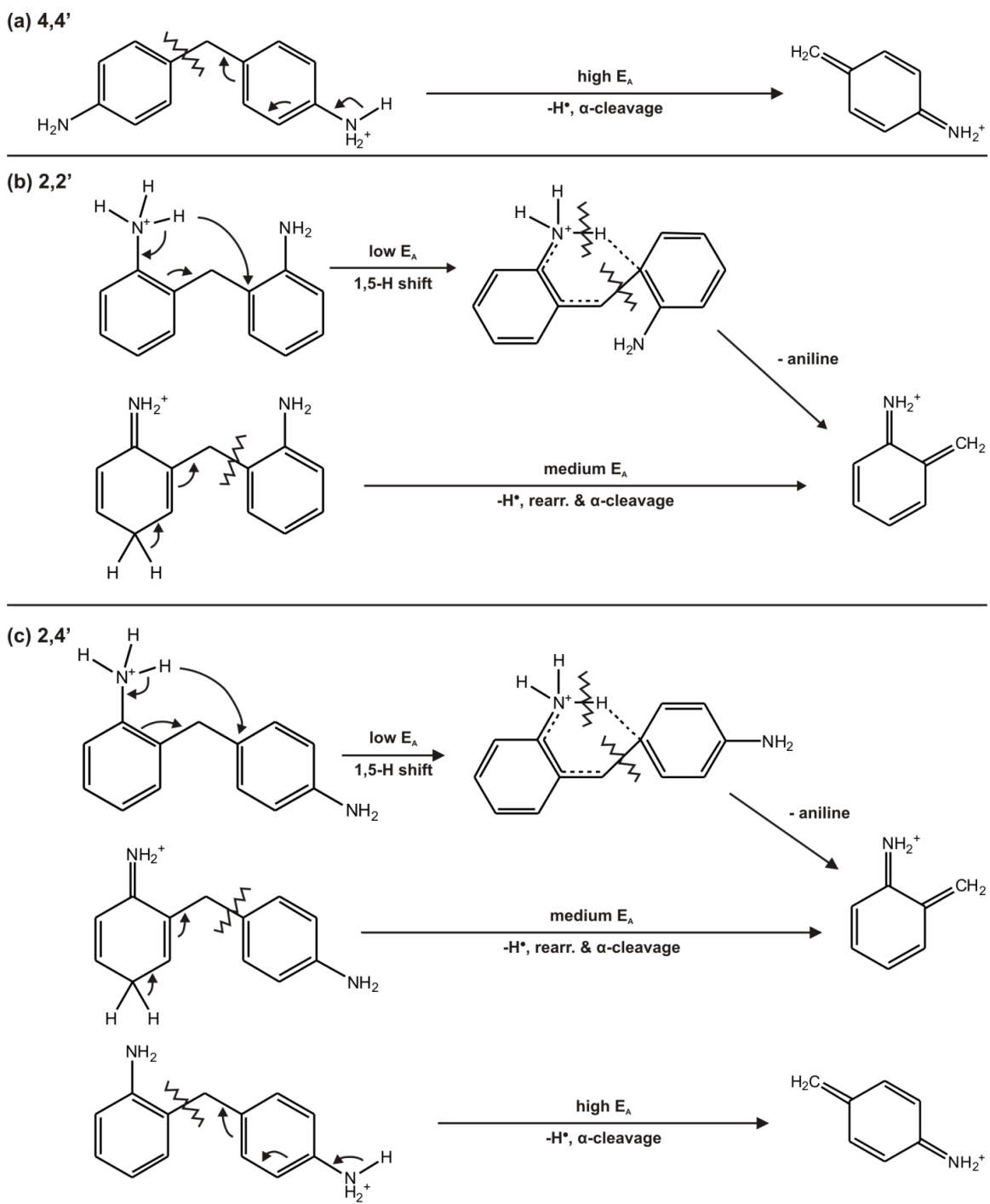


**Figure 4-9.** Proposed protonated structures and 199 Da  $\rightarrow$  106 Da fragmentation pathways for MDA isomers. Activation energy is abbreviated  $E_A$ .

rearrangement upon collisional activation. In contrast, protonation at the *p*-NH<sub>2</sub> results in a more stable conformation which fragments through a mechanism similar to that of 4,4'-MDA.

#### **4.4 Conclusions**

In this study, MDA structural isomers were characterized and differentiated by their gas-phase stabilities and potential protonation sites using a combination of structural insights guided by MS, IM, and theoretical modeling. These results confirm that, similar to aniline, MDA may be protonated at amine positions or at ring positions in the gas-phase. Structural differences between positional isomers play a large role in determining the gas-phase stability as does the site of protonation. The collective use of tandem MS, IM-MS, IM-MS/MS, and computational methods allowed us to gain significant structural understanding of this system and suggests that a holistic approach to studying positional isomers is of great utility.

A more thorough understanding of MDA behavior in the gas-phase will lead to a more comprehensive characterization of industrial MDA mixtures and better understanding of polyurethane fragmentation in mass spectrometry. These results on the dimeric isomers suggest IM-MS methods of characterizing larger multimers and MDA mixtures will prove beneficial to fully understand not only the molecular composition of the sample but also the structural differences between isobaric species within the sample.

#### **4.5 Acknowledgements**

Thank you to Dr. Stefan Wershofen for providing MDA samples and Tiffany Onifer for assistance. We also acknowledge the support of Dr. Don Stec and the Vanderbilt NMR facilities which is supported by the National Institute of Health (NIH, S10 RR019022). Additionally, thank you to the Vanderbilt Center for Structural Biology and Dr. Terry Lybrand for computational support and the Searle Systems Biology and Bioengineering Undergraduate Research Experience (SyBBURE) Program for summer support for N.W.K. This research was funded by the Defense Threat Reduction Agency under Grants HDTRA1-09-1-00-13 and DTRA100271 A-5196; and the Defense Advanced Research Projects Agency under Grant W911NF-12-2-0036.



#### 4.6 References

1. Tracy, J. B.; Crowe, M. C.; Parker, J. F.; Hampe, O.; Fields-Zinna, C. A.; Dass, A.; Murray, R. W. Electrospray Ionization Mass Spectrometry of Uniform and Mixed Monolayer Nanoparticles:  $\text{Au}_{25}(\text{SCH}_2\text{CH}_2\text{Ph})_{18}$  and Mixed Monolayer  $\text{Au}_{25}(\text{SCH}_2\text{CH}_2\text{Ph})_{18-x}(\text{SR})_x$ . *J. Amer. Chem. Soc.* **2007**, *129*, 16209-16215.
2. Dass, A.; Stevenson, A.; Dubay, G. R.; Tracy, J. B.; Murray, R. W. Nanoparticle MALDI-TOF Mass Spectrometry without Fragmentation:  $\text{Au}_{25}(\text{SCH}_2\text{CH}_2\text{Ph})_{18}$  and Mixed Monolayer  $\text{Au}_{25}(\text{SCH}_2\text{CH}_2\text{Ph})_{18-x}(\text{L})_x$ . *J. Amer. Chem. Soc.* **2008**, *130*, 5940-5946.
3. Harkness, K. M.; Cliffel, D. E.; McLean, J. A. Characterization of Thiolate-protected Gold Nanoparticles by Mass Spectrometry. *Analyst* **2010**, *135*, 868-874.
4. Kasuya, A.; Sivamohan, R.; Barnakov, Y. A.; Dmitruk, I. M.; Nirasawa, T.; Romanyuk, V. R.; Kumar, V.; Mamykin, S. V.; Tohji, K.; Jeyadevan, B.; Shinoda, K.; Kudo, T.; Terasaki, O.; Liu, Z.; Belosludov, R. V.; Sundararajan, V.; Kawazoe, Y. *Nat. Mater.* **2004**, *3*, 99-102.
5. Scheffer, A.; Engelhard, C.; Sperling, M.; Buscher, W. ICP-MS as a New Tool for the Determination of Gold Nanoparticles in Bioanalytical Applications. *Anal. Bioanal. Chem.* **2008**, *390*, 249-252.
6. Gardella, Jr., J. A.; Hercules, D. M. Static Secondary Ion Mass Spectrometry of Polymer Systems. *Anal. Chem.* **1980**, *52*, 226-232.
7. Bahr, U.; Deppe, A.; Karas, M.; Hillenkamp, F. Mass Spectrometry of Synthetic Polymers by UV-Matrix-Assisted Laser Desorption/Ionization. *Anal. Chem.* **1992**, *64*, 2866-2869.
8. Hanton, S. D. Mass Spectrometry of Polymers and Polymer Surfaces. *Chem. Rev.* **2001**, *101*, 527-569.
9. Fenn, J. B.; Mann, M.; Meng, C. K.; Wong, S. F.; Whitehouse, C. M. Electrospray Ionization for Mass Spectrometry of Large Biomolecules. *Science* **1989**, *246*, 64-71.
10. Chattopadhyay, D. K.; Raju, K. V. S. N. Structural Engineering of Polyurethane Coatings for High Performance Applications. *Prog. Polym. Sci.* **2007**, *32*, 352-418.
11. Eifler, W.; Ick, J. Method for Making a Polyamine. U.S. Patent 4,189,443, February 19, 1980.
12. van den Berg, H.; van der Ham, L.; Gutierrez, H.; Odu, S.; Roelofs, T.; de Weerd, J. Phosgene Free Route to Methyl Diphenyl Diisocyanate (MDI): A Technical and Economical Evaluation. *Chem. Eng. J.* **2012**, *207*, 254-257.
13. Skarping, G.; Dalene, M. Determination of 4,4'-methylenediphenyldianiline (MDA) and Identification of Isomers in Technical-grade MDA in Hydrolysed Plasma and Urine from Workers Exposed to Methylene Diphenyldiisocyanate by Gas Chromatography - Mass Spectrometry. *J. Chromatogr. B.* **1995**, *663*, 209-216.
14. Cocker, J.; Brown, L. C.; Wilson, H. K.; Rollins, K. A GC/MS Method for the Determination of 4,4'-diaminodiphenylmethane and Substituted Analogues in Urine. *J. Anal. Toxicol.* **1988**, *12*, 9-14.

15. Bailey, E.; Brooks, A. G.; Bird, I.; Farmer, P. B.; Street, B. Monitoring Exposure to 4,4'-methylenedianiline by the Gas Chromatography - Mass Spectrometry Determination of Adducts to Hemoglobin. *Anal. Biochem.* **1990**, *190*, 175-181.
16. Chen, K.; Dugas, T. R.; Cole, R. B. Identification of Metabolites of 4,4'-methylenedianiline in Vascular Smooth Muscle Cells by Liquid Chromatography - Electrospray Tandem Mass Spectrometry. *J. Mass Spectrom.* **2006**, *41*, 728-734.
17. Chen, K.; Dugas, T. R.; Cole, R. B. Liquid Chromatography - Electrospray Tandem Mass Spectrometry Investigations of Fragmentation Pathways of Biliary 4,4'-methylenedianiline Conjugates Produced in Rats. *Anal. Bioanal. Chem.* **2008**, *391*, 271-278.
18. Chen, K.; Cole, R. B.; Santa Cruz, V.; Blakeney, E. W.; Kanz, M. F.; Dugas, T. R. Characterization of Biliary Conjugates of 4,4'-methylenedianiline in Male versus Female Rats. *Toxicol. Appl. Pharmacol.* **2008**, *232*, 190-202.
19. Johnson, J. R.; Karlsson, D.; Dalene, M.; Skarping, G. Determination of Aromatic Amines in Aqueous Extracts of Polyurethane Foam using Hydrophilic Interaction Liquid Chromatography and Mass Spectrometry. *Anal. Chem. Acta* **2010**, *678*, 117-123.
20. Pezo, D.; Fedeli, M.; Bosetti, O.; Nerín, C. Aromatic Amines from Polyurethane Adhesives in Food Packaging: the Challenge of Identification and Pattern Recognition using Quadrupole - Time of Flight - Mass Spectrometry<sup>E</sup>. *Anal. Chem. Acta* **2012**, *756*, 49-59.
21. Wang, C. Y.; Li, H. Q.; Wang, L. G.; Cao, Y.; Liu, H. T.; Zhang, Y. Insights on the Mechanism for Synthesis of Methylenedianiline from Aniline and Formaldehyde through HPLC-MS and Isotope Tracer Studies. *Chin. Chem. Lett.* **2012**, *23*, 1254-1258.
22. McDaniel, E. W. *Collision Phenomena in Ionized Gases*. Wiley: New York, 1964.
23. McDaniel, E. W.; Mason, E. A. *The Mobility and Diffusion of Ions in Gases*. Wiley: New York, 1973.
24. Mason, E. A. Ion Mobility: Its Role in Plasma Chromatography. In *Plasma Chromatography*; Carr, T. W., Ed.; Plenum Press: New York, 1984; pp 43-93.
25. Eiceman, G. A.; Karpas, Z. *Ion Mobility Spectrometry, 2<sup>nd</sup> Edition*. CRC Press: Boca Raton, 2004.
26. Ruotolo, B. T.; Benesch, J. L. P.; Sandercock, A. M.; Hyung, S.-J.; Robinson, C. V. Ion Mobility - Mass Spectrometry Analysis of Large Protein Complexes. *Nat. Protoc.* **2008**, *3*, 1139-1152.
27. Wilkins, C. L.; Trimpin, S. *Ion Mobility Spectrometry-Mass Spectrometry: Theory and Applications*. CRC Press: Boca Raton, 2011.
28. Hines, K. M.; Enders, J. R.; McLean, J. A. Multidimensional Separations by Ion Mobility-Mass Spectrometry. *Encyclopedia of Analytical Chemistry* [Online]; Wiley, Posted December 17, 2012.
29. Hilton, G. R.; Jackson, A. T.; Thalassinou, K.; Scrivens, J. H. Structural Analysis of Synthetic Polymer Mixtures using Ion Mobility and Tandem Mass Spectrometry. *Anal. Chem.* **2008**, *80*, 9720-9725.

30. Gies, A. P.; Kliman, M.; McLean, J. A.; Hercules, D. M. Characterization of Branching in Aramid Polymers Studied by MALDI - Ion Mobility/Mass Spectrometry. *Macromolecules* **2008**, *41*, 8299-8301.
31. Trimpin, S.; Clemmer, D. E. Ion Mobility Spectrometry/Mass Spectrometry Snapshots for Assessing the Molecular Compositions of Complex Polymeric Systems. *Anal. Chem.* **2008**, *80*, 9073-9083.
32. Li, X.; Guo, L.; Casiano-Maldonado, M.; Zhang, D.; Wesdemiotis, C. Top-down Multidimensional Mass Spectrometry Methods for Synthetic Polymer Analysis. *Macromolecules* **2011**, *44*, 4555-4564.
33. Hoskins, J. N.; Trimpin, S.; Grayson, S. M. Architectural Differentiation of Linear and Cyclic Polymeric Isomers by Ion Mobility Spectrometry-Mass Spectrometry. *Macromolecules* **2011**, *44*, 6915-6918.
34. Hagen, D. F. Characterization of Isomeric Compounds by Gas and Plasma Chromatography. *Anal. Chem.* **1979**, *51*, 870-874.
35. Hagen, D. F. Characterization of Isomers by Plasma Chromatography, In *Plasma Chromatography*; Carr, T. W., Ed.; Plenum Press: New York, 1984; pp 115-142.
36. Campuzano, I.; Bush, M. F.; Robinson, C. V.; Beaumont, C.; Richardson, K.; Kim, H.; Kim, H. I. Structural Characterization of Drug-like Compounds by Ion Mobility Mass Spectrometry: Comparison of Theoretical and Experimentally Derived Nitrogen Collision Cross Sections. *Anal. Chem.* **2011**, *84*, 1026-1033.
37. Sleno, L.; Volmer, D. A. Ion Activation Methods for Tandem Mass Spectrometry. *J. Mass Spectrom.* **2004**, *39*, 1091-1112.
38. Rodgers, M. T.; Armentrout, P. B. Noncovalent Metal-ligand Bond Energies as Studied by Threshold Collision-induced Dissociation. *Mass Spectrom. Rev.* **2000**, *19*, 215-247.
39. May, J. C.; Goodwin, C. R.; Lareau, N. M.; Leaptrot, K. L.; Morris, C. B.; Kurulugama, R. T.; Mordehai, A.; Klein, C.; Barry, W.; Darland, E.; Rennie, E.; Overney, G.; Imatani, K.; Stafford, G. C.; Fjeldsted, J. C.; McLean, J. A. Conformational Ordering of Biomolecules in the Gas-Phase: Nitrogen Collision Cross-Sections Measured on a Prototype High Resolution Drift Tube Instrument. Submitted to *Anal. Chem.*
40. Wyttenbach, T.; Bowers, M. T. Gas-phase Conformations: The Ion Mobility / Ion Chromatography Method. In *Modern Mass Spectrometry*, Springer: 2003; pp 207-232.
41. Gaussian 09, Revision A.02, Frisch, M. J.; Trucks, G. W.; Schlegel, H. B.; Scuseria, G. E.; Robb, M. A.; Cheeseman, J. R.; Scalmani, G.; Barone, V.; Mennucci, B.; Petersson, G. A.; Nakatsuji, H.; Caricato, M.; Li, X.; Hratchian, H. P.; Izmaylov, A. F.; Bloino, J.; Zheng, G.; Sonnenberg, J. L.; Hada, M.; Ehara, M.; Toyota, K.; Fukuda, R.; Hasegawa, J.; Ishida, M.; Nakajima, T.; Honda, Y.; Kitao, O.; Nakai, H.; Vreven, T.; Montgomery, Jr., J. A.; Peralta, J. E.; Ogliaro, F.; Bearpark, M.; Heyd, J. J.; Brothers, E.; Kudin, K. N.; Staroverov, V. N.; Kobayashi, R.; Normand, J.; Raghavachari, K.; Rendell, A.; Burant, J. C.; Iyengar, S. S.; Tomasi, J.; Cossi, M.; Rega, N.; Millam, J. M.; Klene, M.; Knox, J. E.; Cross, J. B.; Bakken, V.; Adamo, C.; Jaramillo, J.; Gomperts, R.; Stratmann, R. E.; Yazyev, O.; Austin, A. J.; Cammi, R.; Pomelli, C.; Ochterski, J. W.; Martin, R. L.; Morokuma, K.; Zakrzewski, V. G.; Voth, G. A.; Salvador, P.; Dannenberg, J. J.; Dapprich, S.; Daniels, A. D.; Farkas, O.; Foresman, J. B.; Ortiz, J. V.; Cioslowski, J.; Fox, D. J. Gaussian, Inc., Wallingford CT, 2009.

42. Case, D. A.; Darden, T. A.; Cheatham III, T. E.; Simmerling, C. L.; Wang, J.; Duke, R. E.; Luo, R.; Walker, R. C.; Zhang, W.; Merz, K. M., AMBER 11. *University of California, San Francisco* **2010**, 142.
43. Bayly, C. I.; Cieplak, P.; Cornell, W.; Kollman, P. A. A Well-behaved Electrostatic Potential Based Method using Charge Restraints for Deriving Atomic Charges: the RESP Model. *J. Phys. Chem.* **1993**, *97*, 10269-10280.
44. Wyttenbach, T.; von Helden, G.; Batka, J. J.; Carlat, D.; Bowers, M. T. Effect of the Long-range Potential on Ion Mobility Measurements. *J. Am. Soc. Mass Spectrom.* **1997**, *8*, 275-282.
45. Mesleh, M. F.; Hunter, J. M.; Shvartsburg, A. A.; Schatz, G. C.; Jarrold, M. F. Structural Information from Ion Mobility Measurements: Effects of the Long-range Potential. *J. Phys. Chem.* **1996**, *100*, 16082-16086.
46. Shvartsburg, A. A.; Jarrold, M. F. An Exact Hard-spheres Scattering Model for the Mobilities of Polyatomic Ions. *Chem. Phys. Lett.* **1996**, *261*, 86-91.
47. Bush, M. F.; Campuzano, I. D. G.; Robinson, C. V. Ion Mobility Mass Spectrometry of Peptide Ions: Effects of Drift Gas and Calibration Strategies. *Anal. Chem.* **2012**, *84*, 7124-7130.
48. Rappoport, Z., Ed. *The Chemistry of Anilines*; John Wiley & Sons: Chichester, U.K., 2007.
49. Lau, Y. K.; Kebarle, P. Substituent Effects on the Intrinsic Basicity of Benzene - Proton Affinities of Substituted Benzenes. *J. Am. Chem. Soc.* **1976**, *98*, 7452-7453.
50. Karpas, Z.; Berant, Z.; Stimac, R. An Ion Mobility Spectrometry/Mass Spectrometry (IMS/MS) Study of the Site of Protonation in Anilines. *Struct. Chem.* **1990**, *1*, 201-204.
51. Roy, R. K.; de Proft, F.; Geerlings, P. Site of Protonation in Aniline and Substituted Anilines in the Gas Phase: A Study via the Local Hard and Soft Acids and Bases Concept. *J. Phys. Chem. A* **1998**, *102*, 7035-7040.
52. Russo, N.; Toscano, M.; Grand, A.; Mineva, T. Proton Affinity and Protonation Sites of Aniline. Energetic Behavior and Density Functional Reactivity Indices. *J. Phys. Chem. A* **2000**, *104*, 4017-4021.
53. Lalli, P. M.; Iglesias, B. A.; Toma, H. E.; de Sa, G. F.; Daroda, R. J.; Silva Filho, J. C.; Szulejko, J. E.; Araki, K.; Eberlin, M. N. Protomers: Formation, Separation and Characterization via Travelling Wave Ion Mobility Mass Spectrometry. *J. Mass Spectrom.* **2012**, *47*, 712-719.

## CHAPTER V

### CONCLUSIONS AND FUTURE DIRECTIONS

#### **5.1 Conclusions**

Nanomaterials are uniquely suited as matrices for MALDI-MS due to impressive sensitivity, low background signals, and capabilities in high-spatial-resolution MS imaging of biological samples. In this dissertation, advances using the NIMS platform were detailed so that future researchers may utilize it for single-cell MS imaging. Previous NIMS targets were not transparent, which made it difficult to locate the biological sample on the substrate. To solve this challenge, we introduced semi-transparent pSi thin films as novel NIMS substrates. Although pSi absorbs in the visible, it was found substrates less than 15  $\mu\text{m}$  in thickness allowed sufficient visible light to pass through so that samples can be analyzed using phase-contrast microscopy. Substrates were optimized for both transparency and NIMS performance so that MS imaging of lipids using a single-cell spatial resolution could be performed. Nevertheless, the reproducibility of MS imaging experiments from this substrate was somewhat inconsistent, which inspired us to pursue novel ways of enhancing ion yields from the target. Hybrid NIMS-MALDI matrices were introduced which have affinity towards the NIMS initiator via fluorophilic interactions. One matrix, DHB-59, improved S/N of biological molecules and may be used in MS imaging experiments in the future.

While materials chemistry developments are improving MS-related techniques, structural MS techniques are also proving critical in the characterization of inorganic and organic materials. A comprehensive IM-based approach supported by computational modeling was described for the structural characterization and differentiation of polyurethane-hard-block precursor molecules. It was determined that, in addition to differences in the location of functional groups, protonation site significantly affected the stability of gas-phase analytes. MDA regioisomers were rapidly differentiated using IM-MS and IM-MS/MS based on this principle.

## 5.2 *Dynamic Light Patterning-based NIMS Imaging*

As described in earlier chapters, NIMS targets have been developed for MS imaging of biological substrates. These targets demonstrate impressive limits-of-detection and generate minimal matrix background signals, simplifying the mass spectrum when compared to traditional MALDI-MS which utilizes weak-organic-acid matrix. Nevertheless, two challenges remain in the development and refinement of the NIMS imaging platform which may be addressed in order to perform reproducible, high-spatial-resolution MS imaging at the single-cell level.

Although NIMS has shown good limits-of-detection for metabolites and peptides, it remains a challenge to reproducibly image these molecules from cells. The primary cause of this is the very low volume of a typical mammalian cell, approximately 500 fL for a cell with 10  $\mu\text{m}$  diameter.<sup>1</sup> Therefore, the amounts of biological molecules within a cell are less than normal MS sample amounts. When laser irradiation is used, the majority of cellular material is desorbed from one or several laser pulses at the target; therefore, it is crucial to ensure that the efficiency of ionization for desorbed material is maximized so that all desorbed analytes may be detected rapidly. An additional cause is the complex matrix of cellular material which can lead to ion suppression effects. Further development of VU-59 matrix as described in Chapter 3 may continue to improve ion yields from the NIMS surface. Based on the experiments outlined in that chapter, it appears that VU-59 does not assist in analyte protonation but in fact improves analyte mixing with the NIMS surface and initiator. If structure-activity relationship studies are performed on VU-59 so that proton donation is optimized, it may improve NIMS ion yields such that single-cell sensitivity is reproducibly attained.

Another challenge in single-cell MS and MS imaging is laser spatial resolution, as described in Chapter 1. Within a factor of two or so, resolving power is limited by diffraction to the wavelength of the irradiation, from the equation:

$$\text{Resolving Power} = \frac{1.22 * \lambda * f}{D} \quad (6)$$

where  $\lambda$  is the wavelength of the laser,  $f$  is the focal length, and  $D$  is the diameter of the objective lens used.<sup>2</sup> This means that resolving nanometer-spaced features in cells by MS imaging will likely remain a challenge, even when optical alignment is ideal. It has been shown that imaging resolution can overcome the diffraction limit if the light coupled with a tip within 1 wavelength of the target (near-field). Near-field optical strategies are currently being developed for ICP-MS,<sup>3-4</sup> but it remains unclear if this approach will be able to desorb and/or ionize intact biomolecules.

Due to these challenges with sensitivity and spatial resolution, it is likely the best spatial resolution of our NIMS imaging platform will prove to be 2-3  $\mu\text{m}$ . Current efforts to focus the laser to this diameter are shown in **Figure 5-1**; however, sufficient MS signal cannot be detected from cells at this resolution. The best spatial resolution achieved to date has been 14  $\mu\text{m}$  (see **Fig. 2-6** and **Fig. 2-8**). A spatial resolution of 2-3  $\mu\text{m}$  would be at the cutting-edge of the field, and would allow for the resolution of sub-cellular features in larger cells such as fibroblasts and neurons. In order to achieve this resolution, the dynamic light patterning (DLP) optical system shown in **Figure 5-2** will be re-aligned using the frequency-tripled Tempest Nd:YAG laser (355 nm) at low energy. Once alignment is proper (evaluated by SEM imaging of burn marks as shown in **Fig. 5-1**), laser energy may be increased for MS imaging. High-energy irradiation on the DLP chips can lead to irreversible damage over time. However, these chips are commercially available and may be interchanged as necessary. Combining this optical platform with VU-59 matrix-enhanced NIMS may allow for 2-3  $\mu\text{m}$  spatial resolution. This DLP-NIMS platform could be used for not only single-cell MS imaging but also spatial profiling.

### **5.3 Phosphopeptide-affinity NIMS Targets**

Because NIMS targets are coated with the perfluorinated BisF17 initiator (**Fig. 3-1a**), this allows for analytes which have been tagged with a perfluorinated moiety to have very high affinity to the surface, as shown by Ref. 4 from Chapter 3. NIMS surface derivatization may be tailored for many applications; one particular application of interest is phosphopeptide enrichment. Phosphopeptides are typically enriched using metallic oxides such as titanium dioxide ( $\text{TiO}_2$ ) due

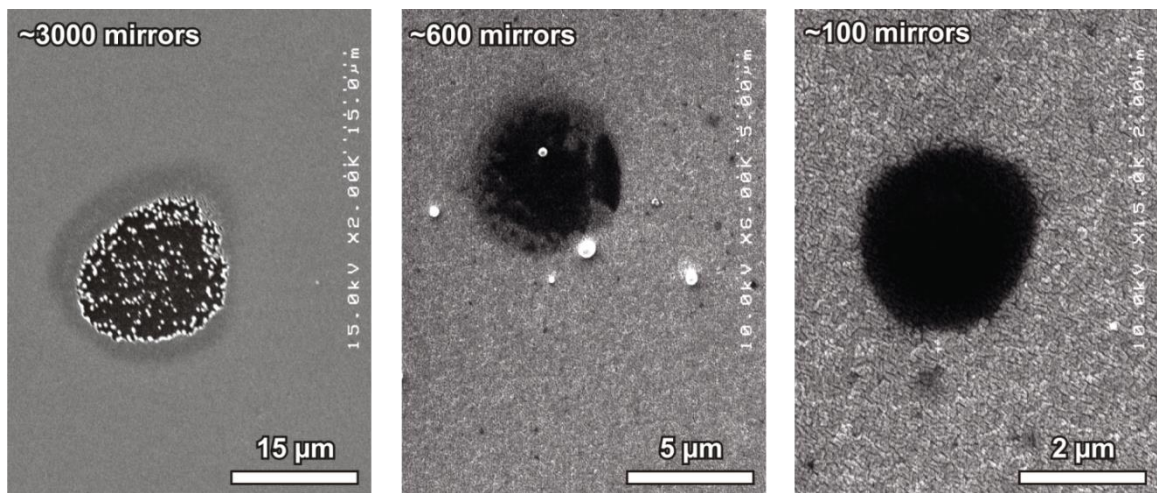


**Figure 5-1.** SEM images of UV laser burn marks on Au reveal laser focusing at target. (*left*) When approx. 3000 DLP mirrors deflect the laser to the target, the beam diameter is 15  $\mu\text{m}$ ; (*center*) when approx. 600 DLP mirrors deflect the laser to the target, the beam diameter is 5  $\mu\text{m}$ ; (*right*) when approx. 100 DLP mirrors deflect the laser to the target, the beam diameter is 2  $\mu\text{m}$ .



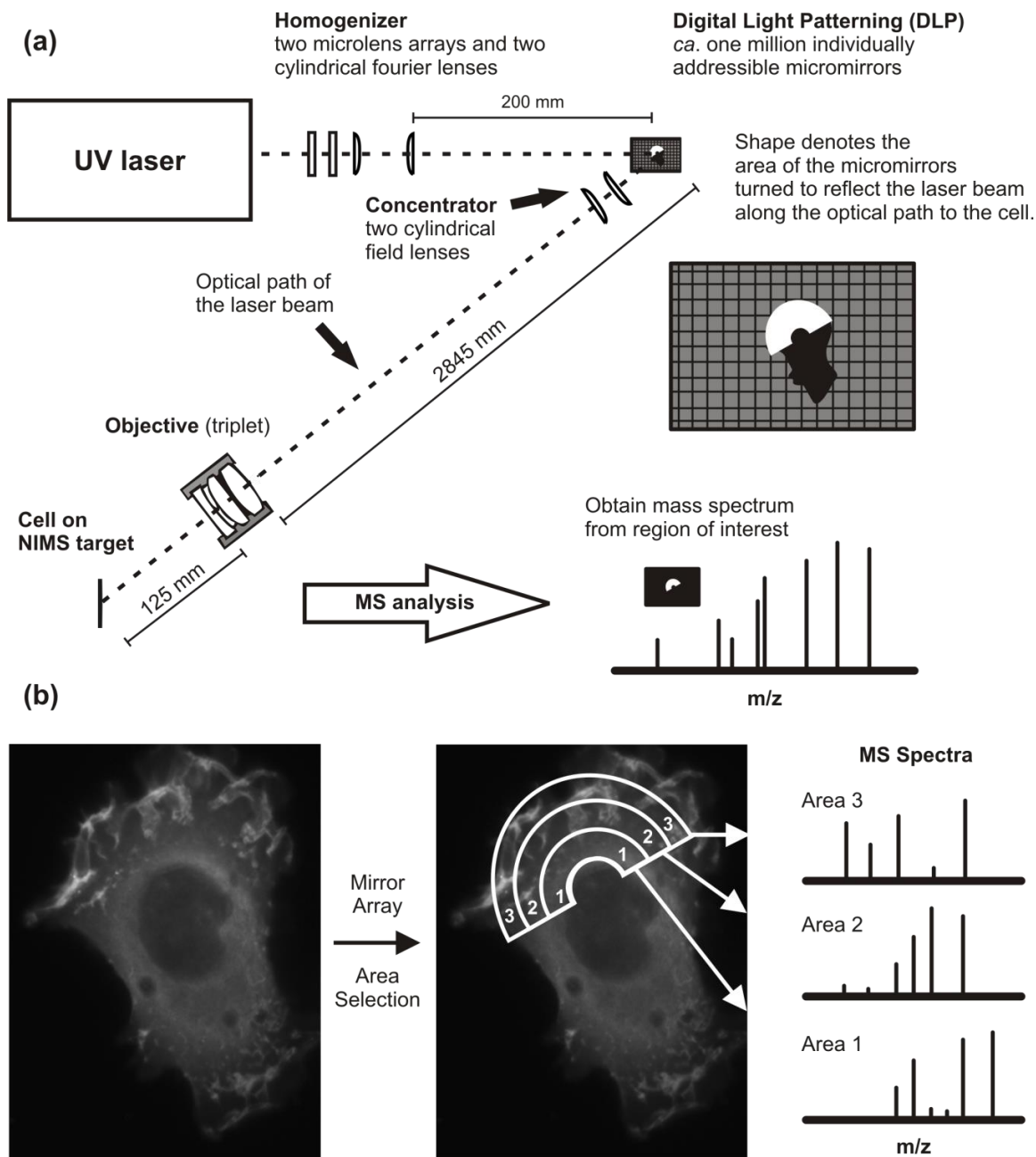


**Figure 5-2.** (a) Schematic of DLP optical train. (b) Thought experiment where the DLP system may be used to generate unique MS profiles within different regions of a cell. Adapted with permission from Kliman, M. *Advanced Structural and Spatial Analysis of Lipids using Ion Mobility - Mass Spectrometry*. Dissertation, Vanderbilt University, Nashville, TN, 2011.

to hard acid-base interactions.<sup>5-6</sup> It is possible combining materials such as these with NIMS sensitivity may lead to both high-specificity and high-sensitivity phosphopeptide analysis.

Initial experiments coupling TiO<sub>2</sub> particles with NIMS substrates for phosphopeptide enrichment are described herein. The potential advantage of coupling high-specificity phosphopeptide pre-concentration methods with NIMS sensitivity is shown in **Figure 5-3**. NIMS is able to detect 8.5 femtomoles of a synthetic phosphopeptide, and 85 attomoles with a S/N of greater than 3.

TiO<sub>2</sub> particles were synthesized from titanium (IV) tetraisopropoxide using a modified sol-gel method<sup>7</sup> and were characterized by SEM and energy dispersive X-ray spectroscopy (EDX) as shown in **Figure 5-4**. Particles were 0.5 ± 0.2 μm in diameter, and were greater than 95% Ti and O by mass. When the interactions between TiO<sub>2</sub> particles and the NIMS target were studied, it was observed that TiO<sub>2</sub> particles had very low affinity for the surface. Particles would rapidly flake off of the substrate. This makes sense chemically, as the perfluorinated BisF17 initiator on the NIMS surface is essentially ambiphobic. Studies on the development of a surface-based phosphopeptide affinity assay on the NIMS substrate were inconclusive for this reason. It is possible that use of the porous silicon target without the BisF17 initiator may circumvent this issue; however, this has not been explored to date.

Another route for phosphopeptide enrichment via NIMS (without TiO<sub>2</sub>) may be derivatization of the phosphorylation site with a perfluorinated tag which sticks to the NIMS initiator. This is a similar idea to that of Brittain *et al.*, who derivatized phosphopeptides with a perfluorinated tag and used a fluororous affinity column to purify them before MS analysis.<sup>8</sup> Due to the high specificity of fluorine-fluorine interactions, the authors were able to readily separate tagged peptides from complex biological matrices such as a Jurkat cell whole protein digest. It was also shown that tagged phosphopeptides fragmented normally for proper identification. Using the NIMS surface as both an affinity target and an ionization source would simplify sample preparation (on-chip washing, no elution step required) and improve MS analysis greatly.

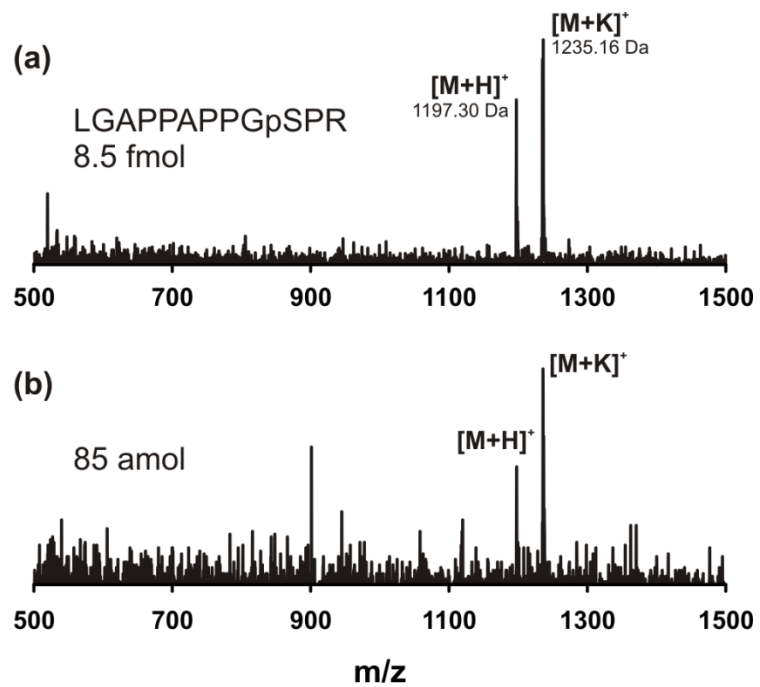


**Figure 5-3.** NIMS detection of LGAPPAPPGpSPR phosphopeptide at (a) 8.5 fmol and (b) 85 amol concentration. Peptide was detected using a Voyager DE-STR mass spectrometer in linear mode.

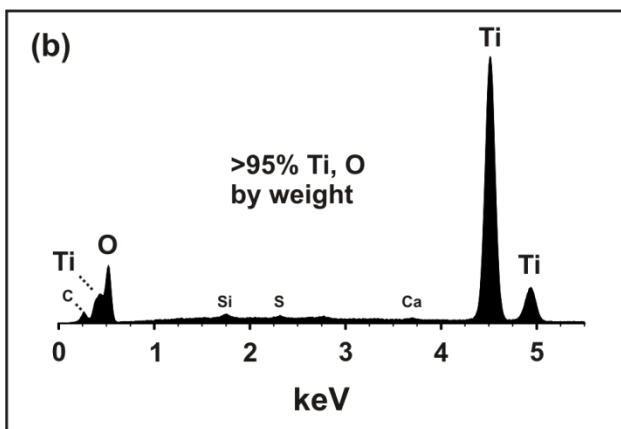
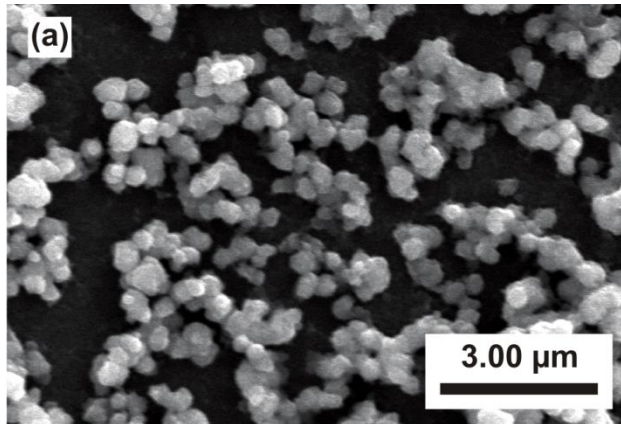


**Figure 5-4.** Characterization of synthesized  $\text{TiO}_2$  particles by (a) SEM and (b) EDX. EDX was performed with the assistance of Dr. Tony Hmelo.

## 5.4 Structural Analysis of Multimeric Polymer Precursor Materials

### *ESI Characterization of Multimers*

The experiments described in Chapter 4 for the analysis of methylenedianiline (MDA) isomers provide a specific roadmap for the analysis of larger MDA multimers. Early studies on larger forms of MDA confirm similar behavior between the dimeric species and the multimers. However, one minor difference has been observed. Multimeric species such as the MDA trimer (**Figure 5-5**) and tetramer ionize as  $[M+H]^+$  similar to MDA dimers, however they also tend to cationize readily as well (e.g.  $[M+Na]^+$  ions) as shown in **Figure 5-6**. Future studies on MDA multimers will focus on cation affinities and the resulting gas-phase stability of the complexes in order to differentiate isobaric structures.

Likewise, complex MDA mixtures of multimers will be analyzed using structural MS. Using the Synapt G2 and G2-S mass spectrometers, tandem MS may be performed after IM separation. This should allow for the separation of isomeric structures by either protonation site or cation affinity, and then differentiation by tandem MS patterns. It is likely this analytical approach will prove useful for not only MDA but also methyl diphenyl diisocyanate (MDI) and even simple polyurethane polymers.

### *MALDI Characterization of MDA Dimers*

Additionally, MDA dimers were analyzed using MALDI. Samples were dissolved for MALDI analysis at a concentration of 1 mg/mL in 9:1 methanol:water containing 0.1% formic acid (v/v). After experimenting with several matrices, CHCA matrix was chosen due to its minimal overlap with MDA signals. CHCA matrix was dissolved at a concentration of 10 mg/mL in 2:1 acetonitrile to water. When metal salts were used, each was at a concentration of 1 mg/mL in the 9:1 methanol to water solvent. Sample, matrix, and cation solutions were then mixed in a 4:5:1 ratio. Traveling-wave mass spectrometers use a frequency-tripled Nd:YAG laser which emit 355 nm ultraviolet light at a 1 kHz pulse repetition rate. Laser attenuation ranged from 200 to 280 (arbitrary units). TOF calibration was performed using CHCA matrix cluster peaks and peptides.

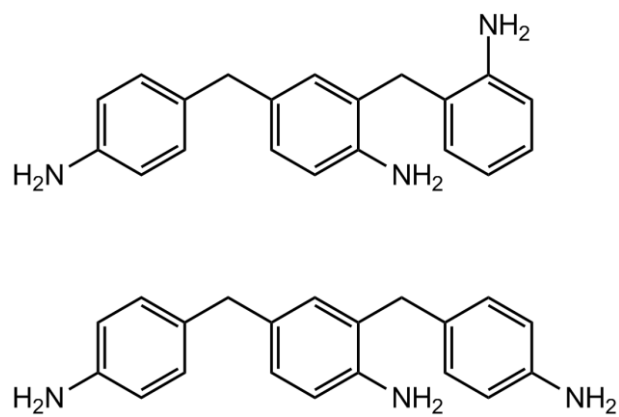


**Figure 5-5.** Two (of eight potential) isobaric trimer structures. To see all unique structures, please consult reference 9.

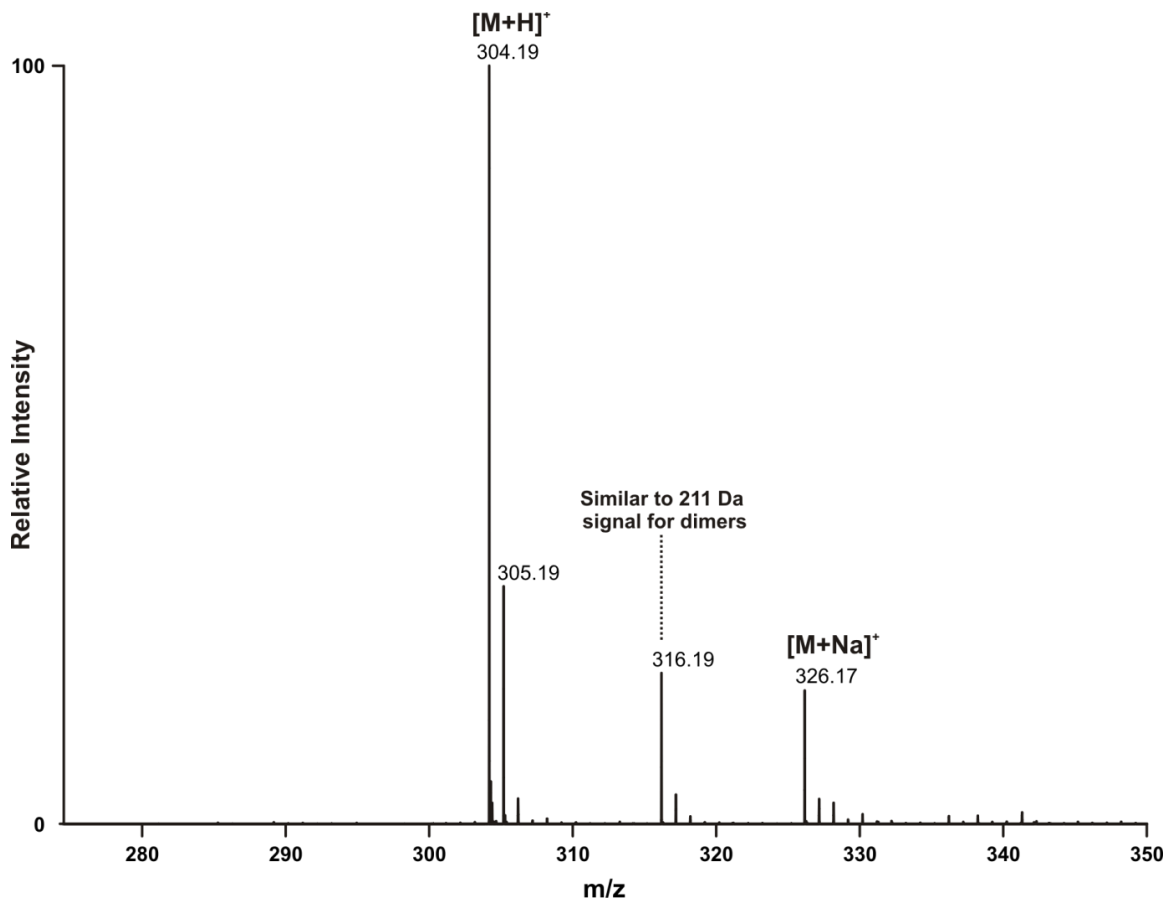
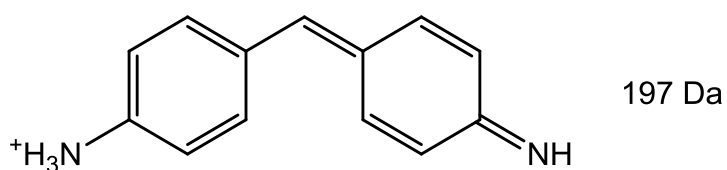
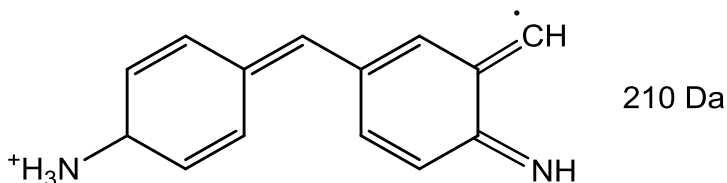
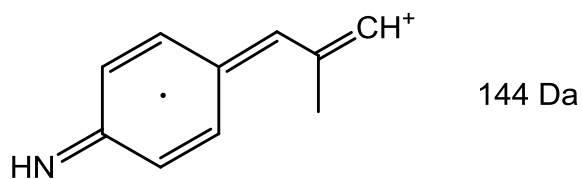


**Figure 5-6.** Zoomed-in mass spectrum of MDA trimer species using ESI. It is likely the 316 Da signal corresponds to the 211 Da signal shown in **Fig. 4-3** with an additional ring. However, more experiments are necessary to confirm this. The trimer also shows a fairly significant  $[M+Na]^+$  signal.

For MALDI data, significant formation of cationized dimers such as  $[M+Na]^+$  was not observed. This was similar to ESI data. Additionally, 4,4'-MDA generated a stronger  $[M+H]^+$  signal and less 106 Da fragmentation than either 2,2'-MDA or 2,4'-MDA. Unlike ESI data, however, the base peak of the 4,4'-MDA spectrum is not the  $[M+H]^+$  signal but instead the  $[M-H]^+$  signal (197 Da). 2,4'-MDA also generated an intense  $[M-H]^+$  signal in MALDI, and showed less fragmentation to 106 Da than in ESI. Of the three isomers, 2,2'-MDA generated the weakest molecular ion signal for all three ions. Tandem MS data for the 197 Da signal is shown in **Figure 5-7**. From the 4,4'-MDA sample, this signal likely corresponds to the following structure:



Many of the possible fragment ion structures for this signal match those shown in **Table 4-1** in Chapter 4. However, the structure(s) of 197 Da signals from 2,2'-MDA and 2,4'-MDA are unclear. The tandem mass spectra show signals with higher  $m/z$  than the parent ion, suggesting ion chemistry is occurring in the MS instrumentation (after quadrupole isolation). Several additional signals were observed in the MALDI-TOFMS spectra as well, including 144 Da and 210 Da. It is likely these are also byproducts of MALDI-induced ion chemistry. Possible structures for the 144 Da and 210 Da signals are presented below:





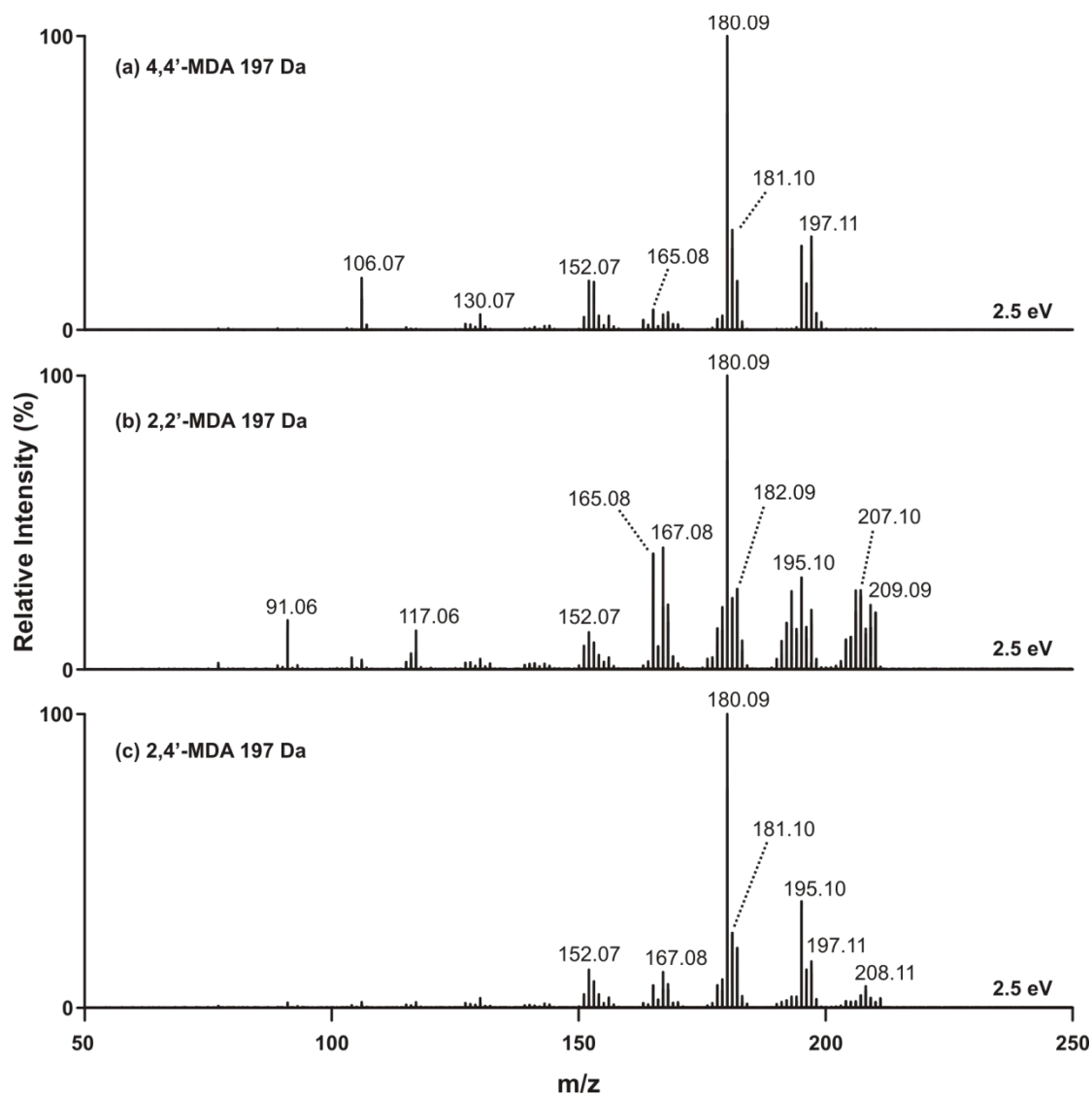


**Figure 5-7.** Tandem mass spectra for 197 Da observed in the MALDI spectrum of each isomer. A center-of-mass collision energy of 2.5 eV was applied (20 eV lab-frame).

It is unclear whether these signals originate from MDA or the MDA-CHCA matrix adducts. Further investigation into the effects of MALDI ionization on MDA isomers by IM-MS and IM-MS/MS is needed.

## 5.5 References

1. Rubakhin, S. S.; Romanova, E. V.; Nemes, P.; Sweedler, J. V. Profiling Metabolites and Peptides in Single Cells. *Nat. Methods* **2011**, *8*, S20-S29.
2. Giancoli, D. C. *Physics for Scientists and Engineers: 3<sup>rd</sup> Edition*; Prentice Hall: Upper Saddle River, 2000.
3. Becker, J. S.; Gorbunoff, A.; Zoriy, M.; Izmer, A.; Kayser, M. Evidence of Near-field Laser Ablation Inductively Coupled Plasma Mass Spectrometry (NF-LA-ICP-MS) at Nanometre Scale for Elemental and Isotopic Analysis on Gels and Biological Samples. *J. Anal. Atom. Spectrom.* **2006**, *21*, 19-25.
4. Zoriy, M. V.; Kayser, M.; Becker, J. S. Possibility of Nano-local Element Analysis by Near-field Laser Ablation Inductively Coupled Plasma Mass Spectrometry (LA-ICP-MS): New Experimental Arrangement and First Application. *Int. J. Mass Spectrom.* **2008**, *273*, 151-155.
5. Lo, C.-Y.; Chen, W.-Y.; Chen, C.-T.; Chen, Y.-C. Rapid Enrichment of Phosphopeptides from Tryptic Digests of Proteins Using Iron Oxide Nanocomposites of Magnetic Particles Coated with Zirconia as the Concentrating Probes. *J. Proteome Res.* **2007**, *6*, 887-893.
6. Thingholm, T. E.; Jorgenson, T. J. D.; Jensen, O. N.; Larsen, M. R. Highly Selective Enrichment of Phosphorylated Peptides using Titanium Dioxide. *Nat. Protoc.* **2006**, *1*, 1929-1935.
7. Eiden-Assmann, S.; Widoniak, J.; Maret, G. Synthesis and Characterization of Porous and Nonporous Monodisperse Colloidal TiO<sub>2</sub> Particles. *Chem. Mater.* **2004**, *16*, 6-11.
8. Brittain, S. M.; Ficarro, S. B.; Brock, A.; Peters, E. C. Enrichment and Analysis of Peptide Subsets using Fluorous Affinity Tags and Mass Spectrometry. *Nat. Biotech.* **2005**, *23*, 463-468.
9. Kwiecien, N. W. Characterization of Methylene Dianiline Synthesis using Advanced Mass Spectrometry Techniques. Undergraduate Honors Thesis, Vanderbilt University, Nashville, TN, 2012.

## APPENDIX

### A. **Protocol for Fabrication of NIMS Substrates**

#### **Cutting**

- (1) Use low resistivity (0.01  $\Omega$ ), p-type (B-doped) < 1 0 0 > silicon wafers
- (2) Use an O-ring to line up area needed for etching apparatus
- (3) Scratch (dull side) edges with diamond tip pen
  - i. Work parallel to cut flat planes

#### **Cleaning** (perform in fume hood)

- (1) Rinse cut wafers with DI H<sub>2</sub>O multiple times
- (2) Dry with nitrogen gas
- (3) Put chips (shiny side up) on the bottom of a large labeled glass beaker
- (4) Slowly add 20mL conc. H<sub>2</sub>SO<sub>4</sub> to beaker
- (5) Slowly add 10mL 30% H<sub>2</sub>O<sub>2</sub>, solution will become hot, give off fumes
  - i. Let piranha soak for 30 minutes
  - ii. **Note:** Piranha solution (2:1 H<sub>2</sub>SO<sub>4</sub>: H<sub>2</sub>O<sub>2</sub>) breaks down traces of organic material. It is explosive upon contact with organic solvents (i.e. acetone, ethanol, *etc.*). Always use stainless steel tweezers and glass beakers, no plastic. Also, do not store hot piranha solution, it will explode due to gas pressure buildup.  
**Always let a (labeled) piranha beaker cool for 24 hours before storage/removal.**
- (6) Remove each wafer with **stainless steel** tweezers one by one, rinsing thoroughly with DI H<sub>2</sub>O and drying with nitrogen (**3x per wafer**).

**Etching** (perform in fume hood)

- i. **Note:** HF is an extremely hazardous chemical. **Consult an HF MSDS sheet before etching. While etching, one should use caution and should be wearing a lab coat, goggles and nitrile gloves (I wear two layers and change the outer layer frequently).** Keep the hood as low as you can while working comfortably. Also, do not use glass beakers with HF, only plastic tweezers, beakers and containers. Know where the calcium gluconate gel is located before you begin.
- (1) Make a 25% HF solution as follows:
    - i. Add 20mL ethanol to plastic bottle. Add 20mL 50% HF solution to bottle. Label bottle "25% HF in EtOH" with name and date. Again, be very careful with HF solutions.
  - (2) Set up Teflon etching apparatus. The easiest way is to put the wafer on the base (w/ O-ring) upside down, put on the silver foil, flip right-side up and slide on. **Make sure silver base electrode is flat on bottom so no leaking occurs.** Tighten, but not too hard.
  - (3) Using plastic droppers, add 25% HF solution to well until base level is completely submerged.
  - (4) Attach **red wire to gold base electrode** and **black wire to platinum wire** electrode. Turn off light in hood.
  - (5) Using LABview software, run etching experiment of choice. Films require 2 phases, a consistent etching phase and high-current, short timescale pulses to break off the bottom layer.
  - (6) Etching procedures:
    - i. **Wafer:** Etch with 24 mA/cm<sup>2</sup> for 600 seconds.
    - ii. **Film:** Etch with 24 mA/cm<sup>2</sup> for 600 seconds. Then etch with 250 mA/cm<sup>2</sup> for 1.7 seconds on, 1.7 seconds off. Repeat 2x. Wait a

minute, then etch with  $210 \text{ mA/cm}^2$  for 1.7 seconds on, 6 seconds off. Repeat 8-10x as needed.

- (7) After etching is complete, remove wires. Remove HF solution with plastic dropper and place in HF waste. Rinse cell with ethanol (**3x minimum**), putting washings in the HF waste beaker. When rinsing films, do not spray ethanol straight on the wafer, but around the edges of the basin. Films will break when sprayed directly.
  - i. **Wafer:** Dismantle cell and rinse wafer with ethanol, dry with nitrogen (**3x**). Place wafer in oven @  $60^\circ \text{C}$  for 5 minutes.
  - ii. **Film:** Dismantle cell so that wafer sits on top. Using plastic tweezers, carefully crack the edges around the circle to break off the film. Fill a petri dish halfway with ethanol, place ITO-coated slide in the dish and carefully transfer film onto the slide. Let dry for a few minutes, you may use a **very** light stream of nitrogen to aid drying. Then place in oven @  $60^\circ \text{C}$  for 5 minutes.
- (8) Let wafer or film sit (covered) for 24+ hours to ensure full oxidation before the next step.

#### **Initiator Loading** (perform in fume hood)

- (1) Continuously spot and remove from surface 1% (by volume)  $\text{HNO}_3$  solution. Be careful not to rinse edges heavily or else film may detach from ITO glass slide.
- (2) Using  $100 \mu\text{L}$  micropipette, spot  $50\text{-}60 \mu\text{L}$  (wafer) or  $20\text{-}30 \mu\text{L}$  (small film) initiator onto porous silicon.
  - i. Let sit in a hood for 45 minutes to 1 hour.
- (3) Remove excess initiator with nitrogen (in the hood). When drying a film, be careful not to use too much pressure or else film will crack and break. The wafers are more stable.
- (4) Dry with nitrogen, use a heat gun (setting 2-4, pointed at the back of the wafer/film, not the top) for 3 to 5 seconds. Repeat this step 3x.

i. Note: You should be able to see the excess initiator remove.

After three drying steps, wafer/film should appear dry.

(5) Let sit for a few minutes before use.

(6) Commonly used initiators are fluorinated compounds. Excess initiator should be collected in a petri dish, absorbed, and stored as solid halogenated waste.

**B. Protocol for SEM of NIMS Substrates**

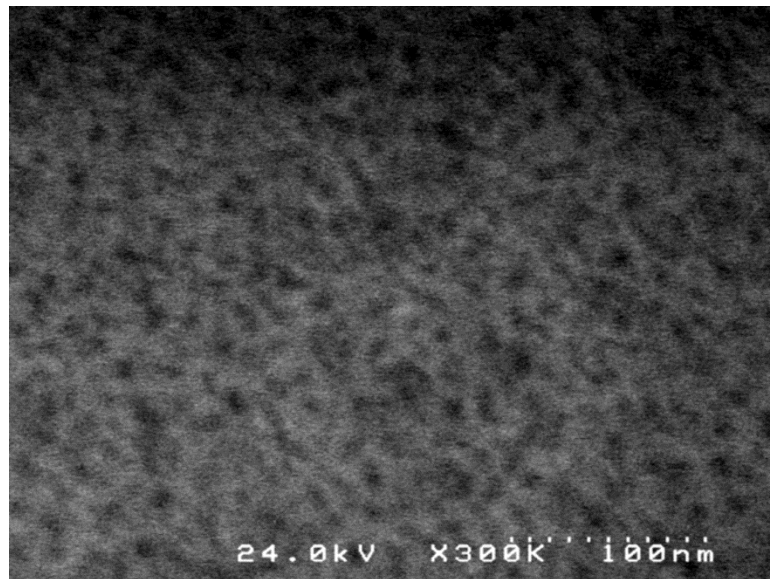
- (1) When imaging *p*-type porous silicon, try to obtain a SEM image with a scale bar around 200 to 300 nm long (approximately 100,000 magnification) to see pores but also capture a large number.
- (2) Open image in ImageJ.
- (3) Optimize pore / background contrast using PROCESS → SMOOTH or SHARPEN and/or IMAGE → ADJUST → BRIGHTNESS/CONTRAST.
- (4) Calibrate image scale with pixels from image. Draw a line across the scale bar on the image. Click on ANALYZE → SET SCALE. The length of the line is already measure in pixels (DISTANCE IN PIXELS). Change KNOWN DISTANCE to distance given next to the image's scale bar, and change UNIT OF LENGTH to nm. Click GLOBAL to apply scale to all images which come from the original image. Scale will have to be readjusted for new images.
- (5) In order to select for pores, use or IMAGE → ADJUST → THRESHOLD. Press APPLY when black pores are only region not highlighted. A black and white image will be created.
- (6) Remove very small / unclear pores by PROCESS → FILTER → MEDIAN. Adjust PIXEL RADIUS as desired and press PREVIEW before removing them.
- (7) Create defined edges for the pores using PROCESS → FIND EDGES.
- (8) Click on ANALYZE → SET MEASUREMENTS. Select FERET'S DIAMETER, LIMIT TO THRESHOLD, SCIENTIFIC NOTATION, DISPLAY LABEL. Feret's Diameter is like a caliper which measures the distance across the pore.



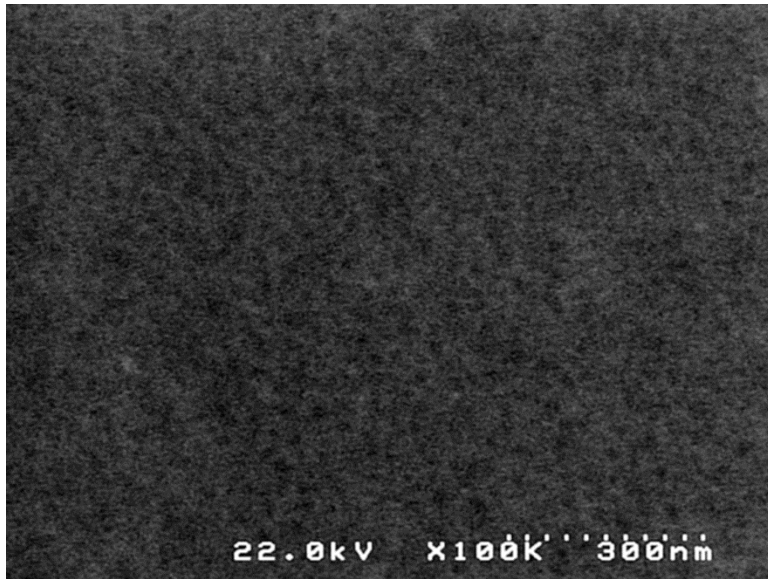
- (9) Click on ANALYZE → ANALYZE PARTICLES. On the SHOW scrollbar, select ELLIPSES. Also check the DISPLAY RESULTS and CLEAR RESULTS (prior ones, if necessary).
- (10) RESULTS pop-up will contain data. The column labeled FERET will contain pore diameters. Within the RESULTS tab, click EDIT → SUMMARIZE to see average, standard deviation, minimum and maximum diameters. RESULTS tab can be saved as an .xls file to be viewed in Microsoft Excel.

**C. SEM Images of NIMS Substrates**

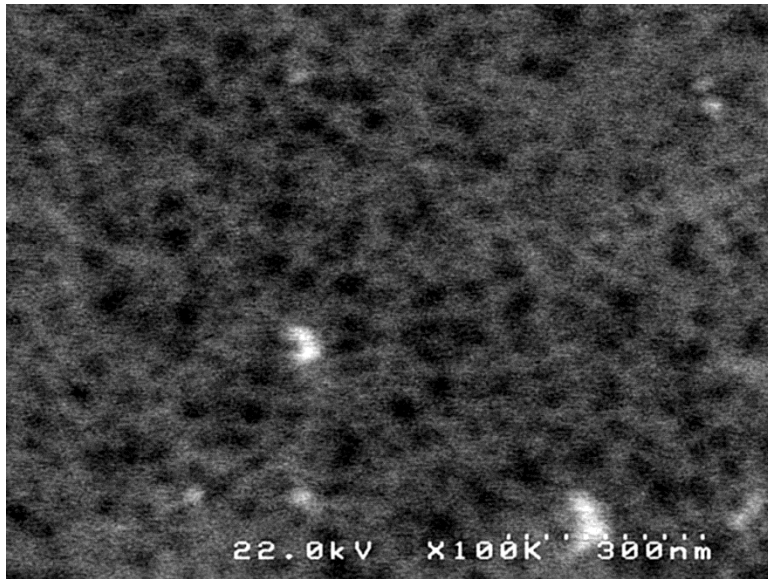
*SEM Images Obtained on Hitachi S-4200 Microscope (Film #1 - #9)*



**Film #1.**



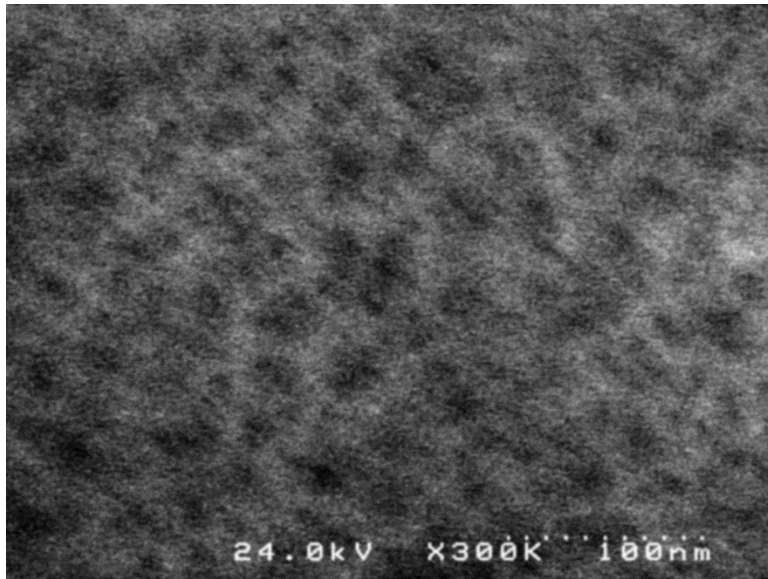
Film #2.



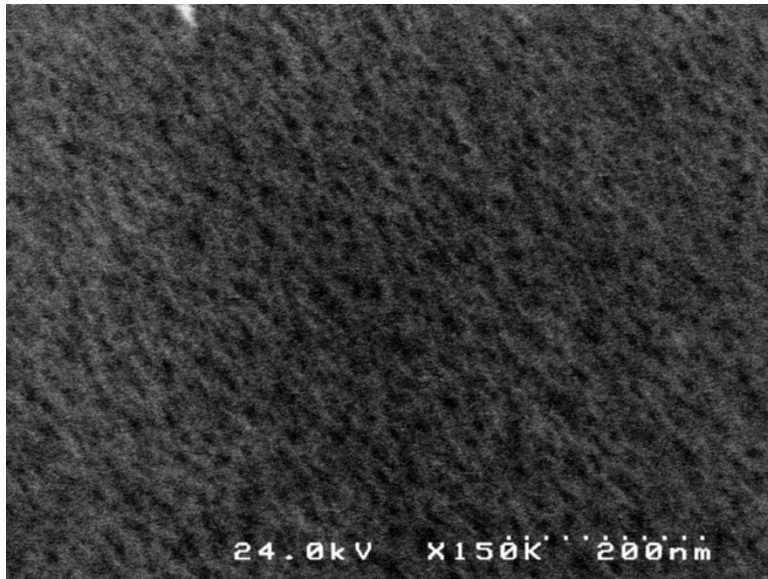
Film #3.



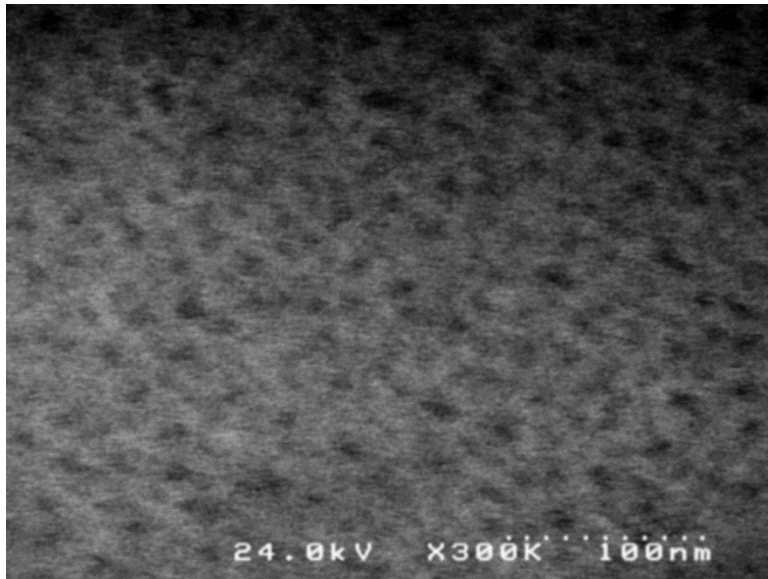
Film #4.



Film #5.

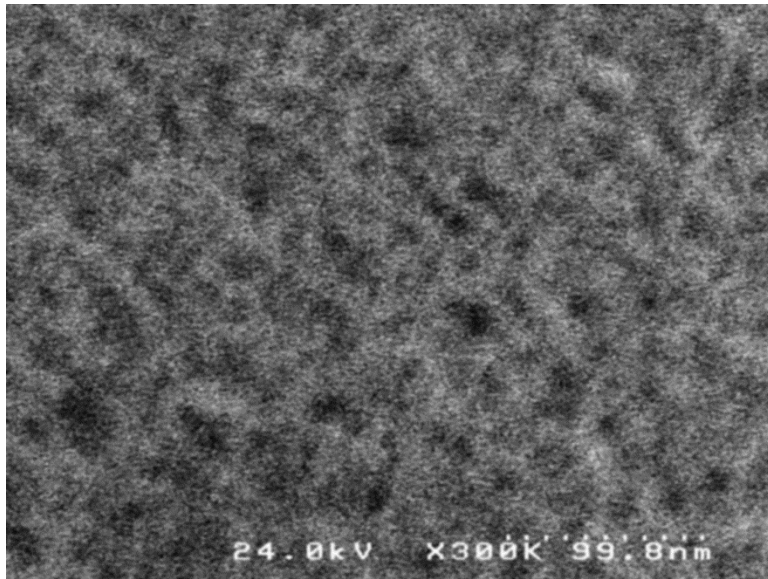


Film #6.

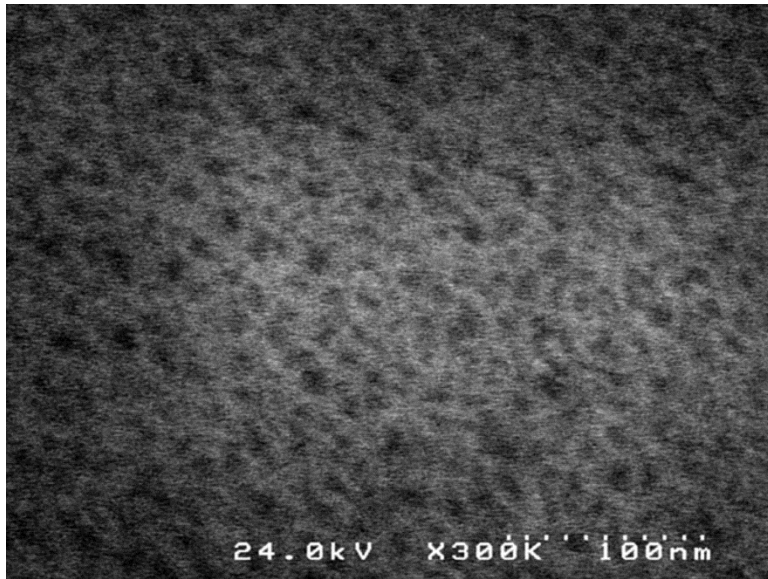


**Film #7.**

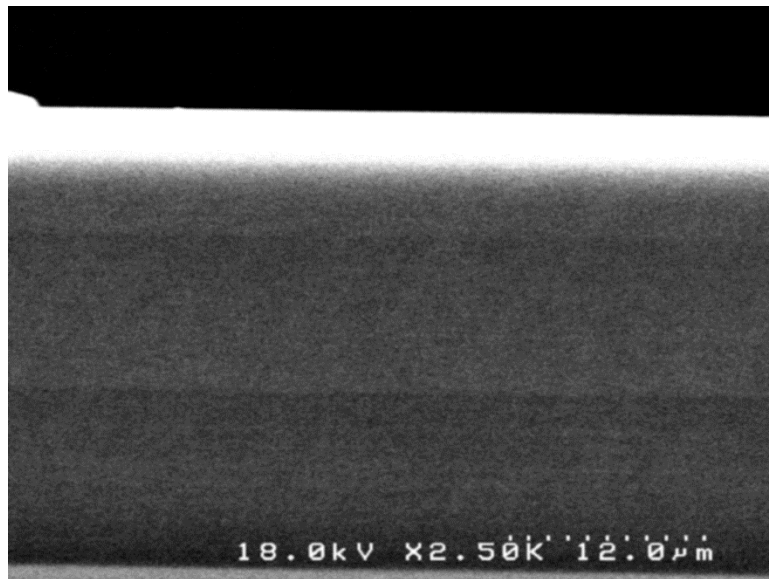




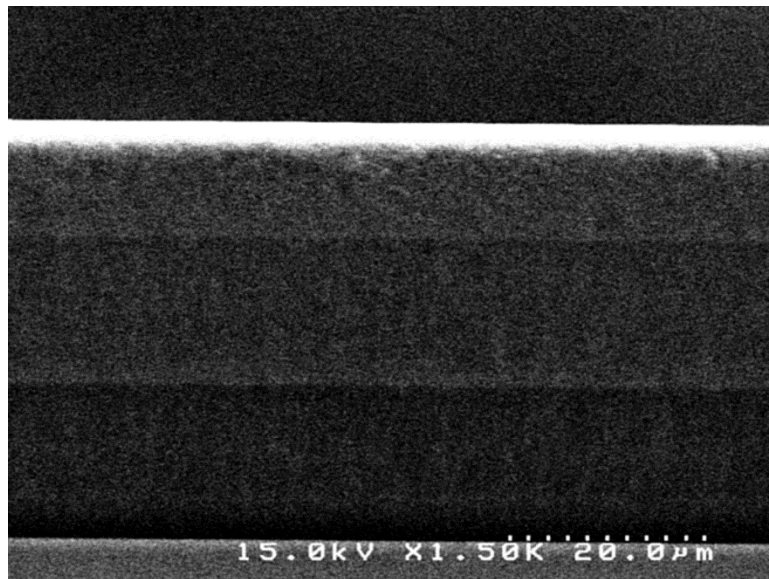
**Film #8.**



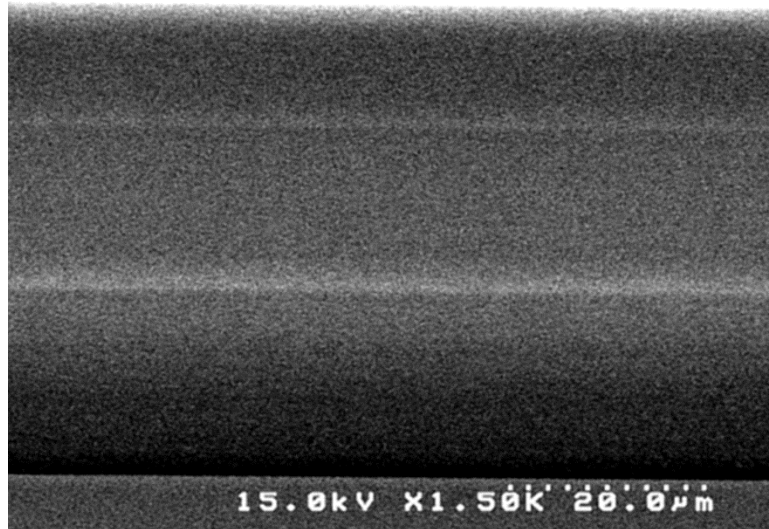
**Film #9.**



Side-view (300 s films).

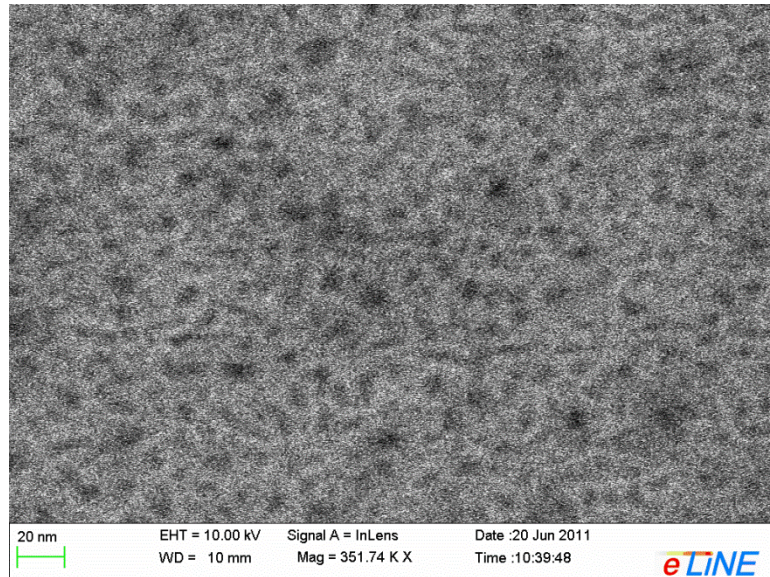


**Side-view (450 s films).**

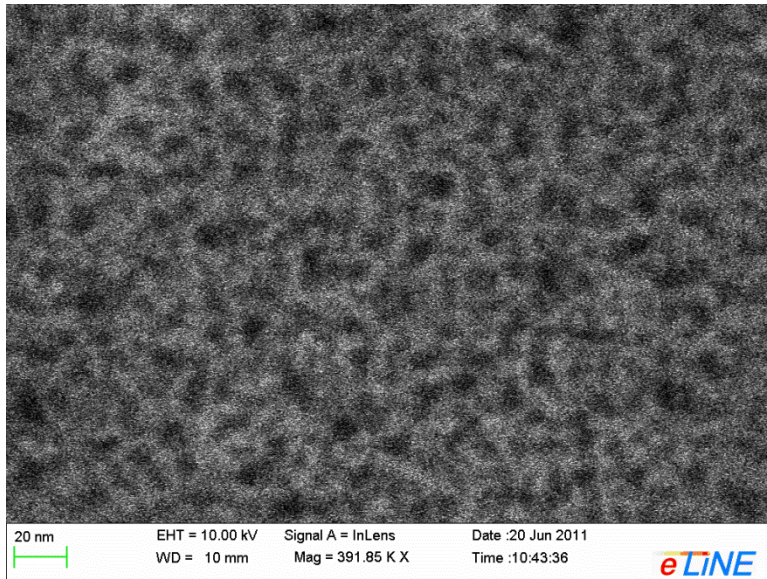


**Side-view (600 s films).**

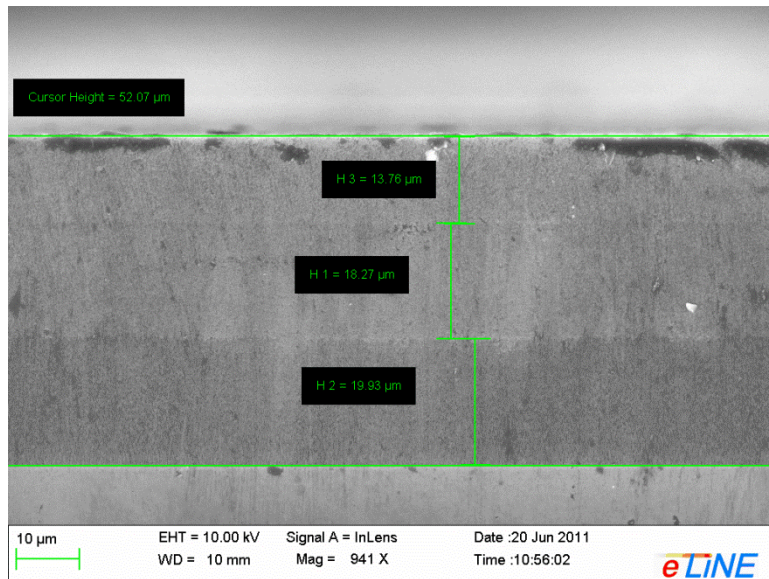
*High-resolution SEM Images Obtained on Raith e-Line (Courtesy of Judson Ryckman)*



**Top-view.**

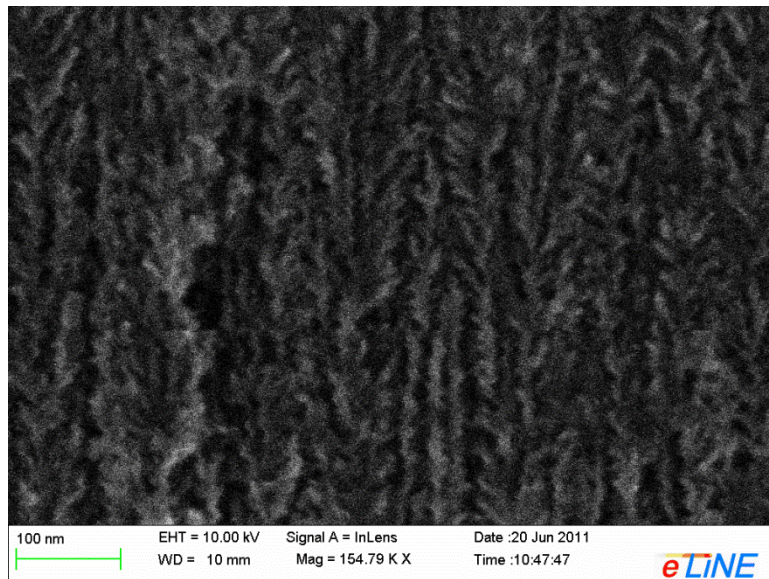


**Top-view (2).**

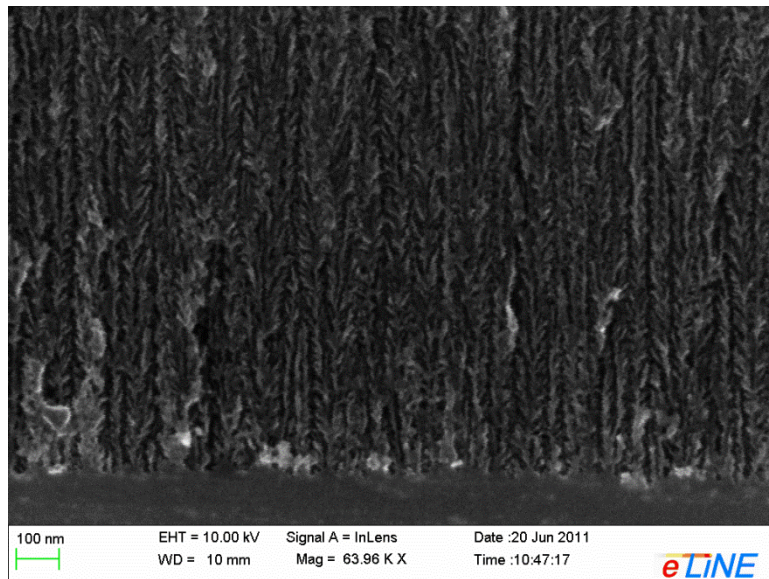


Side-view (zoom out).





**Cross-sectional view (zoom in).**



**Cross-sectional view (zoom in 2).**

## D. NIMS Supplemental Material

### Materials and Methods

Novel compounds were synthesized by Plamen Christov from the VICB Chemical Synthesis Core. All commercial chemicals were of the highest quality available and used without further purification. The reactions were monitored by thin layer chromatography (TLC) on Merck silica gel 60 F<sub>254</sub> plates, visualization with 254 nm UV light.

### NMR Spectroscopy (VICB Core)

<sup>1</sup>H, <sup>13</sup>C and <sup>19</sup>F NMR spectra were recorded on Bruker NMR spectrometers operating at 400, 100 and 380 MHz, respectively, in the indicated solvents. Chemical shifts are noted below.

*Synthesis of (E)-4-(3,3,4,4,5,5,6,6,7,7,8,8,9,9,10,10,10-heptafluorodecyl)benzyl 3-(4-hydroxy-3,5-dimethoxyphenyl)acrylate (VU0470056, or SA-56).*

In a flame dried flask, sinapic acid (100 mg, 0.446 mmols) was added, followed by addition of dry tetrahydrofuran (8 mL). Triphenyl phosphine (118 mg, 0.446 mmols) and 4-(3,3,4,4,5,5,6,6,7,7,8,8,9,9,10,10,10-heptafluorodecyl)benzyl alcohol (247 mg, 0.446 mmols) were added at room temperature. After stirring at room temperature for 15 min, diisopropyl azodicarboxylate (88  $\mu$ L, 0.446 mmols) was added and the reaction mixture was stirred at room temperature overnight. The solvent was removed and the residue was purified by ISCO flash chromatography (hexane and ethyl acetate; 0-5% ethyl acetate for 15 min). Obtained 150 mg of solid product (30%). <sup>1</sup>H-NMR (DMSO-<sub>d6</sub>)  $\delta$  7.58 (d, 1 H, J = 16 Hz), 7.36 (s, 4H), 7.03 (s, 2H), 6.58 (d, 1H, J = 16Hz), 5.17 (s, 2H), 3.79 (s, 6H), 2.91-2.87 (m, 2H), 2.67-2.52 (m, 2H); <sup>13</sup>C NMR(Acetone-<sub>d6</sub>)  $\delta$  166.3, 147.9, 145.4, 139.1, 138.5, 135.1, 128.5, 125.1, 114.8, 105.9, 65.1, 55.7, 32.1, 25.6; <sup>19</sup>F NMR (Acetone-<sub>d6</sub>)  $\delta$  -126.7, -123.9, -123.2, -122.4, -122.2, -114.8, -81.6.

*Synthesis of 4-(3,3,4,4,5,5,6,6,7,7,8,8,9,9,10,10,10-heptadecafluorodecyl)benzyl 2,5-dihydroxybenzoate (VU0470057, or DHB-57).*

In a flame dried flask, 2,5-dihydroxybenzoic acid (50 mg, 0.324 mmols) was added, followed by addition of dry tetrahydrofuran (8 mL). Triphenyl phosphine (85 mg, 0.324 mmols) and 4-(3,3,4,4,5,5,6,6,7,7,8,8,9,9,10,10,10-heptadecafluorodecyl)benzyl alcohol (179 mg, 0.324 mmols) were added at room temperature. After stirring at room temperature for 15 min, diisopropyl azodicarboxylate (64  $\mu$ L, 0.324 mmols) was added and the reaction mixture was stirred at room temperature overnight. The solvent was removed and the residue was purified by ISCO flash chromatography (hexane and ethyl acetate; 0-5% ethyl acetate for 15 min). Obtained 165 mg of solid product (74%).  $^1\text{H-NMR}$  ( $\text{DMSO-}d_6$ )  $\delta$  7.42 (d, 1H, J = 8 Hz), 7.37 (d, 1H, J = 8 Hz), 7.15 (d, 1H, J = 4 Hz), 6.97 (dd, 1H,  $J_1$  = 4Hz,  $J_2$  = 8Hz), 6.83 (d, 1H, J = 8Hz), 5.34 (s, 2H), 2.92-2.88 (m, 2H), 2.58-2.54 (m, 2H);  $^{13}\text{C-NMR}$  ( $\text{Acetone-}d_6$ )  $\delta$  170.3, 155.5, 150.0, 140.3, 134.8, 129.4, 124.4, 118.7, 114.7, 112.6, 67.2, 32.8, 26.4;  $^{19}\text{F NMR}$ ( $\text{Acetone-}d_6$ )  $\delta$  -126.7, -123.9, -123.2, -122.4, -122.2, -114.8, -81.6.

*Synthesis of 2-hydroxy-5-((4,4,5,5,6,6,7,7,7-nonafluoroheptyl)oxy)benzoic acid (VU0470058, or DHB-58).*

In a flame dried flask, 2,5-dihydroxybenzoic acid (50 mg, 0.324 mmols) was added, followed by addition of dry dimethylformamide (7 mL). Sodium hydride (28 mg, 0.712 mmols) was added at room temperature, followed immediately with addition of 3-(perfluorobutyl)propyl iodide (75  $\mu$ L, 0.356 mmols). After stirring at room temperature for 2h, the reaction mixture was cooled down, water (5 mL) and neutralized with hydrochloric acid (0.1 M). Ethyl acetate (75 mL) was added and the organic layers were washed with water (3 x 50 mL). The organic layers were dried over anhydrous magnesium sulfate, filtered and removed in vacuum. The residue was purified by ISCO flash chromatography (methylene chloride and methanol; 0-25% methanol for 15 min). Obtained 84 mg of solid product (62%).  $^1\text{H-NMR}$  ( $\text{DMSO-}d_6$ )  $\delta$  7.27 (d, 1H, J = 4 Hz), 7.15 (dd, 1H,  $J_1$  = 4Hz,  $J_2$  = 8 Hz), 6.98 (d, 1H, J = 8 Hz), 4.03 (tr, 2H, J = 4 Hz), 2.44-2.33 (m, 2H), 2.00-1.91

(m, 2H);  $^{13}\text{C}$  NMR(Acetone- $d_6$ ) 172.4, 157.3, 152.0, 125.2, 119.8, 119.7, 199.0, 114.6, 113.1, 67.9, 28.25, 21.3;  $^{19}\text{F}$  NMR(Acetone- $d_6$ )  $\delta$  -126.7, -124.9, -115.0, -81.9.

*Synthesis of 4-((4,4,5,5,6,6,7,7,8,8,9,9,10,10,11,11,11-heptadecafluoroundecyl)oxy)benzyl 2,5-dihydroxybenzoate (VU0470059, or DHB-59).*

In a flame dried flask, 2,5-dihydroxybenzoic acid (50 mg, 0.324 mmols) was added, followed by addition of dry tetrahydrofuran (8 mL). Triphenyl phosphine (85 mg, 0.324 mmols) and 4-[3-(perfluorooctyl)-1-propyloxy]benzyl alcohol (190 mg, 0.324 mmols) were added at room temperature. After stirring at room temperature for 15 min, diisopropyl azodicarboxylate (64  $\mu\text{L}$ , 0.324 mmols) was added and the reaction mixture was stirred at room temperature overnight. The solvent was removed and the residue was purified by ISCO flash chromatography (methylene chloride and methanol; 0-5% methanol for 15 min). Obtained 94 mg of solid product (40%).  $^1\text{H}$ -NMR (DMSO- $d_6$ )  $\delta$  7.42 (d, 1 H, J = 8 Hz), 7.13 (d, 1H, 3 Hz), 6.99 (d, 1H, J = 8Hz), 6.95 (d, 1H, J= 3Hz), 6.82 (d, 1H, J = 8 Hz), 5.23 (s, 2H), 4.09 (tr, 2H, J = 4 Hz), 2.44-2.33 (m, 2H), 2.03-1.92 (m, 2H),  $^{13}\text{C}$ -NMR (Acetone- $d_6$ )  $\delta$  170.9, 160.0, 155.0, 150.5, 131.3, 129.0, 125.1, 118.9, 115.5, 115.0, 113.0, 67.6, 67.2, 28.3, 21.3,  $^{19}\text{F}$  NMR(Acetone- $d_6$ )  $\delta$  -126.6, -123.9, -123.2, -122.3, -114.7, -81.6.

*Synthesis of (E)-2-cyano-N-(4,4,5,5,6,6,7,7,8,8,9,9,10,10,11,11,11-heptadecafluoroundecyl)-3-(4-hydroxyphenyl)acrylamide. (VU0470060, or CHCA-60).*

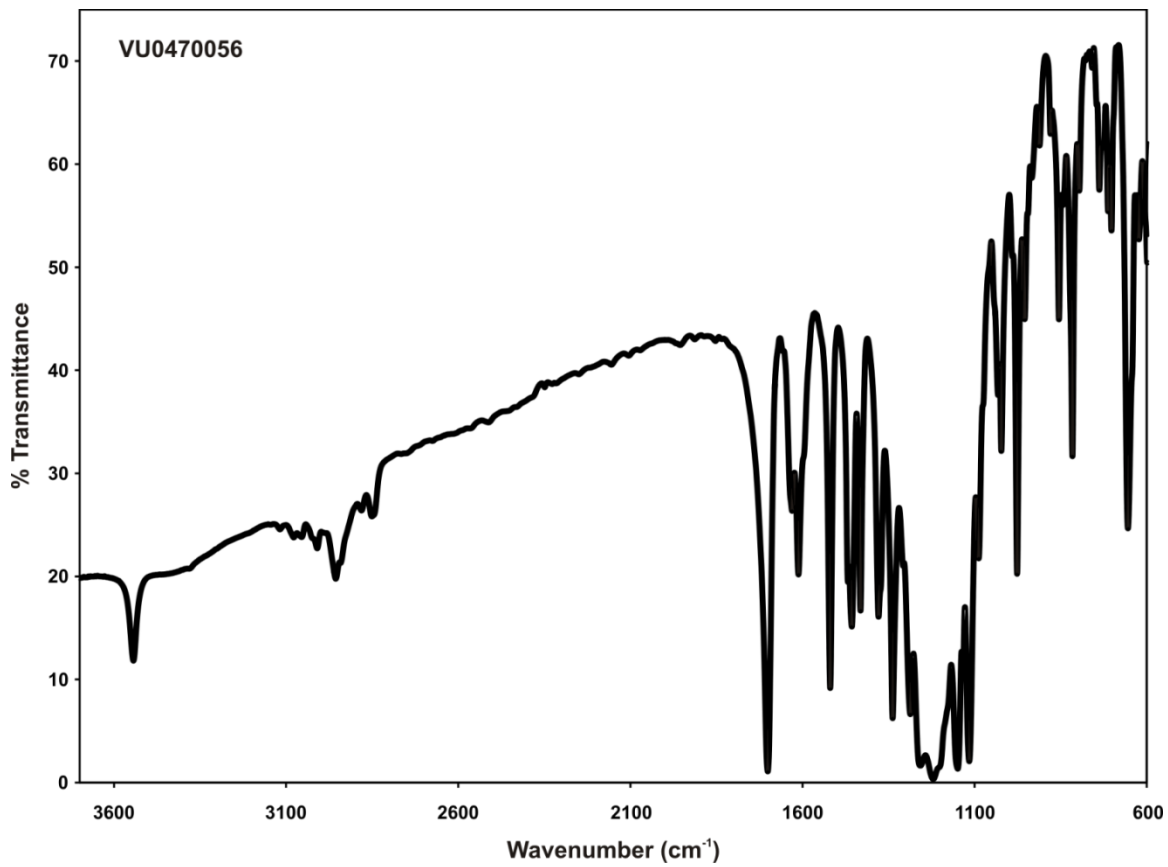
In a flame dried flask, alpha-cyano-4-hydroxycinnamic acid (50 mg, 0.264 mmols) was added, followed by addition of dry dimethylformamide (DMF, 7 mL), 1-ethyl-3-(3-dimethylaminopropyl)carbodiimide (EDC, 56 mg, 0.290 mmols), hydroxybenzotriazole (HOBt, 40 mg, 0.29 mmols) and triethylamine (TEA, 41  $\mu\text{L}$ , 0.29 mmols). After stirring for 15 min at room temperature, 3-(perfluorooctyl)propylamine (70  $\mu\text{L}$ , 0.237 mmols) was added and the reaction mixture was stirred overnight at room temperature. Ethyl acetate (75 ml) was added and the organic layers were washed with water (3 x 50 mL). The organic layers were dried over anhydrous magnesium sulfate, filtered and removed in vacuum. The residue was purified by

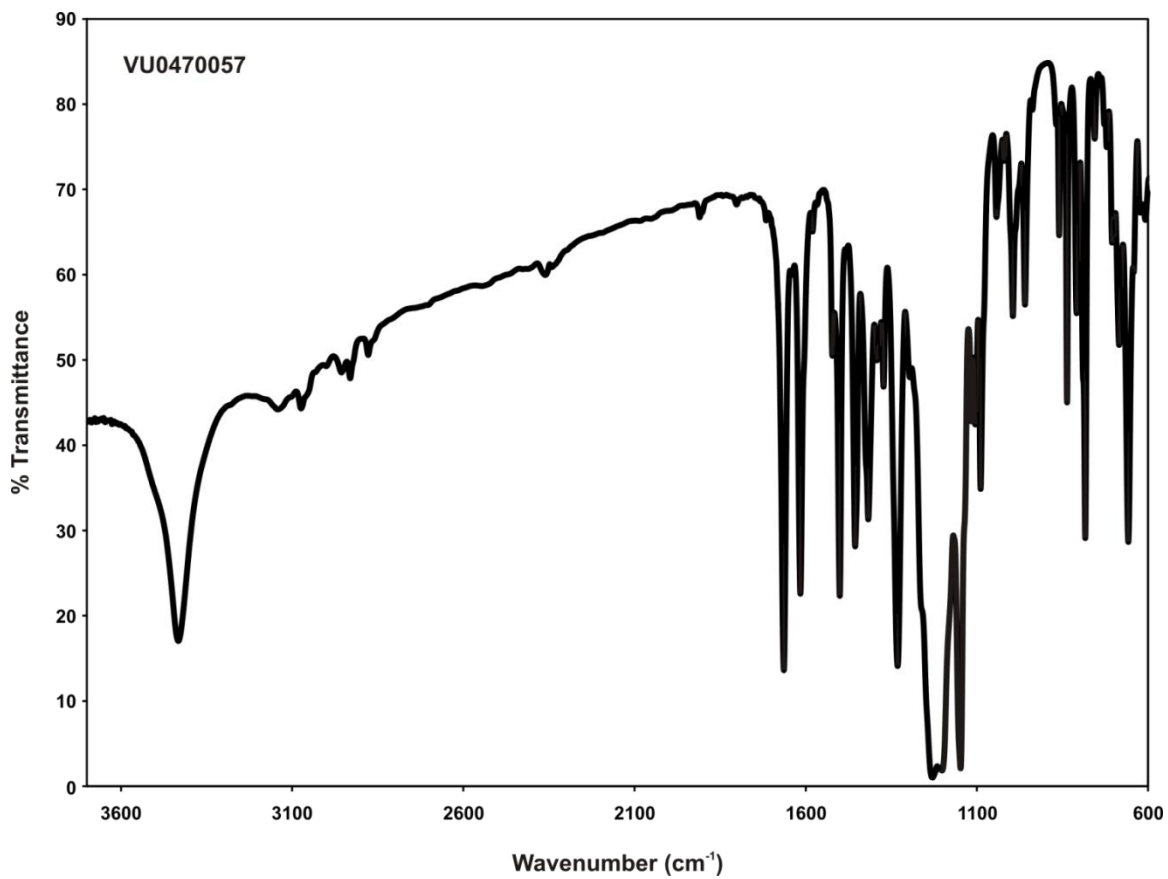
ISCO flash chromatography (methylene chloride and methanol; 0-10% methanol for 15 min). Obtained 100 mg of solid product (65% yield).  $^1\text{H-NMR}$  ( $\text{DMSO-}d_6$ )  $\delta$  8.37 (tr, 1 H,  $J = 4$  Hz), 8.02 (s, 1H), 7.85 (d, 1H,  $J = 8$  Hz), 6.90 (d, 1H,  $J = 8\text{Hz}$ ), 3.20 (tr, 2H,  $J = 4\text{Hz}$ ), 2.27-2.20 (m, 2H), 1.79-1.72 (m, 2H);  $^{13}\text{C-NMR}$  ( $\text{Acetone-}d_6$ )  $\delta$  162.3, 161.0, 151.8, 133.7, 124.5, 117.5, 116.7, 101.6, 39.6, 28.8, 21.1;  $^{19}\text{F NMR}$ ( $\text{Acetone-}d_6$ )  $\delta$  -126.7, -123.9, -123.2, -122.4, -122.2, -114.5, -81.6.

*Note:* all matrices were re-protonated using 0.1% formic acid in 99.9% ethanol (v/v).

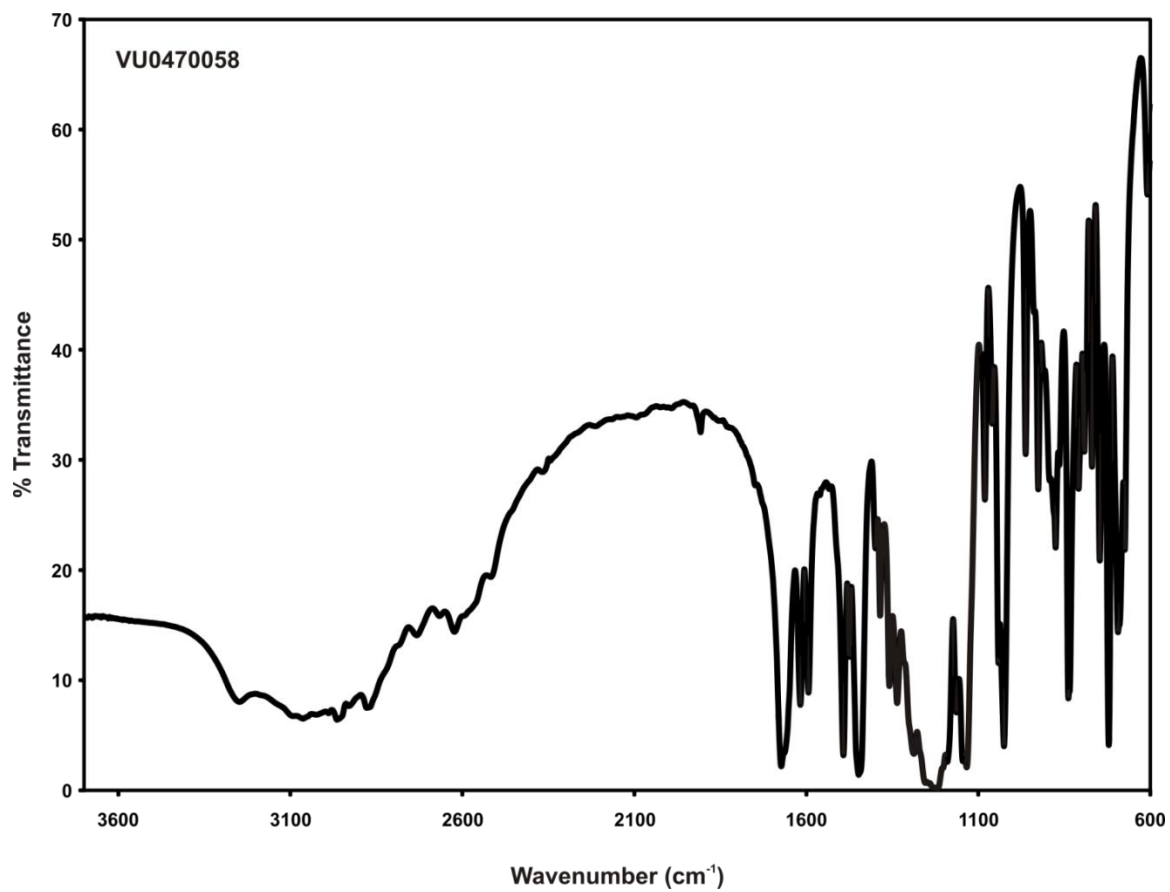
*IR spectroscopy data for 5 compounds (McLean Lab)*

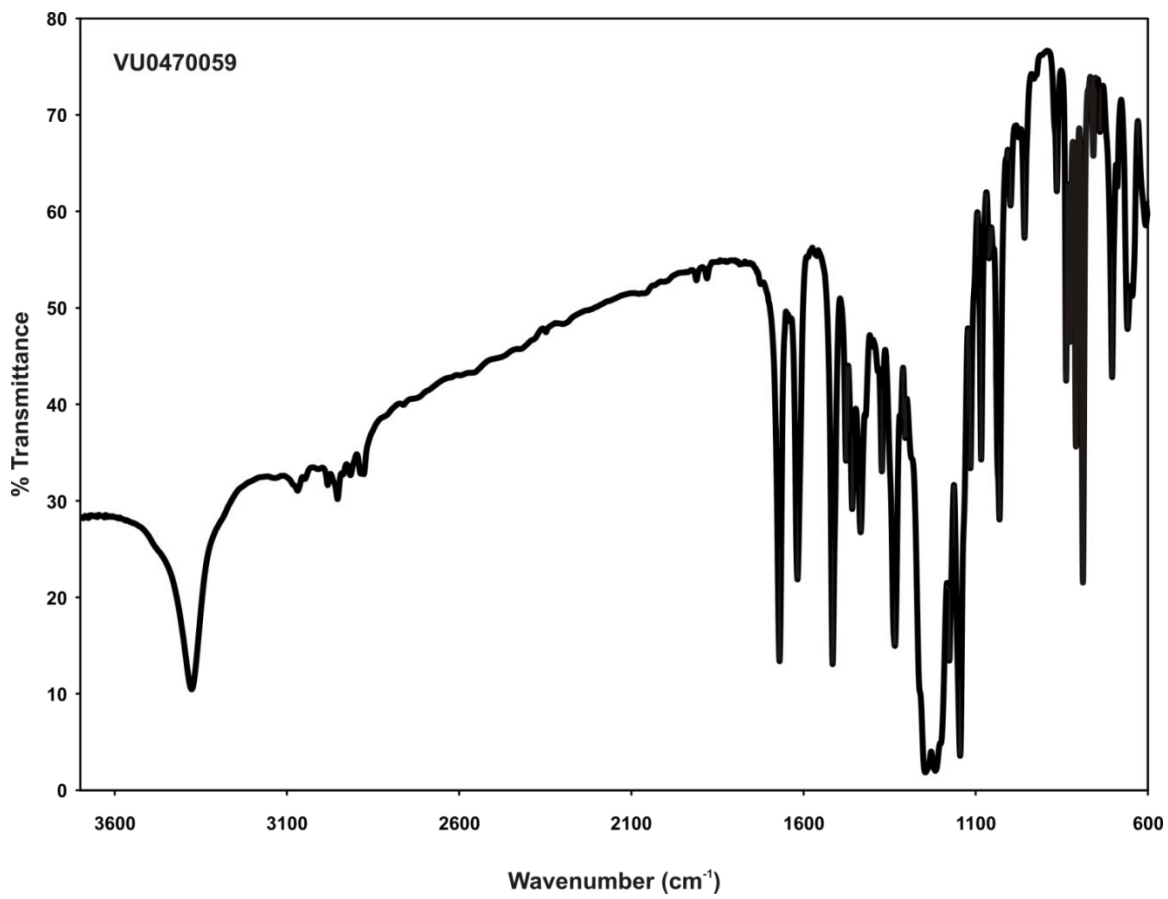
Approximately 250 mg of potassium bromide (KBr) was mixed with 2 mg of each matrix using a mortar and pestle. Approximately 100 mg was placed into a press to form pellets. Data was obtained on a Thermo Nicolet IR spectrometer. No background subtraction or signal correction was performed.

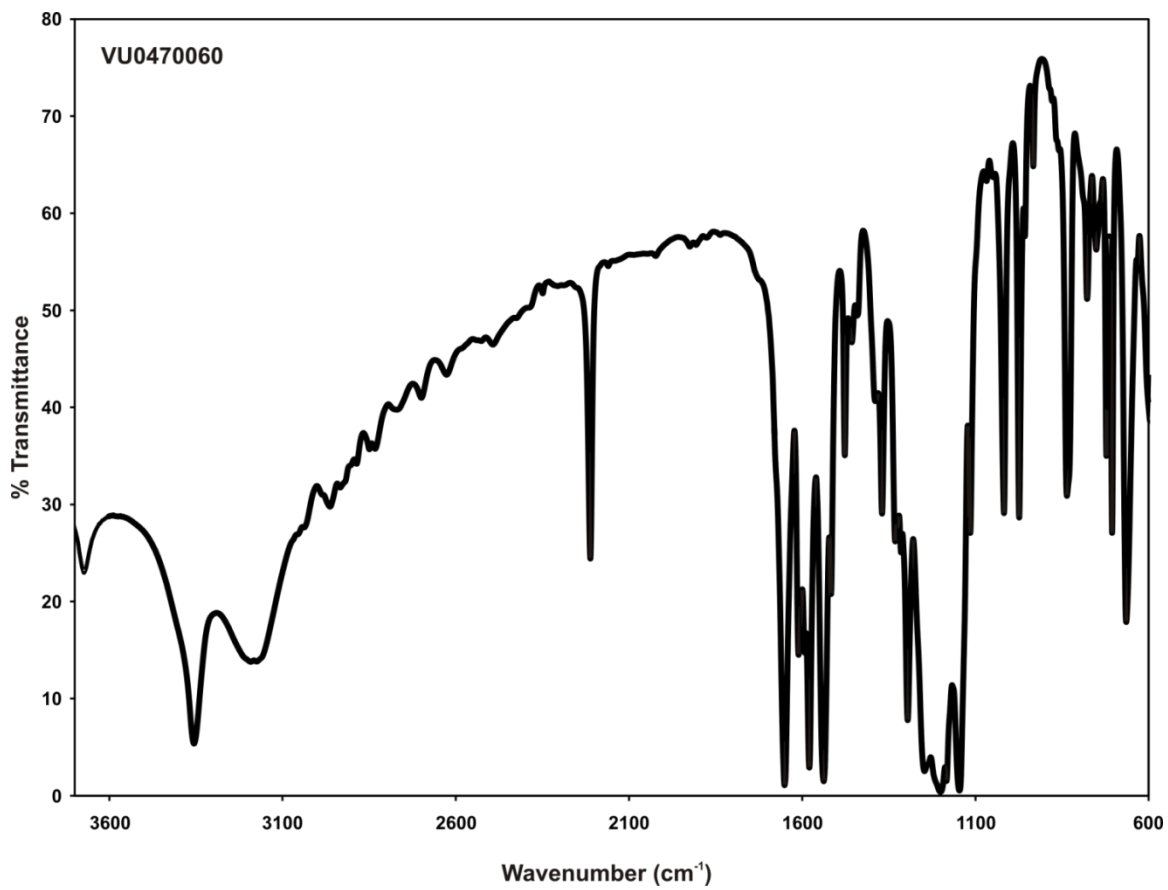










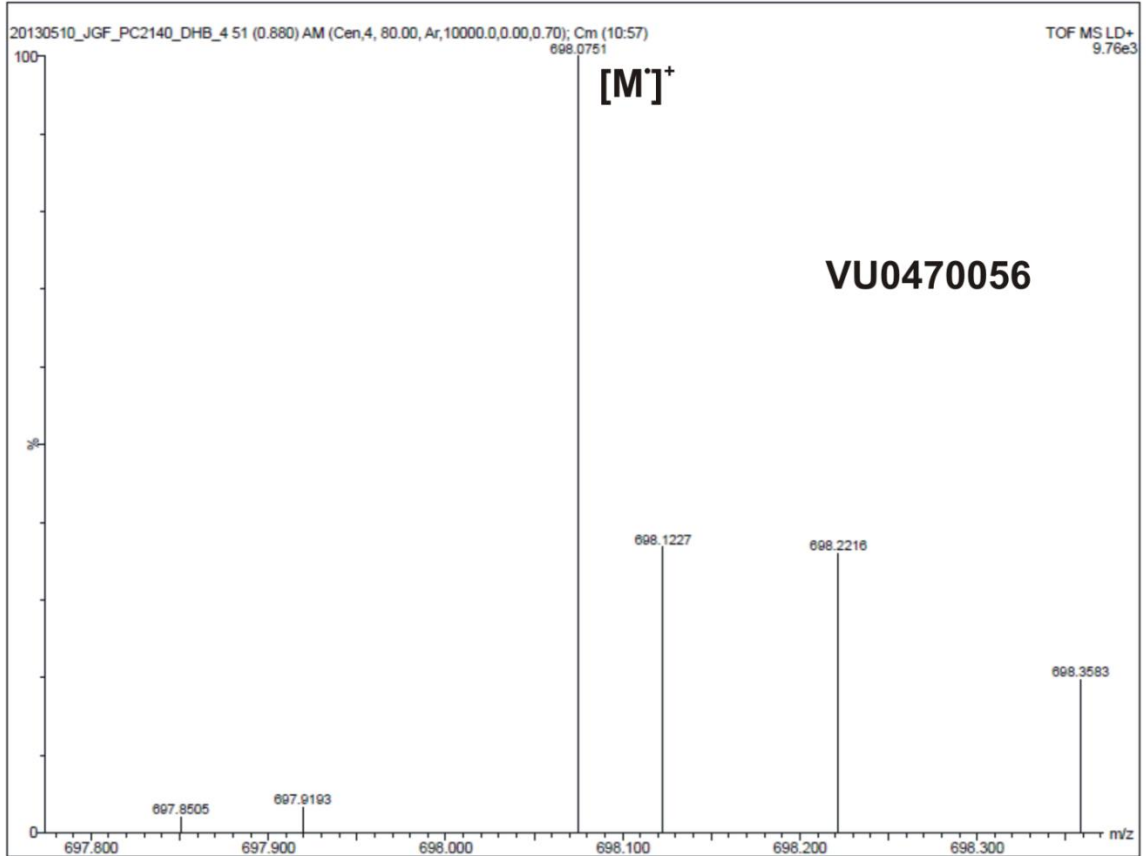


*Accurate MS data for 5 compounds (McLean Lab)*

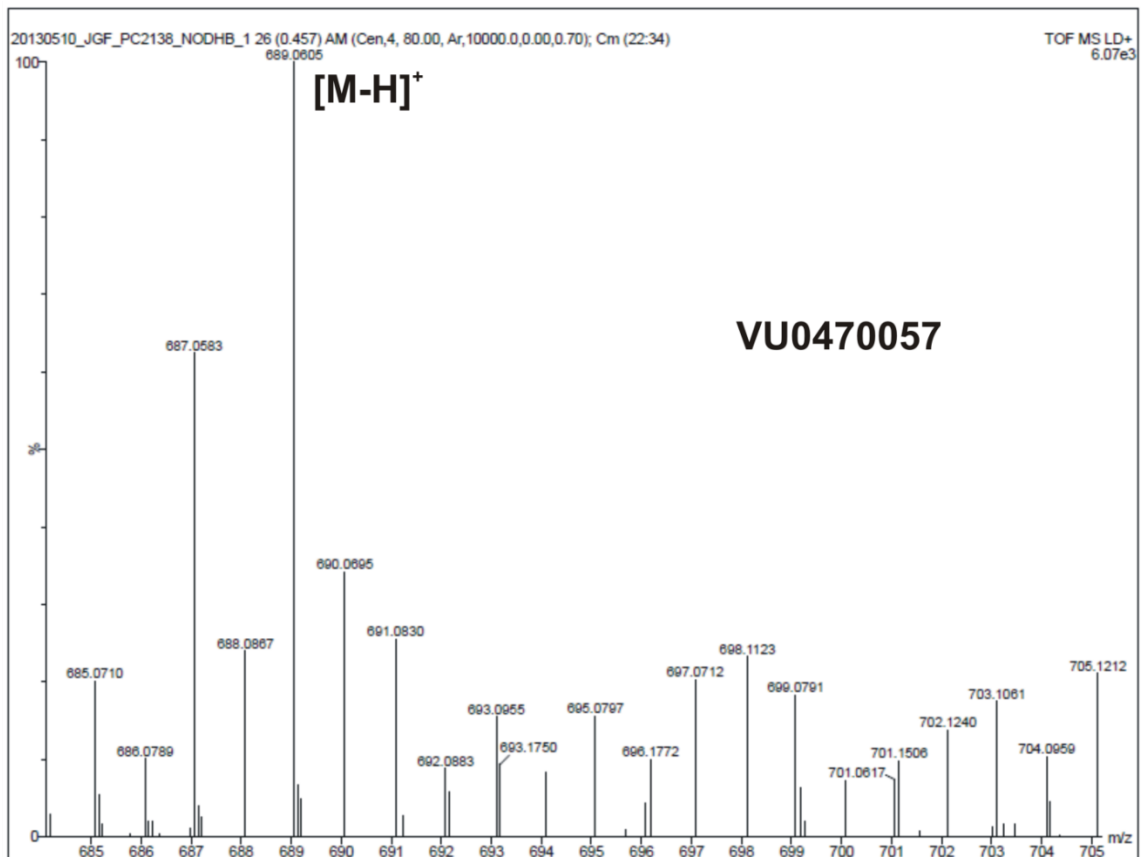
Compounds were dissolved at a concentration of 1 mg/mL in 99.9% ethanol / 0.1% formic acid (v/v), and 1  $\mu$ L of solution was spotted on the plate for each. No additional matrix was added. Accurate mass data were obtained on a Waters Synapt G2-S mass spectrometer in LDI-IM-TOFMS mode using a 355 nm Nd:YAG solid-state laser. Spectra were centered and externally calibrated. After manual calibration, mass errors were less than 5 ppm (see **Table 1**).

Instrument settings were as follows: positive LDI ion mode; mobility TOF; resolution; laser attenuation, 300 (arb. units); mass range, 300-2000 Da; trap gas flow, 2 mL/min; helium cell gas flow, 180, IMS gas flow, 90 mL/min, cooling gas flow, 15; trap DC entrance, 3; trap DC bias, 45; trap DC, -2; trap DC exit, 0; IMS DC entrance, 25; helium cell DC, 35; helium exit, -5; IMS bias, 3; IMS DC exit, 0; transfer DC entrance, 4; transfer DC exit, 15; IMS wave velocity, 650 m/s; IMS wave height, 40 V; mobility trapping release time, 200  $\mu$ s; IMS wave delay, 200  $\mu$ s; source pressure,  $3.79 \times 10^{-4}$  mbar; sample plate pressure,  $3.75 \times 10^{-1}$  mbar; trap pressure,  $2.01 \times 10^{-2}$  mbar; IMS pressure, 3.07 mbar; transfer pressure,  $2.11 \times 10^{-2}$  mbar; TOF pressure,  $6.36 \times 10^{-7}$  mbar.

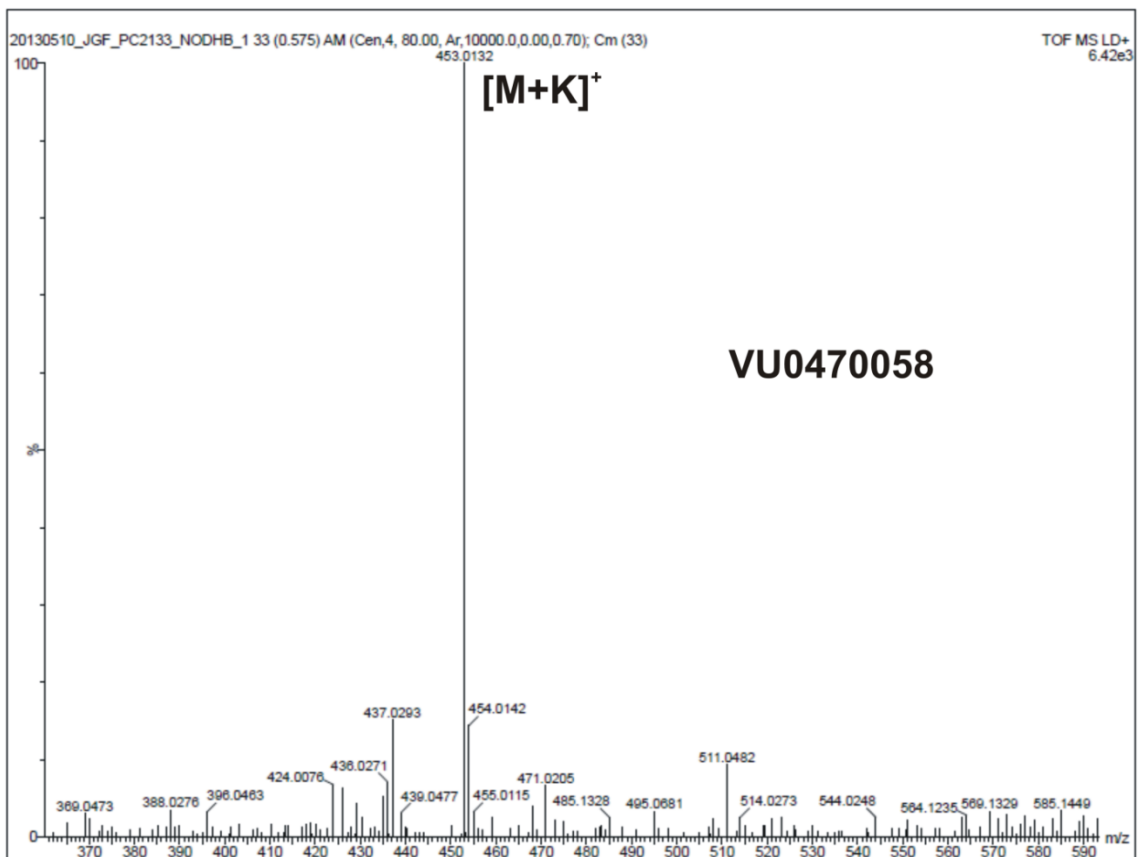
Labeled accurate mass spectra (zoomed-in) and full peak lists ( $m/z$ , intensity) are shown for all compounds below. It is important to mention VU0470056, VU0470057, and VU0470059 photocleaved upon laser irradiation, which led to low parent ion signal intensity. For these compounds, the base peak of the spectrum corresponds to fragmentation at the matrix / linker bond (e.g. **Figure 3-5**); these values are highlighted in yellow.



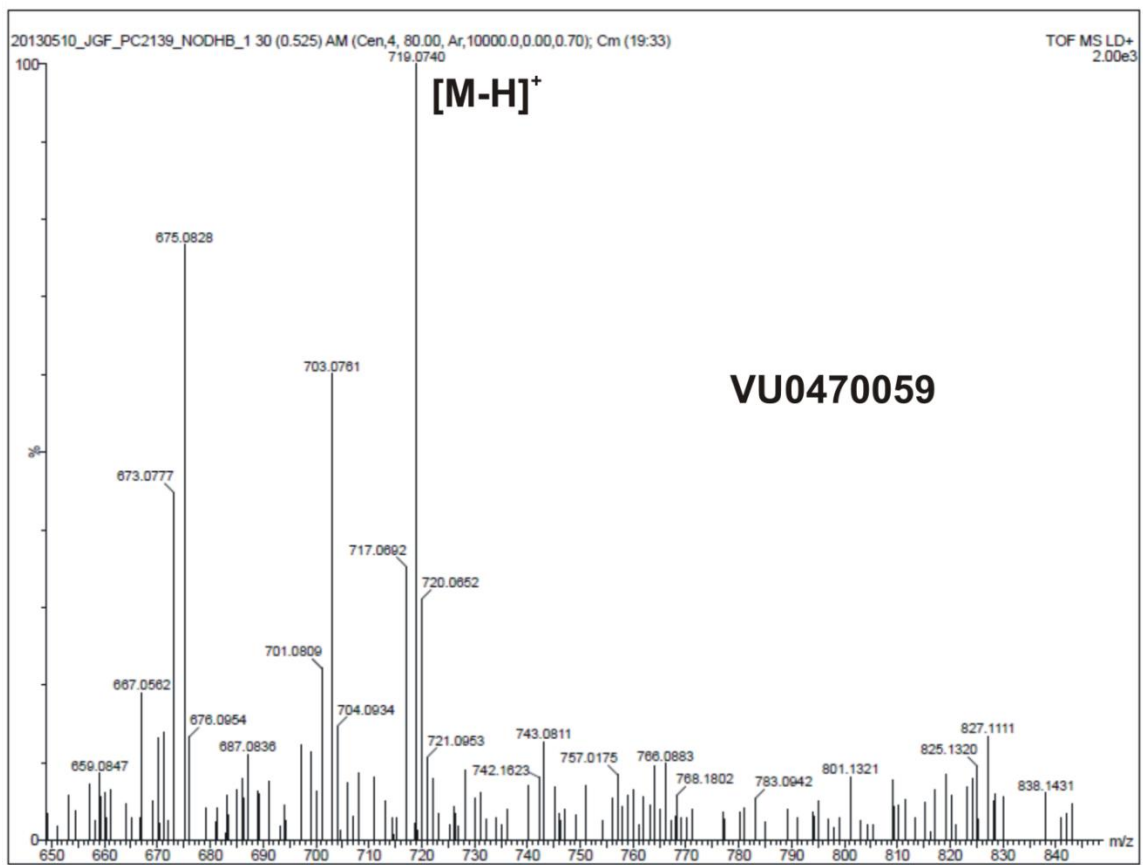
(*m/z*, *intensity*) 300.09, 21128; 301.07, 23180; 311.08, 23262; 313.10, 29017; 323.22, 31365; 324.09, 22525; 326.10, 23746; 327.11, 20948; 335.08, 22278; 337.10, 24568; 339.11, 21213; 409.09, 19567; 435.11, 19075; 461.05, 19105; 479.04, 16277; 481.06, 18822; 499.05, 125165; 500.05, 25053; 513.06, 21776; 516.07, 20138; 517.04, 16968; 519.05, 132970; 520.06, 26944; 533.07, 16887; 536.08, 21472; **537.05, 2353406**; 537.24, 26022; 538.05, 365338; 539.05, 28251; 551.06, 116820; 552.06, 30239; 554.07, 380911; 555.07, 66989; 563.06, 29412; 567.06, 18400; 568.05, 62901; 577.04, 39856; 613.01, 17462; 639.09, 16307; 659.28, 20957; 671.08, 16275; 673.09, 14382; 683.08, 16785; 687.10, 14619; 697.09, 15533; 701.09, 14345; 703.11, 15179; 713.09, 26416; 715.10, 14088; 719.99, 22979; 720.99, 14798; 727.10, 14306; 739.10, 16976; 755.07, 13425; 783.09, 38577; 784.10, 16299; 785.10, 20703; 799.07, 21897; 801.07, 17153; 839.99, 18720; 840.99, 13819; 887.98, 12742; 911.99, 12142; 983.99, 12166; 1007.99, 12300; 1097.08, 18695; 1113.06, 10666; 1199.99, 10274; 1200.98, 10750; 1224.99, 10405.



(*m/z*, *intensity*) 308.29, 16529; 378.38, 9004; 406.41, 6710; 499.05, 43100; 500.05, 7180; 516.07, 7932; 517.04, 6492; 519.05, 30361; 535.03, 5310; 536.03, 7071; 536.08, 6556; **537.05, 2992046**; 537.17, 18548; 537.24, 83200; 537.35, 20380; 537.68, 7568; 538.05, 577798; 538.24, 5743; 539.05, 41135; 551.06, 13276; 552.06, 118713; 553.06, 22430; 554.07, 509631; 555.07, 69214; 556.08, 6790; 561.04, 8649; 563.06, 23807; 566.07, 8203; 567.06, 9031; 568.05, 65653; 569.05, 12198; 575.06, 6202; 577.04, 8671; 587.06, 8060; 589.07, 5807; 591.05, 18405; 594.07, 6467; 601.08, 11673; 603.05, 9556; 617.07, 8285; 625.07, 5349; 627.05, 8064; 629.07, 11350; 630.08, 4917; 637.30, 17592; 639.09, 5735; 641.07, 7950; 643.05, 69804; 644.06, 18094; 645.06, 101078; 646.07, 56622; 647.08, 12781; 655.06, 4961; 657.07, 18570; 658.07, 6014; 659.07, 7023; 660.08, 6938; 661.06, 5161; 669.06, 9571; 671.05, 11220; 672.05, 6859; 673.06, 97796; 674.07, 27806; 675.08, 10064; 683.08, 4833; 687.04, 25708; 688.05, 8254; 689.05, 90659; 690.07, 42781; 691.07, 15265; 692.09, 4778; 697.05, 5979; 699.08, 5447; 703.08, 5201; 704.07, 4798; 707.07, 5073; 712.04, 4715; 713.05, 28196; 714.05, 8290; 728.01, 6769; 729.03, 71950; 730.03, 17555; 731.03, 7241; 753.08, 4725; 781.08, 8304; 797.07, 11640; 798.08, 5761; 809.08, 5824; 826.08, 4631; 1072.12, 3803; 1073.08, 5982; 1090.10, 12987; 1091.11, 5057; 1137.10, 3521; 1165.10, 4900; 1179.08, 8075; 1180.09, 4528; 1181.10, 13520; 1182.10, 13330; 1183.11, 4574; 1209.10, 7749; 1210.11, 4015; 1223.06, 3934; 1225.09, 13448; 1226.10, 18188; 1227.10, 7795; 1228.11, 5676; 1249.08, 3790; 1265.06, 3726.

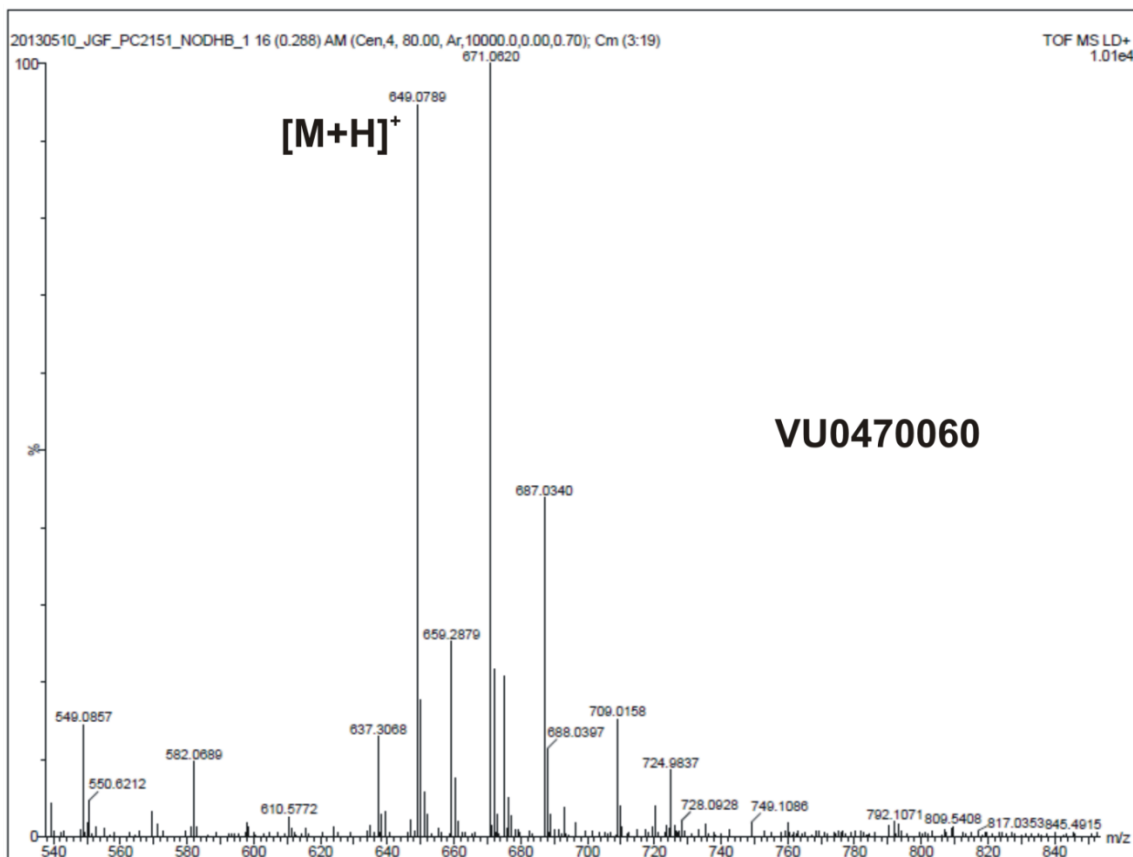


(*m/z*, *intensity*) 311.29, 13968; 323.22, 13092; 372.34, 7053; 388.02, 7997; 414.06, 16363; 426.01, 36984; 427.02, 9152; 429.02, 6908; 429.23, 6562; 432.01, 7249; 436.03, 13963; 437.04, 108562; 438.04, 14790; 442.01, 10143; 444.02, 15340; 452.00, 9540; 453.00, 25033; 454.01, 9170; 455.01, 12448; 459.02, 15978; 460.02, 7891; 469.02, 6649; 470.02, 11793; 471.01, 133940; 472.01, 22089; 473.02, 12153; 486.00, 23519; 487.01, 5470; 488.02, 8285; 489.02, 96975; 490.03, 18672; 491.02, 7422; 494.02, 6051; 495.04, 5966; 498.00, 5544; 504.01, 8502; ; 511.04, 35402; 512.04, 10572; 513.05, 6912; 528.96, 7190; 529.05, 19168; 805.07, 5104; 821.06, 6177; 822.05, 5429; 823.06, 12356; 827.04, 4221; 831.07, 12747; 833.07, 6302; 847.05, 19653; 848.05, 7323; 849.05, 18539; 850.05, 11507; 865.04, 12385; 866.03, 10583; 867.05, 26058; 868.05, 9272; 885.06, 9067.



(*m/z*, *intensity*) 326.37, 10679; 355.06, 6375; 415.03, 5991; 429.08, 5881; 503.10, 5342; 529.06, 29578; 530.06, 6971; 549.06, 19784; 565.04, 7771; 567.05, 994173; 567.25, 5580; 568.06, 172679; 569.06, 14535; 581.04, 8298; 591.17, 6282; 598.06, 15609; 673.06, 6627; 673.09, 9144; 675.07, 11617; 701.07, 7649; 703.07, 9828; 719.06, 21344; 719.99, 61618; 721.00, 48453; 722.00, 14055; 839.99, 10896; 840.99, 7177; 1133.11, 5368.





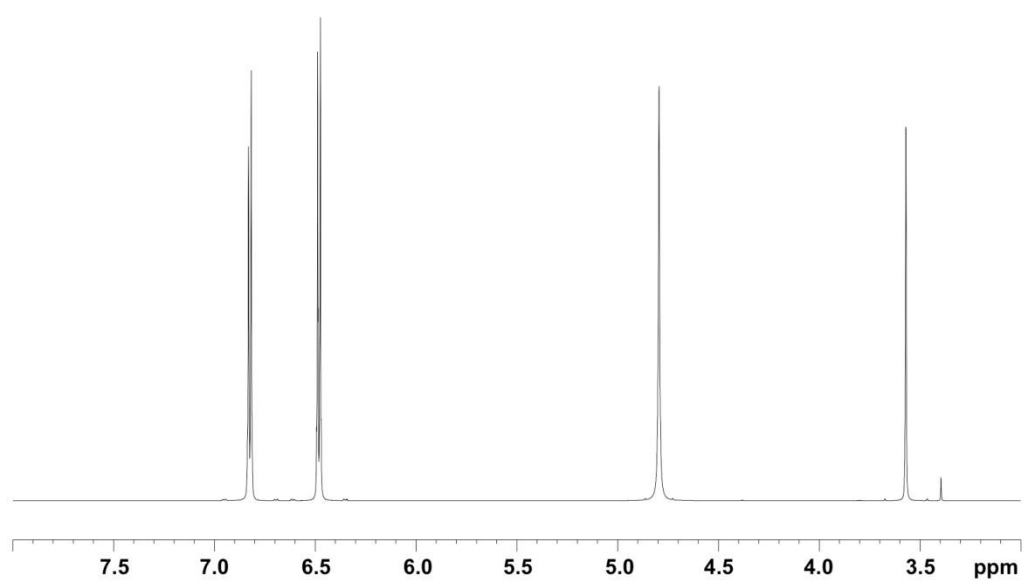
(*m/z*, *intensity*) 478.04, 62103; 549.08, 96071; 567.03, 18591; 582.06, 70100; 633.06, 22109; 647.05, 21411; 649.07, 383354; 650.08, 99480; 651.08, 33789; 653.06, 14780; 659.28, 24952; 669.03, 46236; 671.05, 712993; 672.06, 145621; 673.07, 53306; 675.25, 17284; 685.01, 40315; 687.03, 672079; 688.03, 153933; 689.03, 101162; 690.03, 21025; 693.03, 23813; 705.02, 48360; 706.03, 14156; 707.02, 202425; 708.03, 47337; 709.01, 42833; 724.98, 18908; 725.03, 44792; 1297.13, 25435; 1298.13, 10213; 1319.11, 57524; 1320.12, 25223; 1335.09, 45458; 1336.09, 19009; 1337.10, 9870.

### **E. MDA Supplemental Material**

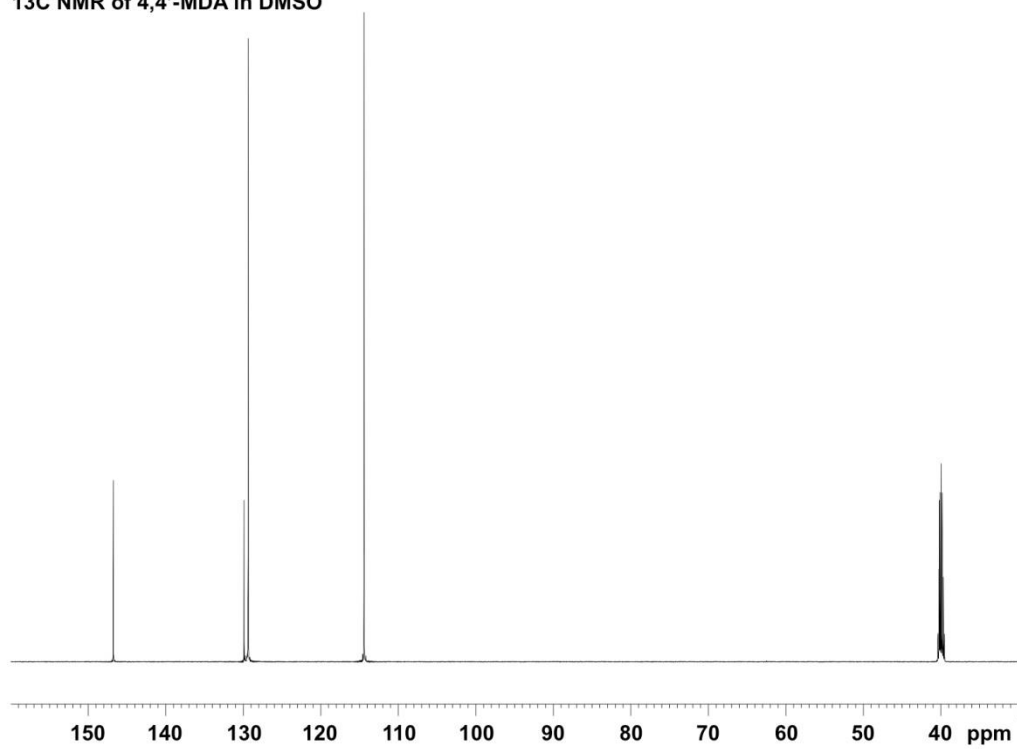
#### *NMR Spectroscopy of Purified MDA Isomers (Don Stec)*

NMR experiments were acquired using a 14.0 T Bruker magnet equipped with a Bruker AV-III console operating at 600.13 MHz. All spectra were acquired in 5mm NMR tubes using a Bruker 5 mm TCI cryogenically cooled NMR probe. Chemical shifts were referenced internally to DMSO (2.49 ppm) which also served as the  $^2\text{H}$  lock solvents. For 1D  $^1\text{H}$  NMR, typical experimental conditions included 32K data points, 13 ppm sweep width, a recycle delay of 1.5 seconds and 64 scans. For 1D  $^{13}\text{C}$  NMR, typical experimental conditions included 32K data points, 250 ppm sweep width,  $20^\circ$  excitation pulse, a recycle delay of 2 seconds and 512 scans. Multiplicity-edited HSQC experiments were acquired using a 1024 x 256 data matrix, a J(C-H) value of 145 Hz which resulted in a multiplicity selection delay of 34 ms, a recycle delay of 1.5 seconds and 64 scans per increment along with GARP decoupling on  $^{13}\text{C}$  during the acquisition time (150 ms). The data was processed using a p/2 shifted squared sine window function and displayed with CH/ $\text{CH}_3$  signals phased positive and  $\text{CH}_2$  signals phased negative.

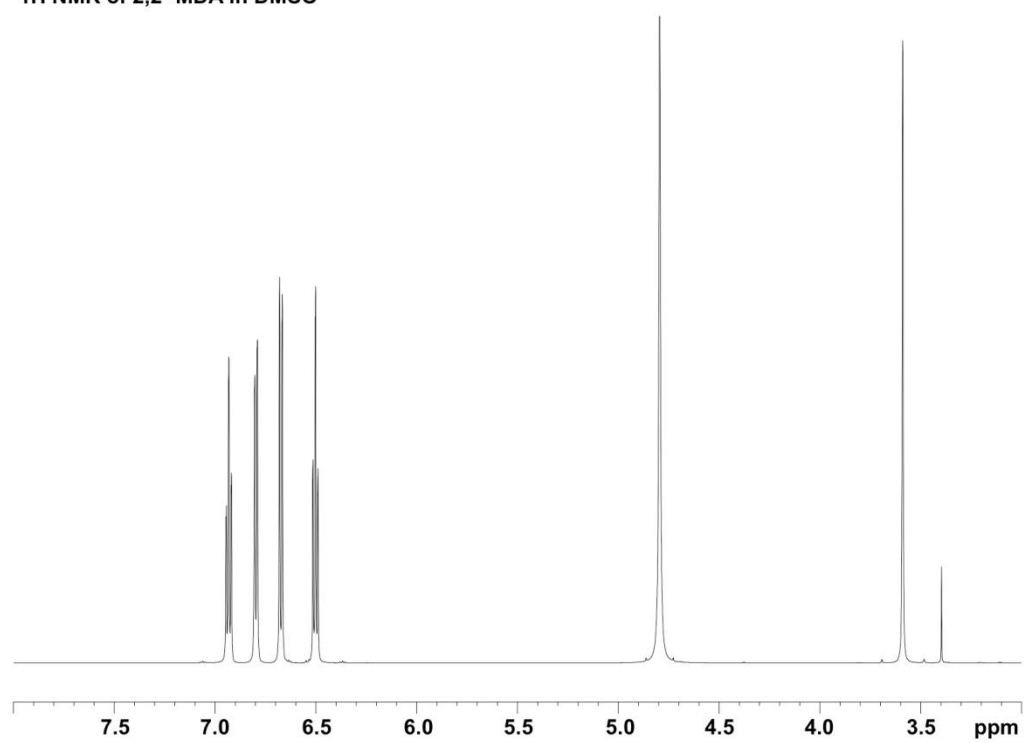
**<sup>1</sup>H NMR of 4,4'-MDA in DMSO**



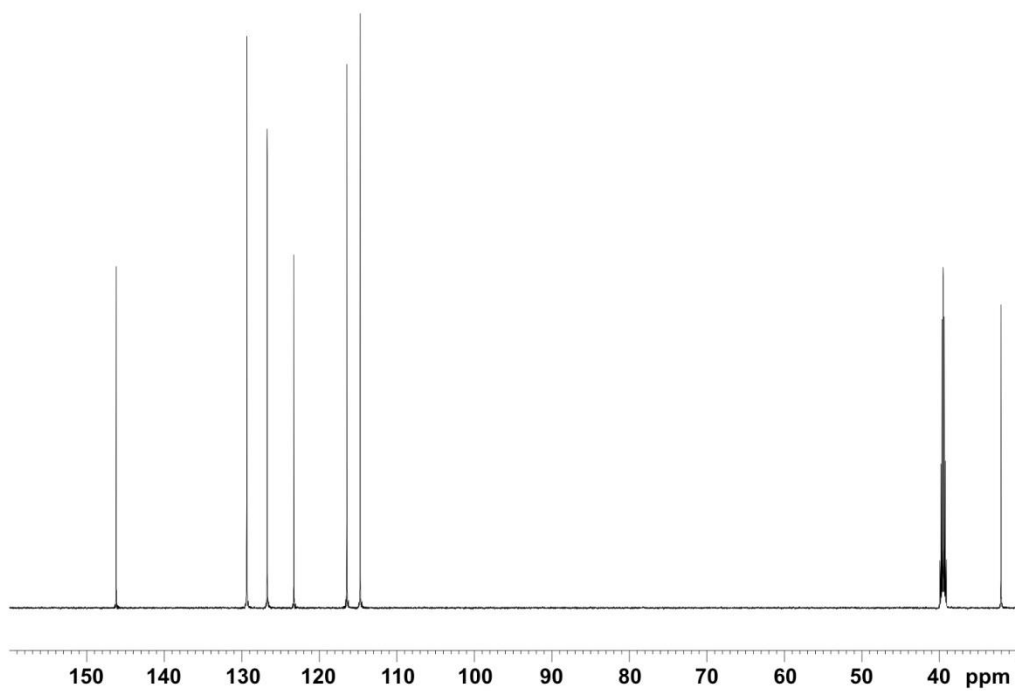
**<sup>13</sup>C NMR of 4,4'-MDA in DMSO**



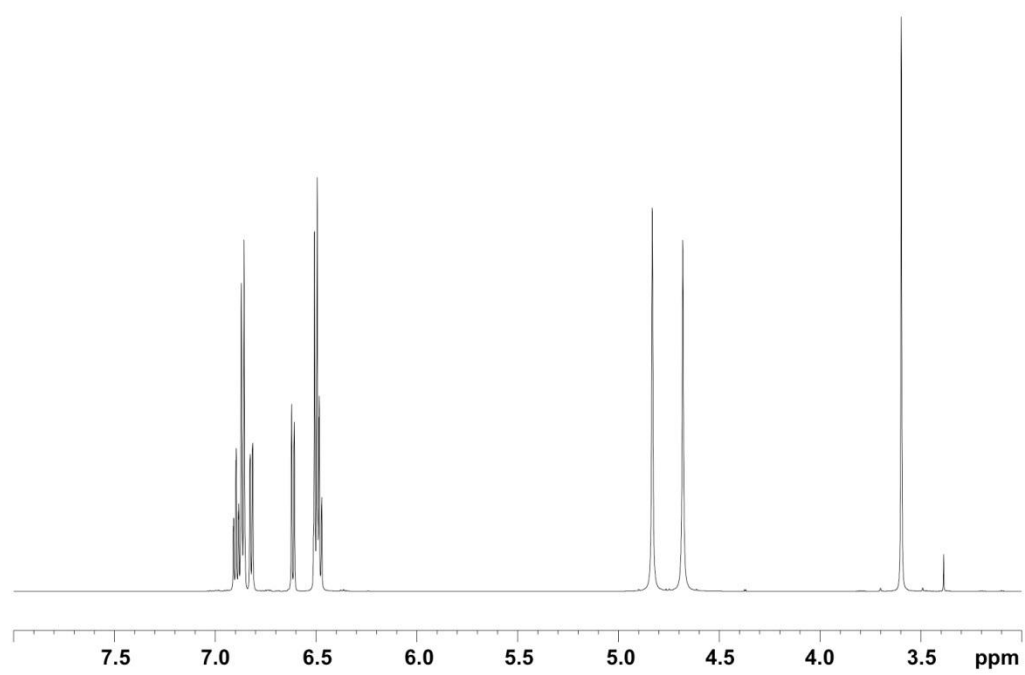
**<sup>1</sup>H NMR of 2,2'-MDA in DMSO**



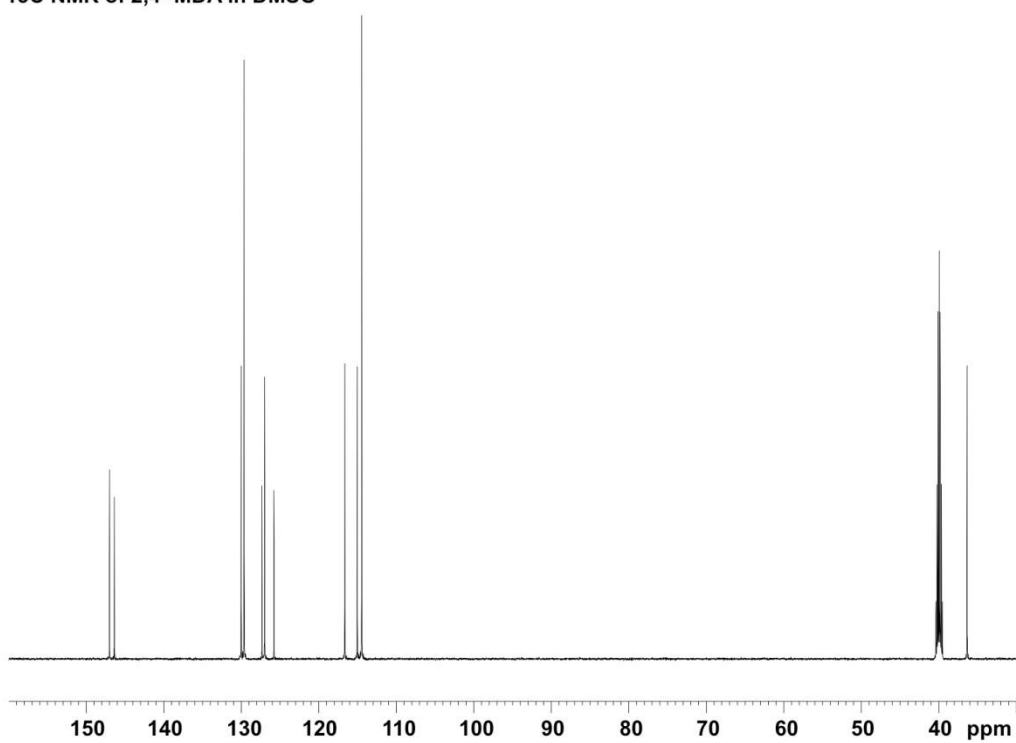
**<sup>13</sup>C NMR of 2,2'-MDA in DMSO**



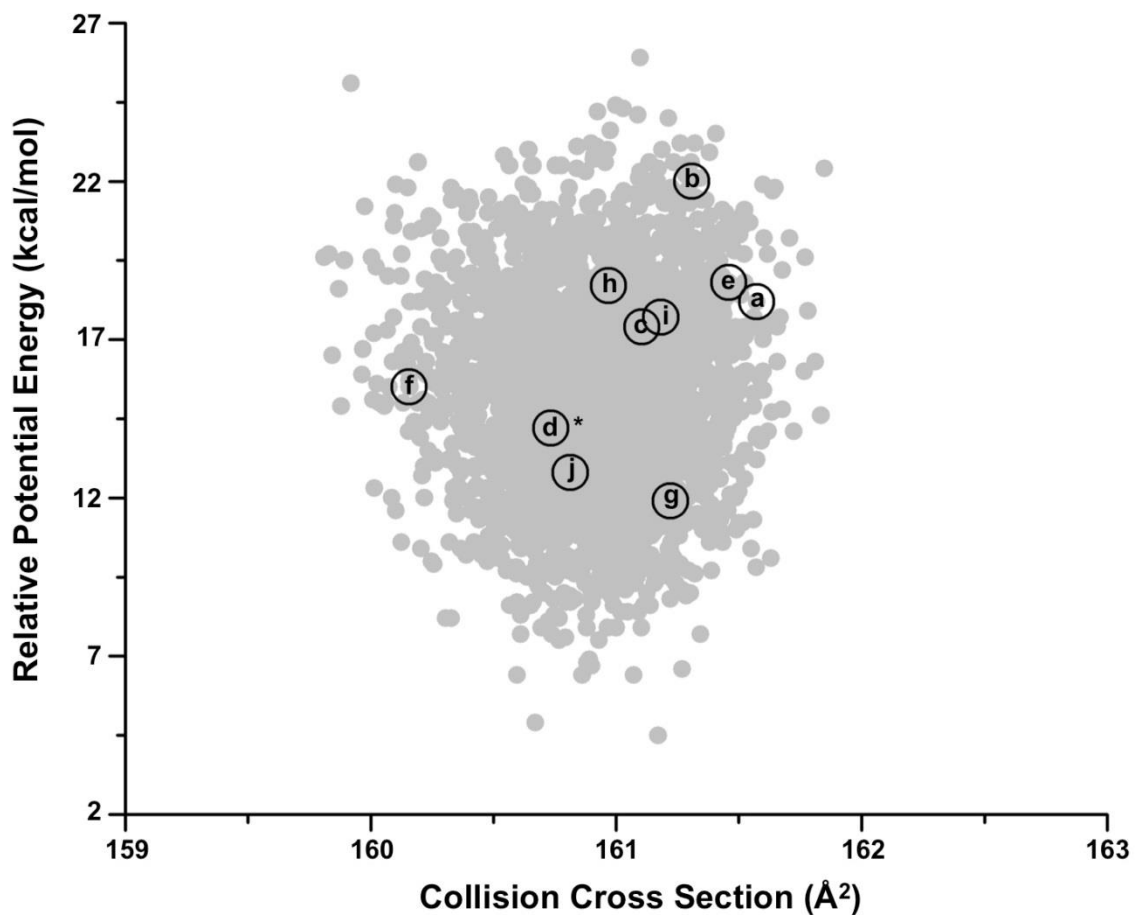
**<sup>1</sup>H NMR of 2,4'-MDA in DMSO**



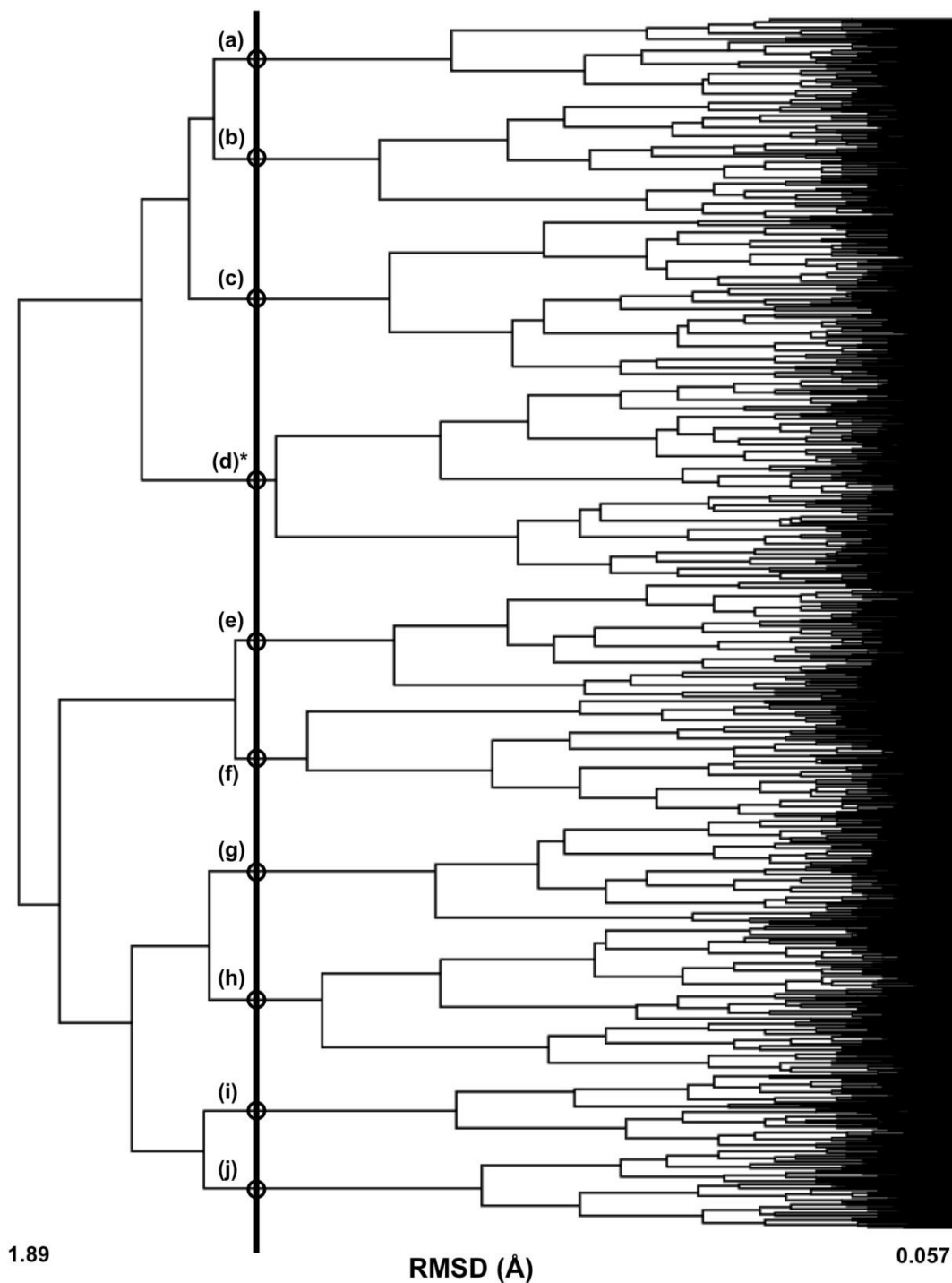
**<sup>13</sup>C NMR of 2,4'-MDA in DMSO**



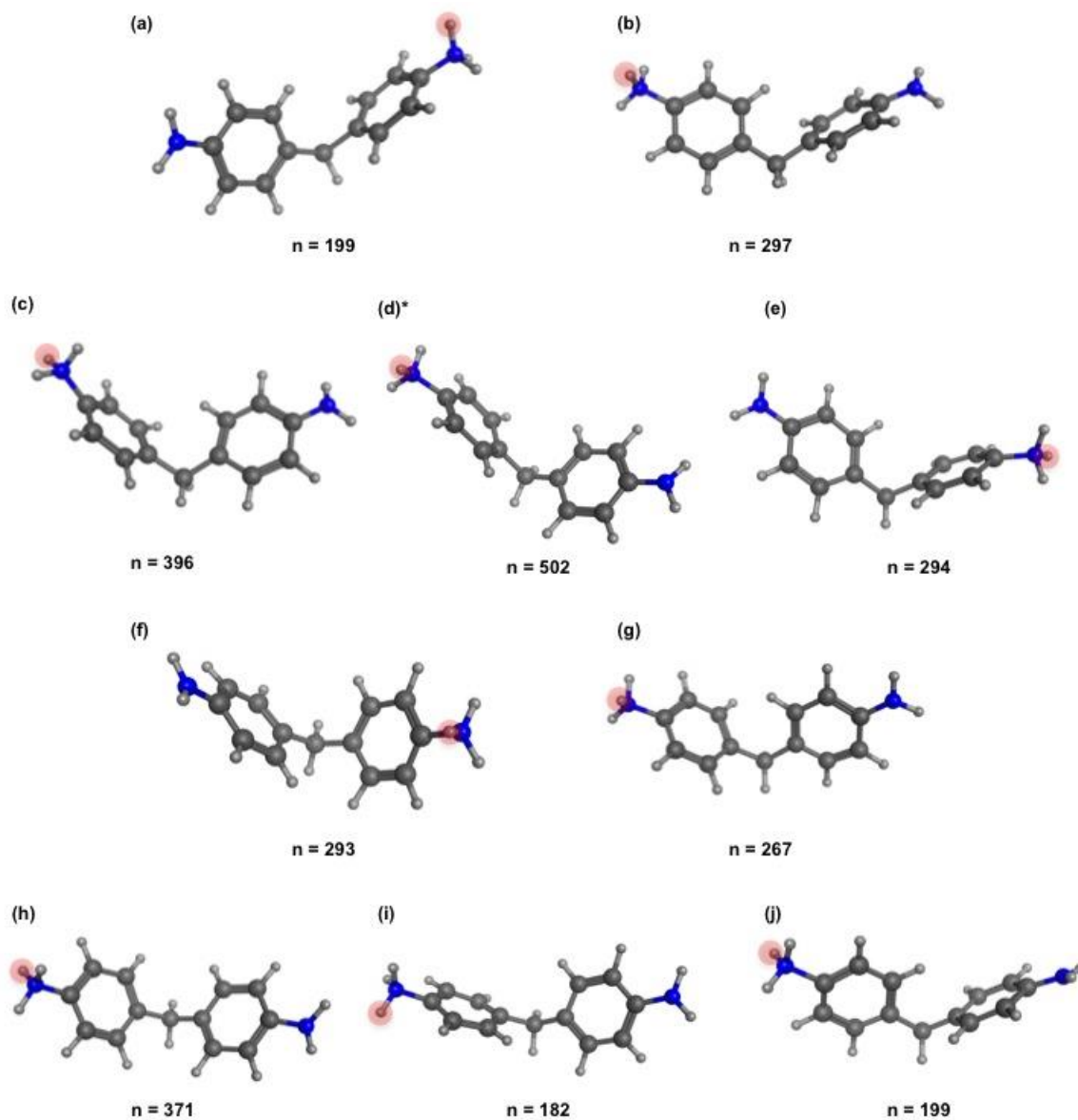




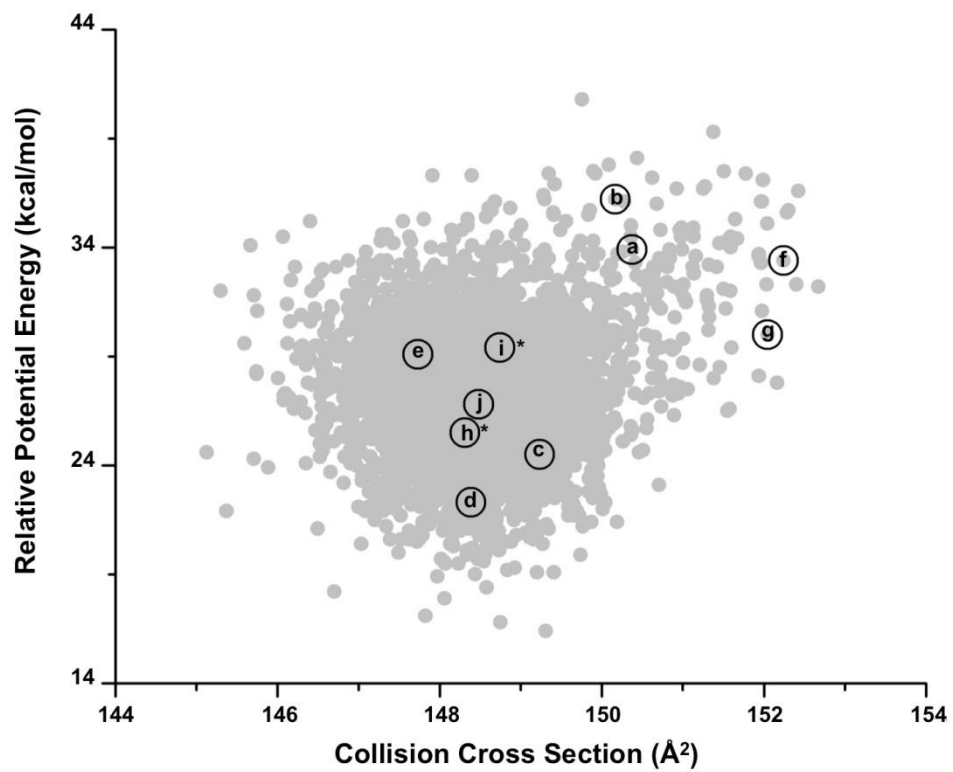
***p*-NH<sub>2</sub> 4,4'-MDA** Conformational space plot for the para-amine protonated 4,4'-MDA. The 3,000 generated conformations are represented in grey, the clustering representative conformations are labeled with letters that correspond to the structures in the following two pages. The asterisk indicates the structures that are shown in Chapter 4.



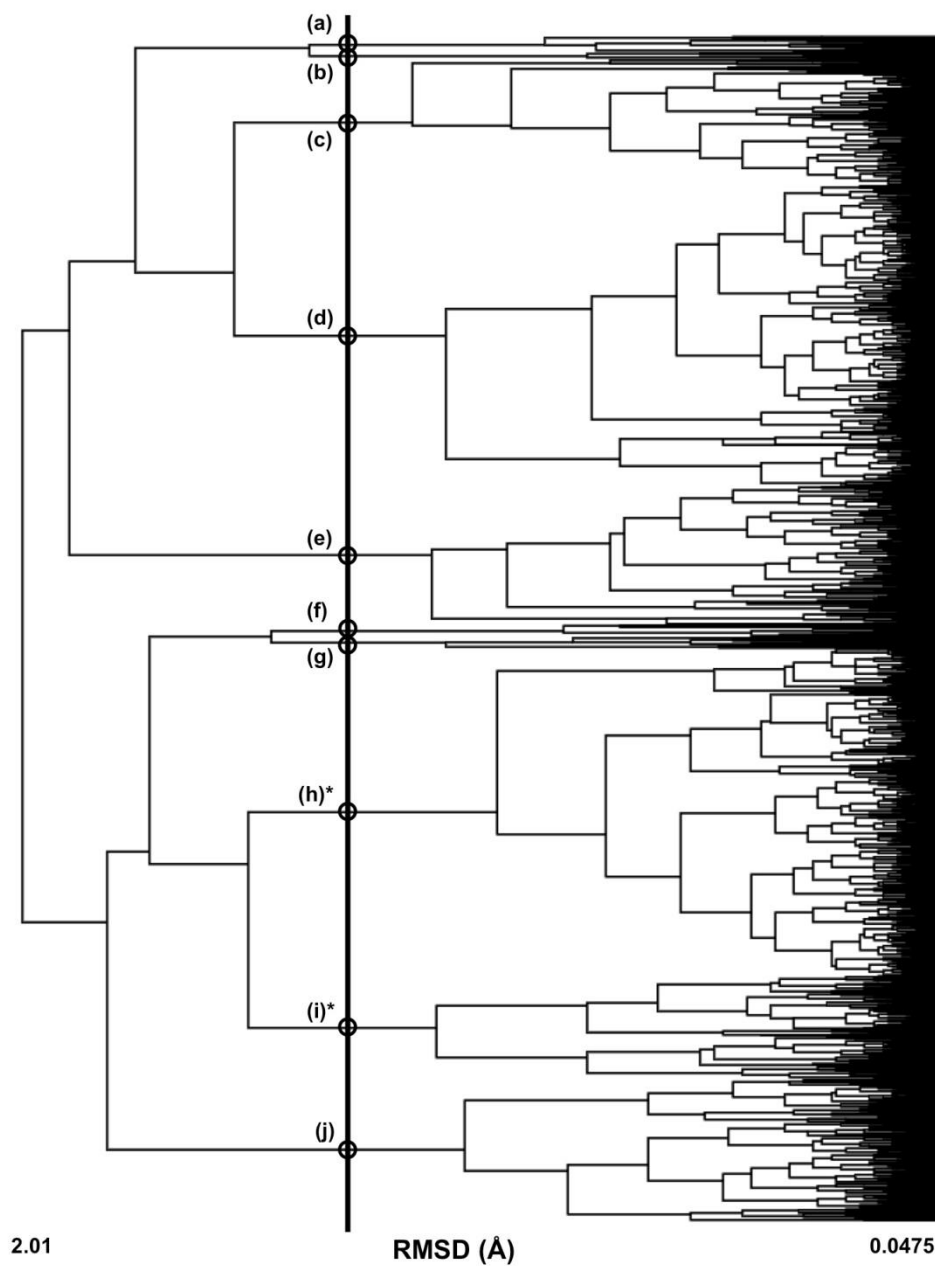
***p*-NH<sub>2</sub> 4,4'-MDA** Clustering analysis of 3,000 conformations of the para-amine protonated 4,4'-MDA. Clustering is based on root mean square distance of atoms of superimposed structures. The vertical black bar indicates the RMSD cutoff (1.40 Å) used to select the conformations (circled) for further analysis. The asterisk represents the structures shown in Chapter 4.



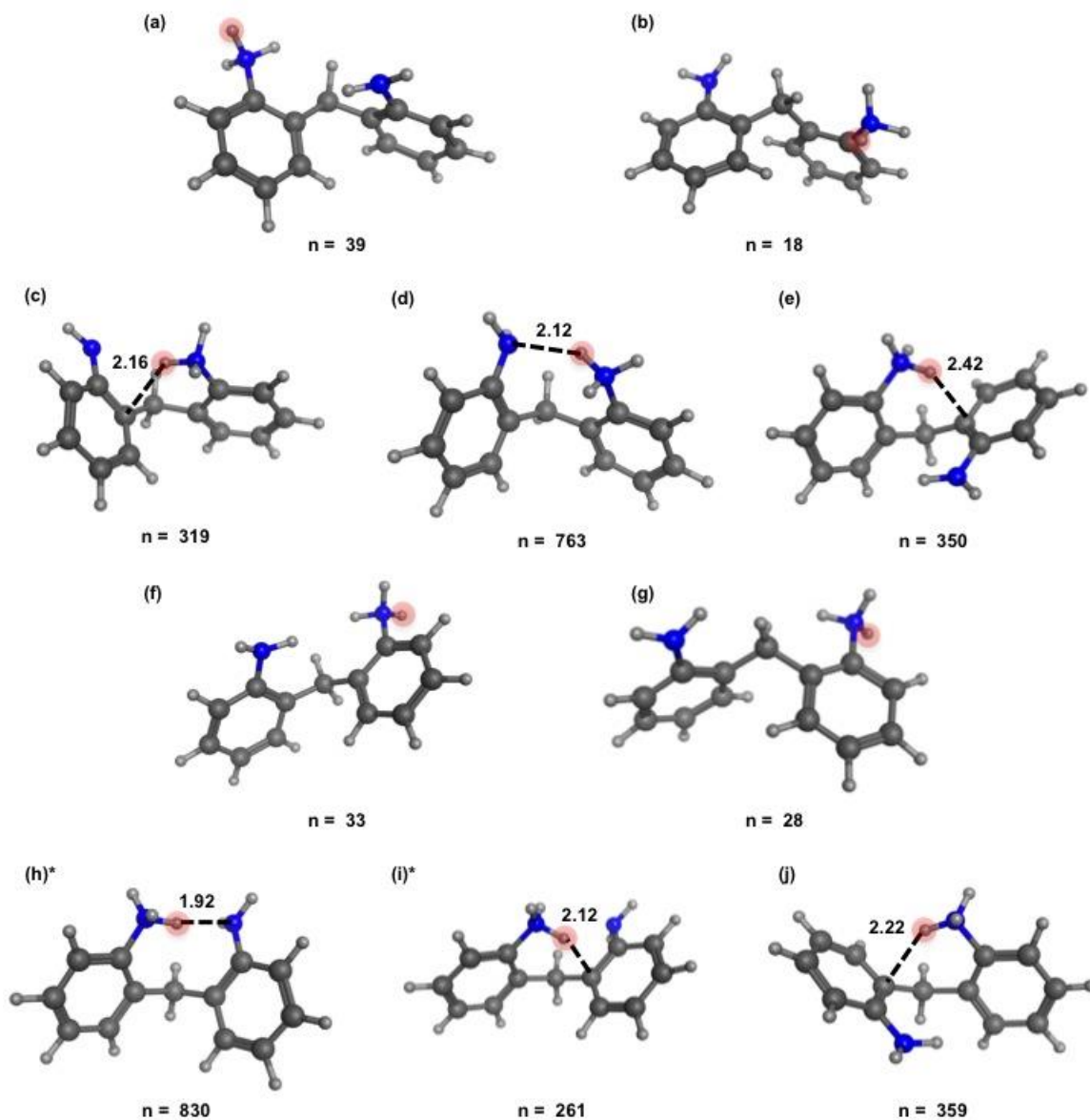
***p*-NH<sub>2</sub> 4,4'-MDA** Representative conformations of the para-amino protonated 4,4'-MDA generated from an elevated temperature molecular dynamic protocol. Carbon atoms are shown in dark grey, hydrogen in light grey, and nitrogen in blue. The asterisk represents the structures shown in Chapter 4. The number of conformations each of these represents from clustering is shown below the conformation.



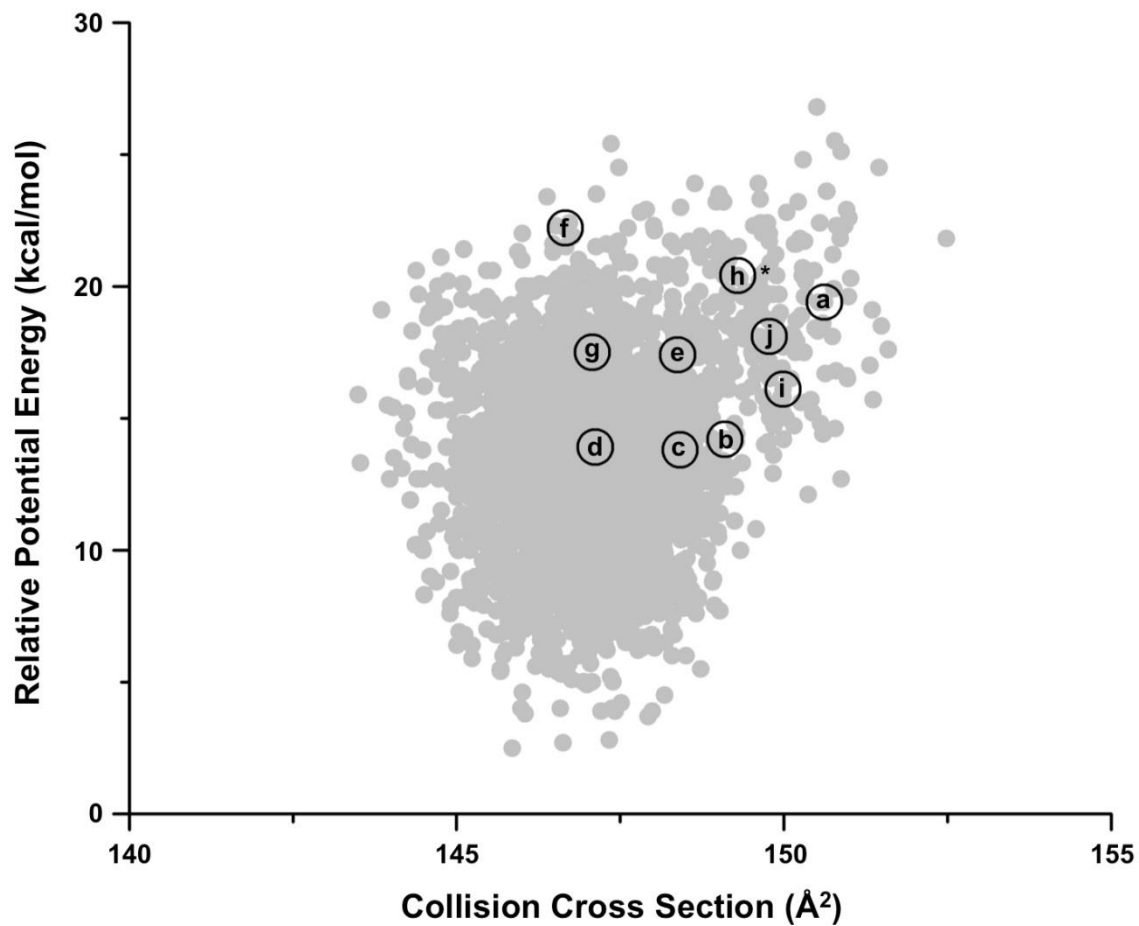
**o-NH<sub>2</sub> 2,2'-MDA** Conformational space plot for the ortho-amine protonated 2,2'-MDA. The 3,000 generated conformations are represented in grey, the clustering representative conformation are labeled with letters that correspond to the structures in on the following two pages. The asterisk indicates the structures that are shown in Chapter 4.



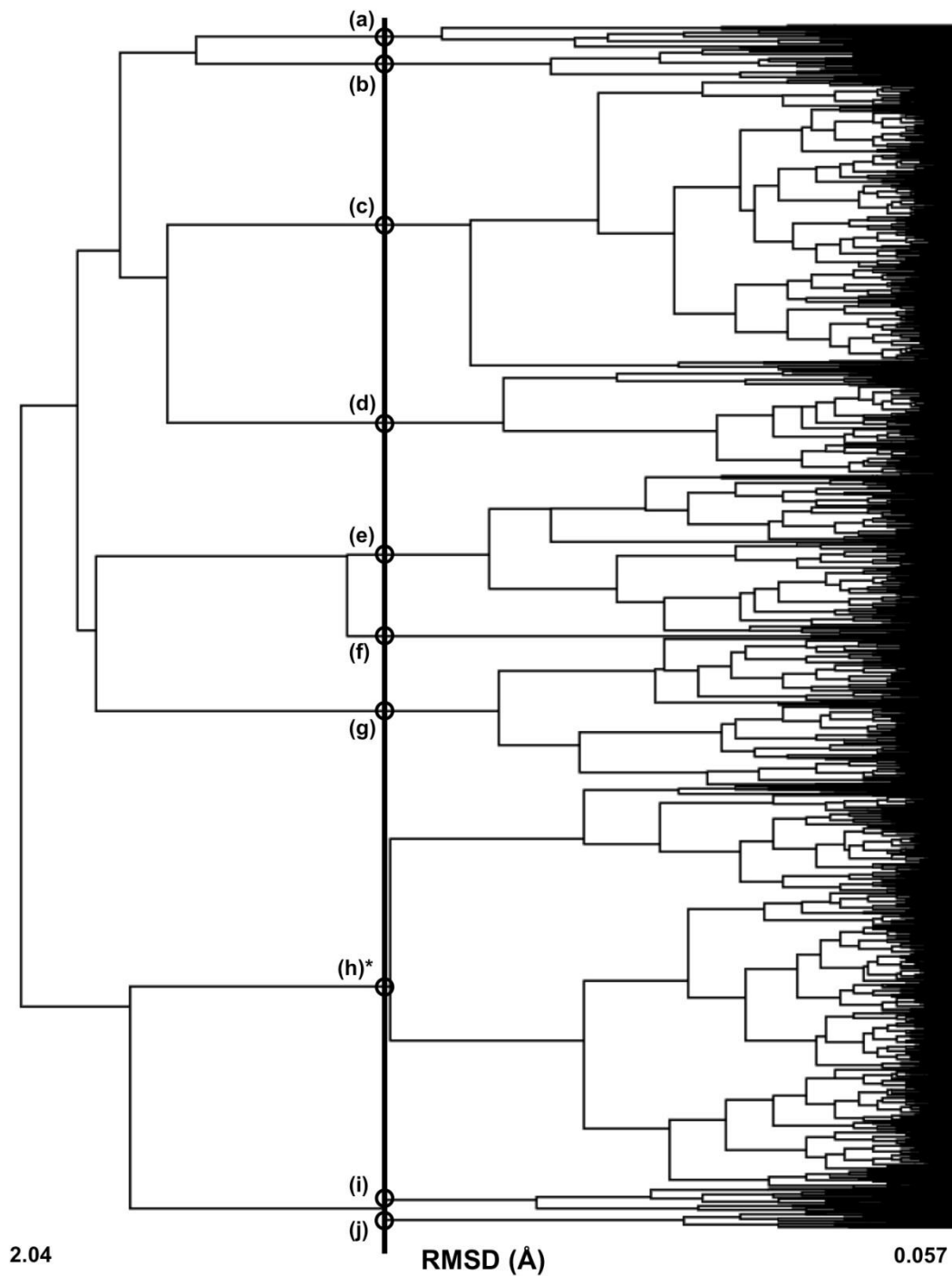
**o-NH<sub>2</sub> 2,2'-MDA** Clustering analysis of 3,000 conformations of the ortho-amine protonated 2,2'-MDA. Clustering is based on root mean square distance of atoms of superimposed structures. The vertical black bar indicates the RMSD cutoff (1.20 Å) used to select the conformations (circled) for further analysis. The asterisk represents the structures shown in Chapter 4.



**o-NH<sub>2</sub> 2,2'-MDA** Representative conformations of the ortho-amine protonated 2,2'-MDA generated from an elevated temperature molecular dynamic protocol. Carbon atoms are shown in dark grey, hydrogen in light grey, and nitrogen in blue. The asterisk represents the structures shown in the paper. The number of conformations each of these represents from clustering is shown below the conformation.

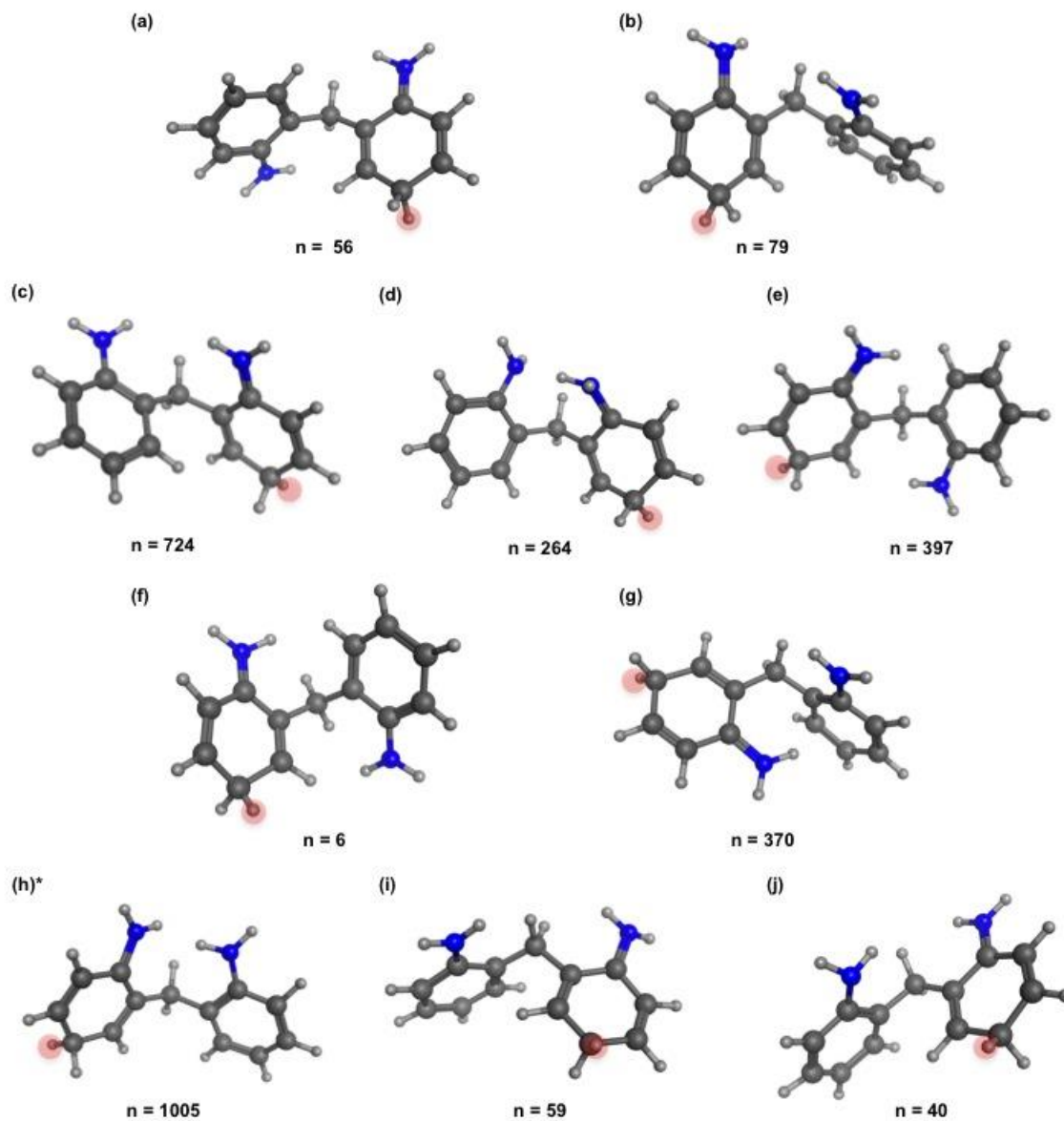


**ring 2,2'-MDA** Conformational space plot for the ring-protonated 2,2'-MDA. The 3,000 generated conformations are represented in grey, the clustering representative conformations are labeled with letters that correspond to the structures in the following two pages. The asterisk indicates the structures that are shown in Chapter 4.

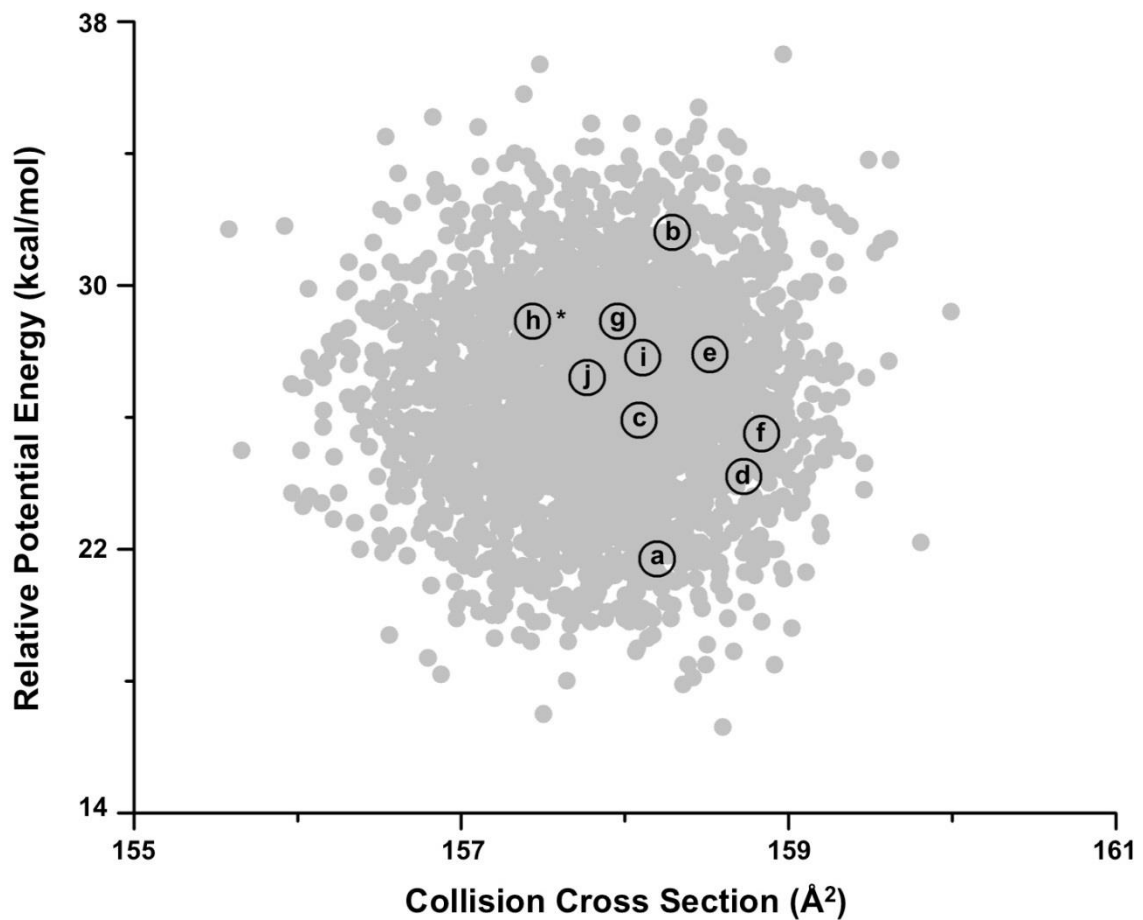


**ring 2,2'-MDA** Clustering analysis of 3,000 conformations of the ring-protonated 2,2'-MDA. Clustering is based on root mean square distance of atoms of superimposed structures. The vertical black bar indicates the RMSD cutoff (1.26 Å) used to select the conformations (circled) for further analysis. The asterisk represents the structures shown in Chapter 4.

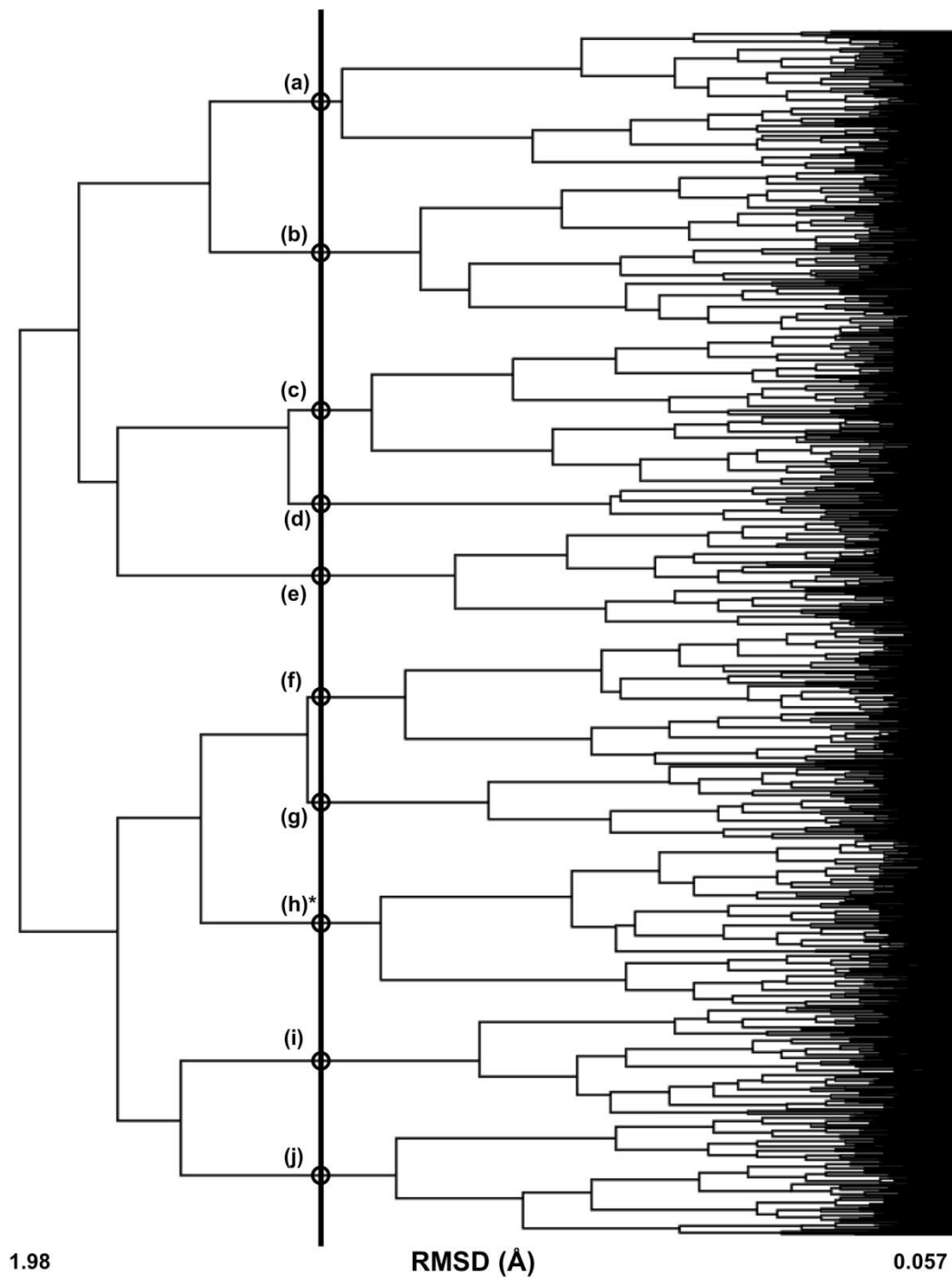




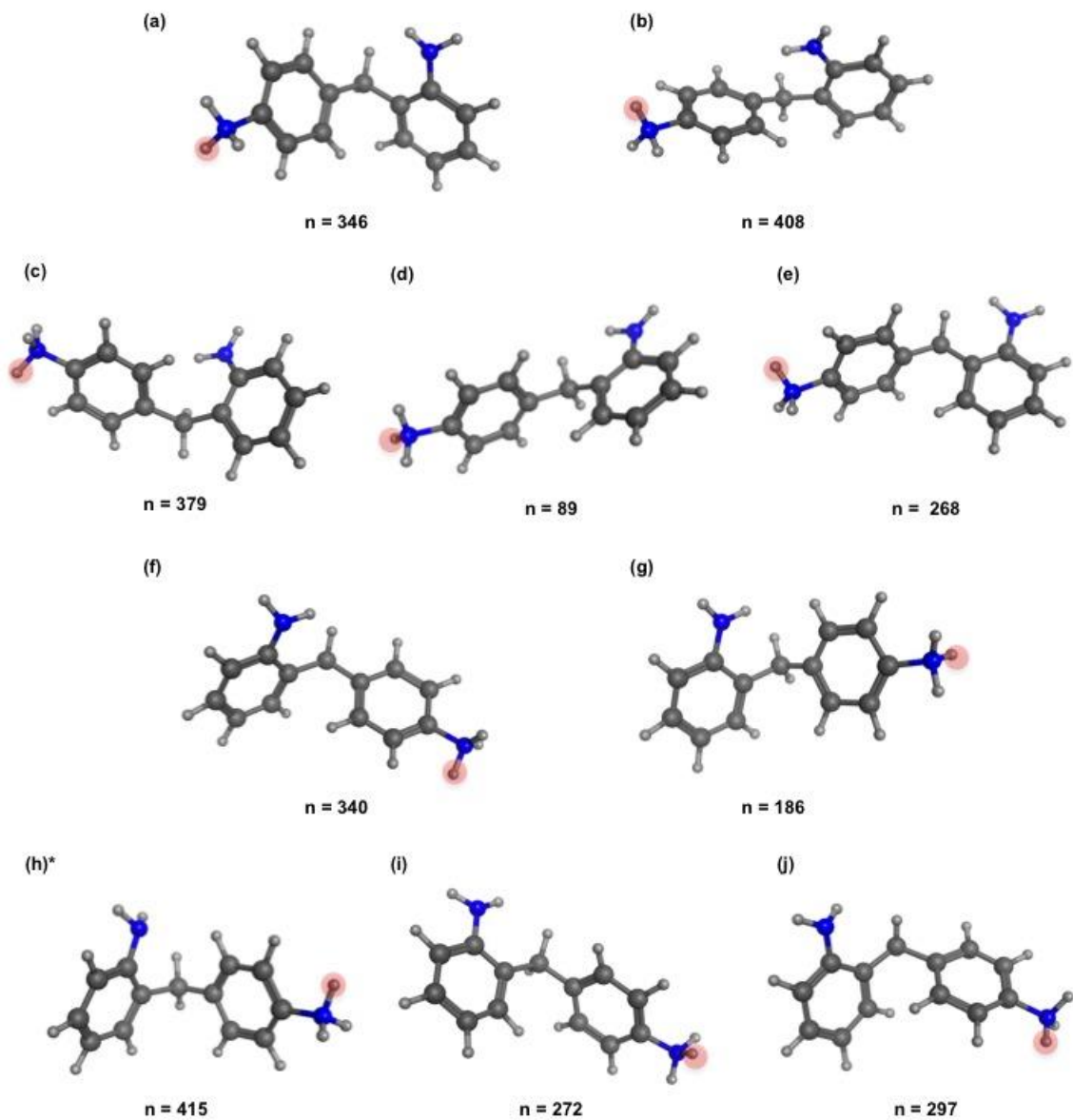
**ring 2,2'-MDA** Representative conformations of the ring-protonated 2,2'-MDA generated from an elevated temperate molecular dynamic protocol. Carbon atoms are shown in dark grey, hydrogen in light grey, and nitrogen in blue. The asterisk represents the structures shown in Chapter 4. The number of conformations each of these represents from clustering is shown below the conformation.



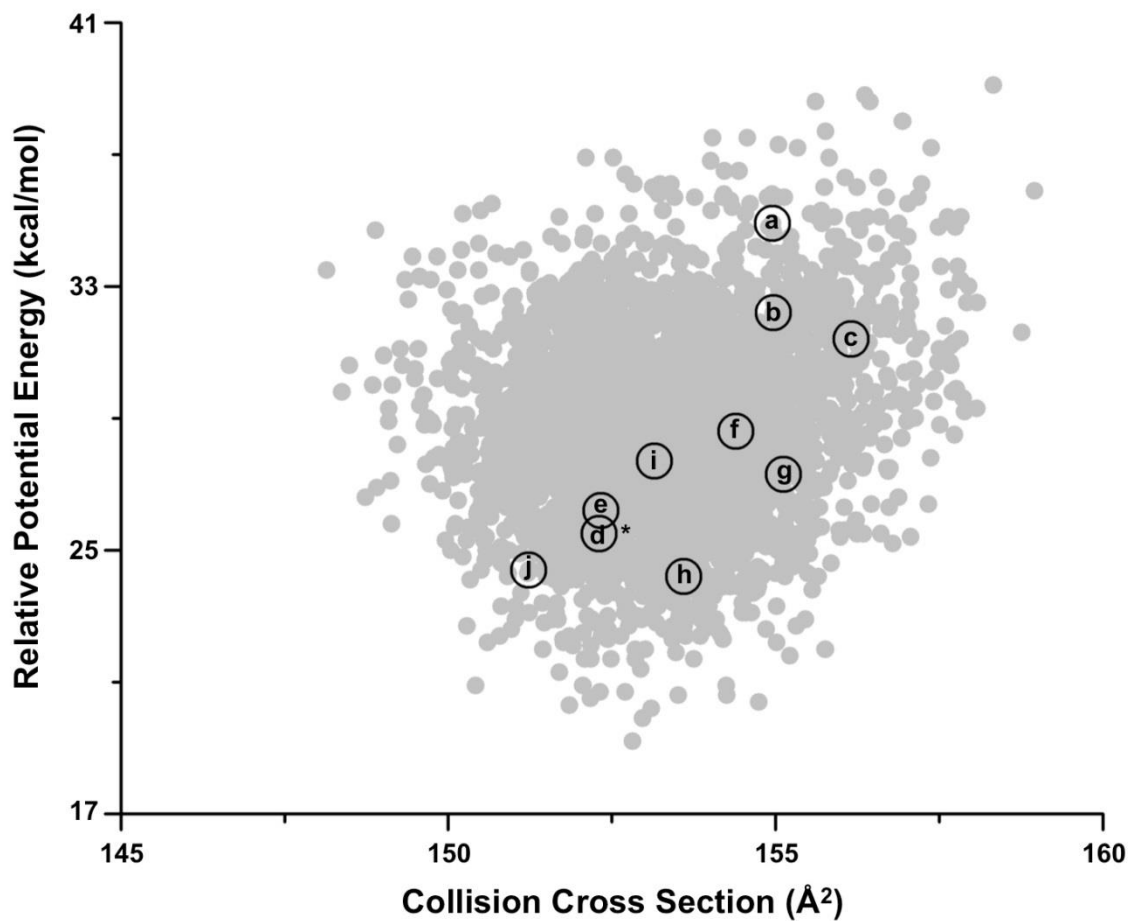
**p-NH<sub>2</sub> 2,4'-MDA** Conformational space plot for the para-amine protonated 2,4'-MDA. The 3,000 generated conformations are represented in grey, the clustering representative conformation are labeled with letters that correspond to the structures in the following two pages. The asterisk indicates the structures that are shown in Chapter 4.



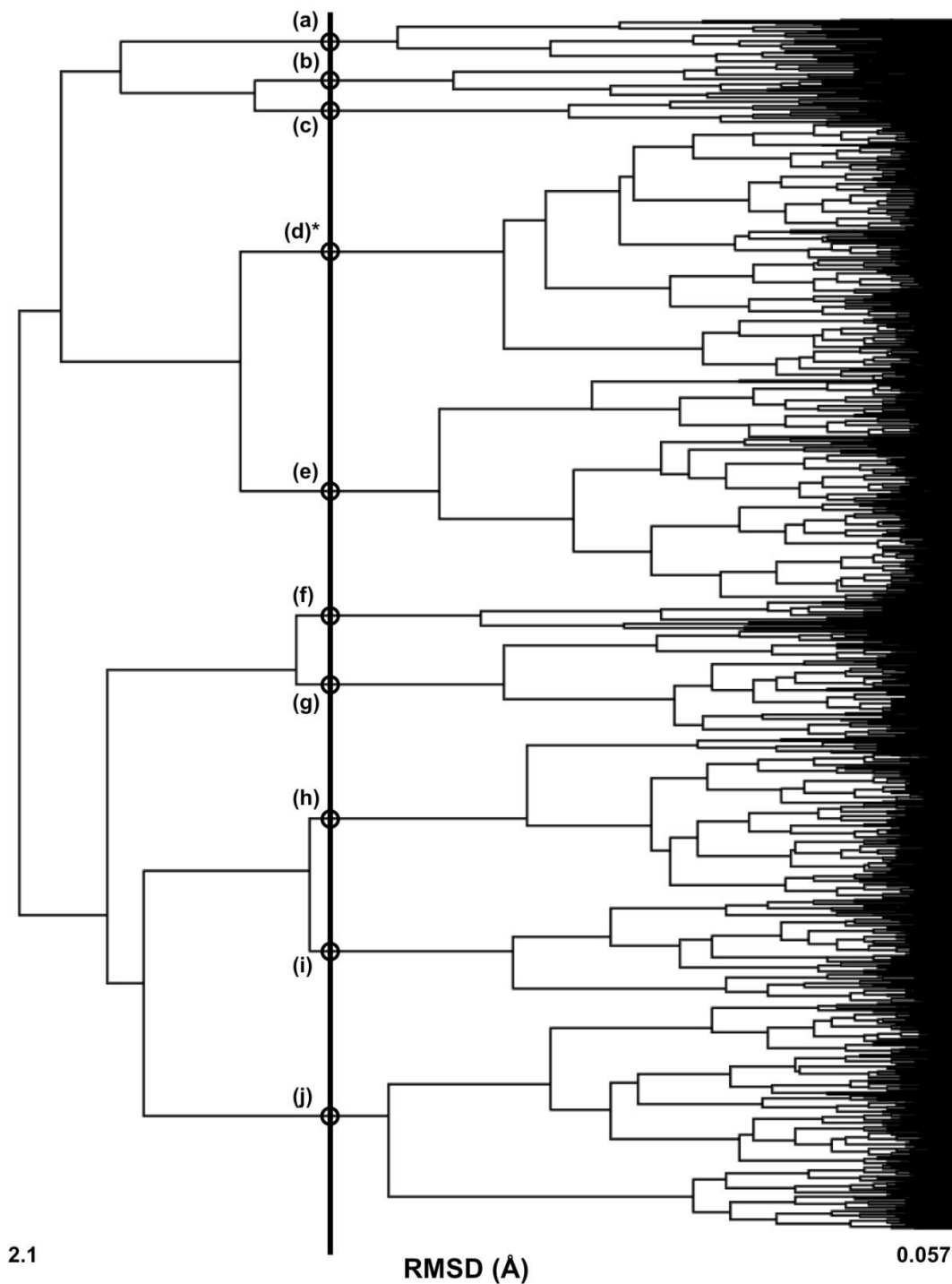
***p*-NH<sub>2</sub> 2,4'-MDA** Clustering analysis of 3,000 conformations of the para-amine protonated 2,4'-MDA. Clustering is based on root mean square distance of atoms of superimposed structures. The vertical black bar indicates the RMSD cutoff (1.35 Å) used to select the conformations (circled) for further analysis. The asterisk represents the structures shown in Chapter 4.



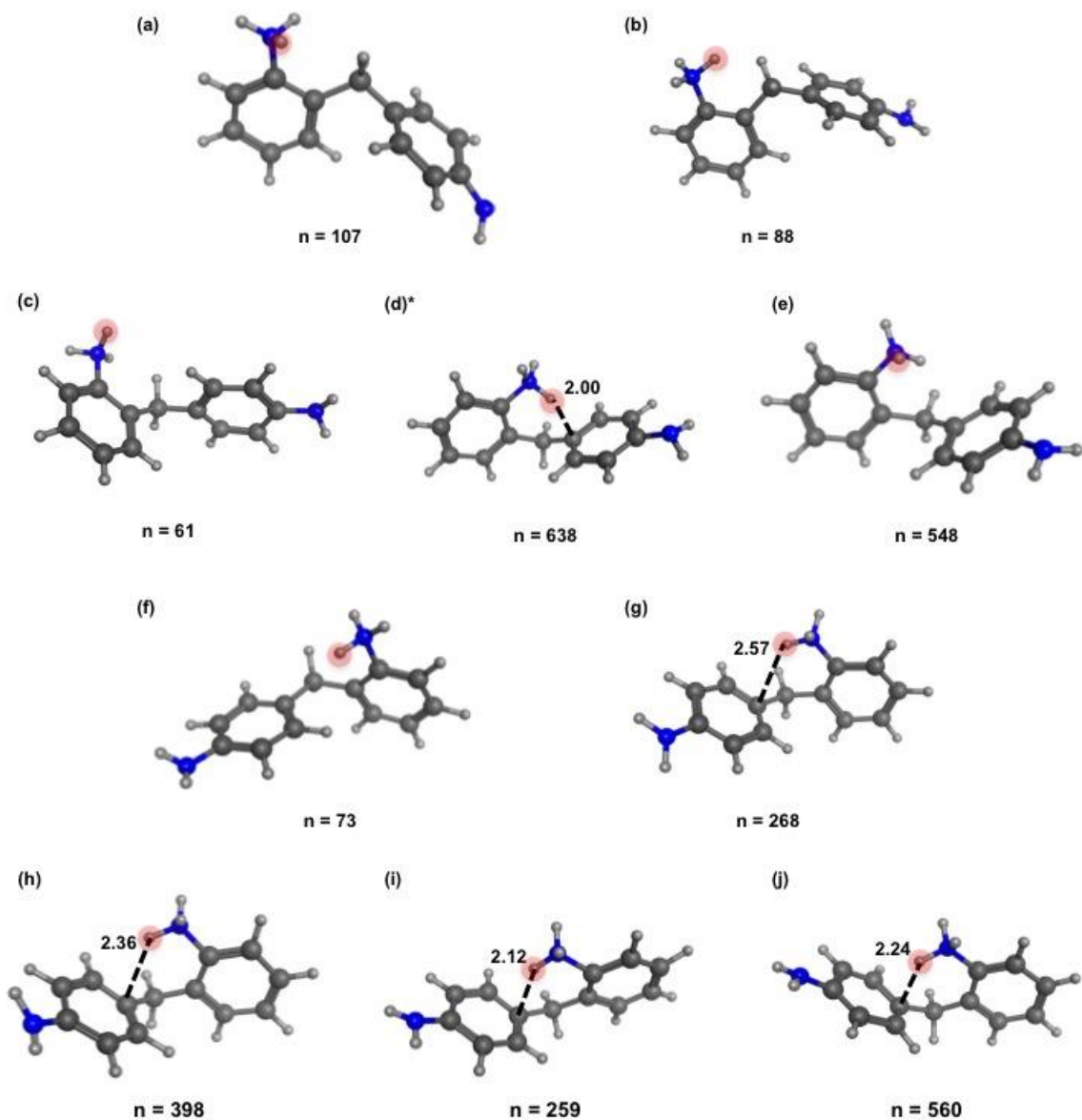
***p*-NH<sub>2</sub> 2,4'-MDA** Representative conformations of the para-amino protonated 2,4'-MDA generated from an elevated temperature molecular dynamic protocol. Carbon atoms are shown in dark grey, hydrogen in light grey, and nitrogen in blue. The asterisk represents the structures shown in Chapter 4. The number of conformations each of these represents from clustering is shown below the conformation.



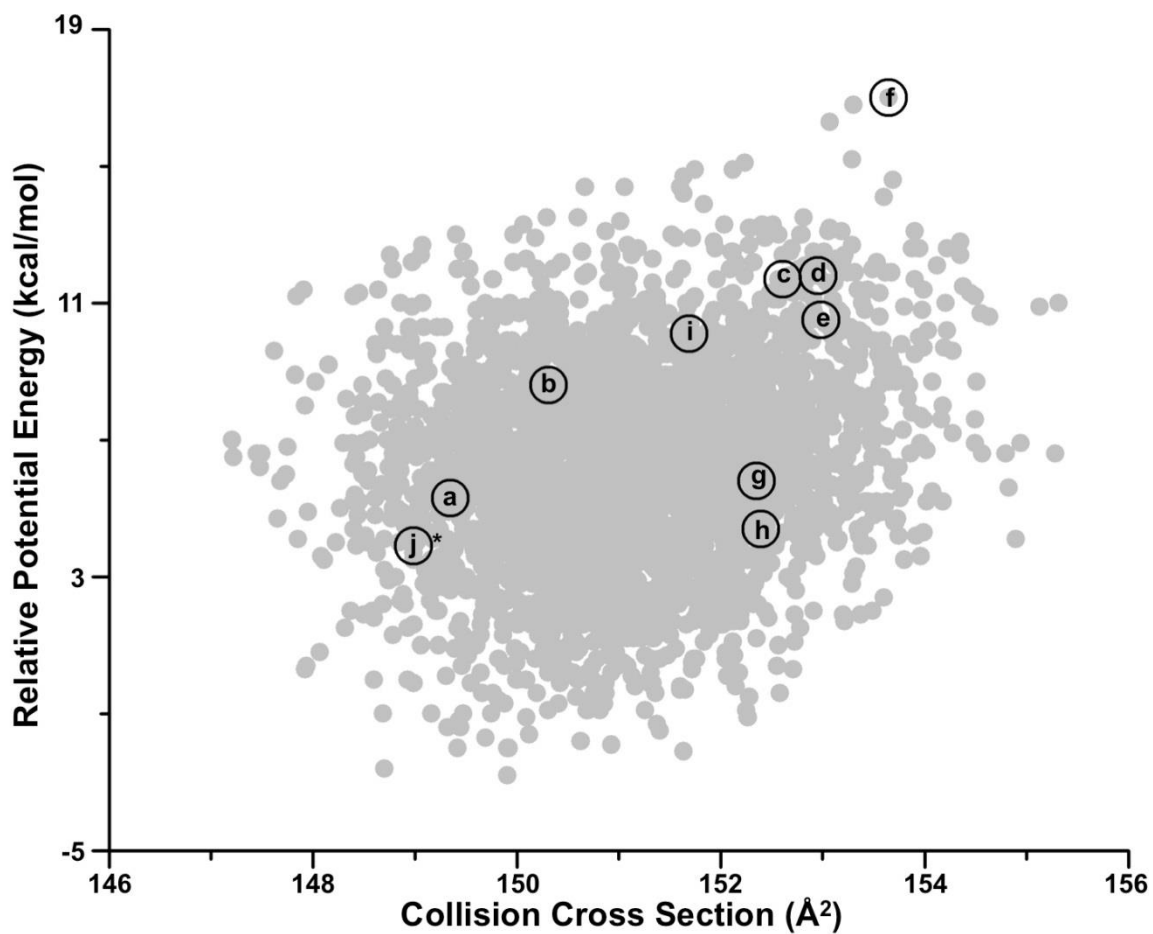
**o-NH<sub>2</sub> 2,4'-MDA** Conformational space plot for ortho-amine protonated 2,4'-MDA. The 3,000 generated conformations are represented in grey, the clustering representative conformations are labeled with letters that correspond to the structures in the following two pages. The asterisk indicates the structures that are shown in Chapter 4.



**o-NH<sub>2</sub> 2,4'-MDA** Clustering analysis of 3,000 conformations of the ortho-amine protonated 2,4'-MDA. Clustering is based on root mean square distance of atoms of superimposed structures. The vertical black bar indicates the RMSD cutoff (1.35 Å) used to select the conformations (circled) for further analysis. The asterisk represents the structures shown in Chapter 4.

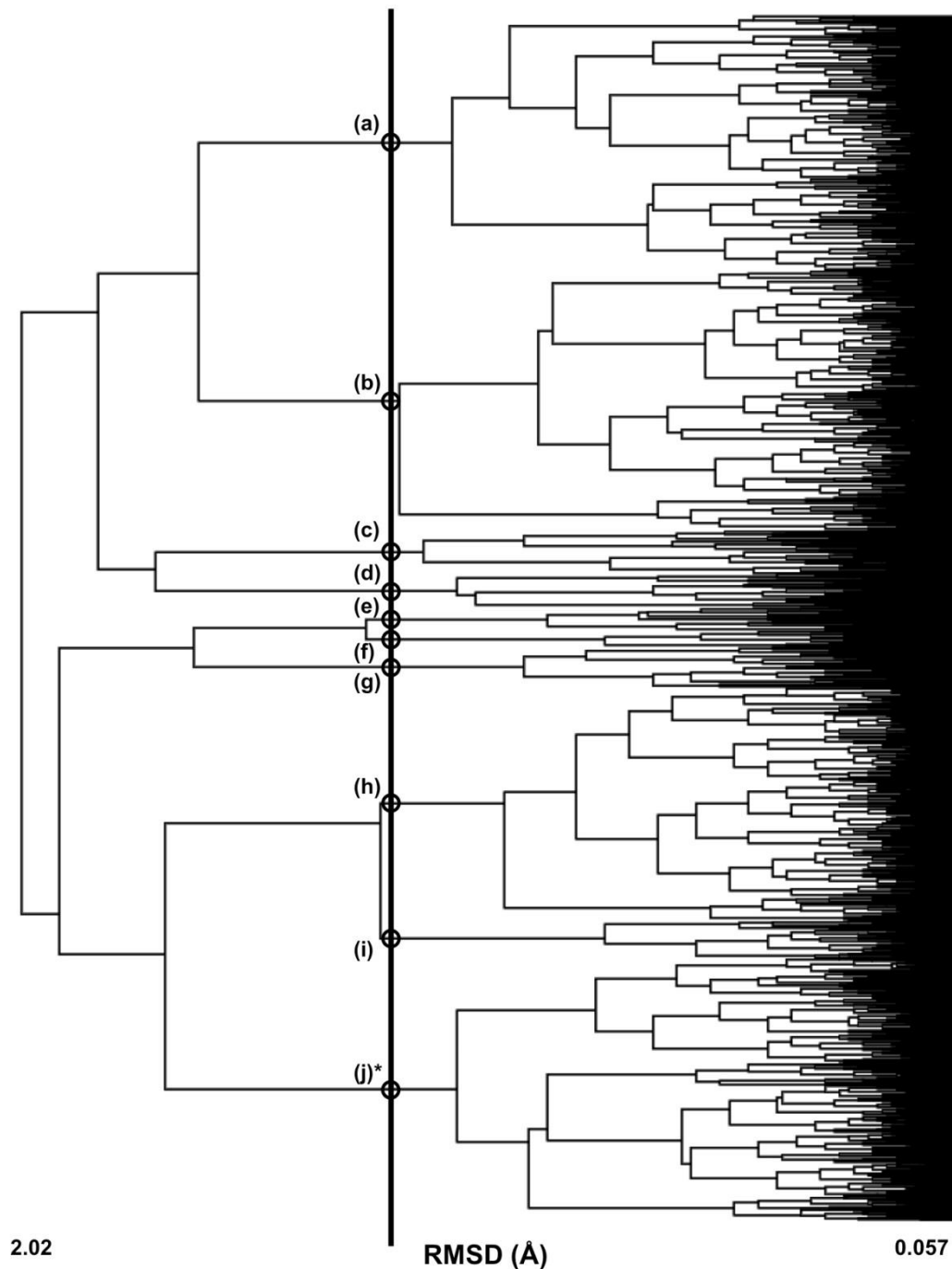


**o-NH<sub>2</sub> 2,4'-MDA** Representative conformations of the ortho-amine protonated 2,4'-MDA generated from an elevated temperature molecular dynamic protocol. Carbon atoms are shown in dark grey, hydrogen in light grey, and nitrogen in blue. The asterisk represents the structures shown in Chapter 4. The number of conformations each of these represents from clustering is shown below the conformation.

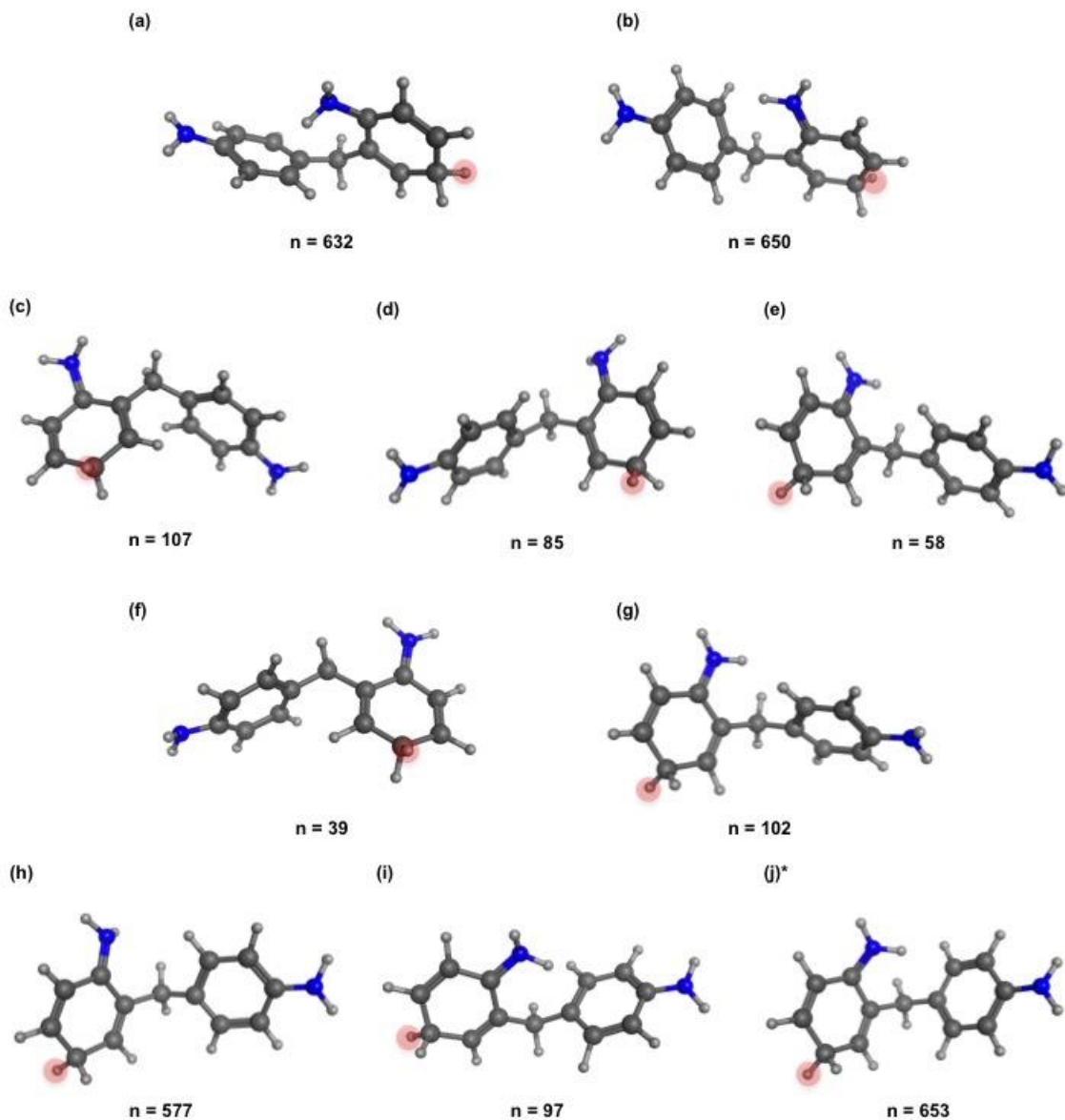


**ring 2,4'-MDA** Conformational space plot for the ring-protonated 2,4'-MDA. The 3,000 generated conformations are represented in grey, the clustering representative conformations are labeled with letters that correspond to the structures in the following two pages. The asterisk indicates the structures that are shown in Chapter 4.





**ring 2,4'-MDA** Clustering analysis of 3,000 conformations of the ring-protonated 2,4'-MDA. Clustering is based on root mean square distance of atoms of superimposed structures. The vertical black bar indicates the RMSD cutoff (1.25 Å) used to select the conformations (circled) for further analysis. The asterisk represents the structures shown in Chapter 4.



**ring 2,4'-MDA** Representative conformations of the ring-protonated 2,4'-MDA generated from an elevated temperate molecular dynamic protocol. Carbon atoms are shown in dark grey, hydrogen in light grey, and nitrogen in blue. The asterisk represents the structures shown in Chapter 4. The number of conformations each of these represents from clustering is shown below the conformation.

F. **Raw Mass Spectrometry Data from Dissertation Figures** (pre-calib.; no baseline corr.)

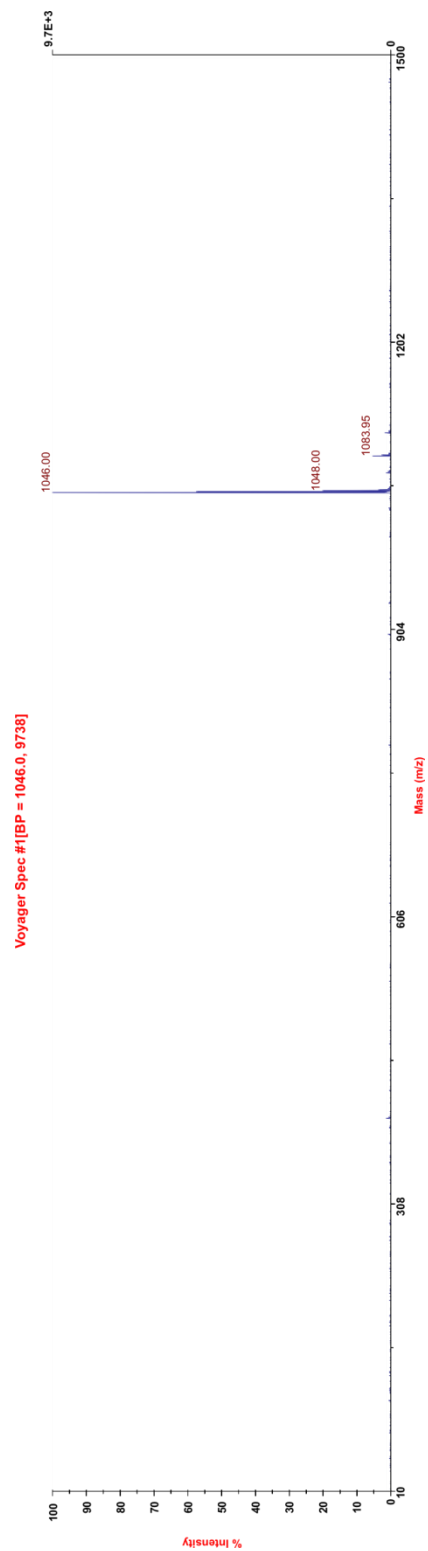


Figure 2-2c (top).

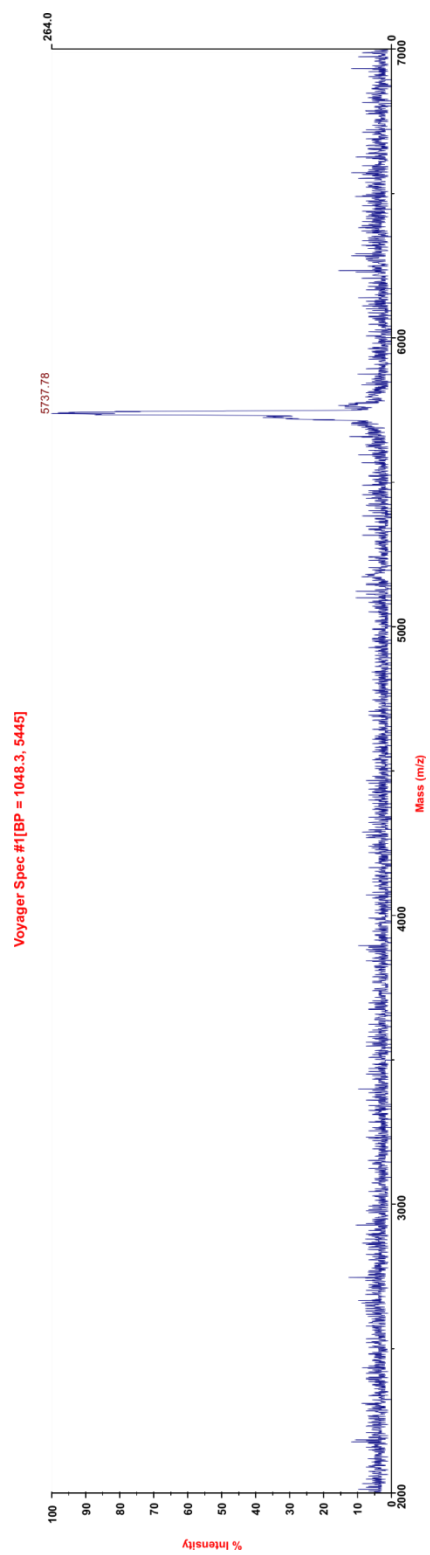


Figure 2-2c (bottom).

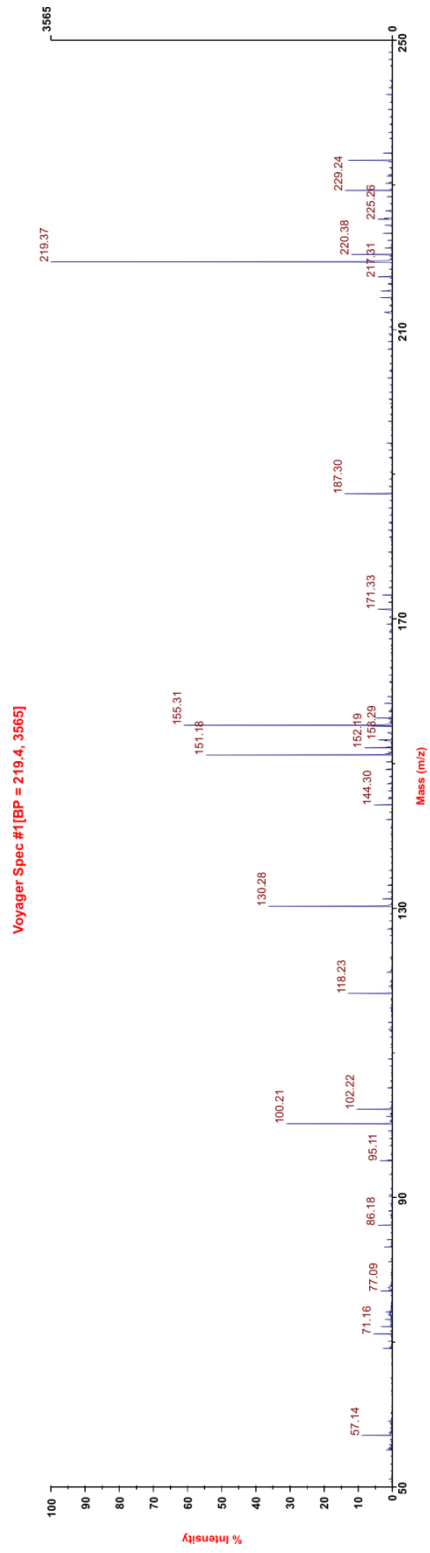


Figure 2-4.

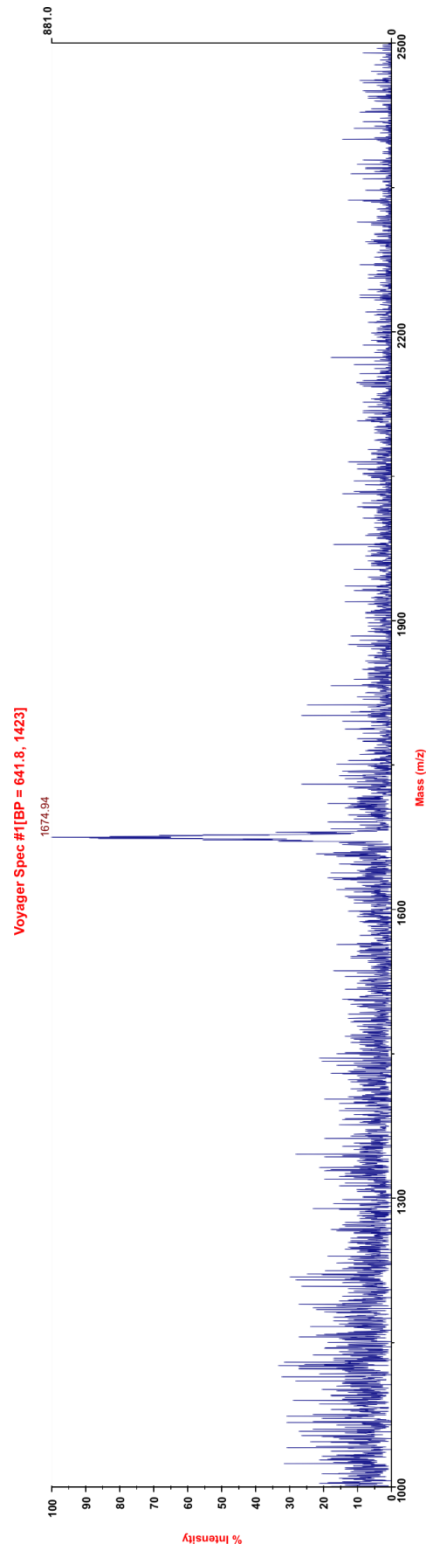


Figure 2-5.

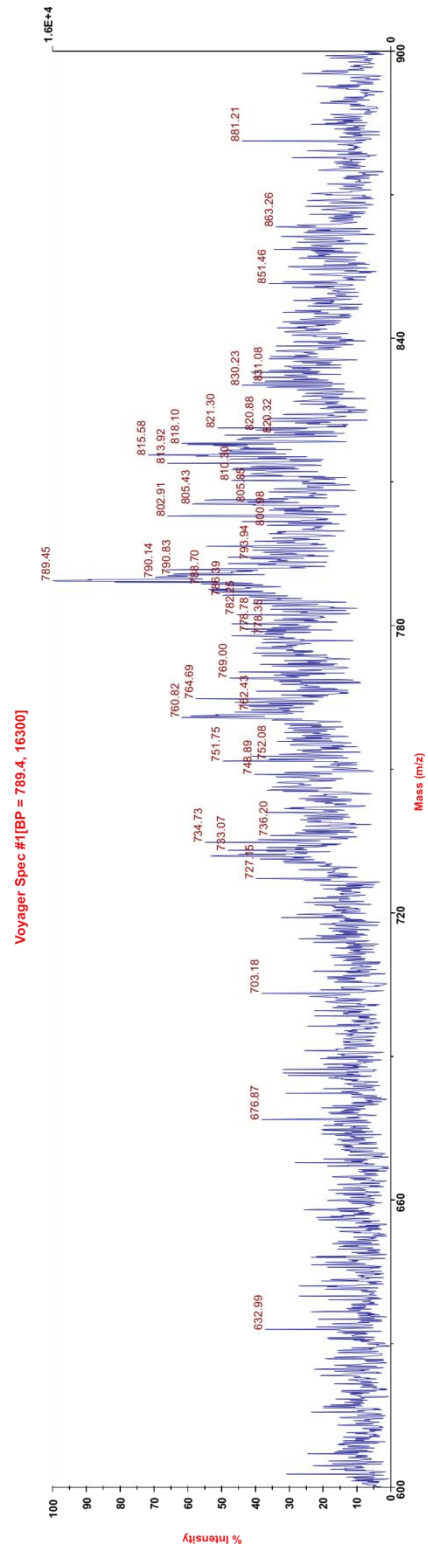


Figure 2-6b.

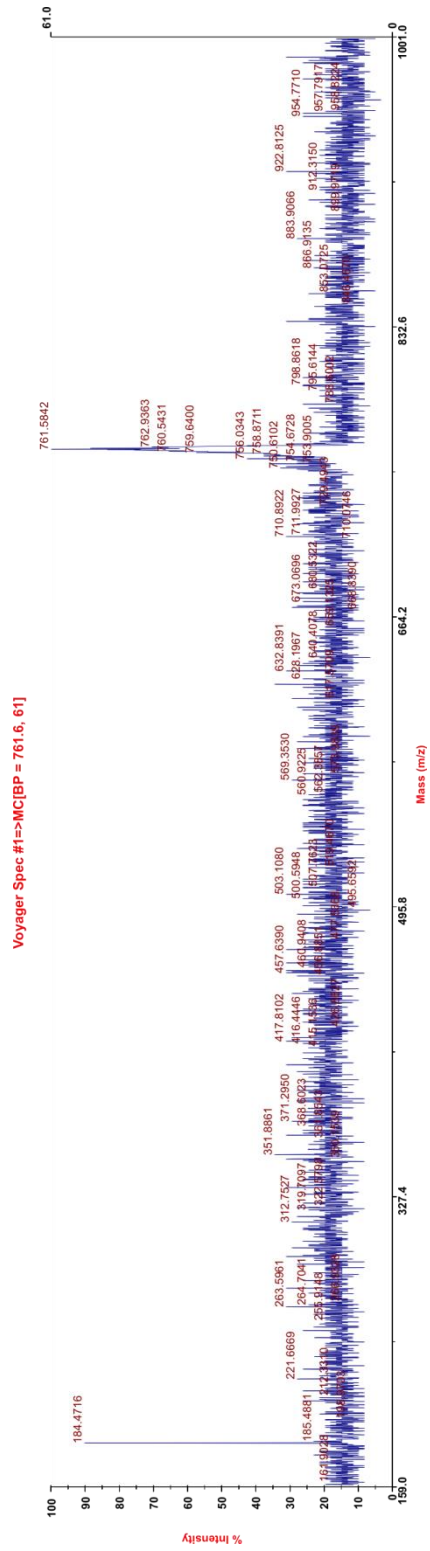


Figure 2-9a.



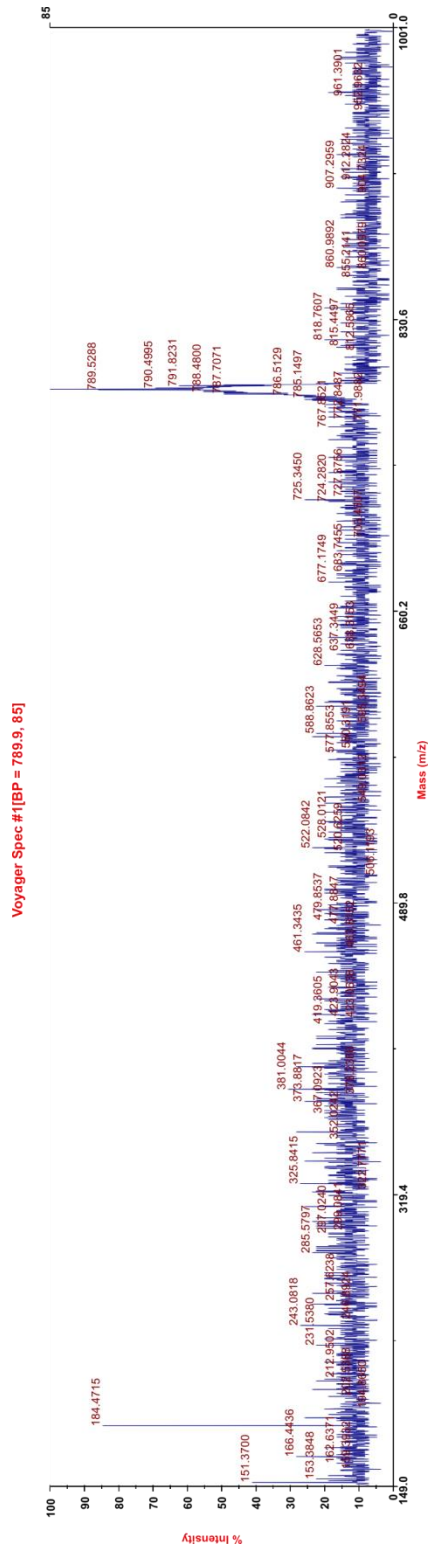


Figure 2-9b.

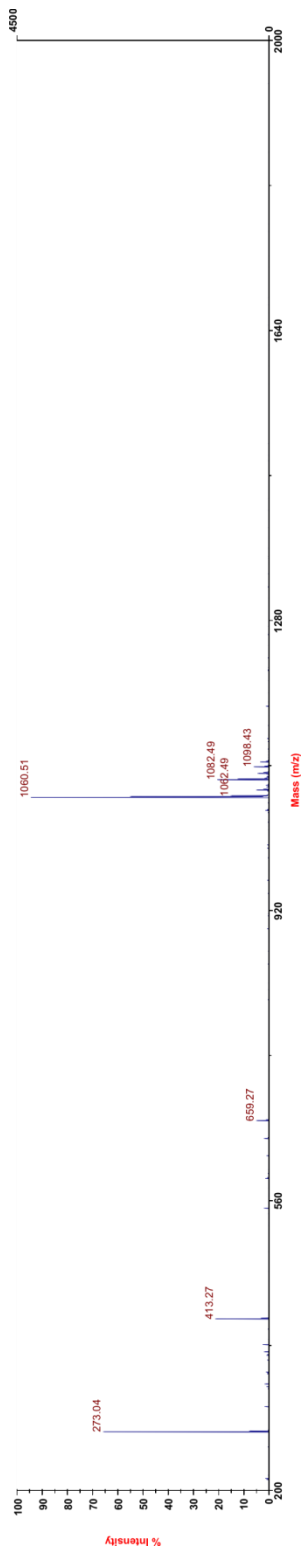


Figure 3-4a.

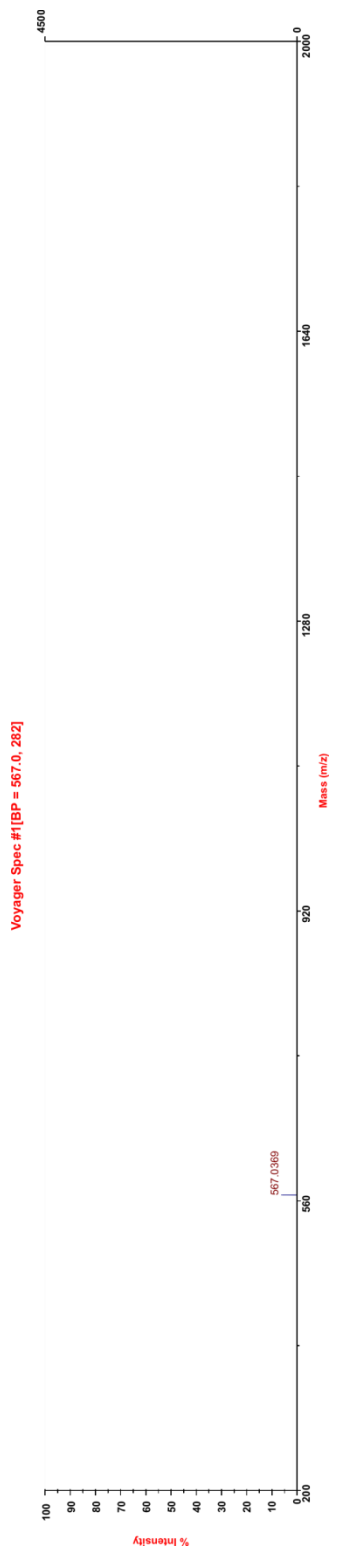


Figure 3-4b.

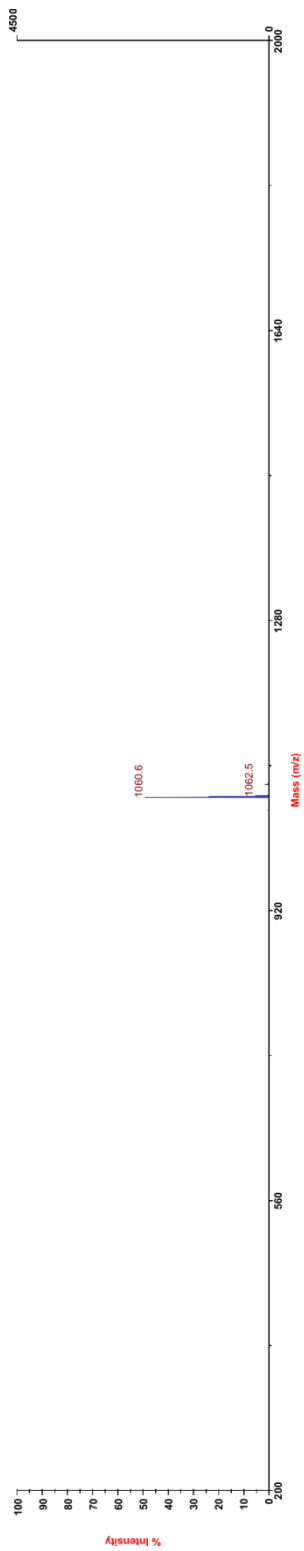


Figure 3-4c.

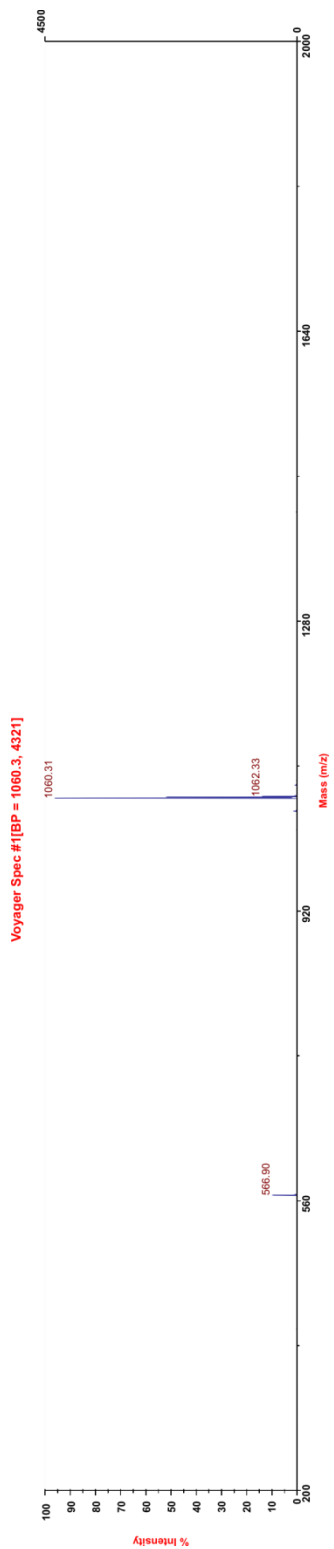


Figure 3-4d.

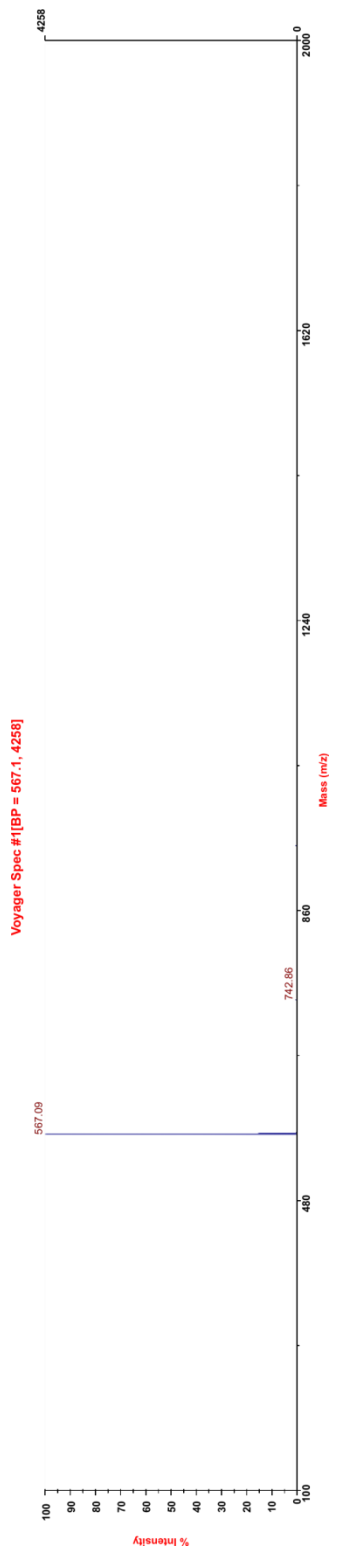


Figure 3-5a.

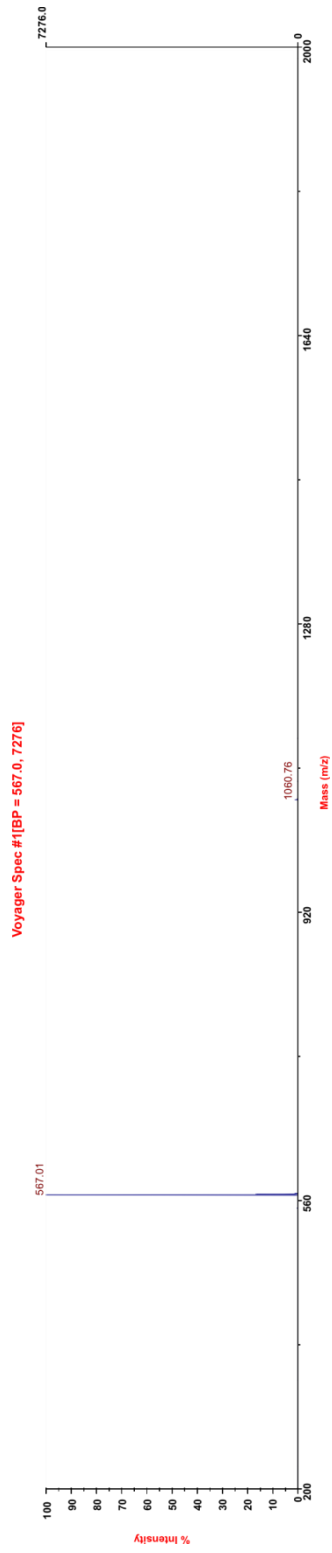


Figure 3-6.

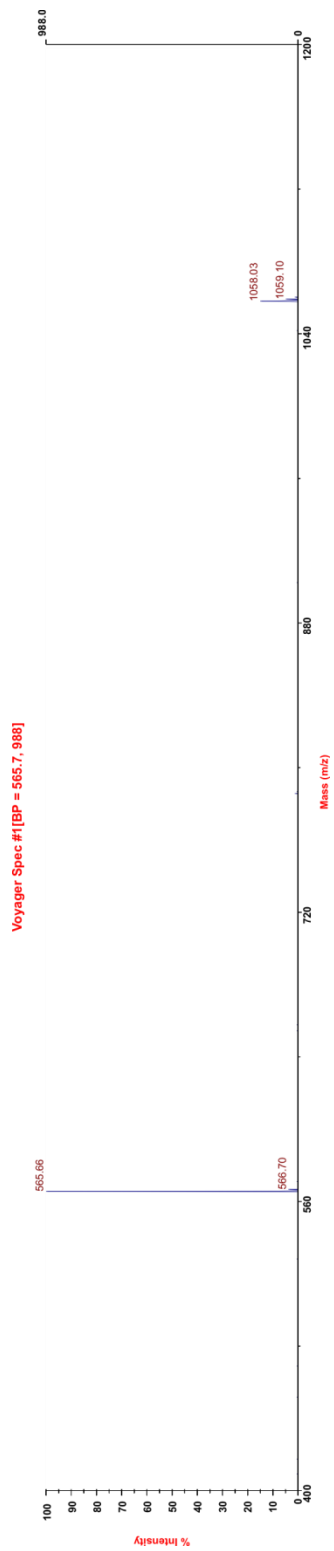


Figure 3-7 (top).



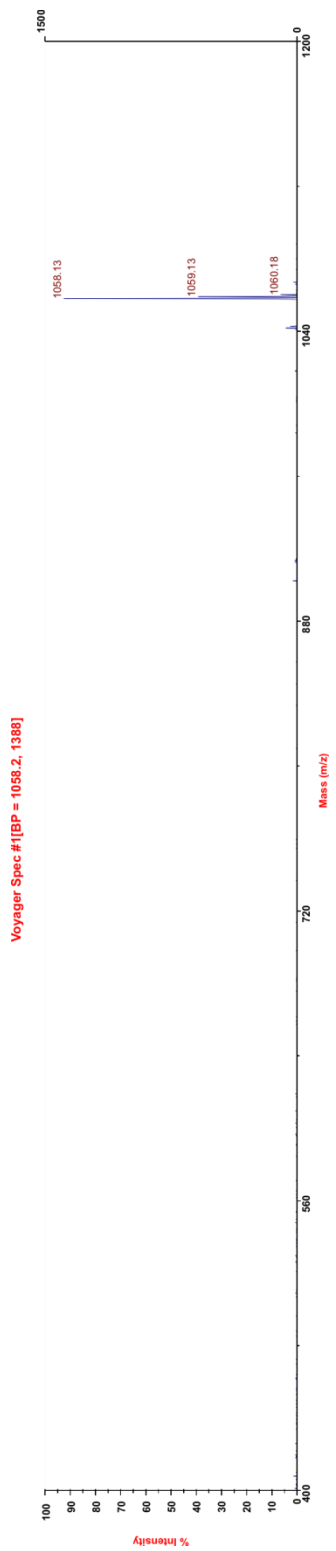


Figure 3-7 (middle).

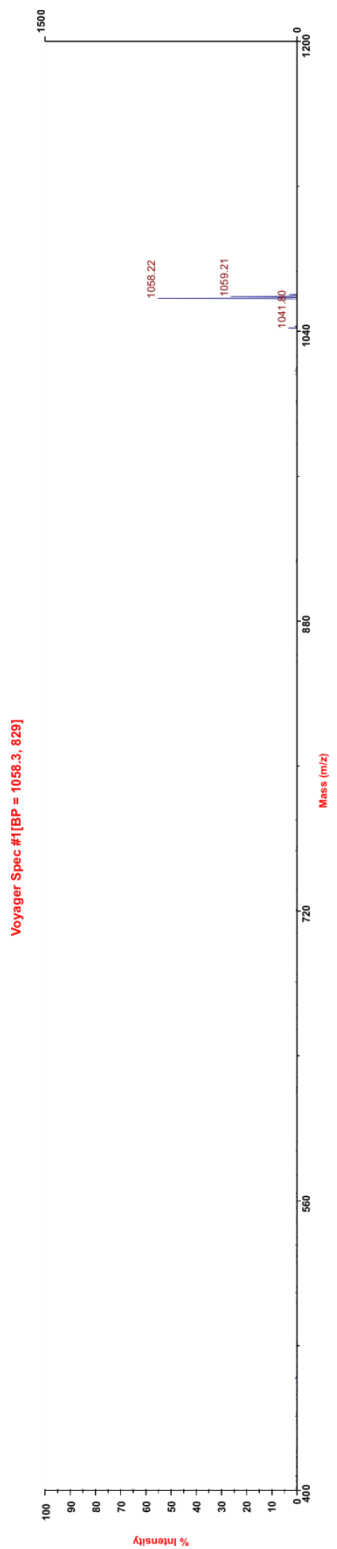


Figure 3-7 (bottom).

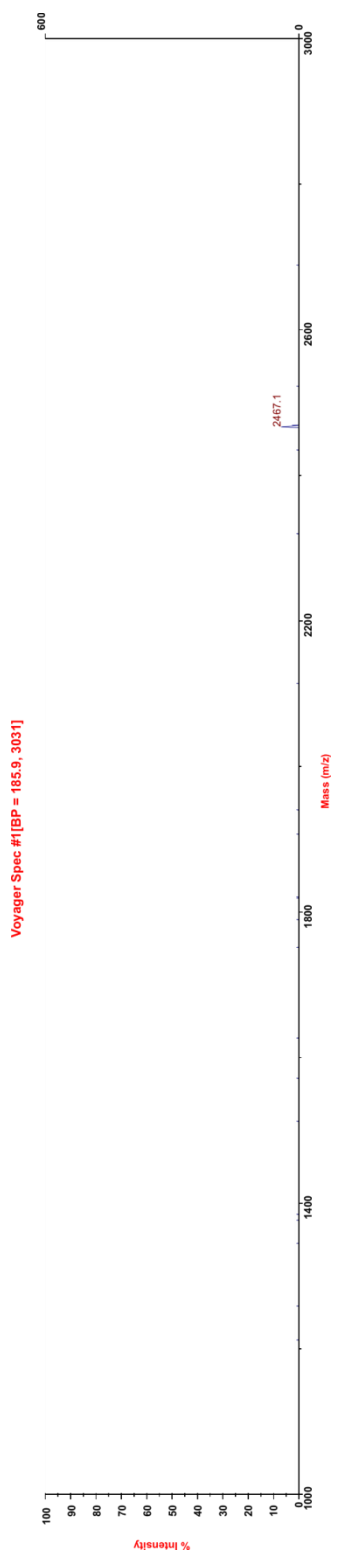


Figure 3-8a (top).

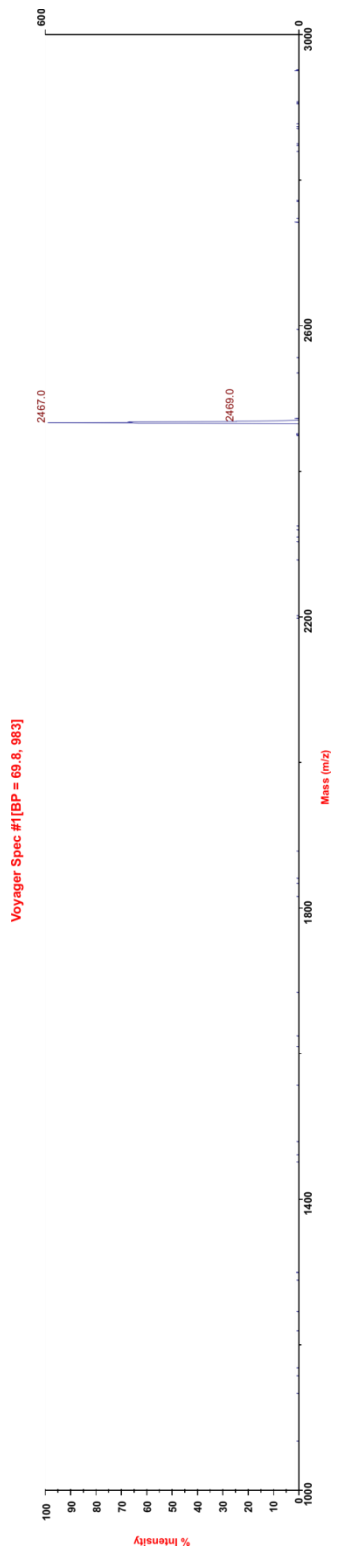


Figure 3-8a (bottom).

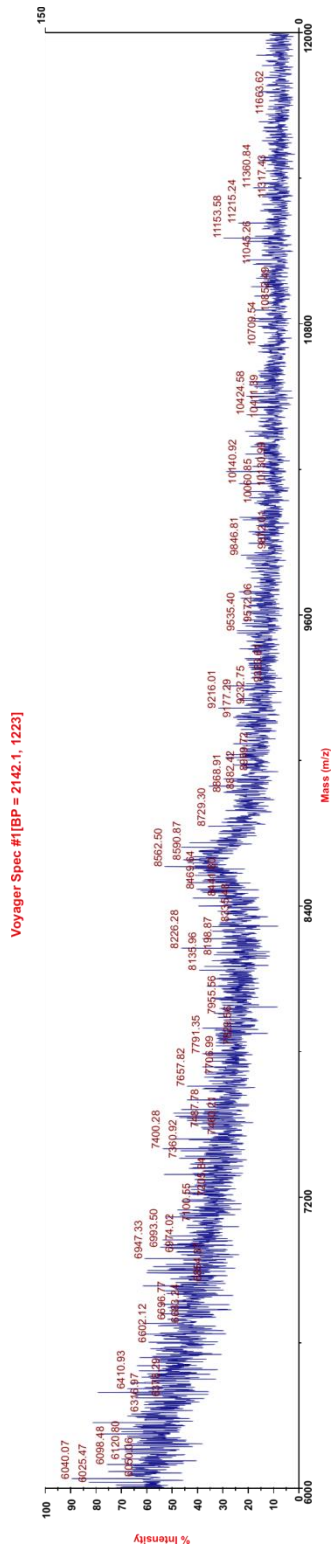


Figure 3-8b (top).

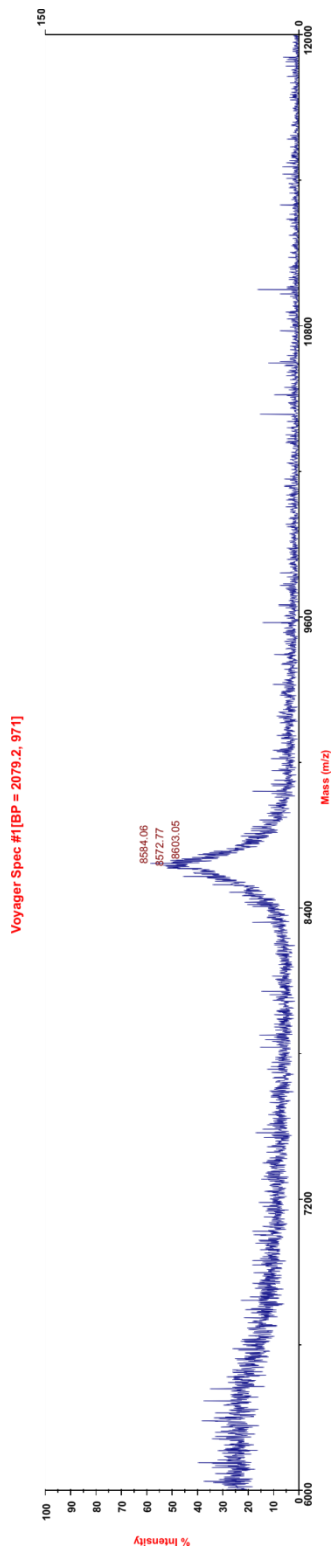


Figure 3-8b (bottom).

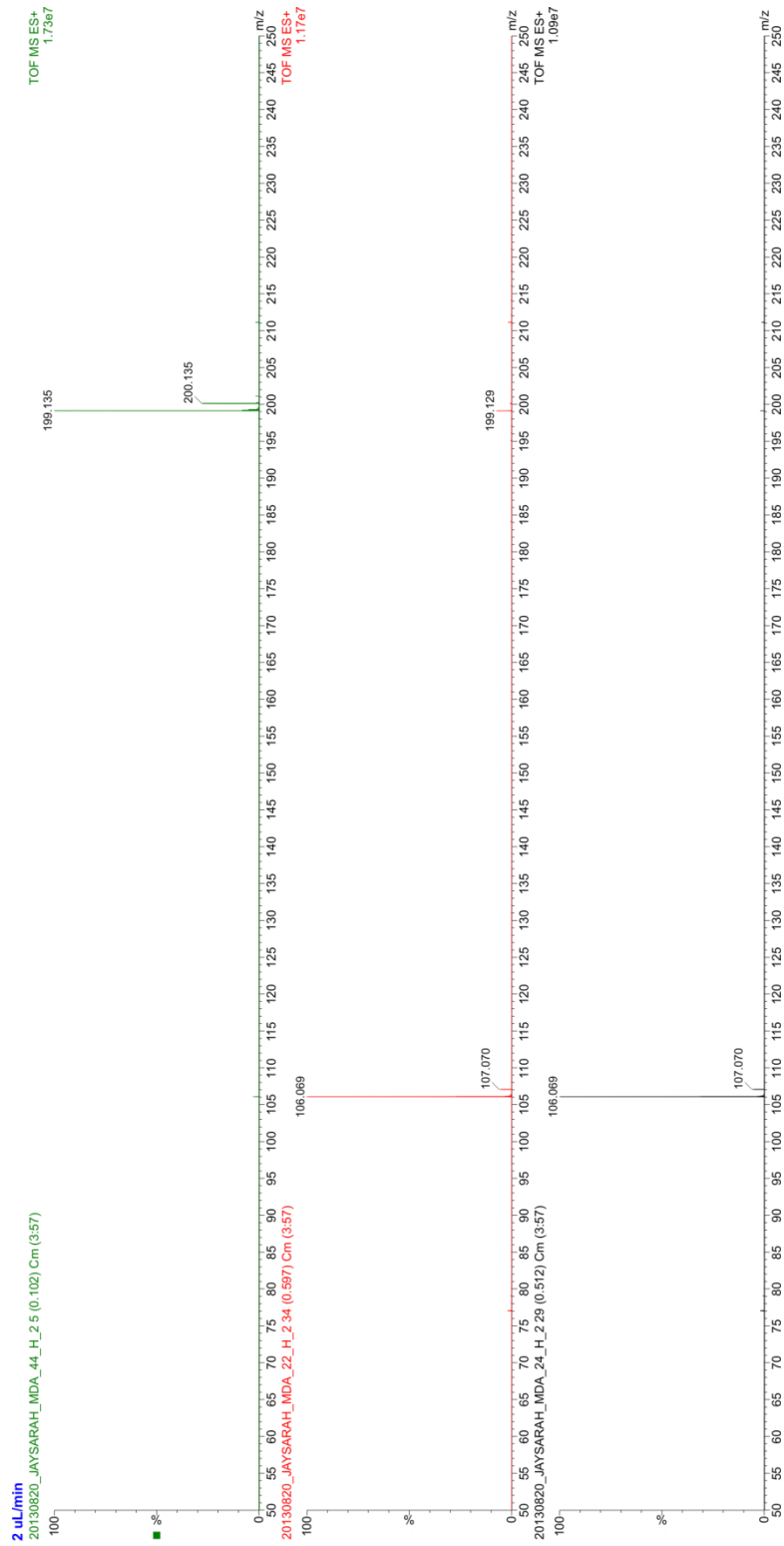


Figure 4-3 (left).

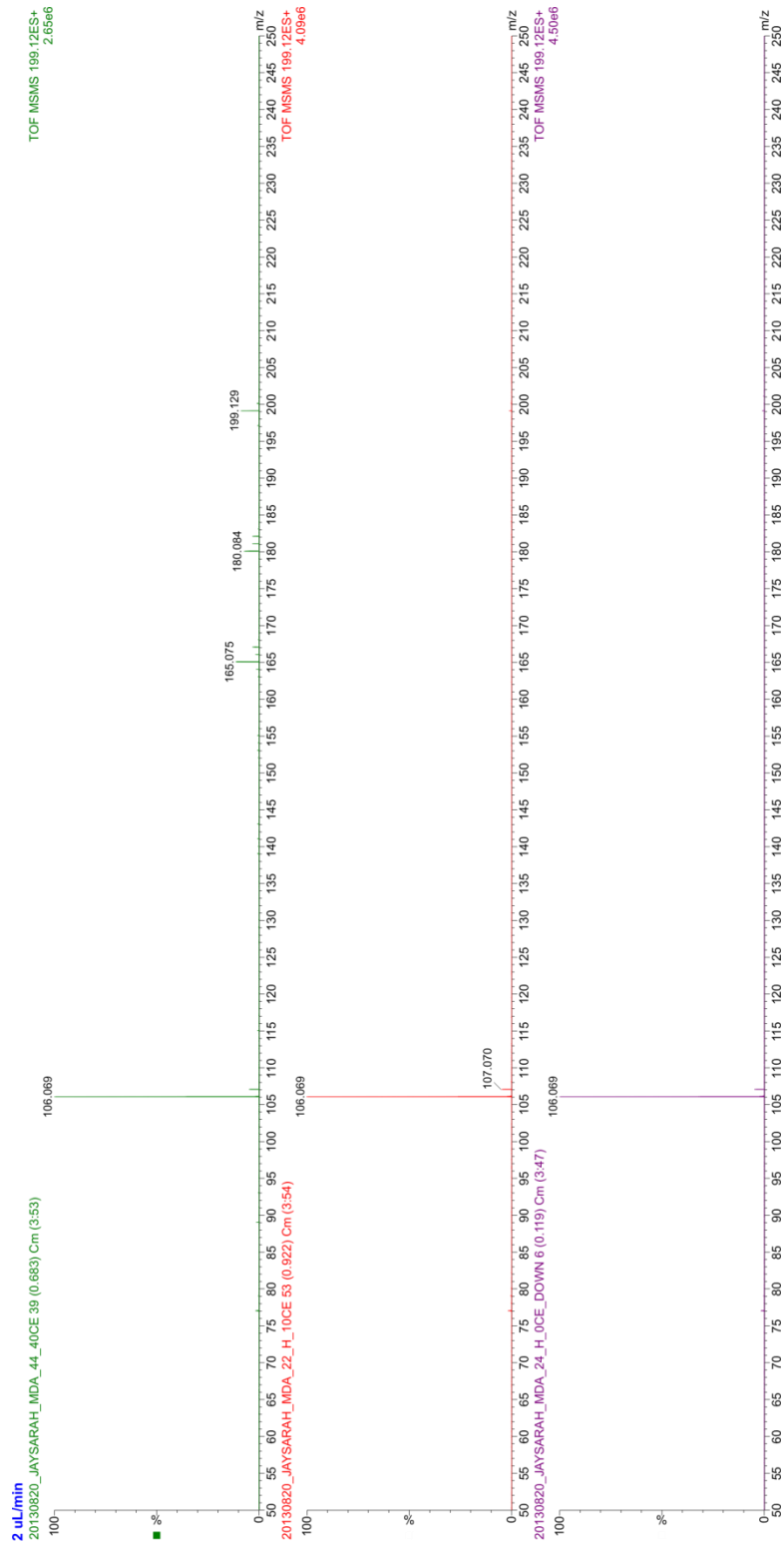


Figure 4-3 (right).



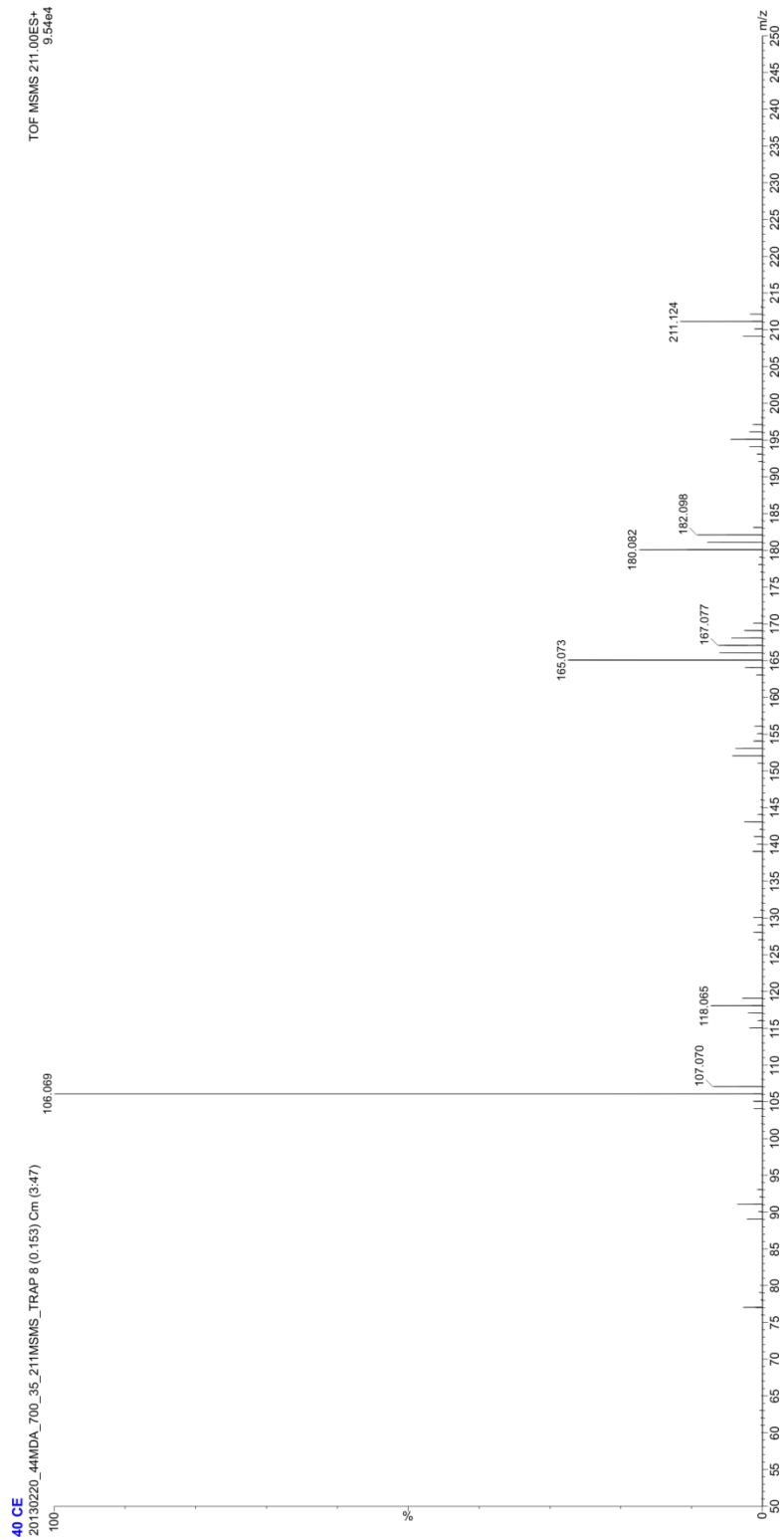


Figure 4-4 (left).

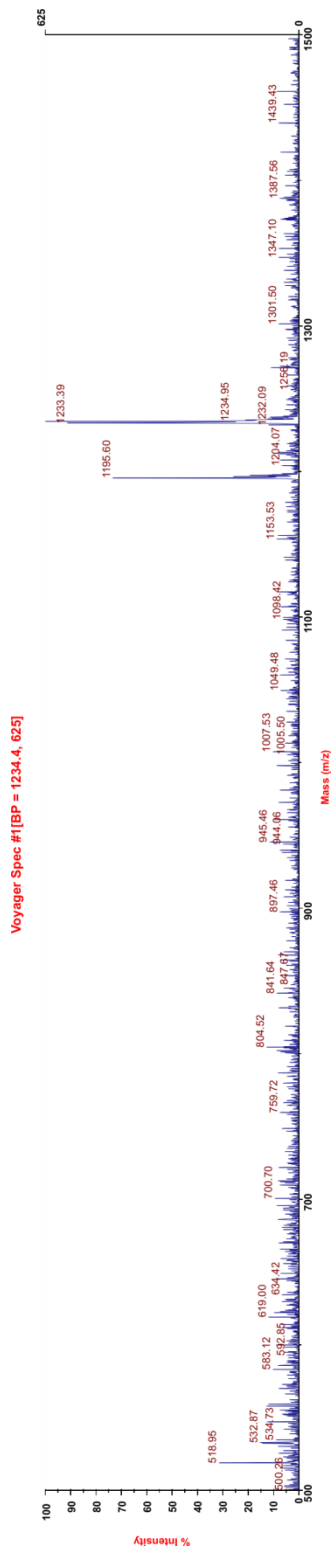


Figure 5-3a.

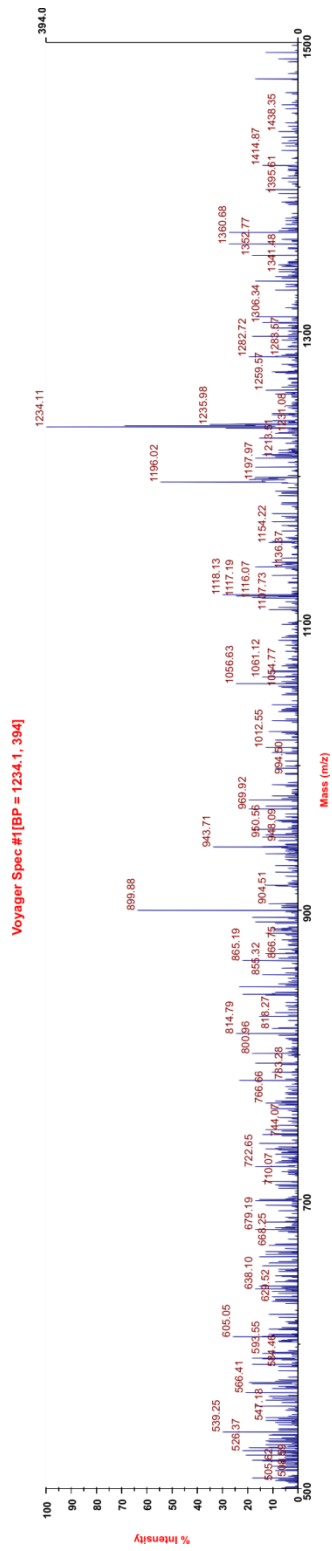


Figure 5-3b.

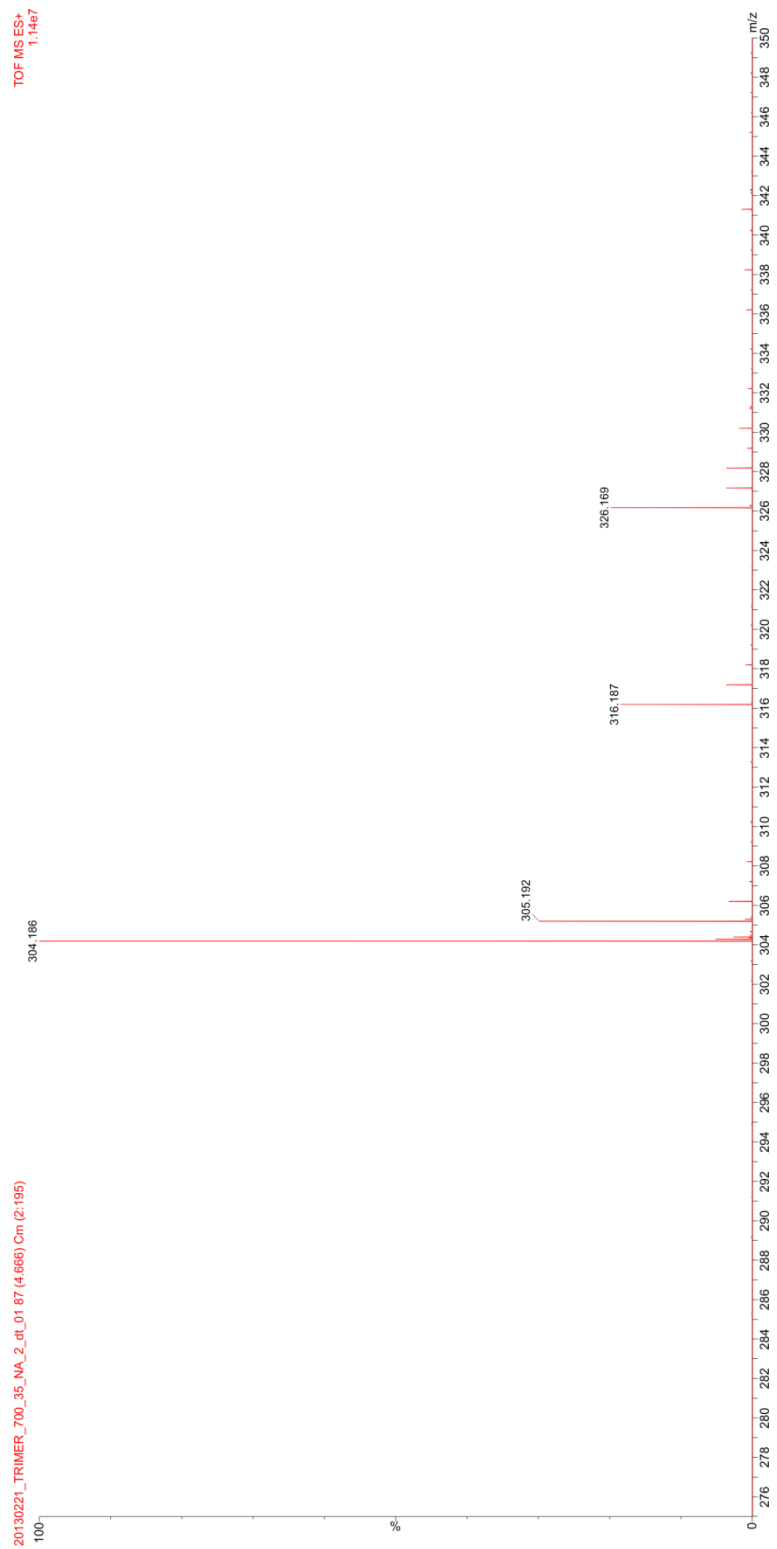


Figure 5-6.

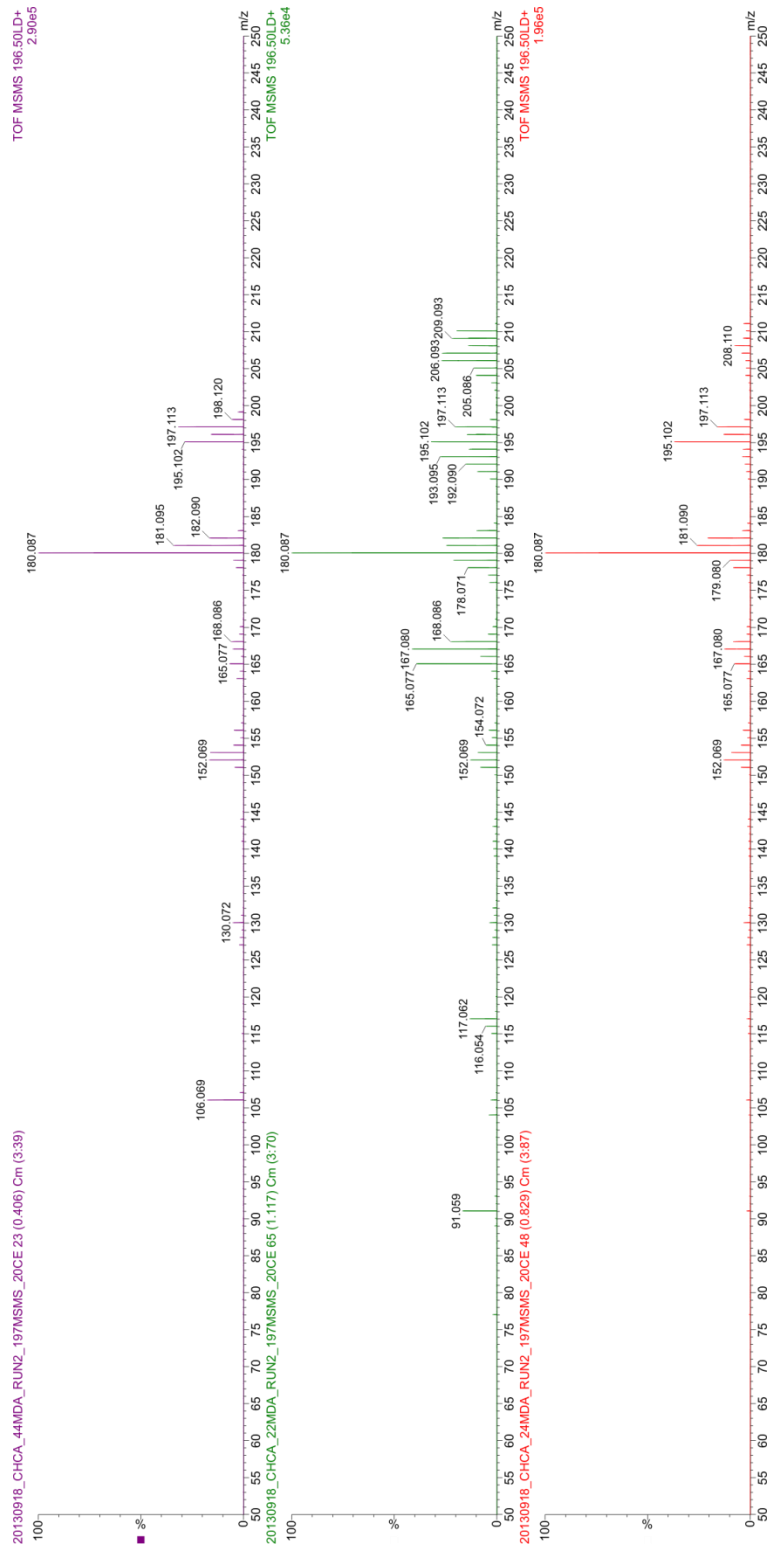


Figure 5-7.

G. Raw Ion Mobility Data from Dissertation Figures (before CCS conversion)

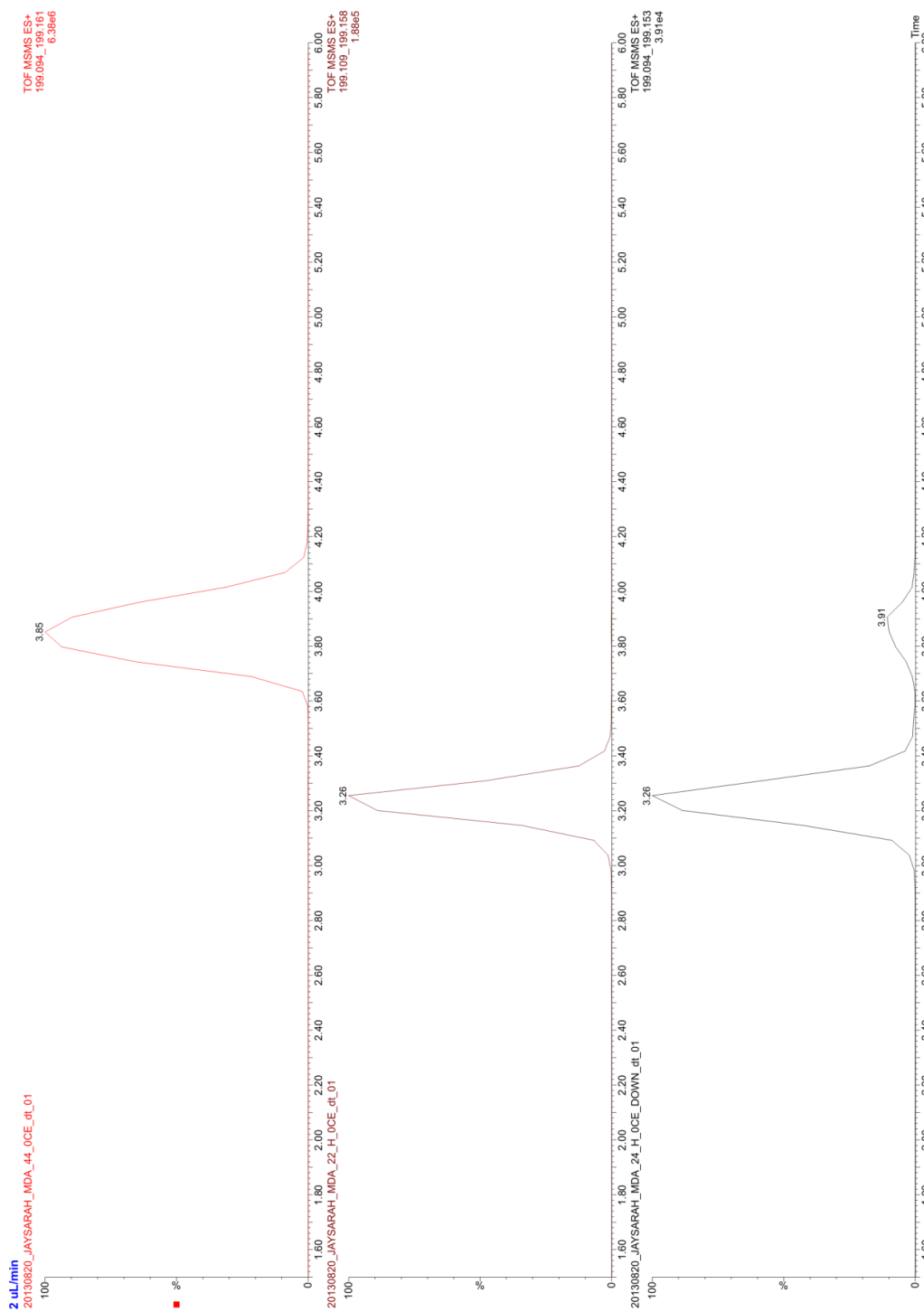


Figure 4-6a.

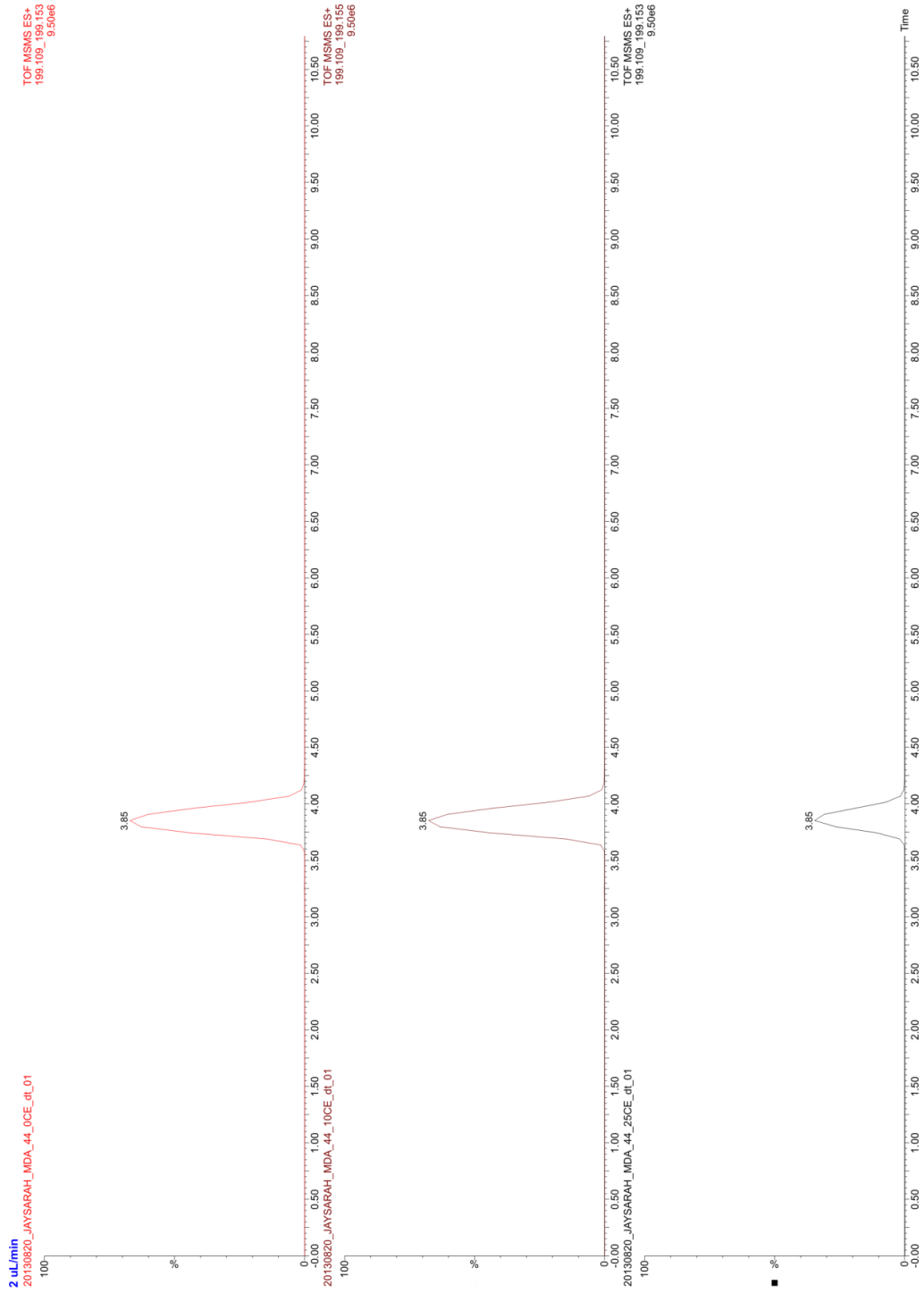


Figure 4-7a.

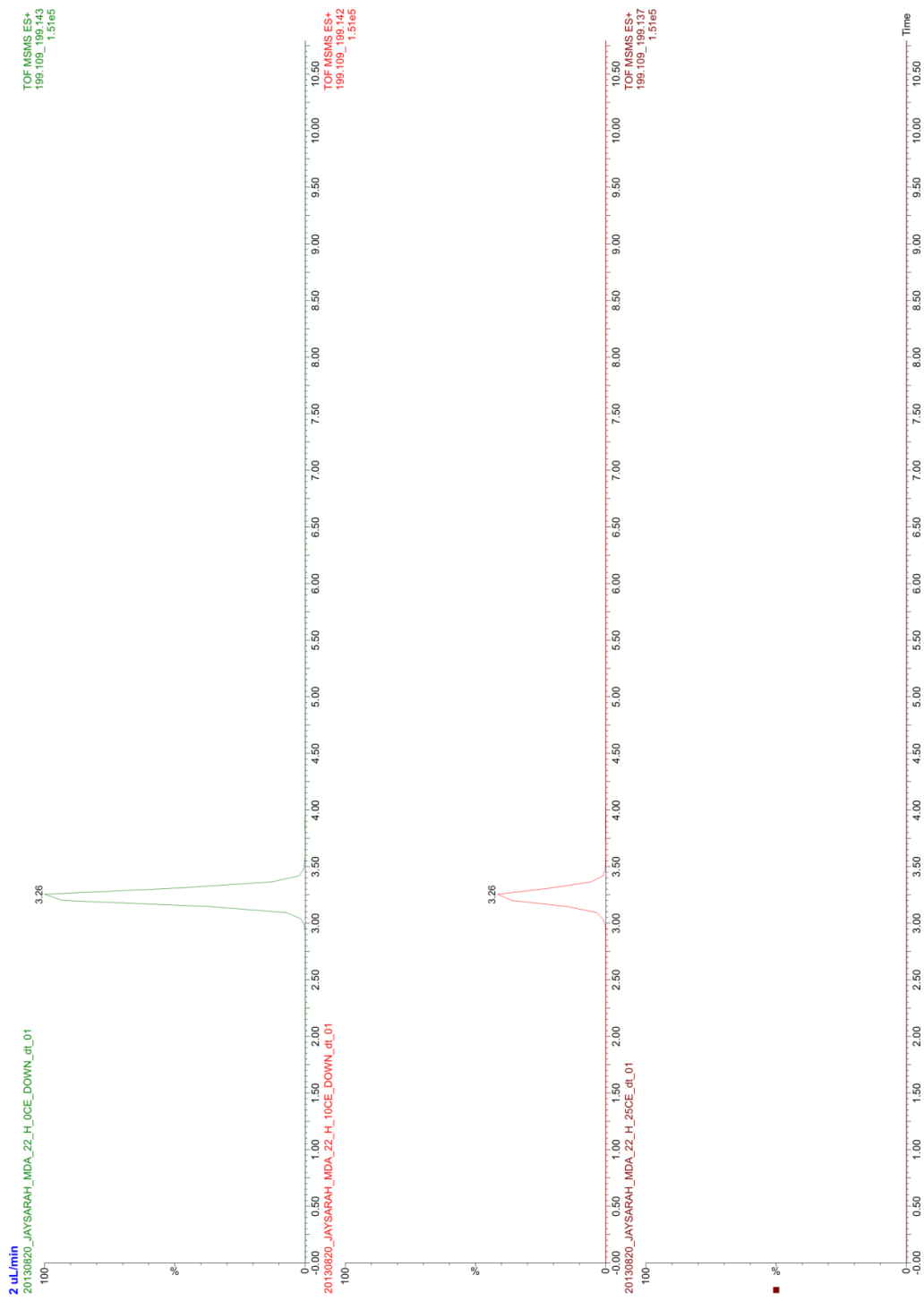


Figure 4-7b.



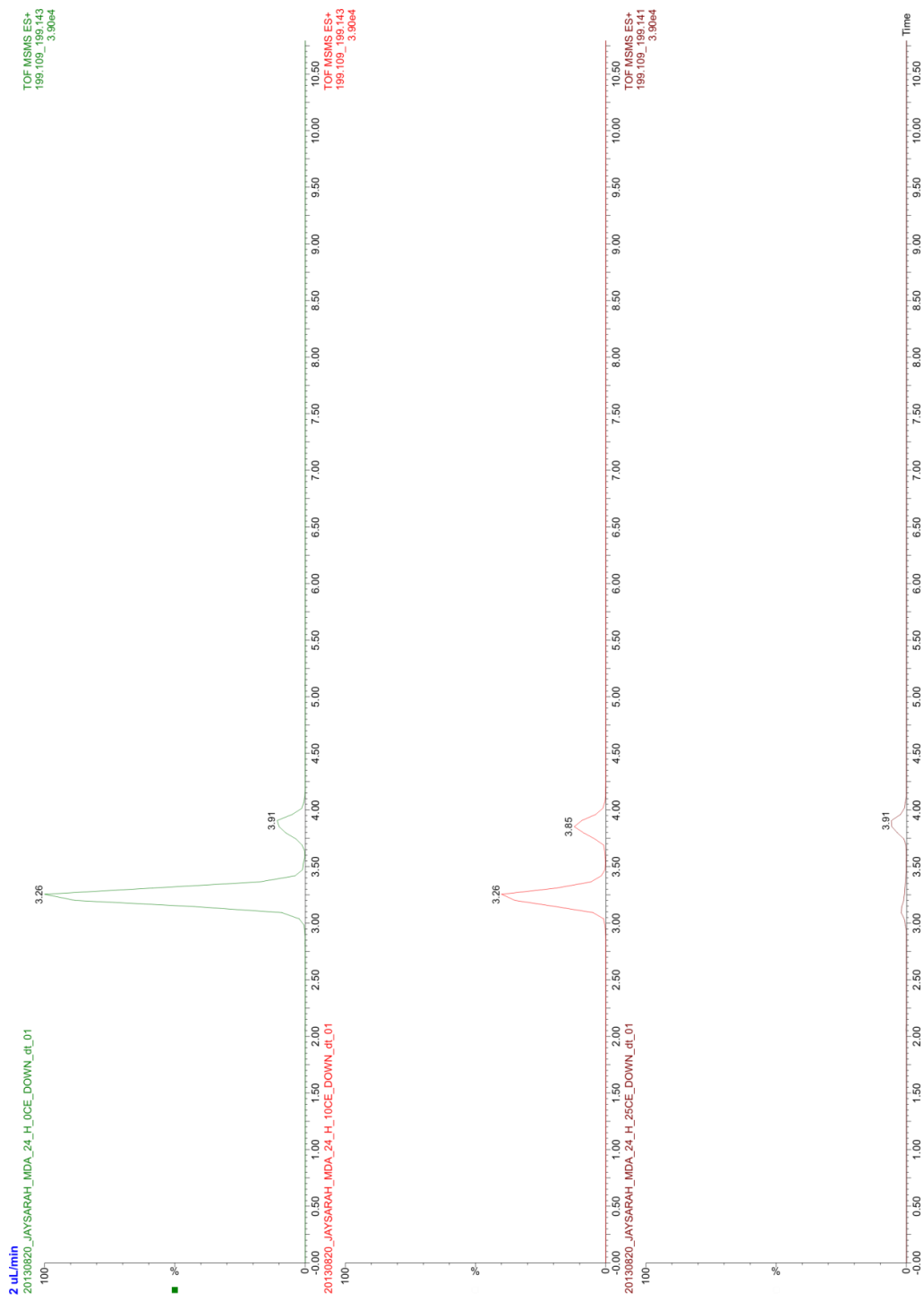


Figure 4-7c.

## H. References of Adaptation for Chapters

At the time of the writing of this dissertation, the chapters were modified from manuscripts either in publication, in submission, or in preparation for submission, as shown below.

- CHAPTER I. Forsythe, J. G.; McLean, J. A. Nanomaterial-based MALDI-MS Imaging of Biological Samples. In preparation for submission to *The Analyst*.
- CHAPTER II. Forsythe, J. G.; Broussard, J. A.; Lawrie, J. L.; Kliman, M.; Jiao, Y.; Weiss, S. M.; Webb, D. J.; McLean, J. A. Semitransparent Nanostructured Films for Imaging Mass Spectrometry and Optical Microscopy. *Anal. Chem.* **2012**, *84*, 10665-10670.
- CHAPTER III. Forsythe, J. G.; Christov, P.; Portonovo, P.; Stow, S. M.; McLean, J. A. Composite Matrix-initiator Surface for Enhanced Nanostructure-initiator Mass Spectrometry. In preparation for submission to *ChemComm*.
- CHAPTER IV. Forsythe, J. G.; Stow, S. M.; Nefzger, H.; Kwiecien, N. W.; May, J. C.; McLean, J. A.; Hercules, D. M. Structural Characterization of Methylenedianiline Regioisomers by Ion Mobility and Mass Spectrometry I. Electrospray Ionization of Dimers. Submitted to *Anal. Chem.*

**I. Curriculum Vitae (Updated 1/2014)**

**Jay G. Forsythe**

Vanderbilt University  
Department of Chemistry  
7330 Stevenson Center  
Station B 351822  
Nashville, TN 37235

Phone: 610 - 291 - 8096 (cell)  
615 - 343 - 4563 (lab)

E-mail: [jay.g.forsythe@vanderbilt.edu](mailto:jay.g.forsythe@vanderbilt.edu)  
[jaygforsythe@gmail.com](mailto:jaygforsythe@gmail.com)

---

**EDUCATION**

**Ph.D. Candidate in Chemistry**

Department of Chemistry, Vanderbilt University, Nashville, TN, 3.71 GPA  
Research Advisor: John A. McLean

**B.S. in Chemistry** (ACS-certified), May 2009

Department of Chemistry, Furman University, Greenville, SC, 3.58 GPA, *cum laude*  
Research Advisors: John F. Wheeler and Sandra K. Wheeler  
Undergraduate Thesis: "Capillary Electrophoresis and Isothermal Titration Calorimetry in the Investigation of Cr(III) Interactions with DNA"

**HONORS, AWARDS, AND FELLOWSHIPS**

2013 College Teaching Certificate, Vanderbilt University Center for Teaching  
2010-12 Teaching Fellow, Department of Chemistry, Vanderbilt University  
2009 American Institute of Chemists Award in Chemistry, Furman University  
2006 Phi Eta Sigma Honor Society, Furman University

**INTELLECTUAL PROPERTY**

2. **Jay G. Forsythe**, Plamen Christov, Padma Portonovo, and John A. McLean, Molecular Strategies for Enhanced Nanostructure-Initiator Mass Spectrometry, US Provisional Patent (Appl. #61831818, June 6, 2013).
1. **Jay G. Forsythe**, Joshua A. Broussard, Jenifer L. Lawrie, Michal Kliman, Yang Jiao, Sharon M. Weiss, Donna J. Webb, and John A. McLean, Semi-transparent Nanostructured Films for Mass Spectrometry and Optical Microscopy of Chemical and Biological Samples, Vanderbilt University Invention Disclosure (#12079, January 4, 2012).

**PUBLICATIONS**

6. Joseph C. Evans, Kelly M. Hines, **Jay G. Forsythe**, John A. McLean, and Donna J. Webb, Phosphorylation Mapping of Asef-2 (*title TBD*), in preparation for submission to *Journal of Proteome Research*.
5. **Jay G. Forsythe**, Plamen Christov, Padma Portonovo, Sarah M. Stow, and John A. McLean, Composite Matrix-Initiator Surface for Enhanced Nanostructure-Initiator Mass Spectrometry, in preparation for submission to *Chemical Communications*.
4. **Jay G. Forsythe** and John A. McLean, Nanomaterial-based MALDI-MS Imaging of Biological Samples, in preparation for submission to *The Analyst*.

3. Libin Xu, Michal Kliman, **Jay G. Forsythe**, Zeljka Korade, Anthony B. Hmelo, Ned A. Porter, and John A. McLean, *In situ* Analysis of Cholesterol and 7-dehydrocholesterol in Cells via Sputtered Silver Nanoparticle-assisted LDI-IM-MS, in preparation for submission to *Analytical Chemistry*.
2. **Jay G. Forsythe**,<sup>#</sup> Sarah M. Stow,<sup>#</sup> Hartmut Nefzger, Nicholas W. Kwiecien, Jody C. May, John A. McLean, and David M. Hercules, Structural Characterization of Methylenedianiline Regioisomers by Ion Mobility and Mass Spectrometry I. Electrospray Ionization of Dimers. Submitted to *Analytical Chemistry*. (<sup>#</sup>co-first author)
1. **Jay G. Forsythe**, Joshua A. Broussard, Jenifer L. Lawrie, Michal Kliman, Yang Jiao, Sharon M. Weiss, Donna J. Webb, and John A. McLean, Semitransparent Nanostructured Films for Imaging Mass Spectrometry and Optical Microscopy, *Anal. Chem.*, **2012**, *84*, 10665-10670.

### PRESENTATIONS

7. **Jay G. Forsythe**, Cody R. Goodwin, Jody C. May, Kelly M. Hines, Nichole M. Lareau, and John A. McLean, Advances in Comprehensive Metabolomic Strategies Using Structural Mass Spectrometry (*talk*), 65<sup>th</sup> SERMACS Meeting, Atlanta, GA, November 2013.
6. **Jay G. Forsythe**, Plamen Christov, Padma Portonovo, Sarah M. Stow, Joshua A. Broussard, Jenifer L. Lawrie, Michal Kliman, Yang Jiao, Sharon M. Weiss, Donna J. Webb, and John A. McLean, Nanostructure-Initiator Mass Spectrometry: Practical Insights, Fundamental Implications, and Emerging Applications (*poster*), 61<sup>st</sup> Meeting of the American Society for Mass Spectrometry, Minneapolis, MN, June 2013.
5. **Jay G. Forsythe**, Michal Kliman, and John A. McLean, Semi-transparent NIMS Substrates for Mass Spectrometry Imaging and Optical Microscopy (*poster*), 60<sup>th</sup> Meeting of the American Society for Mass Spectrometry, Vancouver, BC, Canada, May 2012.
4. **Jay G. Forsythe**, Joshua A. Broussard, Jenifer L. Lawrie, Michal Kliman, Yang Jiao, Sharon M. Weiss, Donna J. Webb, and John A. McLean, Nanostructured Films for Cellular Analysis: Integrating MS Imaging with Optical Microscopy (*poster*), Vanderbilt Institute of Chemical Biology Symposium, Nashville, TN, August 2011.  
*T-3<sup>rd</sup> place*
3. **Jay G. Forsythe**, Michal Kliman, Yang Jiao, Jenifer L. Lawrie, Sharon M. Weiss, and John A. McLean, Optimization of Porous Silicon Films for Nanostructure-Initiator Mass Spectrometry Imaging (*poster*), Vanderbilt Institute of Chemical Biology Symposium, Nashville, TN, August 2010.
2. **Jay G. Forsythe**, Michal Kliman, Joshua A. Broussard, Donna J. Webb, and John A. McLean, Lipid Analysis Using Nanostructure-Initiator Mass Spectrometry (*poster*), 37<sup>th</sup> FACSS Meeting, Raleigh, NC, October 2010.
1. **Jay G. Forsythe**, Floyd E. Stanley, Lydia E. Cronic, Noel A. P. Kane-Maguire, and John F. Wheeler, Chiral Capillary Electrophoresis in the Separation of Diimine Complexes of Cr(III) Exhibiting Potential as DNA Photocleavage Agents (*poster*), John Dorsey Separation Science Award Symposium at the 59<sup>th</sup> SERMACS Meeting, Greenville, SC, October 2007.

## TEACHING EXPERIENCE

### **Guest Lecturer**

Nashville State Community College, Nashville, TN, March 18, 2013

### **Analytical Chemistry Laboratory TA**

Vanderbilt University, Spring 2012

### **General Chemistry Recitation TA**

Vanderbilt University, Fall 2010-11, Fall 2012, Fall 2013

### **General Chemistry Laboratory TA**

Vanderbilt University, Fall 2009 - Spring 2010

### **Chemistry Laboratory Techniques TA**

Furman University, Fall 2008 - Spring 2009

### **ACS Student Chapter (Catalyst) Chemistry Tutor**

Furman University, Fall 2008 - Spring 2009

## AFFILIATIONS

American Society for Mass Spectrometry (ASMS): member 2012 - present

American Chemical Society (ACS): student chapter 2005 - 2009, member 2010 - present

## INSTRUMENTATION AND EXPERIENCE

Graduate Research: MALDI and ESI ionization methods, drift-tube and traveling-wave IM-MS, MALDI-TOFMS instrumentation, imaging MS, nanomaterial-based LDI-MS, UV laser optics, nanomaterial synthesis, electron microscopy, UV-Vis and IR spectroscopy

Undergraduate Research: UV-Vis and IR spectroscopy, chiral capillary electrophoresis, isothermal titration calorimetry, NMR, cyclic voltammetry